IMPERIAL COLLEGE OF SCIENCE, TECHNOLOGY AND MEDICINE

UNIVERSITY OF LONDON

THE IMPROVEMENT OF ULTRASONIC APPARATUS FOR THE ROUTINE INSPECTION OF CONCRETE

by

Robert Long

A thesis submitted to the University of London for the degree of

Doctor of Philosophy

Department of Mechanical Engineering
Imperial College of Science, Technology and Medicine
London SW7 2BX

March 2000

Abstract

The most common application of ultrasonic testing in civil engineering is to determine the velocity of sound in concrete, which is related to concrete quality. This thesis addresses some of the limitations of current commercial apparatus used for determining ultrasonic pulse velocity in concrete. The intention is to recommend improvements to enhance the reliability of measurements and make application more convenient.

The velocity of sound in concrete measured by commercial apparatus is known to vary with the path length being tested. Attenuation of sound in concrete, commercial transducer characteristics, and determination of signal transit times have been investigated. From this study, a function has been derived to correct measurement errors.

Commercial equipment is calibrated by coupling the transducers to a reference bar and setting the apparatus display to a time value stamped on the bar. To validate the time value, an experimental and finite element study have been carried out on wave propagation in a finite length of bar. To aid interpretation of data, signal-processing techniques have been investigated that are suitable for the evaluation of wave velocities in dispersive systems. Results suggest that the time value corresponds to a relatively low energy component propagating at the longitudinal bulk wave velocity. Reliable calibration can be achieved when the apparatus recognises the component, which is dependent on the acoustic coupling made by the transducers to the reference bar.

Currently, viscous couplant must be applied between the transducer face and the concrete surface under test to facilitate signal transmission. Consistent coupling is difficult to achieve and couplant application and removal proves time consuming and inconvenient. Alternative coupling has been investigated; one technique that looks promising is rubber coupling. Contact models have been derived to predict the deformations of rubber coupled devices when loaded onto rough surfaces and thereby predict signal transmission. Experiments and predictions suggest that dry rubber coupling of transducers using a hand held device might not be feasible. However, more convenient coupling has been achieved when wetting a prototype rubber coupled membrane device with very little water.

Acknowledgements

I would like to thank my supervisors, Mike Lowe and Peter Cawley, for giving me the opportunity to study in the NDT group at Imperial College. They provided essential guidance within a subject area that was alien to me prior to commencement of this project.

Welcome advice was often provided by other members of the non-destructive testing group at Imperial College. I enjoyed my studies amongst you. Many thanks to Christophe Aristegui who adapted my computer programs so that they were of some use to others.

I must thank the EPSRC for providing a 3 year scholarship that enabled me to pursue this project.

Lastly, I thank my family and friends. Without your support I am sure I would never have completed let alone started my studies.

Contents

Chapter 3

Correction of measured transit times for apparatus such as the PUNDIT

Chapter 4

Validation of PUNDIT calibration procedure

Chapter 5

Convenient Coupling

Chapter 7

Conclusions and future work

Appendix 1

Signal processing for dispersive systems

Appendix 2

Component drawings for prototype membrane shoes

List of Tables and Figures

Tables

Figures

Nomenclature

A	Wave amplitude, area, coefficient
a	Radius, scale
b	Constant, translation, radius
B	Calibration constant
c	Wave speed, overlap ratio
c	Elastic coefficient matrix
c_{ij}	Elastic constant
C	Constant of integration
C_v	Constant volume function
CA	Contact area
d	Diameter, differential operator
D	Diameter, flexural rigidity
D_N	Large displacement flexural rigidity
E	2.71828... (ln(e)=1)
E	Youngs' Modulus
f	Frequency (Hertz)
F	Total load
F(n,m)	Flexural mode
f(t), g(t)	Time domain functions
F(f), G(ω)	Frequency domain functions
g	Surface profile
G	Maximum surface amplitude
h	Thickness
i	$\sqrt{-1}$, integer
I(r, b)	Influence coefficients
j	Integer
k	Wave number
k(r)	Finite thickness correction factor
L	Path length
L(n,m)	Longitudinal mode
m	Integer, ratio
m_d	Dimple ratio

n	Integer
N	Near field distance, integer, tension component
p	Pressure
P	Wave amplitude
q	Intensity
r	Radius, integer
R_a	Centre line average
R_n	Random number
s	Arc length, integer
S	Stiffness
S	Stress tensor
S_{xy}	Strain vector
t	Time
τ	Dummy time variable
T	Stress tensor
T	Transmission ratio
T_{xy}	Stress vector
u	Displacement
x, y, z	Cartesian co-ordinate axis
x_1, y_2,	Cartesian co-ordinates axis
u	Displacement vector
v_{ph}	Phase velocity
v_{gr}	Group velocity
V	Volts
w	Surface displacement, rotation
w′	Overlap function
w	Rotation vector
W	Load
W_ψ	Wavelet transform coefficient
z	Pulse propagation distance
Z	Acoustic impedance

α	Attenuation coefficient (Nepers/m), radial wave number, angle, contact ratio
β	Wave number, correction factor
β^*	Correlation length
δ	Partial deferential operator
ε	Coefficient, axial wave number
γ	Time constant
∞	Infinity
λ	Wavelength, Lamés constant
μ	Lamés constant
η	Coefficient
ω	Frequency (Radian/s)
ϕ	Phase, probability function
$\psi(t)$	Wavelet function
π	3.141592....
ρ	Density
σ	Standard deviation
σ_m	Surface slope
θ	Angle
ν	Poisson's ratio
ζ	Coefficient
Φ	Accumulative probability distribution
Δ	Interface displacement, dilation
∇	Vector differential operator
∇^2	Laplace operator

Chapter 1

Introduction

1.1 Introduction

Concrete is a complex composite material having a wide variety of specifications. Useful background information on concrete constituents and properties can be found in text given by [Mindess and Young (1981)] and [Neville (1996)]. Should you wish to lay a patio in your back garden or perhaps build a bridge over the Thames or a skyscraper in Manhattan, you may well consider mixing yourself up a batch of concrete. Take one bucket of cement, two buckets of sand and three buckets of graded aggregate to bulk out the volume and reduce shrinkage. You will also require about 1/2 to 3/4 bucket of water depending on the strength desired, and a squeeze of plasticiser to make the mixture more workable. Mix well and pour into a mould of desired shape, compact, and allow to set. Concrete reaches half its strength after about 3 days and 90% after 28 days. What you have is a very versatile, potentially durable composite material, that is strong in compression but about 90% weaker in tension such that structural members subject to tensile stress are reinforced with steel bars. The setting of concrete is not a drying out process but a chemical reaction called hydration, where the calcium silicates in the cement react with the water to form hydrates and is accompanied by the evolution of heat. In the early stages of hydration, water rises and aggregate settles, such that the surface concrete is not representative of the overall volume. The structure of the cement hydrate to a large extent determines the durability of the concrete. There are inherent pores of a few nm, and pores 50 to 100 times larger as a result of the presence of excess water above that required to complete hydration. Additionally there may be air pockets or volumes of lower density due to inadequate compaction. It is also likely that all concrete has an extensive crack system induced by shrinkage, thermal movements, loading and a number of other causes.

Concrete in service is exposed to a wide variety of environments and, because of its physical and chemical nature, may deteriorate as a result [Perkins (1997)]. The pores and the crack system provide passage ways by which acidic moisture and gases that attack the alkaline concrete can penetrate. Once deterioration is apparent, its classification and extent need to be appraised so that appropriate remedial action can be specified.

Routine testing of concrete is primarily concerned with assessing current adequacy and future performance [Bungey and Millard (1996)]. An initial visual inspection of the site can prove valuable in locating deterioration and aid the choice of an appropriate method of test. If you had walked around under the Hammersmith flyover in West London UK in the late 1990s then you may well have noticed the cracking, spalling and brown stains that indicate reinforcement corrosion on the supporting columns. You might also have noticed where appropriate remedial action had not taken place, such that the surface of the deteriorating concrete dislocated and fell off exposing the reinforcement to the atmosphere.

There are several diverse techniques for inspecting concrete in-situ quality or integrity for which detailed references are given in Chapter 2. Each technique has its own particular advantages and limitations, there being no universal panacea. Concrete quality is often assessed by determining concrete strength. The most reliable methods are those that cause the most damage, such as the taking and crushing of cores, and the pull-out (requiring pre-planned inserts to be set in structure) and pull-off tests. Methods that cause little or no surface damage are most suitable for establishing comparative quality since correlation of results to strength is empirical and often unreliable. Ultrasonic pulse velocity measurements in concrete is a well established non-destructive technique. Low frequency narrow band transducers are grease coupled to the structure. The time taken for a pulse to propagate through the material gives the velocity of sound, which is related to concrete quality. Low velocity might signify deterioration or presence of a void since the pulse would have to defract around this, and higher velocities may infer damp concrete.

Ultrasonic testing is particularly attractive due to its relatively low cost, rapid inspection and that it is non-destructive [Bungey and Millard (1996)]. The preferred technique is to mark out a grid pattern on the structure and measure the pulse velocity at each grid point. Results are then often plotted as a 2D surface map to aid the identification of problem areas. Current equipment has limitations, one being that a viscous couplant must be applied to the faces of the transducers to achieve good acoustic coupling. This practice becomes particularly inconvenient, messy and time consuming when performing a large number of measurements on a grid. Additionally it is known that with commercial apparatus the measured velocity varies with the path length being tested. When absolute values of the velocity of sound in concrete are required, this anomaly can become significant.

The work described in this thesis concentrates on developing ideas to improve the current commercial ultrasonic apparatus used for the routine inspection of concrete. An investigation into the cause and effect of measurement errors was conducted in order to recommend

remedial action. Alternative coupling of ultrasonic transducers was investigated to make the technique more convenient. Each of the chapters in this thesis is largely self contained and describes a particular aspect of the project. The order of the chapters approximately follows the chronological order in which the work was carried out by the author.

A description of the material properties of concrete is given in Chapter 2. This provided some background information on concrete alerting the author to the complex composite nature of concrete which is prone to wide specification variations due to the abundance of mixes and construction practices possible. A review of existing and emerging non destructive inspection techniques follows for which detailed references are given. This part of the work was conducted to assess the advantages, disadvantages, limitations, and popularity of pulse velocity ultrasonic apparatus among its competing technologies. The technique was found to stand out for its low cost and rapid inspection. The limitations of unreliable results and inconvenient coupling were identified and proposed to be addressed by this research. The chapter ends with an investigation into the operation of the PUNDIT test equipment [PUNDIT 6 operating manual], which is the standard pulse velocity apparatus used in the UK. It would be to such equipment that improvements recommended in this thesis would apply.

Chapter 3 describes work conducted to investigate the extent of inherent measurement errors associated with commercial pulse velocity apparatus. It is known that the measured pulse velocity varies with the path length being tested for apparatus such as the PUNDIT that adopts threshold crossing to determine signal arrival times. The factors that contribute to this anomaly were investigated. Signal losses due to beam spreading were predicted along with an experimental investigation to obtain functions that describe signal attenuation as a function of excitation frequency due to material properties. Commercial transducer and excitation characteristics was explored to model the pulse emitted from a transducer. From these studies, the extent of the anomaly when testing various concrete mixes was predicted and a function has been derived to correct measurement errors.

The method used to calibrate commercial apparatus prior to conducting pulse velocity measurements was investigated in Chapter 4. Calibration is required when absolute values of the velocity of sound in concrete are required and is achieved by coupling the transducers to a bar and setting the apparatus display to a time value that is stamped on the bar. The time value relates to the time that it would take a longitudinal bulk wave to propagate the length of the bar. A finite element study was conducted to validate the time value since classically bulk wave propagation in a bounded medium is not presumed. To aid interpretation of data,

signal-processing techniques have been investigated that are suitable for the evaluation of wave velocities in dispersive systems. A comparison between the performance of the established phase spectrum technique and two methods developed by the author is presented in Appendix 1. Consideration of processed finite element and experimental results enabled an evaluation of the standard calibration procedure.

The development of hand held devices that would enable the convenient coupling of transducers is dealt with in chapter 5. In this work attention was focused on appraising solid coupling as an alternative to the current practice of using a viscous couplant. The topology of a range of concrete surfaces were surveyed. For rubber contact with such surfaces the characteristics of ultrasonic transmission across a low load interface was investigated experimentally. From this study a relationship between signal transmission and true contact area was argued. Numerical contact models were derived to predict the true contact area as a function of applied load that an axi symmetric body makes when pressed onto a real rough surface and thereby predict signal transmission. Such models would enable the design optimisation of a solid coupling device. A simple to program solution technique was developed to solve the contact model equations. Model predictions were validated against classical analytical solutions and experimental verifications. The performance of dry rubber coupling transducers to concrete was evaluated by employing a combination of experimental results and model predictions. The transmission across a dry coupled low load interface was shown not to be sufficiently strong for most practical applications. However such devices were found to still be attractive when wetted just with water, which would still avoid the inconvenience of conventional viscous coupling.

Chapter 6 reports on the application of convenient coupled devices for the inspection of concrete structures. The development of prototype membrane shoes designed to attach to standard commercial transducers is discussed where model predictions were utilised to optimise the design. A trial inspection of two concrete blocks was conducted so as to compare test results when wet membrane coupling transducers to those when conventional viscous coupling. Performance of a technique was judged by the time to complete an inspection, preparation and clean up times, and repeatability of results.

The main conclusions of chapters 2 to 6 in this thesis are collated in chapter 7. Specific issues that have been raised in this thesis are outlined and appropriate future work proposed.

The work presented in this thesis forms a submission for a Ph. D. In Mechanical engineering from the University of London (Imperial College). Unless otherwise stated, the work is the author's own. It builds on a long history of wave and contact mechanics, which are summarised within the relevant sections of later chapters. As far as the author is aware, the novelty of the work contained in this thesis includes,

- A suggested function to correct pulse velocity measured by commercial equipment for path length tested. Only the extent of the anomaly has been reported previously.

- Signal processing techniques have been developed around the wavelet and Hilbert transforms to extract group velocities from dispersive signals.

- For fractional contact ratios of the order of less than 10%, the case was argued that the signal transmission across an imperfect interface was proportional to true contact area. Established models are known to agree well with experimental results for greater contact areas, however very little work has previously been conducted in this regime.

- Derivation of axi symmetric numerical contact models for solid body and especially liquid filled devices loaded onto real rough surfaces.

- Development of an iterative technique to solve contact equations, which the author suggests is simple to program and structured in an intuitive manner.

- Development of a novel hand held wetted rubber membrane coupled device. Coupling transducers to concrete with such a device was shown to offer improved repeatability of results and make pulse velocity testing of concrete more convenient and less messy.

Chapter 2
Review of the inspection of concrete structures

2.1 Introduction

This chapter provides some background information on the material characteristics of concrete and then reviews some of the non-destructive techniques used to inspect concrete structures. Finally a description of the PUNDIT ultrasonic apparatus is given. It will be to such equipment that recommendations made in this thesis will apply.

2.2 Concrete material characteristics

The following describes the heterogeneous nature of concrete, its inherent volume variations and the need for inspection. Useful background information on concrete constituents and properties can be found in text given by [Mindess and Young (1981)] and [Neville (1996)].

2.2.1 Material Constituents

Concrete is a complex composite material, which begins its life as a mixture of graded stone aggregate particles suspended in a fluid of cement and water and admixtures.

The most common cement material used is Portland cement [PCA (1994)], the manufacture of which consists of heating together ingredients which contain the desired combination of calcium, silicon, aluminium and iron oxides until they fuse to form a clinker. The clinker is ground down with the addition of gypsum to produce the familiar fine powder. The main raw materials are chalk or limestone and shale or clay whose properties are subject to local variations. Aggregates such as gravels, crushed rock and sand are used in concrete chiefly as inert fillers to bulk out the volume and reduce shrinkage during hydration [ACI (1996)]. They are characterised by their mineralogical nature and their form. Admixtures are materials added in relatively small quantities to concrete during the mixing process to modify its properties in the fluid or hardened state.

The overall proportions of the principal ingredients are controlled by the requirements that: when the mass has hardened, it possesses strength and durability for the purpose for which it is

intended; when freshly mixed the mass must be workable; and the cost of the final product be a minimum consistent with accepted quality. Nominally, aggregate occupies 75% of the volume, cement about 15% and water content 10%. The priority when choosing a mix design is strength, which along with permeability of the concrete is governed by the water-cement ratio. For high strength and low permeability the water-cement ratio should be low. The workability that describes the ease of placing and compaction, for a fixed water-cement ratio, is adjusted by choice of aggregate quantity, grading and shape, and also by the assistance of chemical plasticizers. Larger, rounded aggregate tends towards greater workability. It is usual for the coarse aggregate used in structural concrete to have a nominal maximum size of 20mm.

2.2.2 Hardening of the cement paste

The mixture remains fluid or plastic until the development of the cement hydrates which gradually solidify to form a paste that surrounds the aggregate particles and binds them together giving form and strength to the mass [PCA (1994)]. The chemical reaction involves the water and material on the surface of the cement particles forming gel which may have twice the volume of the cement from which it was produced. As hydration proceeds the gel extends outward from each particle to join with gel from other particles, to form a skeletal type structure that strengthens the paste. The process continues over an extended period releasing heat, but occurs at the maximum rate during the first few days. The cement paste, comprising mainly calcium silicate hydrate, has no clearly defined crystalline structure and its actual composition is indeterminate, yet to a very large extent its character determines the durability of the concrete and the nature of any deterioration [Mays (1992)]. Denser pastes gives rise to greater strength and lower permeability. The properties of the hardened cement paste depend upon: the characteristics of the cement; the relative proportions of cement and water by weight; and the completeness of the hydration. The paste has an inherent porosity with very fine pores of about 4 nm in diameter, and considerably larger capillary pores whose volume and pore diameter increase with higher original water-cement ratio (200-500 nm for a water-cement ratio of 0.65). In addition the paste will contain air voids much larger than the capillary pores resulting from incomplete compaction and unhydrated remnants of cement grains. The capillary porosity in the paste makes concrete permeable to liquids and gases. Since hydration is a chemical reaction, the quantity of water required for complete hydration is fixed by the chemistry of the cement. For Portland cements a water-cement ratio of at least 0.23 is required for one month of hydration. However, to achieve full hydration and render the fluid concrete workable, an excess of water is required, such that water-cement ratios vary between 0.4 to 0.7. Thus all concrete has a pore system much larger than that which is inherent [Neville and

Brookes (1990)]. The extra water not used in hydration remains within the pore system and will eventually dry out if climatic conditions or the location of the concrete permit.

2.2.3 Characteristics of the hardened product

The strength of concrete is controlled by: strength of the matrix; strength of the bond between matrix and aggregate; strength of the aggregate and the extent of any crack system. The brittle matrix is reported [Mays (1992)] to demonstrate a viscoelastic nature. Although relatively strong in compression, concrete is weak in tension such that structural members subject to tensile stress are reinforced with steel bars.

Properties vary within a concrete member due mainly to differences of compaction and curing as well as non-uniform supply of material [Waddell and Dobrowoski (1999)]. Compaction and curing variations can be shown to follow well-defined patterns according to the type of structure, whereas the generally small material and mix variations can be assumed to be random.

Compaction and curing effects will depend partially upon construction techniques but also are closely related to member types and location within the member [Neville (1996)]. Compaction may be hindered by reinforcement leading to voids and density variations. Lower levels of structures will experience greater compaction due to hydrostatic effects related to member depth, such that density tends to be higher at the base than in the upper region.

The aim of curing is to ensure that sufficient water is present to enable hydration to proceed. As the extra water not required for hydration evaporates there is a shrinkage of the cement gel. The shrinkage of the gel fraction is restrained by the presence of aggregate. However, widespread cracking can occur if the upper layers of the concrete dry and shrink much more rapidly than the interior. Inadequate curing may also cause strength variations between interior and surface zones in the order of 5-10% [Bungey and Millard (19960] for gravel concretes.

During early hydration there is a tendency for moisture to rise and aggregate to settle known as bleeding. The effect is that the cement paste in the upper portion is diluted and when hardened is weaker than the average at full depth. For this reason coring for strength determination or chemical analysis is not carried out on the top 10% of a sample [Conc. Soc. (1987)]. Some of this bleeding water may be trapped under reinforcement bars and larger pieces of aggregate forming water pockets. Local variations in bleeding rate, or evaporation of water from the

surface at a rate faster than the bleed rate cause bulk volume variations, which lead to cracks if the concrete cannot follow the change in volume. It is likely that nearly all concretes have an extensive system of microcracking induced by drying shrinkage and also by thermal movements [Kay (1992)]. It is not until the cracks become macro-sized that problems arise.

2.2.4 The need for inspection

Assessment of in-situ quality and integrity is primarily concerned with the adequacy of the existing structure and its future performance. Generally it is either the in-situ strength or durability of a structure that is regarded as the most important criterion. Evidence is often required to identify the extent of internal voids and crack systems, as a result of inadequate workmanship. The monitoring of long term changes in material properties, crack systems, and structural performance is a necessary part of any maintenance program. Well designed, compacted and cured structural concrete can be a very durable material. However, concrete in service is exposed to a wide variety of environments and, because of its physical and chemical nature, may deteriorate as a result [Perkins (1997)]. The structure of cement hydrates contains pores or capillaries, and these along with cracks provide passage ways by which acidic moisture and gases that attack the alkaline concrete can penetrate. Once deterioration is apparent its classification and extent need to be appraised so that appropriate remedial action can be specified.

The most reliable methods for assessing concrete strength are those that cause the most damage [Bungey and Millard (1996)] such as the taking and crushing of cores, the pull-test which requires pre-planned inserts to be set into the structure, and the pull off test which does not require preplanning.

Tests that cause little or no surface damage are most suitable for determining comparative concrete quality [Malhotra and Carino (1991)], since correlation of their results to strength values are empirical and often unreliable. There are two methods that are popular, surface hardness and ultrasonic pulse velocity. For both these tests it is recommended that the test be carried out on a grid and the results plotted as a contour map so as to aid location of differences in quality. Testing for local integrity, involving looking for voids, delaminations and other discontinuities, can be assessed by impulse radar, infrared thermograghy and impact echo techniques. Radar is perhaps the most popular, but like all integrity test equipment there is a lot of room for improvement in current signal processing used. It is likely that this is the reason why inspecting for integrity is less common than for strength.

At present civil engineering has the greatest confidence in the most destructive methods of test [Bungey and Millard (1996)]. For a non-destructive test to be accepted would predominantly require that its results are not ambiguous, costs involved with its use are low, and it should be convenient and rapid to employ.

2.3 Concrete non-destructive inspection techniques

The following section discusses the attributes of various non-destructive inspection techniques, both mature and emerging, used for assessing the *in situ* comparative quality and localised integrity of concrete. Non-destructive testing is generally defined as not impairing the intended performance of the element or member under test. When applied to concrete, tests are included that cause localised surface zone damage. All non-destructive methods can be performed directly on the in-situ concrete without removal of a sample although removal of surface finishes is likely to be necessary. For comparative purposes the truly non-destructive methods are the most efficient, since their speed permits a large number of locations to be easily tested. Recommendations for the use of non-destructive methods when testing hardened concrete are given in BS1881: part 201.

2.3.1 Rebound Hammer

The rebound hammer provides an empirical measure of the hardness of a localised area of the concrete surface. The rebound principle is well established and widely accepted for assessment of concrete uniformity, determination of areas of poor quality or deterioration, and to indicate changes in characteristics with time. The most popular equipment, the Schmidt Rebound Hammer, was first developed in the late 1940's by the Swiss engineer Ernst Schmidt as shown in Fig 2.1. The hammer works by impacting a spring loaded mass on a plunger which is in contact with the surface. The distance which the mass rebounds, which is indicated on a sliding scale, is a measure of the hardness of the surface, for which correlation graphs are available [Naik and Malhotra 1991]. The scale reading is known as the rebound number, which is an arbitrary reading that also depends on the energy stored in a given spring and the mass used. Recommendations for the use of the rebound hammer method are given in BS1881:Part 202(45) and ASTM C805(46). It is suggested [Schickert (1994)] that the Schmidt hammer is the most common test carried out on in-situ concrete within Germany, with other tests finding little acceptance.

The technique is well documented, providing numerous references on its use on various structures. It is suggested [Bungey and Millard (1996)] and [Naik and Malhotra (1991)] that the advantages of the method are that it gives a quick rough idea of the quality of concrete, it is simple to operate, requires a low skill level, is robust, weighs less than 2kg, and has a low relative cost of operation. They suggest that the limitations of the technique are;
The test is highly localised and only the concrete within approximately 30mm of the surface contributes to the result, and since the surface layer may not be representative of the concrete at depth, readings can only reflect surface layer stiffness.
If the rebound hammer is to be used to assess strength then it is necessary to determine an individual correlation curve for the concrete under consideration, though in a practical situation it is unlikely that a strength predication can be made to an accuracy of 25%;
The reading is very sensitive to local variations in the concrete, especially to aggregate particles near the surface. It is therefore necessary to take several readings at each test location, accepting the average if the readings agree with statistical criteria;
The surface must be smooth, clean and dry with loose material ground off;
Hammer orientation has an influence on measured values, although correction factors can be used to allow for this effect. Since a smooth, well compacted surface is required for tests, variations of strength due to difficulties in internal compaction cannot be detected with any reliability.

2.3.2 Infrared Thermography

Detection of delaminations or voids by the emerging technique of infrared thermography is based on the principle that sub surface anomalies effect the rate of heat flow through the material. These changes in heat flow cause variations in the surface temperature. For large structures such as bridge decks and highways, solar heating is often sufficient, providing temperature gradients are greater than 2^{o}C. The best time for such testing is usually after sunset when the structure begins to cool down. Procedures for thermography in the investigation of bridge deck delaminations are given in ASTM D4788(234). The technique has been found to be useful in assessing the heat distribution in concrete during hydration [Bungey and Millard (1996)], during which time stresses due to temperature differentials may cause cracking particularly in the surface zone. There is limited documentation of the technique, the main advantage appears to be that large areas can be scanned quickly (15mph on highways) from a distance (up to 20m on bridge decks) on one side [Weil (1992)]. It is also stated that the main disadvantage of the technique is that the depth of a void cannot be determined, although its outer dimensions are evident, suggesting it be combined with radar or ultrasonics inspection. Bungey and Millard [1996] suggest that the main limitations of the technique are its high

relative cost, the skill level required to interpret images and that presently it is suitable for finding only large scale flaws, where the smallest defect that can be detected is reported to be 200mm x 200mm.

2.3.3 Radiation methods

There are three basic radioactive methods that have been steadily developed over recent years for testing of concrete: x-ray radiography; gamma-ray radiography and gamma-ray radiometry. Radiographic methods involve exposing special photographic material to radiation transmitted through a concrete structure. The intensity of the transmitted incident energy is a function of the material traversed and attenuation due to energy absorption and simplified is given by the following equation [Bungey and Millard (1996)]

$$I_x = I_o e^{-\mu m} \qquad 2.1$$

where I_x is the emergent intensity, I_o the incident intensity, μ the mass absorption coefficient and m the mass per unit area of material traversed.

In the x-ray range attenuation is dependent on both the atomic number and density of material, where as for the gamma-ray range, density is the principal factor. X-rays are generated in an x-ray tube when a beam of electrons is accelerated on to a target by a high voltage (typically 8MeV) and stopped suddenly on striking the target. The x-rays produced have different wavelengths and different penetrating powers according to the accelerating voltage. Since the equipment is bulky not much application has been seen outside the laboratory [Nagy (1997)]. Gamma rays are electromagnetic radiation emitted from the nucleus of radioactive elements, and being much more portable, have become the principal radioactive method for on-site use. The choice of source, which is usually a radioactive isotope, depends on the thickness of the concrete involved. Iridium 192 is used for 25-250mm thickness, Cobalt 60 (1.17 and 1.33MeV typically) for 125-500mm. For thickness above 450mm exposure times become relatively long, such that a 6MeV switchable x-ray source which reduces exposure time to 15-20mins is preferable. Kear [1994] reports on the use of radiographic inspection of post-tensioned concrete bridges, suggesting that the short wave length and particle behaviour of the transmitted energy provided high resolution radiograph images of the concrete interior, informing on location of voids and reinforcement. The development of a portable device is discussed by Ewert [1997]. The main disadvantages with radiography were reported to be that it requires access to both sides of structure, the adverse response by public to the use of hazardous radiation and the high radiographic exposure times in concrete. BS 1881:PART

205(272) provides guidance on radiographic work, including suitable sources of radiation, safety precautions and testing procedures.

Gamma radiometry involves the use of a concentrated source and a detector to receive emissions at a localised point on the member under test. There are two techniques of radiometry: the direct and the backscatter method. In direct methods the source and receiver are placed on opposite sides of a member. The intensity of the received signal is an indication of the attenuation due to through transmission. The approach is most often used to measure local density, but may also be adapted to assess member thickness or location of reinforcement. As the high-energy radiation passes through the concrete some is absorbed, some passes through completely, and a considerable amount is scattered by collisions with electrons in the material. The scattering forms the basis of backscatter methods, which are suitable for testing the outer 100mm of concrete. The gamma-ray source and detector angled at approximately 45^{o}, are fixed close together in a suitably screened frame which is placed on the concrete surface.
The main limitations of the technique [Halmshaw (1987)] are that gamma sources cannot be switched off, the 1985 Ionising Radiation Regulations must be complied with, highly trained licensed operators are required and backscatter results are only reliable to limited depths.

2.3.4 Ultrasonic techniques

Ultrasonic methods have been used for assessing comparative strength of concrete, detecting flaws such as voids or cracks, and estimating member thickness. The inspection of concrete by ultrasonic methods is well documented and mature being first established in the 1940's. Ultrasonic techniques involve the propagation and detection of mechanical vibrations that have interacted in some way with the structure under test. When the surface of a semi-infinite solid is excited by a time varying mechanical force, energy is radiated from the source as three distinct types of elastic wave propagation. The fastest of these waves has particle displacements in the direction of travel of the disturbance and is called the longitudinal, compression or P-wave. The compression wave velocity V_P is a function of the dynamic Young's modulus E, the Poisson's ratio υ, and the mass density ρ, [Krautkramer &Krautkramer (1969)], and is given by;

$$V_P = \sqrt{\frac{E(1-\nu)}{\rho(1+\nu)(1-2\nu)}} \qquad 2.2$$

The second fastest is the shear, transverse or S-wave, which has particle displacements perpendicular to the propagation direction. The shear wave velocity V_S is a function of the dynamic shear modulus G and ρ,

$$V_S = \sqrt{\frac{G}{\rho}} \qquad 2.3$$

Young's and the shear moduli are related by

$$E = 2G(1+\nu) \qquad 2.4$$

Compression and shear wave velocities are theoretically interrelated by Poisson's ratio υ, which can be expressed as

$$\nu = \frac{0.5 - (V_S/V_P)^2}{1 - (V_S/V_P)^2} \qquad 2.5$$

The compression and shear waves propagate throughout the material in all directions. The third type of wave-motion produced travels along the surface and has elliptical particle motion, where the component of displacement normal to the surface is greater than the component in the direction of wave propagation. The velocity, V_R, of this surface wave, known as the Rayleigh wave, in simplified form is given by

$$V_R = AV_S \qquad 2.6$$

where A is a function of υ and V_S. The ratio of V_R/ V_S increases as Poisson's ratio increases, but not significantly. For values of υ from zero to 0.5 the ratio of V_R/ V_S changes from approximately 0.87 to 0.96 [Sansalone and Carino (1991)].

Ultrasonic inspection of concrete is basically the evaluation of one or more of these wave velocities. Since wave velocity is a direct indication of stiffness of the material, a higher wave velocity is associated with higher stiffness.

When an ultrasonic wave is incident on a plane boundary between two media, some of the ultrasonic energy is transmitted through the boundary and some is reflected. The percentages of energy transmitted and reflected depend on the specific acoustic impedance , Z,

$$Z = \rho V \qquad 2.7$$

where ρ is the density of the material and V is the velocity of the wave. For two materials of different acoustic impedances Z_1 and Z_2 the percentage energy transmitted E_T is given by Halmshaw [1987] as;

$$E_T = \frac{4Z_1Z_2}{(Z_1+Z_2)^2} \times 100 \qquad 2.8$$

and the reflected energy E_R, by

$$E_R = \left(\frac{Z_1 - Z_2}{Z_1+Z_2} \right)^2 \times 100 \qquad 2.9$$

For amplitude values the square root of the above equations are taken. The equations are valid for both compression and transverse waves, but as a transverse wave cannot be sustained in a liquid, a transverse wave at normal incidence is always completely reflected at a solid/liquid or solid/gas interface.

The resolution of an interrogating signal is indirectly proportional to signal wavelength λ, given by the relationship $c = \lambda f$, where c is the phase velocity and f the frequency of excitation. Additionally, an electro-acoustic transducer has directional properties, where the main energy falls to zero at an angle of divergence θ, given approximately by

$$\sin\theta = \frac{1.22\lambda}{D} \qquad 2.10$$

where D is the diameter of the transducer [Krautkramer &Krautkramer (1969)] . Thus high frequencies in the MHz range are preferred for ultrasonic inspection. In practice an upper limit is imposed on the frequency by very high attenuation of vibrations whose wavelengths are comparable with the grain size of the material to be inspected. For fine grained materials such as steel or aluminium, frequencies of tens of MHz will propagate without undue attenuation, and thus it is possible to produce a pulse in which most of the energy is contained within a beam of about 5^o for a 16mm 5MHz transducer. In structural concrete however, the coarsest aggregate is of the order of 20mm, which imposes a practical upper limit of several hundred kHz. Frequencies of the order of 50kHz to 100kHz are popular for long range inspection of concrete [Bungey and Millard (1996)] (10m for 54kHz to 3m for 82kHz), however these frequencies imply wavelengths around 50mm, which for a standard 50mm diameter transducer, as described in Chapter 3, offers no directional properties at all and low resolution.

Nevertheless, the relation of wave velocities to mechanical properties, low relative cost and speed of operation make ultrasonics a popular choice, with much research being conducted world wide to improve the techniques. The following discusses a selection of techniques, by no means complete, both mature and emerging.

2.3.4.1 Pulse velocity

The most mature ultrasonic concrete inspection technique involves the generation of a pulse, transmitting this to the concrete, receiving and amplifying the pulse and measuring and displaying the time taken. A schematic of the technique is shown in Fig 2.2. In general, repetitive pulses are generated electronically and transmitted into mechanical wave energy by a piezo-electric transducer. Due to the attenuation effects of concrete, through-transmission utilising narrow band (minimal damping) transducers are preferred, so as to maximise the received signal. Good acoustic coupling (maximised transfer coefficient) between the concrete surface and transmitting transducer is provided by a suitable medium such as grease or petroleum jelly. Rough surfaces should be ground down or filled with a quick setting cement. A similar receiving transducer is coupled a known distance *d* away from the transmitter, and upon reception, the mechanical energy is converted back into electric pulses. An electrical timing device measures the interval between onset of excitation and reception and displays the signal transit time *t*. The velocity V_L is then calculated from the relationship

$$V_L = \frac{d}{t} \qquad 2.11$$

Since Poisson's ratio υ, and the mass density ρ, will vary little for concrete mixes with natural aggregates, the relationship between velocity and dynamic elastic modulus may be expected to be reasonably constant [Bungey and Millard (1996)]. However there is no direct relationship between velocity and strength in any medium. For this reason it is advisable to use the technique to acquire a map of velocity measurements which is then an indication of concrete uniformity.

BS 1881 Part 203 gives recommendations on the measurement of ultrasonic pulse velocity and BS 1881 Part 209 gives recommendations for the determination of dynamic modulus. Popovics et al. [1995] report on the comparison of standards that refer to determination of ultrasonic pulse velocity in concrete. Bungey [1991] reports that in the UK the usage of ultrasonic techniques on in situ concrete was almost exclusively limited to measurements of

ultrasonic velocity using through transmission techniques, with frequencies of the order of 50 to 80kHz

The PUNDIT apparatus (description and operation given in Chapter 2.4), manufactured by CNS Farnell London, is a popular choice of equipment for pulse velocity testing of concrete. The manual that accompanies the PUNDIT apparatus suggests that when applying grease to the transducers to ensure good acoustic coupling, care must be taken to eliminate air pockets, apply only a thin layer of couplant and avoid couplant contamination by dust or grit. Due to grease coupling unreliability, readings should be repeated from scratch. The problems of grease coupling when testing metals has been addressed by Drinkwater [1994] by the use of a rubber wheeled probe that eliminates the necessity of grease coupling and would increase the rate of inspection. Alternatively Wu et al. [1997] reports on using conical transducers that require no coupling. An exponentially shaped probe is available from CNS, for testing rough surfaces, but they recommend that it is used as a receiver only, due to the reduced amplitude of the transmitted signal

There is evidence that the measured velocity, for apparatus such as the PUNDIT, will decrease with increasing path length, a typical reduction of 5% for a path length from approximately 3m to 6m is reported [Naik and Malhotra (1991)]. Bungey and Millard [1996] suggest that the path length should be measured to an accuracy of ± 1%, which may be difficult for path lengths less than 500mm, and that the minimum path length is governed by the pulse wavelength being about 85mm for a 54kHz transducer frequency.

2.3.4.2 Pulse echo

The technique was first proposed by Firestone [1940] but has seen little application in the inspection of concrete, though much present research is being undertaken to rectify this. Emerging concrete pulse echo techniques are concerned with the evaluation of concrete from a single surface, with the aim to: detect air filled voids and cracks; locate structural elements such as reinforcement and ducts; and provide information on geometrical dimensions.

The technique requires a short time length pulse (broad in frequency domain) to be transmitted into the structure by a electro-acoustic transducer and received on the same surface by the same (pulse-echo) or an additional transducer (pitch-catch). A schematic of pulse echo is shown in Fig 2.3. Broad band transducers are required for pulse echo so that the pulse length can be less than the distance travelled. A 100kHz transducer and concrete with a sound velocity of 4000m/s results in a 40mm wavelength (from $c = \lambda f$). If a transducer rings down

to 4% of its original amplitude after 5 cycles, this would limit the minimum depth that could be inspected to 200mm (resolution distance). For less than 200mm path length the transducer would be still transmitting significantly while it was trying to receive the smaller amplitude echo. Similarly for pitch catch, the location of the first echo can be within one wavelength of the transducer, while subsequent echoes must be separated by the resolution distance or they will superimpose on the previous echo.

To achieve the broadband transducer characteristics necessary for pulse echo, a suitable material is backed onto the piezoelectric material to damp oscillations. The unwanted effect of this is to reduce the amplitude of the transmitted signal, and the sensitivity of the receiver, hence a reduction in received signal to noise. Attempts over the years have been made to develop pulse echo techniques for the inspection of concrete structures, [Bradfield and Garrfield (1964)], [Howkins (1968)], [Forrest (1977)], all of which suffered from impractical cumbersome transducers. Krause and Wiggenhauser [1997] report that using separate transducers and advanced signal processing techniques is the key to improved pulse echo tests on concrete. He also states that pulse echo inspection of concrete was reported in 1991 to be unpromising due to the backscatter of the pulse off aggregate that contaminates the received signal and the relative insensitivity of broad band transducers which results in low signal to noise, and concludes that a lot of research work is still required to enable identification of voids. Andrews and Hughes [1991] report that tungsten loaded epoxy has desirable low frequency damping characteristics, and that impedance of piezoelectric material should be matched to that of concrete to improve signal to noise ratio. It is additionally suggested that the use of chirp signals significantly increases signal to noise, which is also reported by Koehler et al. [1997]. Weizheng and Yiyoung [1996] report on an array transducer design that has improved directional characteristics and sensitivity, and the use of split spectrum processing. Scickert [1995] reports on using synthetic aperture signal processing that takes advantage of the inherent broad beam divergence, which results in an improved image over conventional B scans. Sansalone and Carino [1991] report that time domain processing has been exclusively used in applications where pulse echo or pitch catch methods have been used on concrete structures. Also, since it is difficult to construct low frequency, broad band transducers with desirable directional characteristics, there are no currently available commercial transducers for pulse echo testing of concrete. Most researchers have instead resorted to pitch catch where a higher damped transducer is used as a transmitter and a lightly damped one for receiving.

2.3.4.3 Impact echo

The technique was first investigated [Sansalone and Carino (1986)] for the location of flaws within concrete. It involves introducing stress waves into a test object by spring loaded mechanical impact and monitoring the dynamic displacements caused by the arrival of waves reflected from internal defects and external boundaries.

The force-time history of an elastic impact may be approximated as a half-sine curve, whose period is determined by the contact time T_c, and is given by Johnson [1985],

$$T_c = 2.87\left(\frac{m^2}{RE^{*2}V}\right)^{1/5} \qquad 2.12$$

where m is the mass of the impactor, R the impactor radius, V is the velocity of approach and, E^* the averaged Young's modulus between impactor and surface materials given by

$$\frac{1}{E^*} = \frac{\left(1-\upsilon_1{}^2\right)}{E_1} + \frac{\left(1-\upsilon_2{}^2\right)}{E_2} \qquad 2.13$$

where E and υ are the Young's modulus and Poisson's ratio of the materials. The frequency content of the pulse which is a function of contact time affects the size of the defect that can be detected. As the contact time decreases, the frequency content of the pulse becomes more broad band at a higher centre frequency, and defects nearer the surface can be detected. The receiving transducer is often a broadband conically shaped displacement transducer, whose shape ensures good contact and least interference with the resonating pulse. A schematic of the impact echo for determination of material velocity and reinforcement bar depth is shown in Fig 2.4a and Fig. 2.4b respectively. Impact on the surface generates a stress pulse, which is reflected back and forth between the impacted surface and internal defects and other external surfaces, such that a resonance condition is created. Each time the compression wave arrives at the top surface it causes a downward displacement. The time between successive downward displacements is the time, Δt, it takes for the compression wave to propagate and is given by

$$\Delta t = \frac{2d}{V_p} \qquad 2.14$$

Where d is the distance to the reflector and V_P the compression wave velocity. The frequency of the P-wave arrivals at the top surface is equal to the inverse of the arrival time, given by

$$f = \frac{1}{\Delta t} = \frac{V_P}{2d} \qquad 2.15$$

The recorded displacement wave forms are studied in the frequency domain, where any peak can be related to the distance to a reflector if the P-wave velocity is known. Likewise, if the thickness of a member is known then the compression wave velocity can be calculated. The amplitude of the peak is directly related to the mismatch in impedance between the two materials on the two sides of an interface. The greater the mismatch the greater the amplitude of the resonant frequency will be.

Popovics and Achenbach [1996] report that the main limitation to the technique is the lack of control on the frequency content (typically up to 30kHz centre frequency) and directional characteristics of the input signal. It is suggested that the technique would benefit from the use of electromagnetic transducers, such as modal shakers. Davies et al. [1996] assess the advantages and limitations of impact echo for the evaluation of highway pavements, and reports that due to the high energy stress pulse relatively long distances in concrete can be tested. Krause [1997] reports on commercially available impact echo concrete test equipment, giving the fact that the apparatus is light, portable, quick to use, and simple to operate, as the main advantages of the technique. The accuracy of the technique has been investigated by Nazarian and Baker [1996]. On average, the thickness could be measured with an accuracy of 5% dependent on aggregate size. The technique has been used to determine crack depth to an accuracy of 10% and reinforcement location [Lin et al. (1996)]. It is reported [Sansalone and Carino (1991)] that there is currently no standard for impact echo testing of concrete structures.

2.3.4.4 Spectral Analysis of Surface Waves - SASW

The applicability of surface wave phase velocity measurements for the evaluation of layered concrete structures such as pavements was first studied by Jones [1962] in the 1960's. The intention was that measurements of the velocities of the surface Rayleigh waves generated are capable of providing information concerning the elastic properties of the materials in the pavement layers. The initial approach experimentally measured the wavelengths of steady state harmonic surface waves on concrete and bituminous highways, which had good agreement with theoretically obtained dispersion curves. In the 1980's [Stokoe and Nazerine (1986)] the technique was improved by using a transient stress wave source, obtained by mechanical impact, which had the advantage of being a broad band input that contained many frequencies

rather than just one. At a depth below the surface of about 1½ wavelengths, the amplitude in each component wavelength is about 1/10 of the amplitude on the surface [Sanaslone and Carino (1991)]. Thus the depth of penetration of surface waves depends on their frequency, longer period waves penetrate deeper than shorter waves, such that short wavelengths sample properties at small depths and waves with long wavelengths reflect properties at larger depths. With the additional knowledge of the shear wave velocity in the concrete, the elastic properties of the layered medium are calculated from the experimentally obtained dispersion curves by an inversion process, with an accuracy of about 4 to 5% [Nazarian and Baker (1991)]. A present SASW technique uses two vertical acceleration transducers placed a known horizontal distance from the impact source [Wu (1995)]. The dispersion curve of the surface waves (dependence of the phase velocity on the frequency) is obtained by analysing the phase spectra of the received signals given by [Akhlaghi and Cogill (1994)];

$$\theta_i = \tan^{-1} \frac{\mathrm{Im}(z)}{\mathrm{Re}(z)} \qquad 2.16$$

where θ is the phase angle, and z the complex motion in the frequency domain. The phase lag of motion between two observed points of two transducers $\Delta\theta_i$ is given by

$$\Delta\theta_i = \theta_{1i} - \theta_{2i} \qquad 2.17$$

where subscripts 1 and 2 denote transducer number. The wavelength, λ_i, is given by:

$$\lambda = \frac{2\pi d}{\Delta\theta_i} \qquad 2.18$$

where d is the distance between transducers. By noting $c = \lambda f$, the corresponding phase velocity, c, can be readily determined, and hence the experimentally obtained dispersion curve. A similar technique reported [Wu et al. (1995)] , establishes Rayleigh and surface skimming longitudinal wave velocities in the time domain. [Akhaghi et al. (1995)] describes the technique for analysing pavements, and suggests that the results vary by less than 10% with respect to other techniques. The main advantages of the technique are given that it is single sided and the variation in velocity with depth can be determined so that the extent of surface layer deterioration can be estimated. The limitations are that, complex signal processing presently limits applications in the field, it is only applicable to surface layer properties, the

technique requires the structure to act as a wave guide so it is only suitable for inspecting slabs and skilled operators are required to interpret the test data.

2.3.5 Ground Penetrating Radar (GPR)

GPR is a relatively new technique for civil engineering applications, with a range of equipment commercially available for the assessment of compaction of granular fill materials around civil structures, detection of moisture in construction materials and inspection of bridge decks for voids. The technique relies on an electromagnetic wave which is propagated into the material under investigation by means of a combined antenna, comprising transmitter and adjacent receiver. A schematic of GPR is shown in Fig 2.5.

Examination of the reflected waveforms, from interfaces between materials of different dielectric constants, enables the structure of the materials under investigation to be analysed. The propagation of an electromagnetic wave through low-loss dielectric materials, such as most common geological media and concrete, is dependent upon a variety of variables. The velocity of the pulse depends upon the dielectric constant of the material, and in simplified form is given by the following formula [Chen et al. (1994)],

$$v = \frac{c}{\sqrt{\varepsilon_r}} \qquad 2.19$$

where c is the velocity of light, and ε_r is the relative dielectric constant of concrete, which if known allows the depth of reflective features to be calculated. The strength of the reflected signal depends upon the magnitude of the change in dielectric properties at an interface. The ratio of the reflected wave amplitude to the incident wave amplitude at an interface, known as the reflection coefficient, is given by

$$R_{1,2} = \frac{\sqrt{\varepsilon_{r1}} - \sqrt{\varepsilon_{r2}}}{\sqrt{\varepsilon_{r1}} + \sqrt{\varepsilon_{r2}}} \qquad 2.20$$

The subscripts 1 and 2 denote the first and second media at the interface. The ratio of transmitted wave to incident wave known as the transmission coefficient is;

$$T_{1,2} = \frac{2\sqrt{\varepsilon_{r1}}}{\sqrt{\varepsilon_{r1}} + \sqrt{\varepsilon_{r2}}} \qquad 2.21$$

A polarity change in the reflected pulse may be caused if the material beyond the interface has a higher dielectric constant. Attenuation of the radar signal is influenced by the material conductivity, which increases with moisture content.

A meeting at the IEE, London was attended by the author in January 1997, where the NDT of highway pavements was discussed, particularly the critical appraisal of GPR. A number of presentations were given by GPR researchers and end users, with a mixed reception by the audience (GPR not being the universal panacea as sometimes reported). At this meeting problems associated with the technique were presented [Hardy and Gordon (1997)].

Fairfield et al. [1995] report on radar measurement of density variations around an arch bridge. By measuring the pulse velocity for a known path length, the dielectric constant was obtained. The technique proved to be a cost-effective NDT method, due to rapid one sided inspection, low manpower and limited site preparation. Bungey [1991] reporting on the operational aspects of GPR, suggests that skilled image interpretation is required even after signal processing, since the radar picture does not often resemble the form of embedded features, where circular type sections reflect a complex hyperbolic pattern due to the diverging nature of the beam. Likewise, Saarenkento and Soderqvist [1994] reporting on radar bridge deck inspection in Finland, suggests the greatest problem is the present manual interpretation required. Warhurst et al. [1993] report on inspection of highway pavements, finding that scattered signal power was too low to permit detection of objects deeper than 125mm in concrete. Similarly Bungey and Millard [1996] suggest that detection of air filled voids is limited to 50mm since the difference in relative permittivity of air to concrete of 1:6 results in a low reflection intensity, and that using a 1GHz antenna, typical penetration depths are only 500mm for dry concrete and 300mm for water saturated concrete. Malhotra and Carino [1991] report that GPR is most suitable in assessing with reasonable accuracy the water content of fresh concrete mixes or moisture content of hardened concrete, since for thickness determination it is difficult to predict the success of an investigation unless a knowledge of the structure's dielectric constants is known.

2.3.6 Review of non-destructive inspection techniques

It is obvious that there is no existing universal technique for non-destructive inspection of concrete. Depending on the investigation to be undertaken, the advantages and limitations of a technique should be assessed to find the most appropriate that will provide the level of information required. Radioactive methods provide excellent internal images, for the location

of reinforcements, though the technique is time consuming and safety regulations make it restrictive. With GPR it is difficult to interpret the radar scans since the image does not often resemble the form of the embedded features. Current research is addressing signal processing to make the technique amenable to automation. Impact echo techniques have little control on the frequency content of the input signal and along with surface wave methods are best suited to inspection of layered structures such as pavement systems. Preferred pulse velocity techniques require access to both sides of a structure. The basic nature of the adopted signal processing leads to the measured velocity being a function of the path length measured and the need for viscous coupling makes the technique inconvenient. Alternative coupling that does not significantly reduce signal to noise would improve testing speed. Pulse echo is conceptually perhaps the most simple method. The technique is common for the inspection of metals, but the development of suitable transducers for testing of concrete is a difficult undertaking, and as such there are few devices known to be commercially available.

At present civil engineering has the greatest confidence in the most destructive methods of test. For a non-destructive test to be accepted would predominantly require that its results are not ambiguous, costs involved with its use are low, and it should be convenient and rapid to employ. Of the techniques reviewed, the pulse velocity technique offers the lowest cost of use [Bungey 1996]. All ultrasonic techniques are governed by the unfriendly heterogeneous nature of concrete and in particular the presence of aggregate which restricts transducer frequencies to generally below 100kHz. It is generally thought that because of this that ultrasonic techniques cannot be developed further. However, there is scope for improvement of the pulse velocity method by addressing the unreliability of measurements and making testing more convenient by finding an alternative method of coupling the transducers. It was felt that such improvements could be achieved. The same level confidence was not given to developing the pulse echo technique for concrete inspection.

Currently the apparatus most often used in the UK for pulse velocity testing of concrete is the PUNDIT apparatus manufactured by CNS Farnell, London. Similar equipment in appearance and operation known as the V-Meter [James Electronics, Chicago] is available in the USA. A thorough investigation of the PUNDIT equipment operation was conducted prior to researching the improvement of the technique.

2.4 The PUNDIT test equipment

This section describes the popular test equipment PUNDIT used for the evaluation of concrete pulse velocity and then discusses its various modes of operation. The apparatus which is

manufactured by CNS Farnell, London, derives its name from the initial letters of the full title of “Portable Ultrasonic Non-Destructive Digital Indicating Tester”. Its use is not limited to concrete having extensive reported applications in the testing of: geological materials such as rock, chalk, granite, frozen soils and sandstone; timber and glued laminates; cast iron, spheroidal graphite and asphalt; ceramics; frozen meat and bone structure; and carbon and graphite materials.

2.4.1 The PUNDIT apparatus description

The apparatus has been designed with operation in the field in mind. As such the PUNDIT unit is portable and rugged. The dimensions of the unit are 185 x 130 x 185mm, and it weighs in at 3kg. The ambient temperature range to which the equipment may be operated is 0^{o}C to 45^{o}C. The test equipment provides a means of generating a pulse, transmitting this to the concrete, receiving and amplifying the pulse and measuring and displaying the time taken. A simplified system diagram is shown in Figure 2.6.

The apparatus can be conveniently divided into the following parts:

1. Pulse generator
2. Set reference display
3. Receiver amplifier
4. Timing pulse oscillator, Gate and counter
5. Power supply
6. Outputs
7. Transducers and leads

2.4.1.1 Pulse generator

The pulse generator comprises an Extra High Tension EHT power unit, a Thyristor and a Uni-Junction Transistor UJT pulse generator. The capacitance of the transmitting transducer is charged to a potential of 1.2kV or 500V as selected by a switch on the rear panel. This capacitance is then rapidly discharged through a thyristor triggered by the UJT at a repetition rate of 10 or 100Hz as selected by the Pulse Repetition Frequency PRF switch. The repetition frequencies are derived, by division, from the 10MHz crystal timing pulse oscillator. Discharging the capacitance causes the transmitter to be shock excited and so vibrate at its own natural frequency. The pulse generator board is mounted in a screened compartment.

Figure 2.7 shows a time trace of the 500V PUNDIT excitation pulse, obtained by attenuating the signal and connecting to an oscilloscope, that shows typical capacitor discharge characteristics.

2.4.1.2 Set reference delay

The delay between the pulse applied to the transducer and the output from the receiving transducer when the two are coupled face to face is typically 2μs. To eliminate this delay the counter is inhibited for the duration of the reset pulse. A nominal 0.5 to 10μs variable delay control sets the duration of the reset pulse for the different types of transducers and cables. This control is used in conjunction with a reference bar that has a recorded transmission time of typically 26μs.

2.4.1.3 Receiver amplifier

After transmission through the material under test the ultrasonic pulse is converted to an electrical signal in the receiving transducer. The received signal is then amplified to produce a 'Stop' pulse coincident with the onset of the leading edge of the received signal waveform. The receiving amplifier has an input impedance of 500kΩ and is sensitive to signals above 250μV. The receiving amplifier board is mounted in a screened compartment.

2.4.1.4 Timing pulse oscillator, gate and counter

A 10MHz quartz crystal oscillator module generates timing pulses. This allows a maximum resolution of 0.1μs. For longer transmission distances above 400m, the resolution can be switched to the 1μs range.

A bi-stable circuit is used to control the gate. On receipt of the 'Start' pulse from the Set Ref stage the binary changes state and opens the gate, timing pulses are passed through the gate to the counter. The gate is closed when the 'Stop' pulse from the receiver amplifier is applied to the other side of the gate control bi-stable. Following the 'Stop' pulse the counter is latched and the LCD on the front panel indicates the transit time. The reading is updated at a rate of 2Hz with a range of 0.1μs to 9999μs. If a signal is not received the LCD will automatically blank. The electronic circuit of the apparatus uses High-Speed CMOS ($MM7_4HC$) integrated circuits.

2.4.1.5 Power supply

For field use an internal Nickel Cadmium battery will, when fully charged, supply power for about 12 hours continuous use. The battery voltage is monitored by a micro-power sensor which, when the voltage is near to discharged state, will cause an LCD to flash. When the instrument is used on the 95/125V or 190/250V, 50-60Hz AC mains, a built in constant current charger will continuously trickle charge the battery, or the full charge can be enabled when the battery is fully discharged.

2.4.1.6 Outputs

Available from BNC sockets on the rear panel are: an analogue pulse with a length equal to the transit time; an oscilloscope output that provides an exact copy of the received signal for outputs up to 0.4V; and a positive trigger pulse of 3.5V with a rise time of 2μs which is synchronised with excitation pulse onset.

2.4.1.7 Transducers

The transducers consist of lead zirconate titanate (PZT4) ceramic piezo electric elements in stainless steel cases. The elements are tightly held on the inside face of the case to provide good acoustic transmission. The transducer assembly is sufficiently robust to withstand conditions experienced in the field. Fig. 2.8 shows a schematic of the PUNDIT transducer internals. The shock excitation provided by the pulse generator causes the transducer to vibrate at its own natural frequency, governed by the size and stiffness of the whole transducer assembly. Different sizes of piezo electric element and case enable a range of transducer centre frequencies from 24kHz to 200kHz suitable for testing of concrete. To achieve maximum pulse amplitude that helps to overcome the attenuating characteristics of concrete, the transducer vibrations are minimally damped, so as to maximise the energy content within a narrow band of the centre frequency. As such, a long train of pulses is supplied by the transmitter, where the rise time to maximum amplitude, and the number of cycles produced before signal decays to a minimum, are inversely proportional to the bandwidth. Apart from the standard transducers, exponentially shaped conical probes are available which make a point contact, being suitable for coupling to rough surfaces or awkward geometries. An additional receiver amplifier is recommended due to the significant reduction in received signal amplitude. For the rapid inspection of smooth surface materials such as granite or marble, 78kHz and 370kHz wheel probes are available. All transducers are fitted with a cable socket to allow the use of co-axial cables of different lengths.

2.4.2 Operation of apparatus

The operation of PUNDIT complies with recommendations given in BS1881:Part 203. Operation can be divided into the following stages;

2.4.2.1 Set reference

Prior to use, the apparatus should be calibrated. There is an inherent time delay in circuitry that must be removed for accurate evaluation of signal transit times. The delay is removed by a calibration procedure that employs a reference bar. The PRF switch should be set to 10pps. A smear of grease is applied to both transducer faces, and the transducers are then firmly pressed on to the ends of the bar, and excited by the PUNDIT. The SET REF control is then adjusted until the time value stamped on the reference bar is read on the LCD. For maximum accuracy it is recommended the LCD be set to the 0.1μs range.

2.4.2.2 Applying couplant, surface preparation

Good acoustical coupling between concrete surface and the face of the transducers is essential. Mediums such as silicone grease, medium bearing grease or liquid soap are ideal for smooth surfaces, and water pump grease or thick petroleum jelly for rough surfaces. Air pockets must be eliminated and transducers should be thoroughly cleaned and a new film of couplant applied in-between tests. If the concrete surface is very rough then it may have to be ground smooth, or filled with a suitable quick setting mortar. For application to awkward profiles such as the internals of tubular structures, the use of an exponentially tipped probe is recommended.

2.4.2.3 Inspection technique and interpretation of results

BS1181: Part 203 suggests that the basic transducer configurations as shown in Fig. 2.9 are

1) Opposite faces (direct through transmission), which allows the maximum transfer of energy between transducers, and so should be used when ever circumstances permit;
2) Adjacent faces (semi-direct transmission);
3) Same face (indirect transmission), which leads to only a small percentage of the transmitted energy arriving at the receiver.

It is recommended that the pulse velocity technique is most valuable for determining concrete uniformity. Heterogeneities such as variation in materials, mixing, and compaction in a

concrete structure will cause variations in measured pulse velocity. The preferred configuration is required so as to be able to mark out a regular grid pattern on opposite faces of the concrete structure as shown in Fig. 2.10. Viscous couplant is then applied to each grid point so as to facilitate signal transmission. The transducers are then applied in through transmission configuration to each grid point. The PUNDIT apparatus is used to excite one of the transducers and the received signal for the other is monitored to determine the signal transit time. The equipment displays the indicated time and this is recorded. Due to the difficulties in achieving consistent coupling, it is recommended that readings at each point be repeated until a minimum value is obtained. Once the completed grid has similarly been inspected, the results are often plotted as a 2D surface map as shown in Fig. 2.11. The variations in pulse velocity displayed on the contour map are then used to identify areas of concern.

The measured pulse transit time can be influenced by [Malhotra and Carino (1991)];

a) Aggregate size, grading, type and content. The higher the aggregate-cement ratio, the lower the compressive strength of the concrete and hence the lower the pulse velocity
b) The degree of hydration.
c) original water-cement ratio. Lower proportions of cement lead to lower compressive strengths.
d) The degree of compaction. Pulse velocity is related to density. Inadequate compaction such as honeycombing will result in a decrease in pulse velocity
e) Moisture content, where the pulse velocity may be up to 5% higher in wet concrete than through the same dry concrete, since the velocity in water is faster than it is in air.
f) Presence of voids of greater dimensions than signal wavelength results in lower transit times, since the sound would have to defract around these.
g) Presence of reinforcement, where providing their orientation is known, correction factors can be applied [BS 4408, Part 5].
h) Path length, where for concrete with 30mm size aggregate it is not recommended to have a path length below 100mm, and with increasing distance the apparent velocity decreases.

It is suggested [Tomsett (1992)] that for tests conducted on a single concrete block, a pulse velocity deviation of 1.5% would indicate good construction standards. When testing a complete structure this value could increases to 6-9% and still indicate good standards overall. By contrast, Bungey [1991] reports that the presence of alkali-silica reaction (concrete cancer) can reduce the pulse velocity by 20%. In general, defects or deterioration are located by greater deviations in pulse velocity on the contour map. Decisions concerning the seriousness will nominally require an estimate of concrete strength, where it is preferable to resort to partially destructive methods, or core sampling.

2.4.3 Summary

Familiarisation with the PUNDIT pulse velocity test equipment was undertaken. The 54kHz transducers were disassembled and their design noted. The PUNDIT test equipment characteristics of particular interest are:

i) For 50mm diameter transducers, when testing concrete, there are unlikely to be directional characteristics for transducers with centre frequencies below 80kHz,

ii) The reference bar has a calibrated value stamped on it, which would appear to coincide with the time that a longitudinal wave would take to propagate along it.

iii) The digitisation rate of 10MHz relates to an accuracy in measured time of arrival of 0.1μs;

iv) The transducers are narrow band, such that they ring on for a number of cycles.

v) The shock excitation pulse is allowed to decay in time, which presently has an unknown effect on the pulse shape.

vi) The signal transit is determined from the time when the received signal goes above a 250μV threshold. As the signal decreases in amplitude towards the threshold value, the threshold will be triggered off a later phase of the received signal. If the amplitude of the first half cycle falls below 250μV, then a later period of the signal of sufficient amplitude will trigger the circuitry.

vii) To enable good acoustic coupling, a layer of couplant must be applied to the transducer faces. This is inconvenient to apply and to remove, and it is difficult to obtain consistent coupling.

2.5 Conclusion

The material characteristics of concrete have been investigated. It was noted that concrete properties are extremely variable due to the plethora of mixes and fabrication practices that are possible. At present civil engineering has the greatest confidence in the most destructive methods of test. Their disenchantment with non-destructive methods results from the occasional exaggerated claim of the performance of a technique. For a non-destructive test to be accepted would predominantly require that its results are not ambiguous, costs involved with its use are low, and it should be convenient and rapid to employ. The ultrasonic pulse velocity method was identified to satisfy the cost requirement, but have room for improvement concerning reliability of results and convenience of application. It was decided to modernise the pulse velocity technique by addressing these limitations.

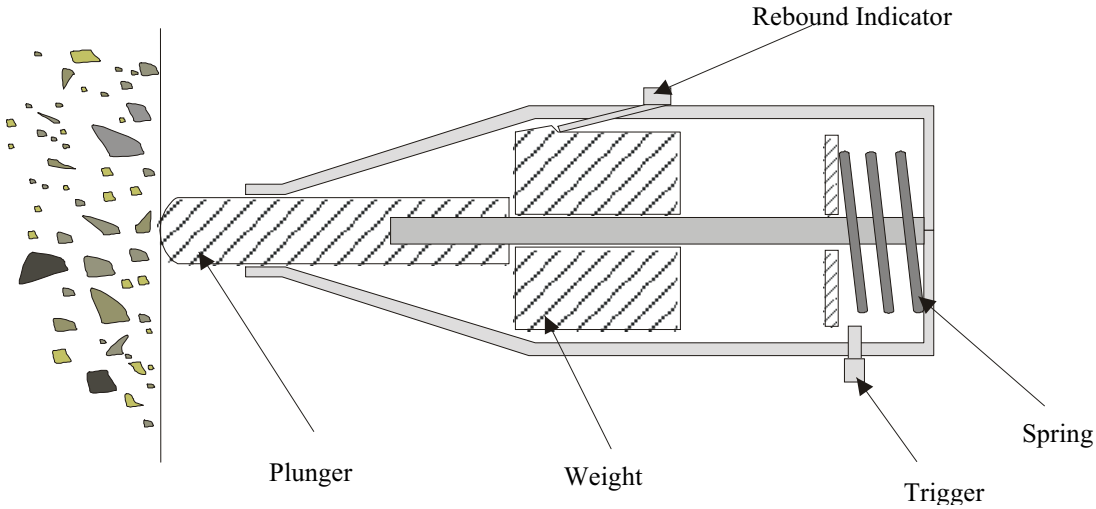

Figure 2.1. Concrete surface hardness testing – schematic of Schmidt Hammer

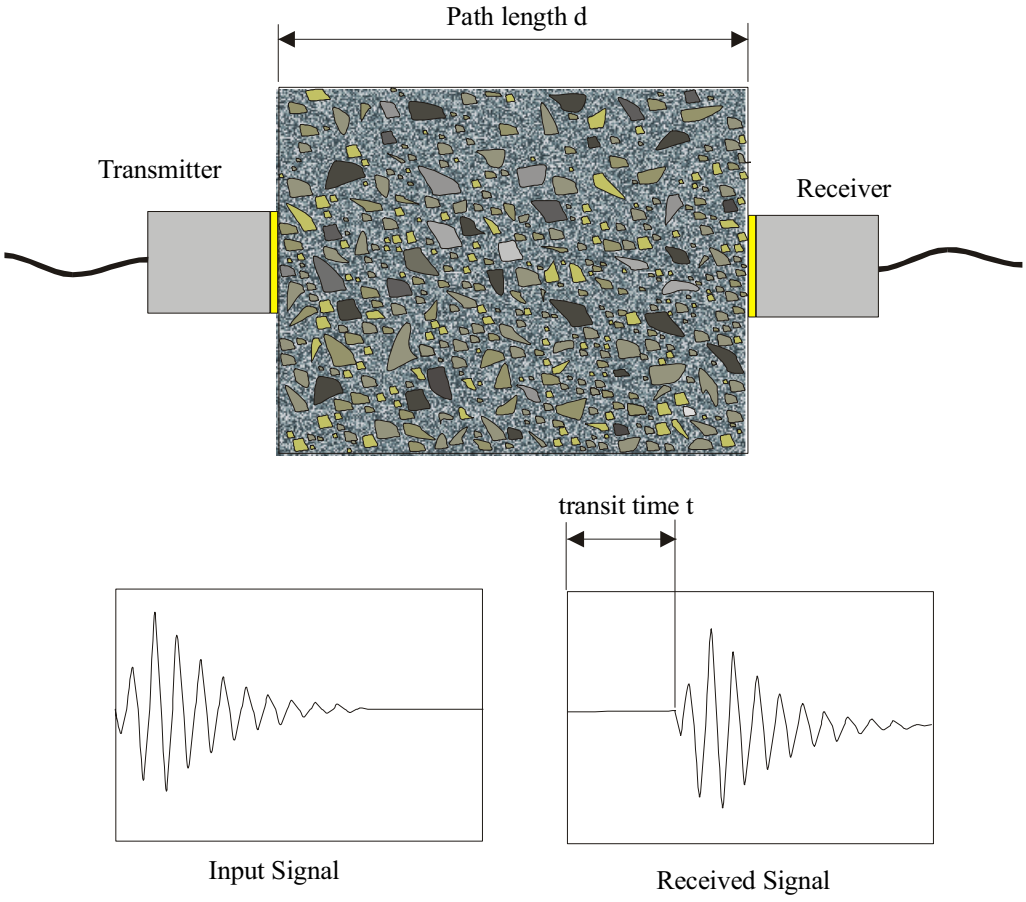

Figure 2.2. Schematic of concrete ultrasonic pulse velocity testing.

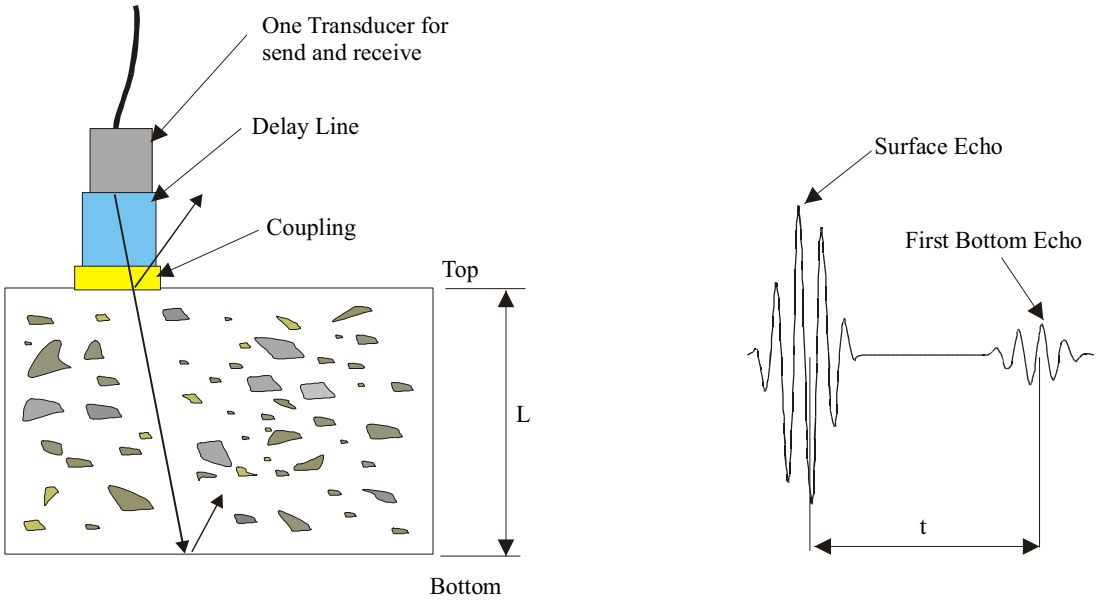

Figure 2.3. Schematic of concrete ultrasonic pulse echo testing

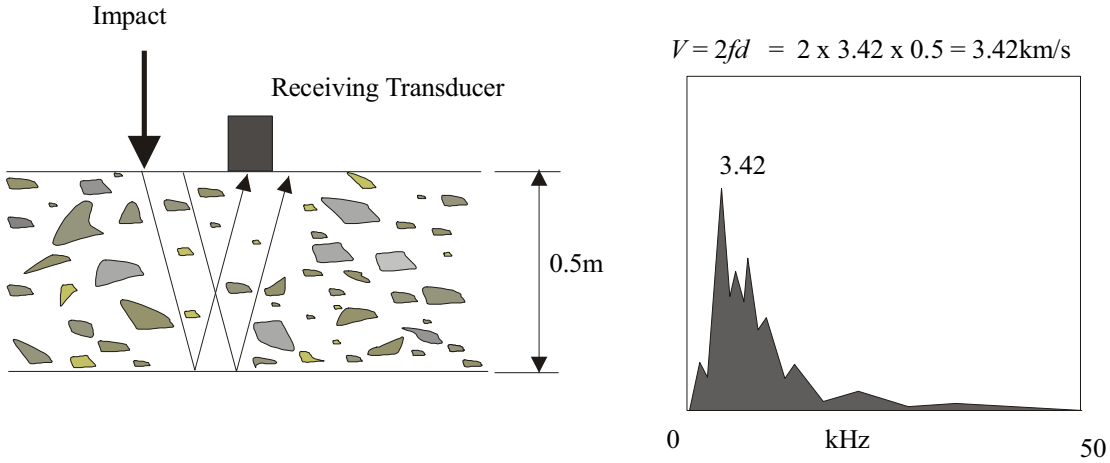

Figure 2.4a. Impact echo technique. Determination of sound velocity for known slab depth

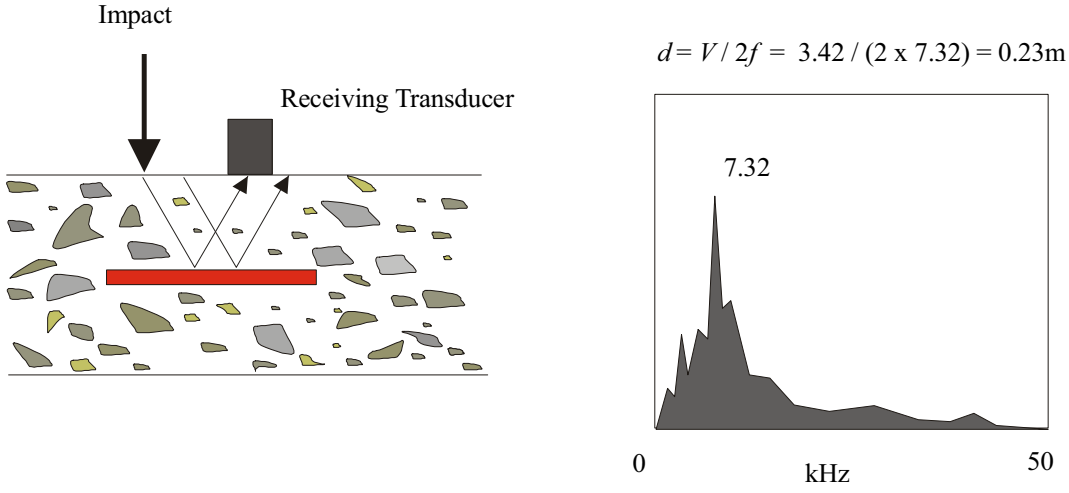

Figure 2.4b. Impact echo. Determination of reinforcement bar depth for known sound velocity.

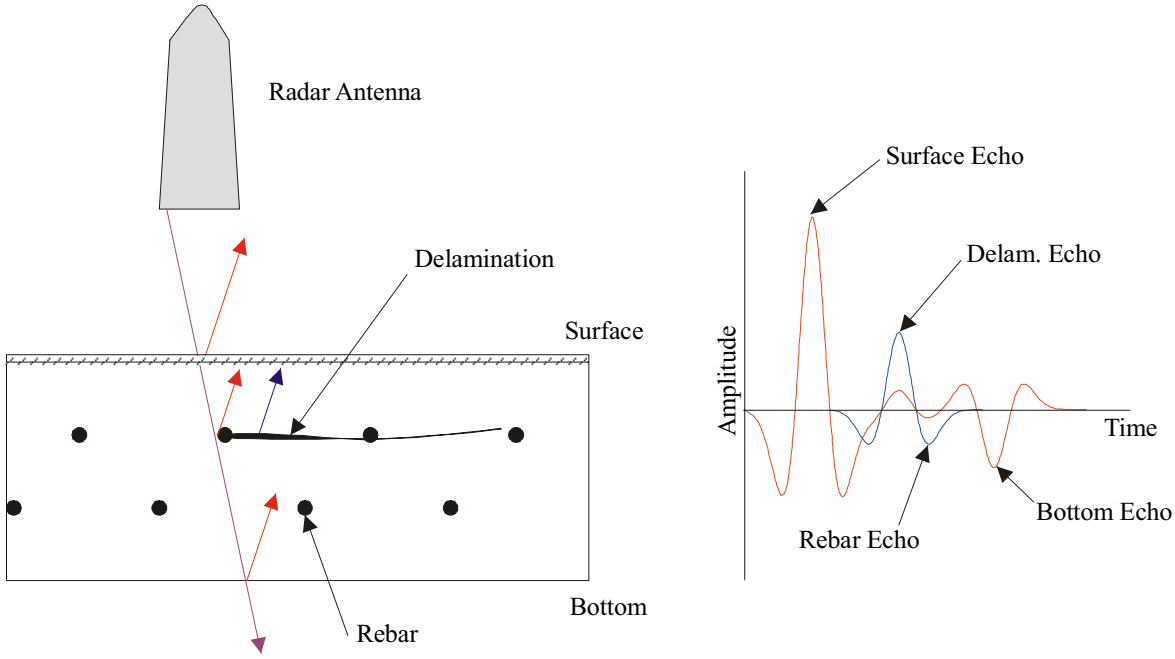

Figure 2.5. Ground Penetrating Radar. Location of reinforcement bar or delaminations.

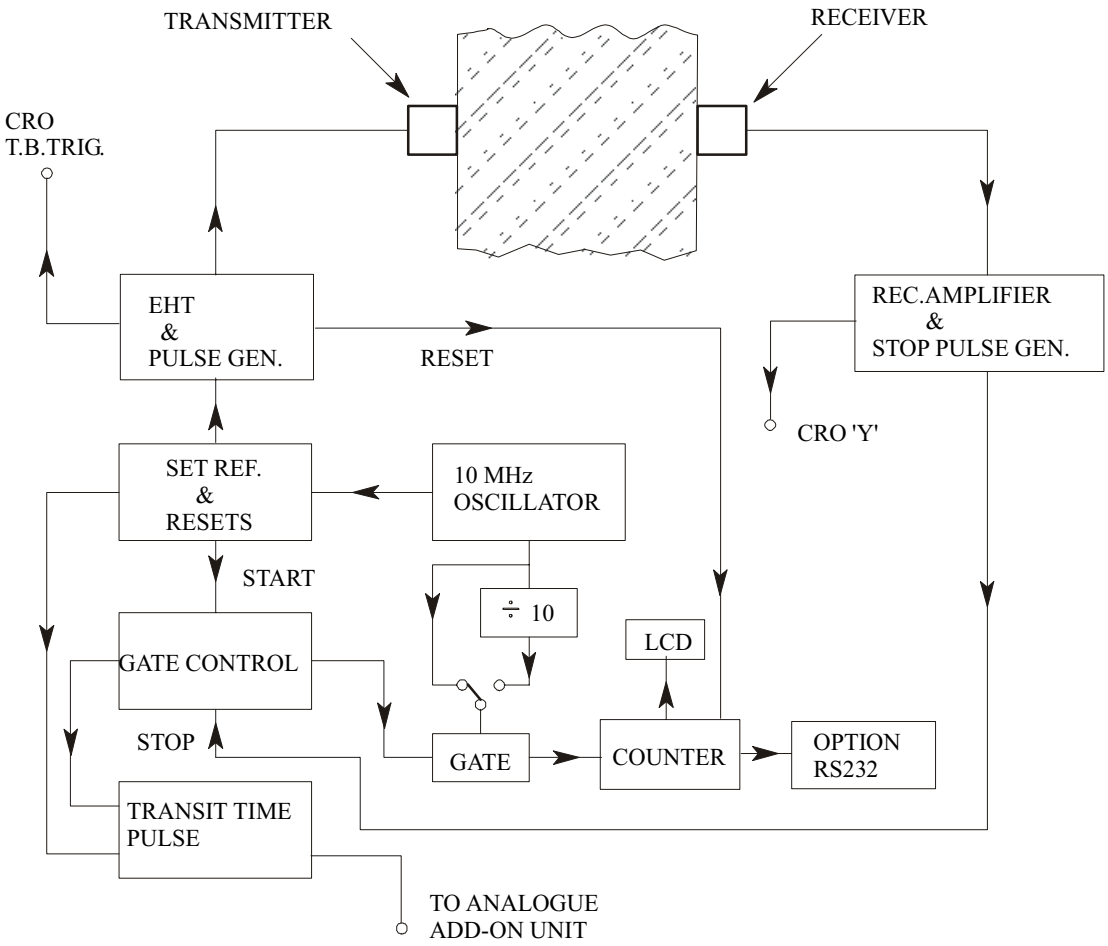

Figure 2.6. PUNDIT system diagram

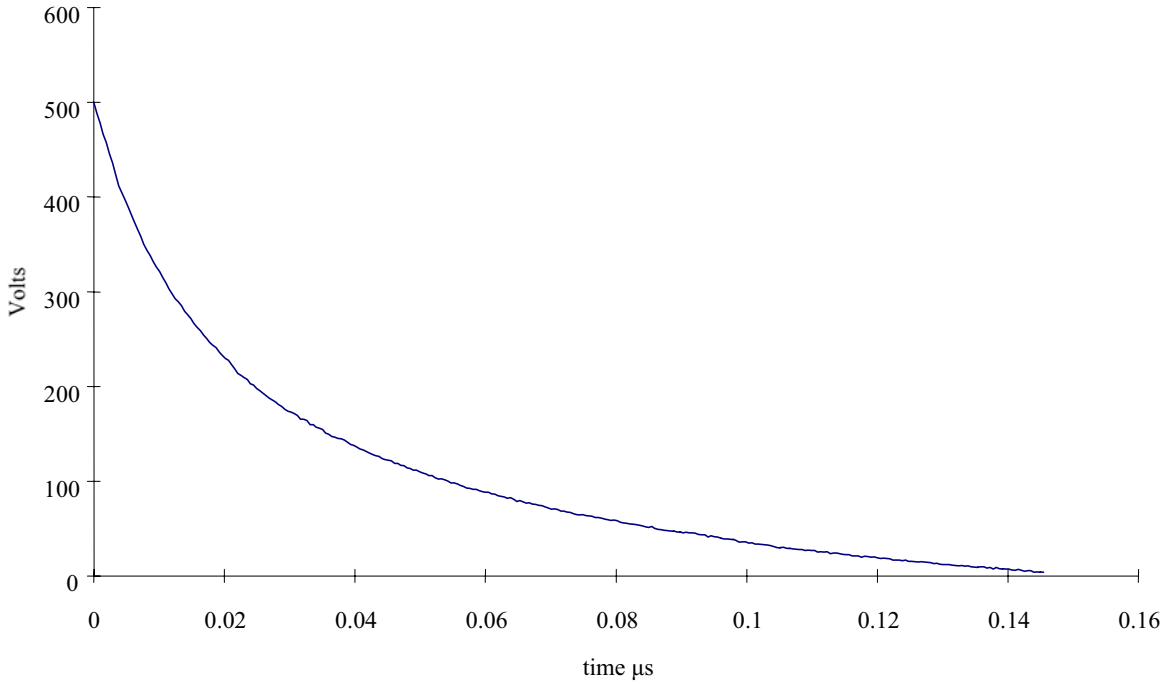

Figure 2.7. PUNDIT 500 volt excitation pulse

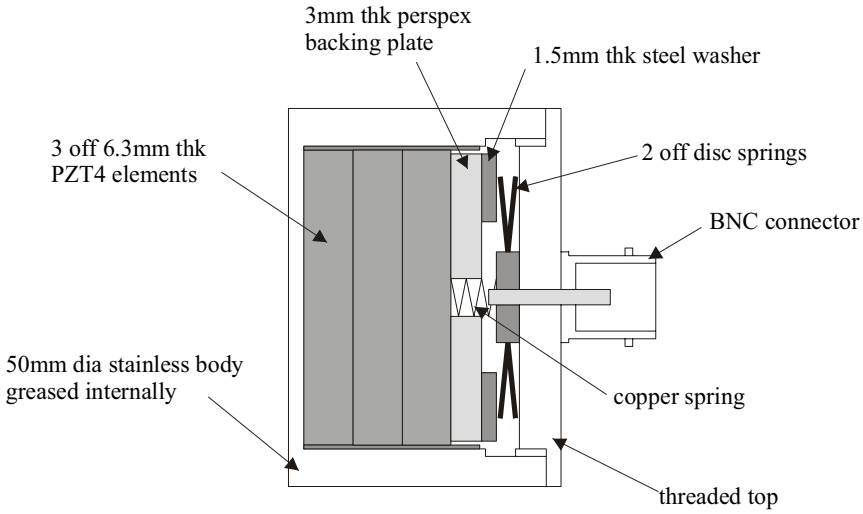

Figure 2.8. Schematic of internals of PUNDIT 54kHz Transducers

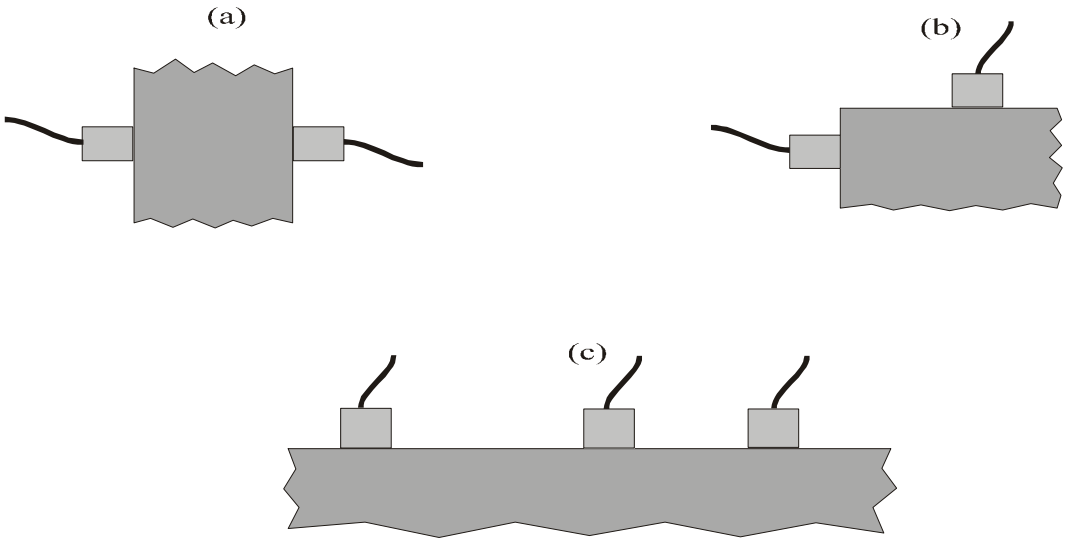

Figure 2.9. Configurations for pulse velocity measurements. (a) Direct through transmission method (b) semi Indirect method (c) Indirect surface method

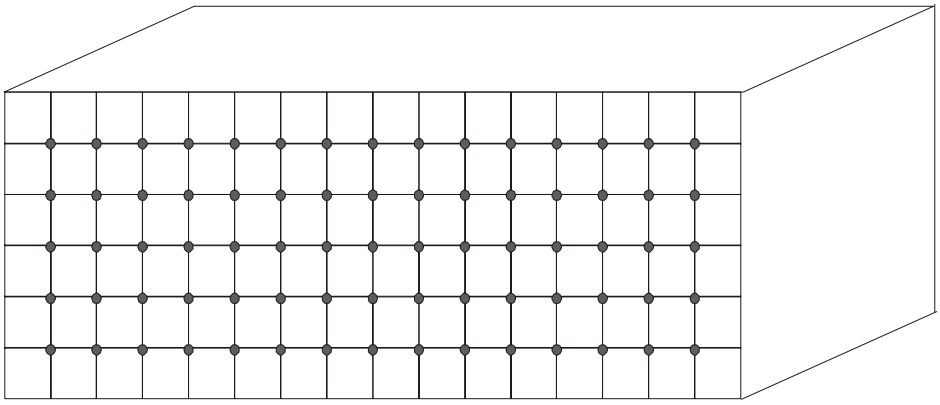

Figure 2.10. Schematic of grid pattern marked out on concrete structure for the determination of concrete uniformity.

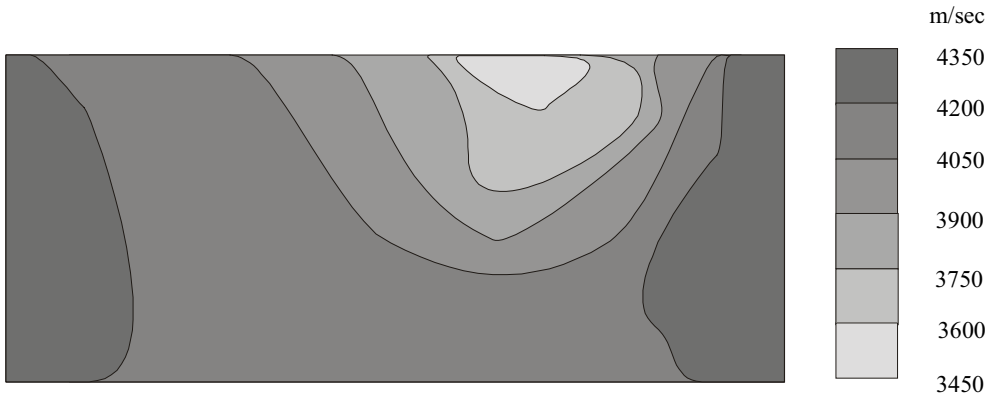

Figure 2.11. Plotting signal transit times for each grid point as a 2D surface map to aid the identification of problem areas.

Chapter 3

Correction of measured transit times for apparatus such as the PUNDIT

3.1 Introduction

It is generally recognised that the most valuable use of pulse velocity measurements in concrete is for a comparative study to aid the indication of problem areas [Sansalone and Carino (1991)]. Not withstanding, a number of concrete inspection techniques have been developed that require an accurate evaluation of the absolute velocity of sound in concrete. To achieve this, various correction functions to the measured pulse velocity are given to correct for temperature and influence of reinforcement bars [BS1181: Part 203 (86)] for example. Minimum path lengths are recommended that depend on the signal wavelength, below these values the measurement of pulse velocity becomes unreliable. Additionally, for apparatus such as the PUNDIT that uses threshold crossing to evaluate received signal arrivals, there is evidence [Bungey and Millard (1996)] that the measured pulse velocity varies as a function of the path length inspected. The same effect was communicated to the author [Ballard (1996)] during a meeting with G. Ballard of GB Geotechnics Cambridge, a company that specialises in civil engineering non destructive testing. By contrast, the reduction in measured pulse velocity as a function of path length is suggested to be usually small [BS1181:Part 203 (86)] and well within recommended time tolerances. The purpose of the work reported in this chapter was to estimate the extent of the pulse velocity measurement error and to recommend a correction function when using the standard commercial transducers.

3.2 Description of anomaly for narrow band transducers

The effect of the greater attenuation of high frequency components of the received pulse is described in [BS1181:Part 203 (86)]. The result is said to be a less clearly defined pulse onset, such that the apparatus triggers off a later phase of the received signal. It is suggested that for path lengths of 100mm to 3m, the error in pulse velocity measurement due to the loss of frequency components is well within the ±1% time tolerance recommended. For apparatus, such as the PUNDIT, that uses threshold crossing, the measured pulse velocity is reported by Bungey and Millard [1996] to reduce by a value of 5% for path lengths between 3m and 6m. The author suggests that this anomaly is directly related to the loss of signal amplitude. As the path length tested increases, so the signal amplitude decays due to the effects of beam spreading and material attenuation. As the signal amplitude decreases the point on the signal, which coincides

with the threshold value will then occur at a later phase and so the received signal is perceived to arrive later.

To illustrate the suggested effect a typical signal that the PUNDIT apparatus would receive was obtained experimentally. The standard 54kHz PUNDIT transducers were coupled in through-transmission configuration to a 100mm thick aluminium block whose lateral dimensions were sufficient such that any reflections off boundaries should not interfere with the received first two cycles. The PUNDIT apparatus 500V pulse was used to excite one of the transducers while the received signal from the other was averaged on an oscilloscope. The averaged received signal $a(t)$ is shown in Fig 3.1 where the first half cycle has additionally been halved in amplitude and shown as $a(t)/2$. If a horizontal line is drawn which represents an arbitrary negative threshold crossing, then it is straightforward to see that the threshold is crossed later for the lower amplitude signal. For this case, the function shown in Fig. 3.2 illustrates what the PUNDIT measured transit time would be as a function of the maximum amplitude of the received first half cycle. If the amplitude of the first half cycle falls below the 250μV PUNDIT threshold, then the measured transit time would jump almost one period of the received signal as the apparatus triggers off the portion of the signal up to the next negative peak. For 54kHz wave propagation in unbounded material this appears to be the extent of the problem since it has been observed that all following negative peaks are of lower amplitude. However, if as in Fig 3.1 the material is bounded then the possibility of constructive interference of reflections might result in some additional peaks of higher amplitude. It was recognised that any correction function should be simplistic in nature for it to be practical, such that the system will be considered non dispersive and the dimensions of the media will be greater than the signal wavelength.

In order to estimate the extent of the effect and to provide a correction function for propagation in unbounded media it was found necessary to predict the signal decay as a function of path length tested and have an approximation that describes the profile of the early part of the received signal. To accomplish this, the following sections describe: modelling the loss of signal strength due to beam spreading, the experimental determination of the loss of signal strength due to material attenuation and the approximation of transfer functions. From these investigations it was possible for a given aggregate size to predict the variation of measured velocity as a function of path length, and to provide a general correction function.

3.3 Signal losses due to beam spreading

As acoustic energy spreads out into a medium so the magnitude of the disturbance at the wave front decreases by some function to satisfy the principle of energy conservation. The acoustic field that arises from an ultrasonic transducer can be modelled according to Huygens' principle

[Graff (1975)], which states that any linear wave phenomenon can be analysed by the superposition of simple sources properly selected in phase and amplitude to represent the physical situation. A simple source is a point source which radiates spherical waves in three dimensions and cylindrical waves in two dimensions. The two dimensional approximation assumes plain strain which is not appropriate for this problem. Therefore only the characteristics of spherical radiation will be reviewed. For this work the modelling of the acoustic field generated by an ultrasonic transducer will be greatly simplified by making the following assumptions:

1) The transducer operates in a uniform manner across its surface, such that it may be considered as a simple piston source,
2) Only compression waves are radiated from the transducer, which is a reasonable far field approximation,
3) For the narrow band transducers the excitation can be approximated as being continuous (steady state) at a single given frequency, which in the far field is a reasonable approximation [Rose (1999)],
4) Wave amplitudes are small, such that the propagation of sound in the medium can be described by first-order equations, which allows the system to be linear,
5) The medium that supports the acoustic field can be considered as an isotropic, homogeneous infinite half space. This is an acceptable assumption even for concrete if the interacting signal is of a wavelength greater than the aggregate size.

3.3.1 Spherical radiation approximation

The derivation of losses due to beam spreading is well known but is included here for completeness. Following the approach of Junger & Feit [1986], the three dimensional wave equation can be written as

$$\nabla^2 p - \left(\frac{\rho}{B}\right)\frac{\partial^2 p}{\partial t^2} = 0 \qquad 3.1$$

where p is the time dependent sound pressure, ρ the density of the medium, B the bulk modulus and ∇^2 represents the Laplacian operator. For spherical coordinates as shown in Fig 3.3, where the field is independent of angles ϕ and θ, the Laplacian operator takes the form

$$\nabla^2 = \frac{\partial}{\partial R^2} + \frac{2}{R}\frac{\partial}{\partial R} \qquad 3.2$$

For steady state conditions, equation 3.2 can be written in terms of the wave number *k*, in the form of a Helmholtz equation given as

$$\left(\nabla^2 + k^2\right)p = 0 \qquad 3.3$$

The complex wave number is given as

$$k = \beta + i\alpha \qquad 3.4$$

where

$$\beta = \frac{\omega}{c} = \frac{2\pi}{\lambda} \qquad 3.5$$

is the real part that relates frequency ω and velocity *c* to wave length λ, and α is an attenuation constant with the units of Nepers/metre. Substituting equation 3.3 into equation 3.2 gives

$$\left(\frac{\partial}{\partial R^2} + \frac{2}{R}\frac{\partial}{\partial R} + k^2\right)p(R) = 0 \qquad 3.6$$

The pressure satisfying this equation is one-dimensional, in that it depends on a single co-ordinate *R*. It can be verified that the general solution of this equation is

$$p(R) = \frac{1}{R}\left(e^{ikR} + e^{-ikR}\right) \qquad 3.7$$

The first term in equation 3.7 represents outgoing waves and the second term represents waves that converge on the source. Since it can be shown that converging waves do not arise in an infinite half space the (e^{-ikR}) term can be ignored. Thus from equation 3.7 the pressure amplitude a distance *R* from a point source is given as

$$p(R) = \frac{e^{ikR}}{R} \qquad 3.8$$

where it can be seen that the pressure amplitude decays with increasing distance from the source *R* which is defined as spherical spreading loss. An axi symmetric transducer of radius *a* as shown in Figure 3.4 can be approximated by a finite number of point sources, where each point source represents the elemental area

$$dA = rdrd\theta \qquad 3.9$$

For a general Cartesian point in the acoustic field, the pressure amplitude that arises from a finite number of point sources is obtained by substituting equation 3.9 into equation 3.8 and integrating over the transducer face

$$p(x_2, y_2, z_2) = \int_0^a \int_0^{2\pi} A_r \frac{\exp(ikR)}{R} r d\theta dr \qquad 3.10$$

with

$$R = \sqrt{(x_2 - x_1)^2 + (y_2 - y_1)^2 + (z_2 - z_1)^2} \qquad 3.11$$

where the subscript 1 refers to a point on the transducer face and subscript 2 refers to a point in the field. The function A_r represents the axi symmetric amplitude distribution over the transducer face, which for a piston transducer is a constant. An analytical solution to equation 3.10 is not trivial and so it is often solved numerically. For a flat face transducer radiating into a non attenuating medium, a simplified solution can be given for the on-axis pressure distribution. For this case $x_2 = y_1 = z_2 = 0$, and because of the axi-symmetric location of the field point, the θ integration becomes unnecessary, such that $x_1 = 0$ and $z_1 = r$, and setting y_2=y, results in

$$p(y) = \int_0^a \frac{\exp\left(ik\sqrt{y^2 + r^2}\right)}{\sqrt{y^2 + r^2}} r dr \qquad 3.12$$

By setting u=$\sqrt{y^2 + r^2}$ equation 3.12 becomes

$$p(y) = \int_y^{\sqrt{y^2+a^2}} \exp(iku) du = -\frac{i}{k}\left\{\exp\left[ik\left(\sqrt{y^2 + a^2}\right)\right] - \exp(iky)\right\} \qquad 3.13$$

The exponential can be combined into a sine term by the use of trigonometric identities giving

$$\left|p_y\right| = p_0 2\left|\sin\frac{k}{2}\left[\left(\sqrt{y^2 + a^2}\right) - y\right]\right| \qquad 3.14$$

where p_0 is the pressure at y=0. The characteristics of equation 3.14 are that, the magnitude of p_y fluctuates up until a last maximum known as the near field or Fresnel zone, and then decays at

the rate y^{-1} in the far field or the Fraunhofer region. The location of a maximum or minimum is when

$$\frac{k}{2}\left[\left(\sqrt{y^2+a^2}\right)-y\right]=m\frac{\pi}{2} \qquad 3.15$$

where m is an odd integer for a maximum and an even integer for a minimum. The last maximum at $y=N$, occurs for $m=1$, such that equation 3.15 becomes

$$N=\frac{d^2-\lambda^2}{4\lambda} \qquad 3.16$$

where d is the diameter of the transducer. The diameters of the PUNDIT supplied transducers are 50mm for 24, 37 and 54kHz transducers and 33mm for the 82kHz transducer. The pulse velocity for ordinary concrete can be taken to be 3660m/s [Naik and Malhotra (1991)]. Applying this data to equation 3.16 results in a negative value of N for all cases. This reveals that all the standard transducers can be considered to act as a point source, or in other words only far field approximations apply. For ranges in excess of 3N from the transducer face, the approximations $\sin x = x$ and $(1+x)^n = 1+nx$ can be used, such that equation 3.14 can be simplified to

$$p_{(y)N>3}=p_0\frac{ka^2}{4y} \qquad 3.17$$

which describes spherical spreading loss as in equation 3.8. Alternatively if the pressure is known at some distance R in the far field, then the pressure at y further along can be given as

$$p_y=p_R\frac{R}{y} \qquad 3.18$$

3.4 Signal losses in concrete due to material attenuation

The conventional pulse echo technique for measuring sound attenuation in materials such as metals requires the reception of multiple echoes in the thickness direction of the material under test [Papadakis (1990)]. For assessment on concrete, the pulse echo technique is impractical since scattering off aggregate interferes with returning pulses. A through transmission technique

was devised for this work where the amplitudes of signals propagated in aluminium were compared to those for concrete. From equation 3.8, the ratio of the signal amplitude for concrete p_c over the reference signal amplitude for aluminium p_a is given as

$$\frac{p_c}{p_a} = \frac{y_a e^{i(\beta_c y_c - \omega t)} e^{-\alpha_c y_c}}{y_c e^{i(\beta_a y_a - \omega t)} e^{-\alpha_a y_a}} \qquad 3.19$$

where α_a, β_a, y_a and α_c, β_c, y_c represent the attenuation coefficient, real wave number and path length for aluminium and concrete respectively. If the signal amplitudes are compared at the same phase ωt and the attenuation in aluminium is considered negligible at kHz frequencies then in terms of α_c and units of Nepers/m (an abbreviation of Napier who introduced logarithms) equation 3.19 reduces to

$$\alpha_c(f) = \frac{-1}{y_c} \ln\left(A \frac{p_c(f)}{p_a(f)} \right) \qquad 3.20$$

where the constant A represents differences in beam spreading (far field approximation) together with variations in the acoustic coupling of transducers. The evaluation of the constant A is not trivial, and it is reported [Bungey (1991)] that attenuation measurements are extremely sensitive to the quality of contact made between transducers and concrete surface.

Attenuation mechanisms can be attributed to beam spreading, absorption and scattering . Beam spreading was explored in the previous section. Absorption is said to indicate the quantity of the ultrasonic energy transformed into heat [Fay (1991)]. Three regimes of scattering are given that relate to the ratio of the object diameter to the signal wavelength. When the diameter of the scatterer is very small compared to the ultrasonic wavelength then Rayleigh scattering occurs. Here the scattered fields off the objects interact with each other and it is more convenient to consider the interaction of the wave with all the objects. Losses due to Rayleigh scattering are said to increase with the 4^{th} power of frequency [Fay (1991)]. When the object diameter is of the same order of magnitude as the wavelength then stochastic scattering occurs. Here the scattered field is strongly directionally dependent and the extent of the scattering is said to increase by the 2^{nd} power of the frequency. When the object is large compared to the wavelength each object has its own scattering field. Termed diffuse scattering, most of the incident energy is scattered back off the object and is independent of the frequency. It is usual for the coarse aggregate in structural concrete to have an aggregate size of 20mm. From the set of standard transducers and wave velocity described above, using the appropriate 54kHz transducers would result in a wave propagating in concrete with a wavelength of 68mm. For such an object wavelength ratio, this would place the scattered field in the Rayleigh scattering regime.

Curves that relate frequency *f*, mean diameter of scatterer *D*, to attenuation α, generally take the following form [Krautkramer & Krautkramer (1968)];

$$\alpha = af + bD^3 f^4 \qquad 3.21$$

which is valid for $\lambda/D>3$. If this condition is fulfilled and it is assumed that the second term will prove to be negligible compared to the first, then α would be proportional to *f*. For an experimental set of data that shows this linearity, the evaluation of the constant *A* in equation 3.20 becomes unnecessary, since a fitted straight line to this data will have the same slope whatever the value.

Very little information was found on concrete attenuation, which is not surprising since there is an extensive range of mixes possible. In general attenuation coefficients for concrete are given for specific transducer centre frequencies such as 7 to 13 Nepers/m at 200kHz [Kaye and Laby (1995)] which is not very useful. Some experiments were therefore conducted on three different concrete blocks that could be said to represent typical mixes encountered. The fully cured sample concrete blocks were of 200mm diameter and 300mm long and were made up with compositions shown in Table 3.1. In general the samples can be described as mortar, and concrete with 5mm or 10mm aggregate where the aggregate had been graded by a process of sieving. When obtaining data for the concrete samples it was found that the most favourable signals were acquired for transmission through the diameter mid way along the length as shown in Fig 3.5. The transducers used for this work were a pair of Alltran compression transducers [Alleyne (1991)] that were originally developed for the inspection of process pipe-work. The active element area is approximately 3mm by 14mm and in general these transducers are often excited by tone burst with a centre frequency in the region of 60kHz to 80kHz. The transducers are broad band in this region since they are operated away from their approximate 150kHz resonance frequency. With this and $\lambda/D>3$ in mind the excitation used was a 5 cycle tone burst at centre frequencies of 50 to 130kHz at increments of 5kHz. The reference signals were obtained by propagating the same signals in a 300mm diameter 300mm long aluminium bar. Signal attenuation in the aluminium bar can be considered negligible, such that reflections off boundaries could significantly interfere with the received signal. This effect was reduced by coupling the transducers off centre at either end of the bar in the configuration shown in Fig 3.6. Over the range of frequencies of interest, the amplitudes of the first and second received positive peaks after propagation in aluminium are shown in Fig. 3.7. For the evaluation of the attenuation coefficient, the amplitudes of the set of signals propagated in a concrete sample were compared to the reference signals. Equation 3.17 suggests the longer path length and greater wave velocity for the aluminium bar will result in greater signal losses due to beam

spreading. This however is accounted for in the constant A in equation 3.20 and is of no concern. An example of the 80kHz centre frequency received signal for 5mm aggregate concrete (continuous line) compared to that for aluminium (dashed line) is shown in Fig 3.8. For this case, signal losses due to beam spreading in the aluminium bar, given by equation 3.17, are approximately 3 times greater than for propagation in the shorter concrete block. If the losses due to material attenuation in concrete are of lower magnitude than the relative losses due to beam spreading, then the received signal in aluminium will be of lower amplitude than for concrete. This is the case for the example shown in Fig. 3.8.

The experimental results for the mortar, 5mm and 10mm aggregate concrete are shown in Fig 3.9, Fig 3.10 and Fig 3.11 respectively, where circles represent the attenuation coefficient $\alpha(f)$ evaluated by comparing the amplitude of the first positive peak and triangles for evaluation by the second received peak. A straight line has been fitted to the data points and the constant A adjusted so that the data is separated for clarity. All results obtained using the ratio of the first peaks show good agreement to the assumption that for $\lambda/D>3$ the attenuation coefficient for concrete can be considered as a linear function of frequency. In general this approximation improves for more highly attenuative materials since any interfering scattering or reflections off boundaries can be considered to have been significantly attenuated. The evaluated attenuation coefficients for the samples are listed in Table 3.2 along with the evaluated actual longitudinal bulk velocity. The actual bulk velocity was determined by establishing the time delay between the received signal when the transducers were coupled together and the received signal that had propagated down the block.

3.5 Modelling received signal

This section reports on the derivation of simplistic time domain functions that describe the profile of the early part of the signal received by the PUNDIT transducers. A schematic of the transfer function for the transducers coupled to a medium is shown in Fig. 3.12, where in the time domain;

$f(t)$ represents the PUNDIT electrical input signal,

$h_1^{-1}(t)$ is the transducer transfer function that converts an electrical impulse signal into a mechanical displacement,

$c(t)$ is the impulse response of the coupling and medium in which the signal propagates,

$h_2(t)$ represents the transducer transfer function that converts an mechanical impulse into an electrical signal, from which the output is given by the convolution product

$$g(t) = f(t) * h_1^{-1}(t) * c(t) * h_2(t) \qquad 3.22$$

The transfer function $h_2(t)$ can be obtained by the pencil lead break test [Berthelot et al. (1993)], but obtaining $h_1^{-1}(t)$ is not so straightforward. For simplification it will be assumed that the frequency response of the coupling medium is flat, such that $c(t)$ can be approximated by a Dirac function with the effect of introducing a time delay. The transfer functions $h_1^{-1}(t)$ and $h_2(t)$ can then be lumped together as $h(t)$ which can be obtained by through transmission coupling the transducers to a non dispersive system, exciting one with a near impulse and recording the output from the other. The Convolution Theorem [Randall (1977)] states that a Fourier Transform (either forward or inverse) transforms a convolution into a multiplication and vice versa. The forward Fourier transform of $g(t)$ that represents the transducer-transducer electrical output can then be given in a more convenient form as

$$G(f) = F(f) \cdot H(f) \qquad 3.23$$

where $H(f)$ refers to the electrical impulse response of the transducer-transducer arrangement and $F(f)$ the PUNDIT excitation pulse.

Since the PUNDIT transducers are narrow band in nature, $h(t)$ can be approximated by a function that has been used for modelling similar acoustic emission signals [Perez (1997)], where a carrier signal of centre frequency ω_o is modulated by a window function and is given by

$$h(t) = \eta t^{\xi} e^{-\zeta \omega t} \sin(\omega_0 t) \qquad 3.24$$

where η, ξ and ζ are constants. The modulation is characterised by an exponential decay, a non zero rise time and attains a maximum amplitude at the time

$$t = \frac{\xi}{\zeta \omega_o} \qquad 3.25$$

such that the magnitude of η is chosen to obtain the desired maximum amplitude at this time.

The PUNDIT excitation pulse is characterised by the discharge of a capacitor which is commonly approximated by the function

$$f(t) = Ae^{-\gamma t} \text{ for } t \geq 0 \qquad 3.26$$

where γ is the time constant which is inversely proportional to the product of circuit resistance and capacitance. With a 54kHz transducer acting as a load, the excitation pulse from the PUNDIT apparatus was monitored as shown in Fig. 3.13. By fitting an exponential curve to the experimental data an approximate value for the time constant was found to be $\gamma \approx 24000\ s^{-1}$.

To assess what the characteristics of the output $g(t)$ might be, it is convenient to apply the forward Fourier transform to equation 3.26 such that

$$F(f) = A\int_0^\infty e^{-\gamma t} e^{-i2\pi ft}\, dt$$

$$= A\int_0^\infty e^{-(\gamma + i2\pi f)t}\, dt$$

$$= -\frac{A}{(\gamma + i2\pi f)}\left[e^{-(\gamma + i2\pi f)t}\right]_0^\infty$$

$$F(f) = \frac{A}{\gamma}\frac{1 - i2\pi f/\gamma}{1 + (2\pi f/\gamma)^2} \qquad 3.27$$

Since equation 3.27 is complex, application to equation 3.23 will result in the phase of the output $G(f)$ differing to that for the impulse response $H(f)$ by some function of frequency. By applying the experimentally evaluated time constant to equation 3.27 the phase shift can be predicted which is shown in Fig 3.14. It can be seen that in general the PUNDIT excitation applies a near π/2 phase lag to the transducer response. This effect has important consequences on the profile of the received signal, particularly up to the first negative peak. Fig 3.15 shows the normalised approximations for the PUNDIT excitation $f(t)$, the transducer-transducer impulse response $h(t)$ and the resulting output $g(t)$. It can be seen that the first negative peak of $g(t)$ coincides with the phase $\omega_o t \approx \pi$ of $h(t)$, after which $g(t)$ lags $h(t)$ by approximately π/2 radians. Rather than try to find a function to approximate the complete received signal, it is simpler to approximate the signal for the first two negative peaks separately. This is all that is necessary for the aim of the analysis. Appropriate functions were found to be

$$g(t) = \frac{P}{2}\left[1 - \cos(\omega_0 t)\right] \qquad \text{for } \omega_0 t \le \pi \qquad 3.28$$

$$g(t) = \sin\left(\omega_0 t - \frac{5\pi}{2}\right)Pm \qquad \text{for } \frac{5\pi}{2} \le \omega_0 t \le 3\pi \qquad 3.29$$

where P and Pm represent the magnitude of the first and second negative peaks respectively. Since equations 3.28 and 3.29 are derived for narrow band signals they can be said to be valid for the 24kHz to 82kHz range of narrow band commercial transducers. For comparison, Fig 3.16 shows good agreement between equation 3.28 and the early part of the experimental received signal that was shown in Fig. 3.1.

3.6 Correction for the variation in measured pulse velocity

The proposed correction function assumes that the threshold is triggered by the received signal up to the first negative peak as in Fig 3.1. For triggering off the first negative peak, if we take the output $g(t)$ to equal the threshold value P_{TH} =250μV and rearrange equation 3.28, then the predicted additional transit time t_P that corresponds to the point where the signal will cross the threshold can be given as

$$t_P = \cos^{-1}\left(1 - \frac{2P_{TH}}{P}\right)\frac{1}{\omega_0} \qquad 3.30$$

where P is the amplitude of the first negative peak and ω_o is the transducer centre frequency. Equation 3.30 is the proposed function for correcting the variation in measured pulse velocity, which as intended is simplistic in nature to allow its use. However, practical application would require that the amplitude of the first negative peak P be known for which present commercial apparatus has no current standard facility.

3.7 Predicting the variation in measured pulse velocity

It has been shown that for a typical concrete type medium, commercial transducers operating in the frequency range of 24kHz to 83kHz can be considered to act as a point source. Experimental results found that ultrasonic attenuation in concrete can be considered to be a linear function of frequency for $\lambda/D>3$. For the prediction of the signal amplitude p_y as a function of path length y, the signal losses due to attenuation can then be applied to equation 3.18 to give

$$p_y = p_R\left(\frac{R}{y}\right)e^{-\alpha f y} \qquad 3.31$$

where p_R is the signal amplitude at a distance R from the transducer due to beam spreading only.

Setting the amplitude of the first negative peak to $P = p_y$ and substituting equation 3.31 into equation 3.30 gives the predicted additional transit time that will be measured as

$$t_P = \cos^{-1}\left(1 - \frac{2P_{TH}}{p_R}\left(\frac{y}{R}\right)e^{\alpha y f_0}\right)\frac{1}{2\pi f_0} \qquad \text{for } p_y > T \qquad 3.32$$

which is valid if triggering off the received signal up to the first negative peak. Predictions showed that if the magnitude of the first negative peak falls below the threshold then it would be possible to trigger off the signal up to the second negative peak. The magnitude of the second negative peak can be given as mp_y where m is the ratio of the second over the first negative peak. When triggering up to the next negative peak $p_y < T < mp_y$ the predicted additional transit time is obtained from equation 3.29 in a similar manner as before and is given as

$$t_{mP} = \left[\sin^{-1}\left(\frac{P_{TH}}{mp_R}\frac{y}{R}e^{\alpha y f_0}\right) + \frac{5\pi}{2}\right]\frac{1}{2\pi f_0} \quad \text{for } p_y < T < mp_y \qquad 3.33$$

In section 3.2, the 500V excitation pulse was propagated in a 100mm thick aluminium block, and the received signal monitored which is shown in Fig 3.1. Within the frequency range of interest, material attenuation in aluminium can be considered to be negligible. For an approximate value of P_R it is therefore reasonable to use the experimental value obtained for the magnitude of the first negative peak of the signal propagated in aluminium. Thus at R=100mm, for the maximum 1000V excitation an appropriate value is p_R= 8V. In fact the exact value is not critical since losses due to beam spreading and material attenuation soon become dominant. Additionally from these results an approximate value for the ratio of the second over the first negative peak of m=1.5 was obtained. If we take the actual longitudinal bulk velocity of the material as c_L, (evaluation of c_L is described in section 3.4) then the predicted variation in measured pulse velocity $c_L(y)$ as a function of path length tested y will be given as

$$c_L(y) = \left(\frac{y}{y + c_L t_P}\right)c_L \quad \text{for } y > \lambda \qquad 3.34$$

Using the evaluated attenuation coefficients and actual velocities for the samples as in table 3.2, the predictions for the variation in measured velocity as a function of path length tested for the mortar, 5mm and 10mm concrete samples are shown in Figures 3.17 through to 3.19. For the short path lengths tested, all plots are typified by the measured velocity initially increasing as a function of path length, particularly so for the mortar predictions. This effect has been confirmed experimentally [Bungey (1980)] and is probably part of the argument that leads to the recommendations of minimum path lengths that can be inspected [BS1181:Part 203 (86)]. After

the initial rise the measured pulse velocity as a function of path length tested flattens off. In this region it is predicted that the actual velocity in the material will never be measured. Following this, the predicted measured pulse velocity falls rapidly which corresponds to when the signal amplitude of the first peak falls below the magnitude of the threshold. The apparatus no longer recognises the first arrival and will then be triggered off the second negative peak. The predicted measurement error for the 37kHz and 24kHz transducers applied to 10mm aggregate concrete in Fig 3.19 is about –4.4%. A typical reduction of the measured velocity of 5% for a path length between 3m to 6m is reported [Bungey (1996)]. Thus the predictions for this case have confirmed that the extent of the anomaly is indeed as published.

Generally, if the threshold is being triggered off the received signal up to the first negative peak, then the order of the variation is predicted to be in the region of a 1% reduction, which is recommended in [BS1181:Part 203 (86)]. To ensure triggering off the early part of the signal, since the second negative peak was shown to be about 1.5 times the magnitude of the first, any received signal below twice the threshold value should be rejected. Like the proposed correction function this would require the apparatus to determine the received signal amplitude, which it presently does not have the capacity to do.

3.8 Conclusion

An investigation was conducted to estimate the extent of the reported anomaly that the pulse velocity measured by threshold crossing, such as is done by the apparatus PUNDIT apparatus, varies with the path length tested. The intention was to recommend a correction function for the standard narrow band type transducers.

The change in pulse shape as a function of distance propagated was modelled by considering signal losses and transducer and excitation characteristics. The commercial transducers have been shown to act as a point source such that the signal experiences spherical beam spreading as it propagates. Experiments were conducted to evaluate material attenuation in three samples that could be said to represent typical concrete mixes encountered. Attenuation coefficients in mortar, 5mm and 10mm aggregate concrete samples were found to be adequately approximated by a linear function of frequency for signal wavelengths greater than three times aggregate size. The transfer function of the PUNDIT transducers was investigated where it was found that the first half cycle of the received signal lasts for approximately twice the normal time period.

For the early part of the received signal up to the first negative peak a correction function was proposed which would require the amplitude of the peak to be known. The function was

simplistic in nature so that its calculation could be achieved by relatively unskilled labour with a common calculator. However, the current standard PUNDIT apparatus does not have the facility to determine signal amplitudes so some additional equipment or modification would be required.

The research on signal losses due to beam spreading and material attenuation was applied to the correction function so as to estimate the extent of the anomaly. It was found that as long as the threshold is triggered off the received signal up to the first negative peak the measured velocity would be only about 1% lower then the actual, which is the British Standard recommended limit. However if the magnitude of the first negative peak is below the threshold then triggering off the second negative peak is possible. It is confirmed that for this case reductions in the pulse velocity of around 5% are likely for path lengths of 3 to 5m.

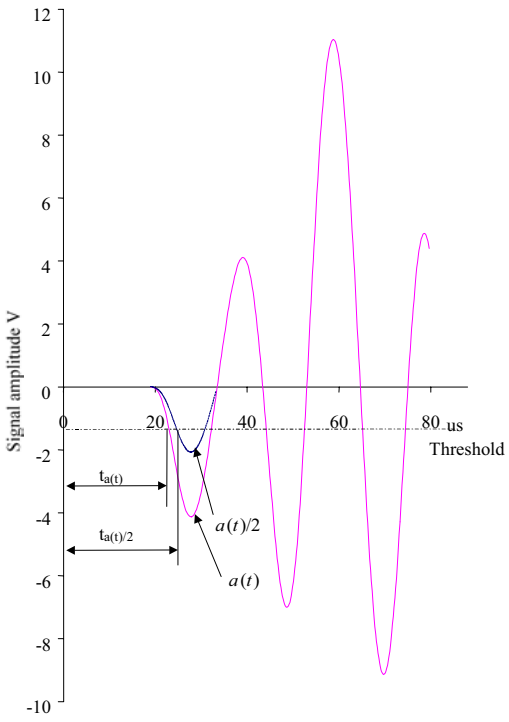

Figure 3.1 Signal $a(t)$ received by Pundit apparatus (100mm thick aluminium) showing the effect a decrease in signal amplitude $a(t)/2$ has on the point the threshold is crossed.

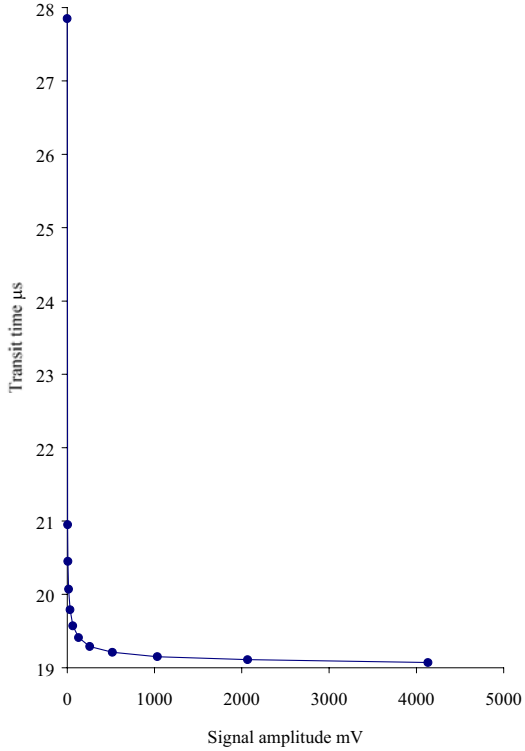

Figure 3.2 Predicted Pundit measured signal transit time (100mm thick aluminium) as a function of maximum amplitude of the received first half cycle of signal $a(t)$.

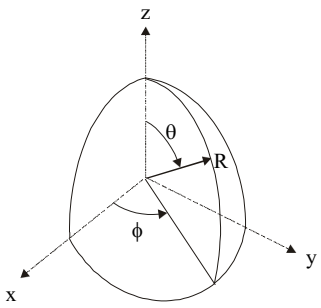

Figure 3.3 Spherical coordinate system

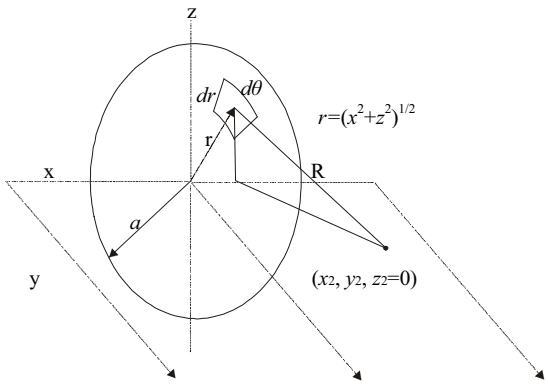

Figure 3.4 Approximation of transducer by superposition of point sources

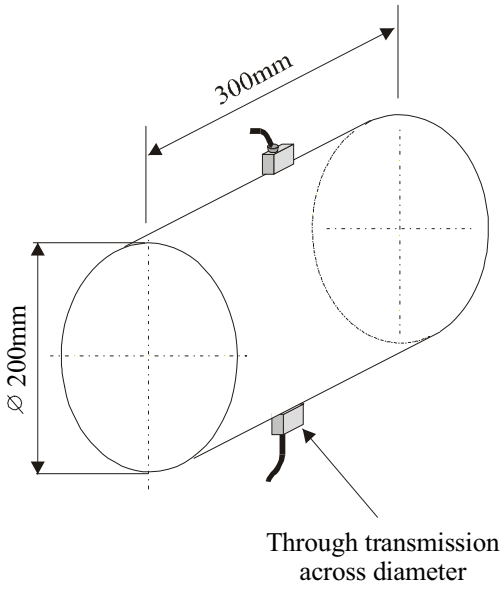

Figure 3.5 Application of transducers to concrete sample to obtain signals for concrete attenuation measurement

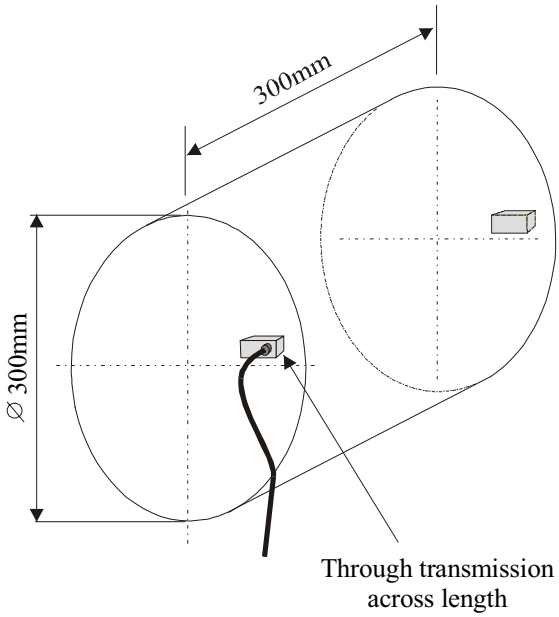

Figure 3.6 Application of transducers to aluminium block to obtain reference signals for concrete attenuation measurement

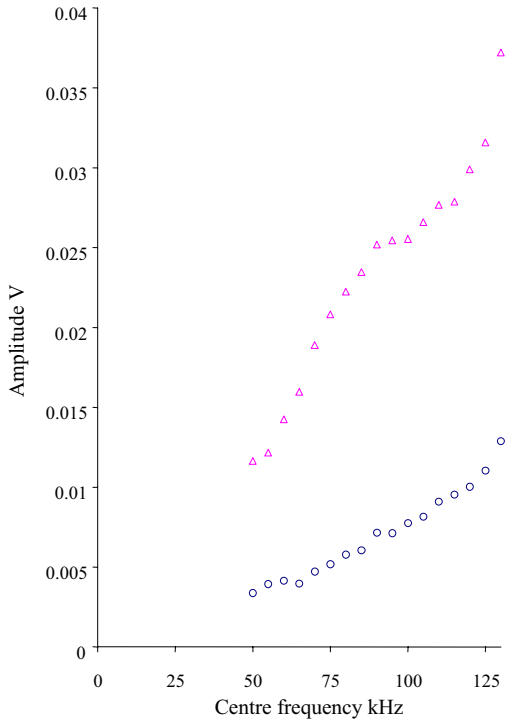

Figure 3.7. Magnitude of first (circles) and second (triangles) peak of received reference signal as a function of excitation centre frequency.

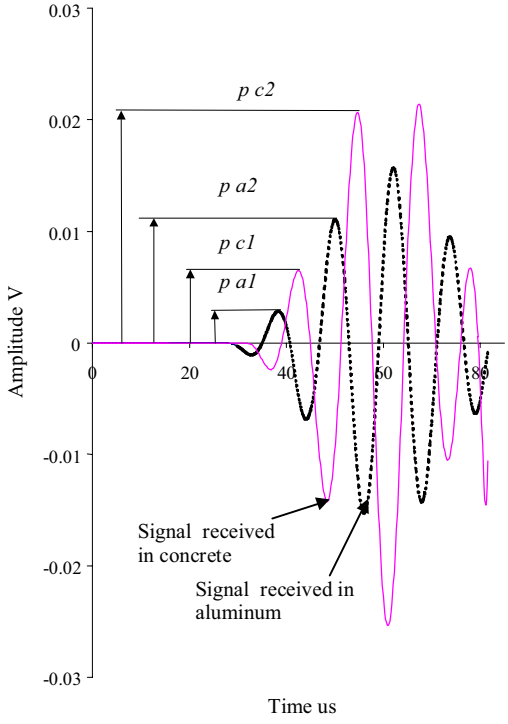

Figure 3.8. Example received signals for 80kHz centre frequency 5 cycle tone burst for aluminium (dashed line) and 5mm aggregate concrete (continuous).

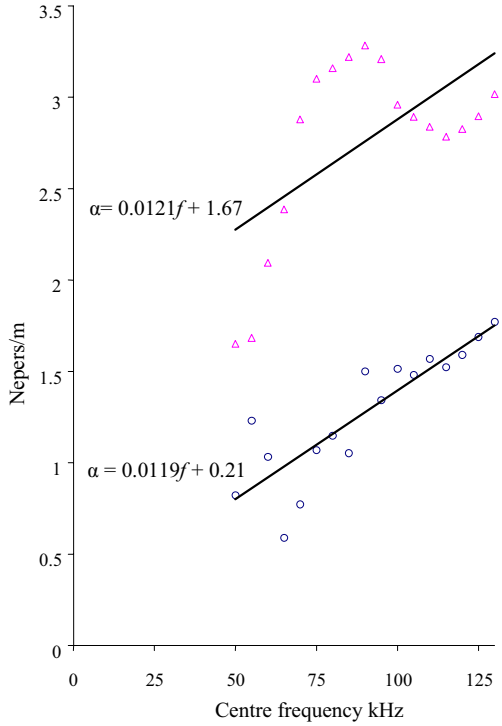

Figure 3.9. Mortar attenuation coefficient α(*f*), evaluation by amplitude of first received peak (circles) and second peak (triangles).

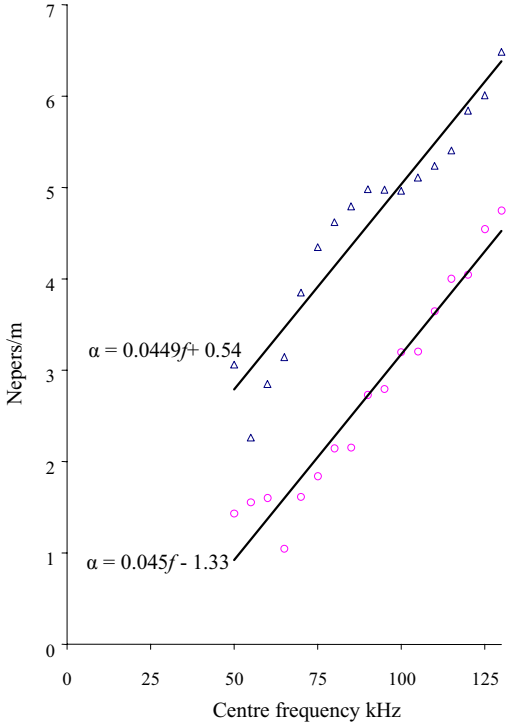

Figure 3.10. Concrete (5mm aggregate) attenuation coefficient α(*f*), evaluation by amplitude of first received peak (circles) and second peak (triangles).

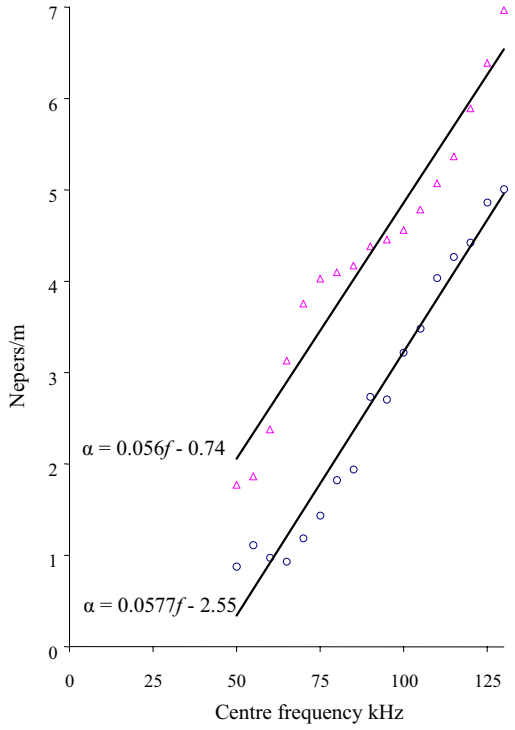

Figure 3.11. Concrete (10mm aggregate) attenuation coefficient α(*f*), evaluation by amplitude of first received peak (circles) and second peak (triangles).

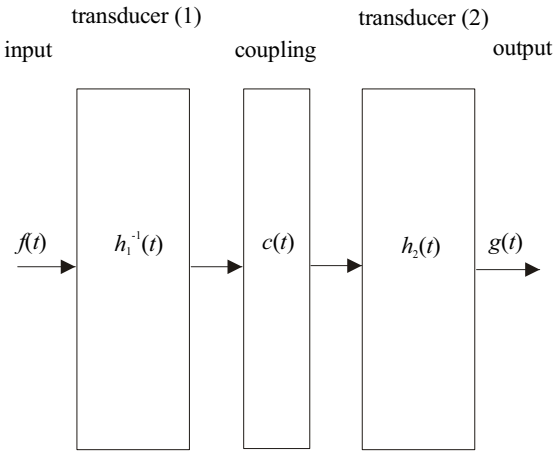

Figure 3.12. Schematic of transducer transfer function.

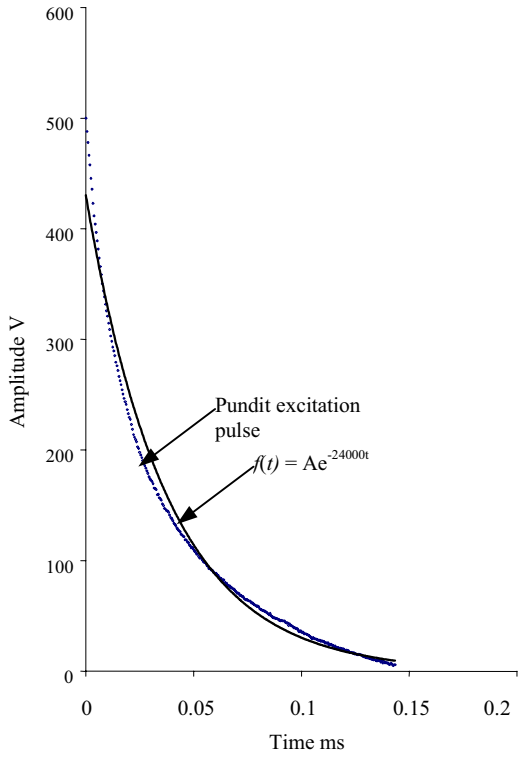

Figure 3.13. Pundit 500V excitation pulse and fitted exponential decay.

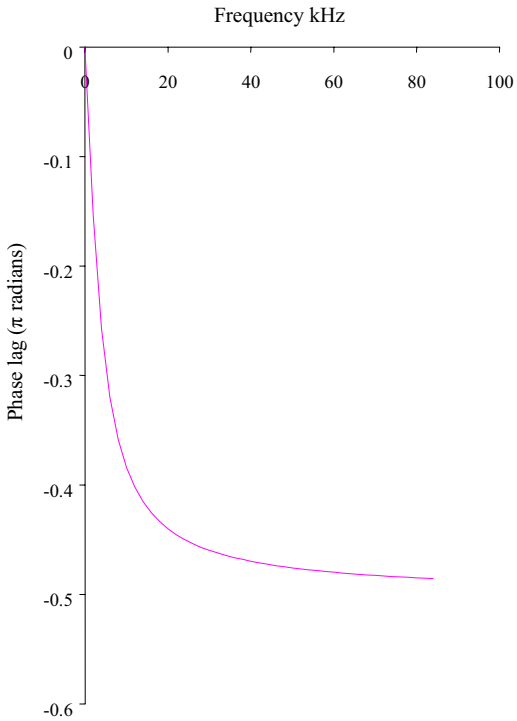

Figure 3.14. Phase(*f*) of Pundit 500V excitation pulse.

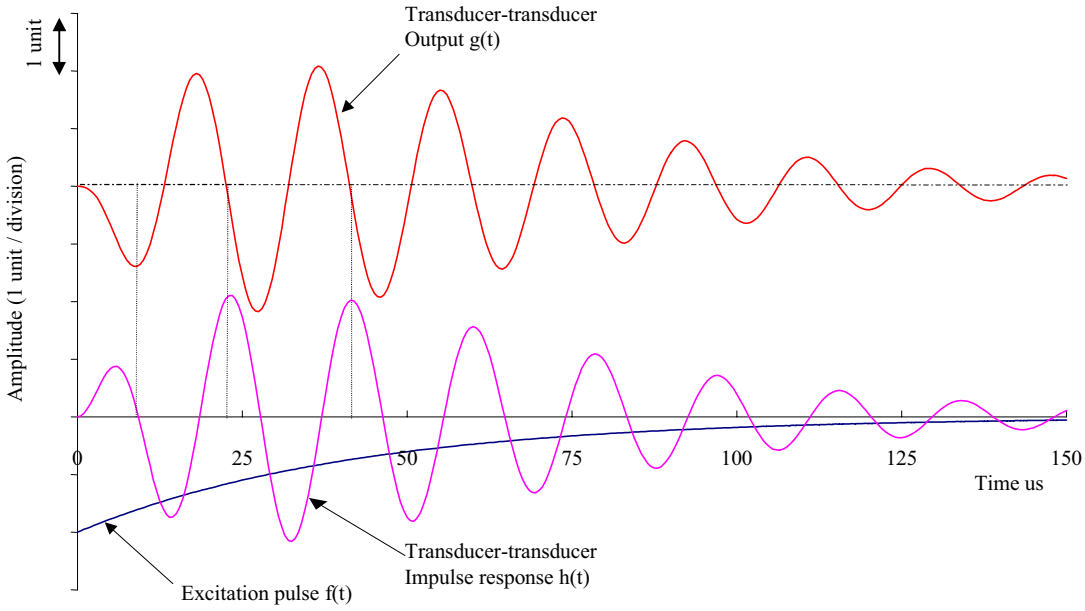

Figure 3.15. Predicted output *g*(*t*) from Pundit 54kHz transducers when excited by Pundit 500V excitation pulse *f*(*t*), to illustrate phase lag between *g*(*t*) and impulse response *h*(*t*).

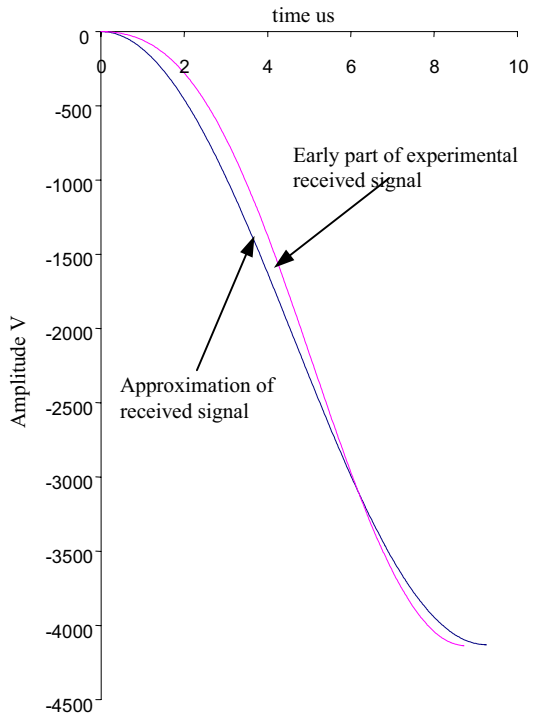

Figure 3.16. Comparison of early part of received signal in Fig 3.1 and approximation by equation 3.28.

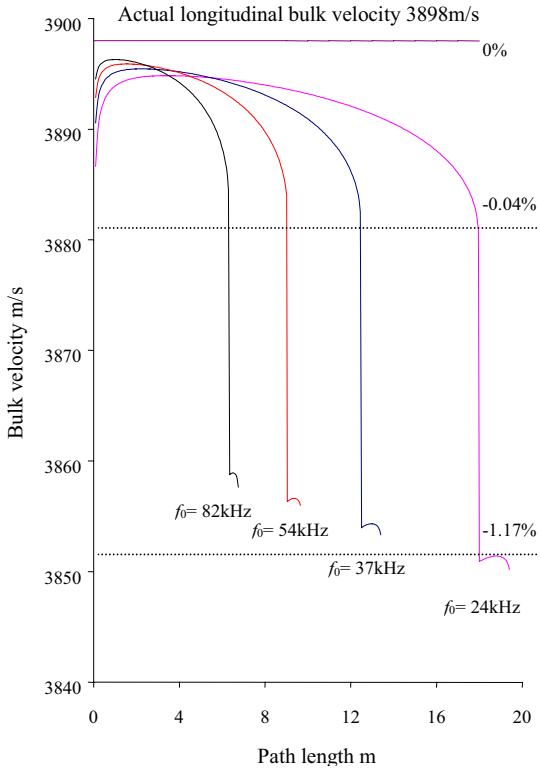

Figure 3.17 Prediction of measured bulk velocity as a function of path length tested using Pundit transducers when testing mortar.

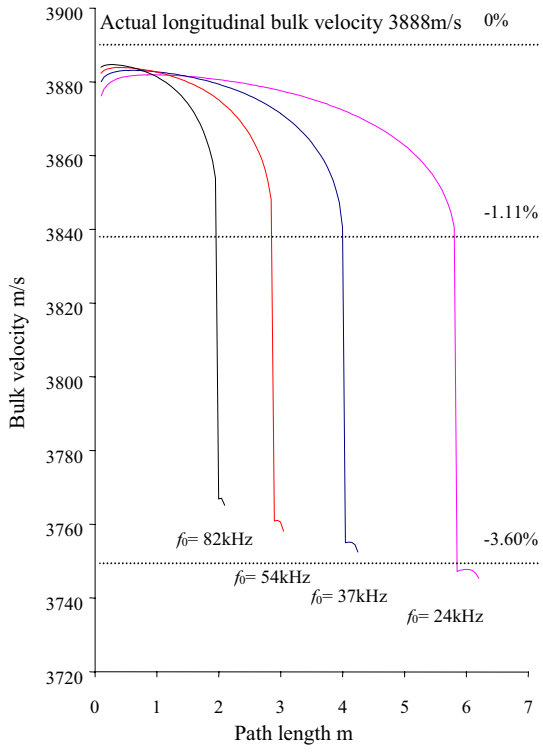

Figure 3.18 Prediction of measured bulk velocity as a function of path length tested using Pundit transducers when testing 5mm aggregate concrete.

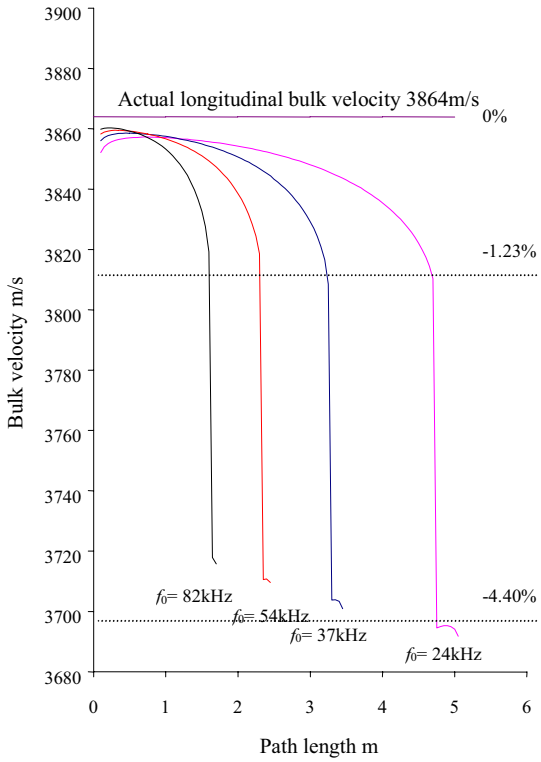

Figure 3.19 Prediction of measured bulk velocity as a function of path length tested using Pundit transducers when testing 10mm aggregate concrete.

mix	Mortar	concrete 5mm aggregate	concrete 10mm aggregate
5mm aggregate		2.5 kg	
10mm aggregate			2.5 kg
Builders sand	2.0 kg	1.0 kg	1.0 kg
Cement	2.222 kg	1.111 kg	1.111 kg
Added water	0.788 kg	0.389 kg	0.389 kg
Total	5.0 kg	5.0 kg	5.0 kg
Added water/cement ratio	0.35	0.35	0.35

Table 3.1 Composition of concrete samples for evaluation of attenuation coefficients

mix	Mortar	concrete 5mm aggregate	concrete 10mm aggregate
Attenuation coefficient (kHz Nepers/m) for $\lambda/D>3$	0.012	0.0454	0.0568
Longitudinal bulk velocity c_L	3898m/s	3888m/s	3864m/s

Table 3.2 Attenuation coefficients and velocities evaluated for concrete samples

Chapter 4

Validation of PUNDIT calibration procedure

4.1 Introduction

There is an inherent time delay in the circuitry of the PUNDIT apparatus that must be removed for the accurate determination of signal transit times. Calibration is achieved using a reference bar on which a time value is stamped. The question arises as to what mode of wave propagation the transit time stamped on the bar refers to, is the value correct, and does the technique itself introduce errors. The purpose of this chapter is to validate this calibration procedure theoretically and experimentally and to make recommendations as required. Axi symmetric finite element models were used to model wave propagation in a finite length of bar. The interpretation of model and experimental results required employment of signal processing techniques that are suitable for analysing dispersive signals. A wavelet and Hilbert transform technique have been developed to extract group velocity from linear chirp type signals. These techniques are presented within Appendix 1 where they are compared to the established phase spectrum method.

4.2 Reference bar description

The method of determining the transit time between pulse onset and reception by the PUNDIT apparatus is described in detail in section 2.4.2. Briefly, when the two transducers are coupled face to face, separated by a thin film of grease, we can consider the path length to be zero. For this set up the circuitry measures an inherent time delay of typically 2μs. To correct for this condition the transducers are first coupled to a reference bar. The set reference control knob on the front panel of the apparatus is then rotated (the position of which determines the duration over which the counter is initially inhibited) until the LCD display reads a time value that is stamped on the bar. If the calibrated value stamped on the bar is in error by a value greater than typically 2μs then the calibration procedure itself will introduce errors.

An illustration of the reference bar supplied with the standard apparatus is shown in Fig. 4.1. It consists of a 50mm diameter aluminium portion of length L_a equal to 153mm, to which at each end is bonded marginally smaller diameter brass protection discs of thickness L_b equal to 3mm. The dimensions are probably chosen to suit the 50mm diameter transducers and 153mm is equivalent to the imperial length of 6 inches. A calibration value of t_{cal}= 25.8μs is stamped

on the bar, which can be shown to relate to the time it would take a bulk longitudinal wave to propagate over the bar length. The nature of bulk and guided waves will be investigated in the sections that follow. The approximate bulk longitudinal velocities for aluminium c_{1a} and brass c_{1b} are 6328m/s and 4400m/s respectively. The time for a bulk wave to propagate through an unbounded body of the same lateral dimensions as the bar would be

$$t_{bulk} = \frac{L_a}{c_{1a}} + 2\frac{L_b}{c_{1b}} = \frac{0.153}{6328} + 2\frac{0.003}{4400} = 25.5\mu s \approx t_{cal} \qquad 4.1$$

which agrees somewhat with the value stamped on the bar.

A simple experiment was performed to investigate whether the calibrated value stamped on the bar is valid. The 54kHz transducers were coupled face to face by a smear of grease. Excitation and reception was enabled using the PUNDIT apparatus. For this zero path length condition the apparatus LCD display was adjusted to read 0.1μs. The transducers were then coupled to the reference bar resulting in a reading of 26.0μs on the LCD display. Thus, the apparatus suggests that the reference bar acts as a 25.9μs time delay, which allowing for numerical rounding up agrees with the value stamped on the bar. It therefore appears that some energy is indeed propagating at the bulk longitudinal velocity and is of significant magnitude so as to trigger the 250μV PUNDIT threshold.

The reference bar diameter is finite, which results in the bar acting as a wave guide, and so propagation of bulk waves cannot be assumed. In contrast to the bulk longitudinal and shear waves that exist in a boundless material, an infinite number of guided waves can exist in a finite structure. The velocity of propagation of a guided mode, unlike bulk waves, is a function of frequency. It is generally assumed that the maximum velocity that a wave can propagate in a bar is the bar velocity which for an aluminium bar corresponds to a value of 5120m/s. Classical solutions for what modes propagate in a bar assume steady state propagation in a bar of infinite length such that transient effects far from the source have decayed to zero. For a finite length of bar the accepted solution for guided waves may not be applicable, since sufficient interaction of bulk waves with the boundaries may not take place for mode conversion to provide the required axial and radial components. At what point the bar mode solutions are acceptable or ‘when is a bar a bar?’ is probably a function of the characteristics of excitation, bar diameter, and bar length. It is thus important to investigate the characteristics of wave propagation in bounded and unbounded media in order to verify the reference bar calibration value.

4.3 Wave propagation possibilities in the reference bar

This section investigates the possible modes of wave propagation that might exist in the reference bar. The well known theory used to describe the characteristics of stress waves in unbounded media and infinitely long bars will be briefly described. Neither of these solutions fully describes the problem since the bar is obviously bounded and of finite length. However, the investigation will benefit from the analysis since no exact solution for wave propagation in finite bars is known by the author. Where possible vector analysis will be used since it allows formulae of continuum mechanics to be written in a much shorter form than would otherwise be possible. In all analysis, the material will be assumed to be homogeneous, isotropic, linearly elastic and non-absorbing, which is an acceptable assumption for the aluminium reference bar.

4.3.1 Wave propagation in unbounded media – bulk waves

Bulk waves exist in infinite homogeneous bodies and propagate indefinitely without being interrupted by boundaries or interfaces. The properties of these waves are determined by the relationships between propagation direction and the constitutive properties of the medium. It can be shown that within an unbounded isotropic medium only two possible waves can propagate, being longitudinal or shear waves. Longitudinal waves have polarisation directed along the propagation direction, whereas shear waves have polarisation normal to the propagation direction. The derivation of the bulk wave velocities comes in a variety of approaches where here we borrow from [Malvern (1969), Kolsky (1963), and Redwood (1960) for example]. Though essentially bookwork, presenting the derivation in the following manner forms useful background information.

When an elastic body is deformed, the forces are transmitted within the body by means of elastic forces acting between neighbouring particles. The state of stress within the body can be defined by taking material particles to be small volume elements of some orthogonal coordinate system. Cartesian coordinates will be used where x_1, x_2, x_3, denote the directions as shown in Fig. 4.2. The force per unit area on a plane normal to the direction of the $+x_1$ axis is a stress vector having three components, denoted by T_{11}, T_{12}, and T_{13}. The first subscript denotes the normal direction of the plane, while the second identifies the vector component direction. Similarly, the forces per unit area on a plane area whose normals are in the $+x_2$ and $+x_3$ directions will have components denoted by T_{21}, T_{22}, T_{23} and T_{31}, T_{32}, T_{33} respectively. It may be shown that these nine stress components are sufficient to specify fully the state of stress for the element. Under triaxial loading, Hooke's law expresses each stress component as a linear combination of all the strains given as

$$T_{ij} = c_{ijrs} S_{rs} \qquad 4.2$$

where *i* can be *1,2*, or *3*, and where for a given *i*, the summation over the subscript *j* is understood; likewise with *r* and *s*. The nine equations given by equation 4.2 require a total of 81 elastic constants c_{ijrs}, but not all of these are independent. For small displacement, the strain tensor S_{rs} can be defined as

$$S_{rs} = \frac{1}{2}\left(\frac{\partial u_r}{\partial x_s} + \frac{\partial u_s}{\partial x_r} \right) \qquad 4.3$$

where *u* is the particle displacement. It should be noted that for convenience the factor of a half is present for the shear stains in contrast to the engineering definition, this will be corrected for in the next step. It can be seen from the definition of equation 4.3 that S_{rs} is a symmetric tensor such that S_{21} can be replaced with S_{12} and so on. Symmetry of T_{ij} and S_{rs} reduces the number of independent elastic constant to 36 and enables a reduced notation with fewer subscripts to be used. The standard reduced notation for the strain tensor **S** can be expressed in matrix form

$$\mathrm{S} = \begin{bmatrix} S_{11} & S_{12} & S_{13} \\ S_{21} & S_{22} & S_{23} \\ S_{31} & S_{32} & S_{33} \end{bmatrix} = \begin{bmatrix} S_1 & 0.5S_6 & 0.5S_5 \\ 0.5S_6 & S_2 & 0.5S_4 \\ 0.5S_5 & 0.5S_4 & S_3 \end{bmatrix} \qquad 4.4$$

The notation for stress tensor **T** can be expressed as

$$\mathrm{T} = \begin{bmatrix} T_{11} & T_{12} & T_{13} \\ T_{21} & T_{22} & T_{23} \\ T_{31} & T_{32} & T_{33} \end{bmatrix} = \begin{bmatrix} T_1 & T_6 & T_5 \\ T_6 & T_2 & T_4 \\ T_5 & T_4 & T_3 \end{bmatrix} \qquad 4.5$$

The subscripts for the reduced notation follow a cyclic order such that 1,2, and 3 represent normal or longitudinal components while subscripts 4,5, and 6 are for tangential or shear components. The relation between stress and strain can now be conveniently represented by the following matrix equation

$$\begin{bmatrix} T_1 \\ T_2 \\ T_3 \\ T_4 \\ T_5 \\ T_6 \end{bmatrix} = \begin{bmatrix} c_{11} & c_{12} & c_{13} & c_{14} & c_{15} & c_{16} \\ c_{21} & c_{22} & c_{23} & c_{24} & c_{25} & c_{26} \\ c_{31} & c_{32} & c_{33} & c_{34} & c_{35} & c_{36} \\ c_{41} & c_{42} & c_{43} & c_{44} & c_{45} & c_{46} \\ c_{51} & c_{52} & c_{53} & c_{54} & c_{55} & c_{56} \\ c_{61} & c_{62} & c_{63} & c_{64} & c_{65} & c_{66} \end{bmatrix} \begin{bmatrix} S_1 \\ S_2 \\ S_3 \\ S_4 \\ S_5 \\ S_6 \end{bmatrix} \qquad 4.6$$

which in vector notation can be written as

$$\mathrm{T} = \mathrm{c} : \mathrm{S} \tag{4.7}$$

For an isotropic solid the coefficient matrix **c** requires just two independent elastic constants, λ and μ, known as Lamé's constants and takes the form

$$\begin{bmatrix} \lambda+2\mu & \lambda & \lambda & 0 & 0 & 0 \\ \lambda & \lambda+2\mu & \lambda & 0 & 0 & 0 \\ \lambda & \lambda & \lambda+2\mu & 0 & 0 & 0 \\ 0 & 0 & 0 & \mu & 0 & 0 \\ 0 & 0 & 0 & 0 & \mu & 0 \\ 0 & 0 & 0 & 0 & 0 & \mu \end{bmatrix} \tag{4.8}$$

For the equation of motion, we apply Newton's second law of motion and the principle of conservation of mass to the elemental volume. Neglecting body forces (e.g. gravity), Euler's equation of motion in vector form [Auld (19900] can be given as

$$\nabla \bullet \mathrm{T} = \rho \frac{\partial^2 \mathrm{u}}{\partial t^2} \tag{4.9}$$

where ρ is the mass density, **u** the displacement vector and *t* is time. Substituting equation 4.7 into equation 4.9 using the coefficients **c** from equation 4.8 results in the vector equivalent of Navier's displacement equation of motion given as [Graff 1975 for example]

$$(\lambda+\mu)\nabla\nabla \bullet \mathrm{u} + \mu\nabla^2 \mathrm{u} = \rho \frac{\partial^2 \mathrm{u}}{\partial t^2} \tag{4.10}$$

where ∇^2 is the Laplace operator and the divergence of **u** defines the material dilatation given by

$$\nabla \bullet \mathrm{u} = \Delta = S_1 + S_2 + S_3 \tag{4.11}$$

The phase velocities of the two possible waves can now be obtained, where for the longitudinal wave velocity c_l a divergence $\nabla\bullet$ is performed on equation 4.10 to give

$$(\lambda+\mu)\nabla \bullet (\nabla\nabla \bullet \mathrm{u}) + \mu\nabla \bullet (\nabla^2 \mathrm{u}) = \rho\nabla \bullet \frac{\partial^2 \mathrm{u}}{\partial t^2} \tag{4.12}$$

Recognising the identities $\nabla \bullet \nabla \equiv \nabla^2, \nabla \bullet \left(\nabla^2 \mathbf{u}\right) = \nabla^2 \left(\nabla \bullet \mathbf{u}\right)$ and that $\nabla \bullet \mathbf{u} = \Delta$ reduces equation 4.12 to

$$(\lambda + 2\mu)\nabla^2 \Delta = \rho \frac{\partial^2 \Delta}{\partial t^2} \qquad 4.13$$

which describes the propagation of the dilatation Δ by a velocity c_1 given as

$$c_1 = \sqrt{\frac{(\lambda + 2\mu)}{\rho}} \qquad 4.14$$

For the velocity of the shear wave c_2 a curl ∇x is performed on equation 4.10 giving

$$(\lambda + \mu)\nabla \mathbf{x}\left(\nabla\nabla \bullet \mathrm{u}\right) + \mu \nabla \mathbf{x}\left(\nabla^2 \mathrm{u}\right) = \rho \nabla \mathbf{x} \frac{\partial^2 \mathrm{u}}{\partial t^2} \qquad 4.15$$

The rotation vector **w** is now introduced which is related to the displacement vector **u** by

$$\mathrm{w} = \frac{1}{2} \nabla \mathbf{x} \mathrm{u} \qquad 4.16$$

where

$$w_{ij} = \frac{1}{2}\left(\frac{\partial u_j}{\partial x_i} - \frac{\partial u_i}{\partial x_j}\right) \qquad 4.17$$

Substituting equation 4.16 into equation 4.15 and recognising the identities $\nabla \mathbf{x}\left(\nabla\nabla \bullet \mathbf{u}\right) = 0$, $\nabla^2 \mathbf{u} = \nabla\nabla \bullet \mathbf{u} - \nabla \mathbf{x} \nabla \mathbf{x} \mathbf{u}$ and that $\nabla \bullet \mathbf{w} = 0$ gives

$$\mu \nabla^2 \mathrm{w} = \rho \frac{\partial^2 \mathrm{w}}{\partial t^2} \qquad 4.18$$

which describes the propagation of the rotation **w** by a velocity c_2 given as

$$c_2 = \sqrt{\frac{\mu}{\rho}} \qquad 4.19$$

Equation 4.18 can also be interpreted as describing equivoluminal waves that propagate at the velocity c_2 since the dilatation is zero, and in the same light equation 4.13 describe irrotational waves.

Before leaving bulk waves, we should consider the propagation of plane waves, which are going to come up later. A plane wave is the case when the particle motion on a plane in space is described by constant phase and amplitude. It can be shown [Graff 1975 for example] that longitudinal and transverse polarised plane waves propagate with velocities equal to the equivalent bulk velocities given in this section.

4.3.2 Classical wave propagation in an infinitely long solid bar

The problem of elastic wave propagation in a bar was first investigated by Pochammer [1876] and independently by Chree [1889]. Their solution to problem is simplified by assuming the bar to be infinitely long such that end effects can be neglected. The equations of motion for an isotropic bar are known to have solutions corresponding to three different types of modes [Love (1927)], being longitudinal, flexural and torsional. For the equations of motion, the approach of Kolsky [1963] and Redwood [1960] will be followed. To enable insertion of the boundary conditions, equation 4.10 is first transformed to cylindrical polar co-ordinates r, θ, z as shown in Fig 4.3, with corresponding displacements u_r, u_θ, u_z. The equations of motion for cylindrical co-ordinates become:

$$\rho\frac{\partial^2 u_r}{\partial t^2} = (\lambda+2\mu)\frac{\partial\Delta}{\partial r} - \frac{2\mu}{r}\frac{\partial w_z}{\partial\theta} + 2\mu\frac{\partial w_\theta}{\partial z} \qquad 4.20$$

$$\rho\frac{\partial^2 u_\theta}{\partial t^2} = (\lambda+2\mu)\frac{1}{r}\frac{\partial\Delta}{\partial\theta} - 2\mu\frac{\partial w_r}{\partial z} + 2\mu\frac{\partial w_z}{\partial r} \qquad 4.21$$

$$\rho\frac{\partial^2 u_z}{\partial t^2} = (\lambda+2\mu)\frac{\partial\Delta}{\partial z} - \frac{2\mu}{r}\frac{\partial}{\partial r}(rw_\theta) + \frac{2\mu}{r}\frac{\partial w_r}{\partial\theta} \qquad 4.22$$

where the dilatation Δ in cylindrical co-ordinates is given by

$$\Delta = \frac{1}{r}\frac{\partial(ru_r)}{\partial r} + \frac{1}{r}\frac{\partial u_\theta}{\partial\theta} + \frac{\partial u_z}{\partial z} \qquad 4.23$$

and the following rotations w_r, w_θ, w_z are components about three orthogonal directions, being along the radius vector r, perpendicular to the rz plane and parallel to the z-axis respectively. They are related to the displacement gradients by:

$$2w_r = \frac{1}{r}\frac{\partial u_z}{\partial \theta} - \frac{\partial u_\theta}{\partial z} \qquad 4.24$$

$$2w_\theta = \frac{1}{r}\frac{\partial u_r}{\partial z} - \frac{\partial u_z}{\partial r} \qquad 4.25$$

$$2w_z = \frac{1}{r}\left[\frac{\partial (r u_\theta)}{\partial r} - \frac{\partial u_r}{\partial \theta}\right] \qquad 4.26$$

where the three equations 4.23 to 4.25 lead to the relation

$$\frac{1}{r}\frac{\partial (r w_r)}{\partial r} + \frac{1}{r}\frac{\partial w_\theta}{\partial \theta} + \frac{\partial w_z}{\partial z} = 0 \qquad 4.27$$

If we consider the bar to be surrounded by a vacuum then there is no medium outside of the bar to support a stress field. Hence there are no tractions on the surface of the bar, and the stress components σ_{rr}, $\sigma_{r\theta}$, and σ_{rz} at $r=a$ should vanish. These are the only boundary conditions that classically are considered. The bar is considered to be infinitely long since end effects are neglected, however in practice the length of the bar should be large in proportion to its radius [Kolsky (1963)]. The relationship between the radial stresses to the strains in cylindrical coordinates are:

$$\sigma_{rr} = \lambda\Delta + 2\mu\frac{\partial u_r}{\partial r} \qquad 4.28$$

$$\sigma_{r\theta} = \mu\left[\frac{1}{r}\frac{\partial u_r}{\partial \theta} + r\frac{\partial}{\partial r}\left(\frac{u_\theta}{r}\right)\right] \qquad 4.29$$

$$\sigma_{rz} = \mu\left[\frac{\partial u_r}{\partial z} + r\frac{\partial u_z}{\partial r}\right] \qquad 4.30$$

We can consider the propagation along the bar in the z direction as an infinite train of sinusoidal waves, where the displacements can be given as

$$u_r = U_{(r)}\cos n\theta \exp(-i\varepsilon z)\exp(i\omega t) \qquad 4.31$$

$$u_\theta = V_{(r)}\sin n\theta \exp(-i\varepsilon z)\exp(i\omega t) \qquad 4.32$$

$$u_z = W_{(r)}\cos n\theta \exp(-i\varepsilon z)\exp(i\omega t) \qquad 4.33$$

where ε is the wave number in the z direction and ω is the frequency.

It can be shown [Kolsky (1963)] that the equations of motion equation 4.20 through to 4.22 lead to Bessel equations requiring that the functions U, V and W must be of the form given by

$$U = C\left\{-A\frac{\partial}{\partial r}J_n(\alpha r)+B\frac{\partial}{\partial r}J_n(\beta r)+n\frac{J_n(\beta r)}{r}\right\} \qquad 4.34$$

$$V = C\left\{A\frac{n}{r}J_n(\alpha r)-B\frac{n}{r}J_n(\beta r)-\frac{\partial}{\partial r}J_n(\beta r)\right\} \qquad 4.35$$

$$W = C\left\{iAk_0J_n(\alpha r)+iB\frac{k_t^2}{k_0^2}J_n(\beta r)\right\} \qquad 4.36$$

where the radial wave numbers are given as

$$\alpha^2 = (\omega/c_1)^2 - \varepsilon^2 \qquad 4.37$$

$$\beta^2 = (\omega/c_2)^2 - \varepsilon^2 \qquad 4.38$$

Including the boundary conditions by setting equations 4.28 through to 4.30 to zero for $r=a$ and substituting the stresses into equations 4.31 through to 4.33 results in three simultaneous equations. The unknowns A, B and C are eliminated to give rise to the Pochammer-Chree frequency equation, which can be written in the form

$$f(\varepsilon_n, \omega_n) = 0 \qquad 4.39$$

where for a given integer value of n (0, 1, 2 etc) the roots of the frequency equation relate axial wave number ε to frequency ω. It is common to display the characteristics of guided waves in projections of wave number, phase or group velocity as a function of frequency. When the phase velocity v_{ph} of a harmonic wave is a function of its frequency or wavelength, then the propagating medium is termed dispersive [Havelock (1914)]. The phase velocity v_{ph} describes the rate at which a constant phase portion of a continuous harmonic wave moves, which for a given frequency ω is defined by

$$v_{ph} = \frac{\omega}{\varepsilon} \qquad 4.40$$

Since continuous excitation is rarely used in NDT, a more meaningful parameter is group velocity v_{gr} that describes the rate at which energy or a packet of waves travel and is given by the derivative

$$v_{gr} = \frac{\partial \omega}{\partial \varepsilon} \qquad 4.41$$

4.3.3 Dispersion curves and mode shapes for the reference bar

This section discusses the dispersion curves for the reference bar, where the bar is assumed to be infinite in length and transient effects are not considered. The dispersion curves and mode shapes were obtained using Disperse [Pavlakovic et al. (1997)] , a program developed at Imperial College NDT laboratory for the solution of wave propagation in plate and cylindrical systems. Briefly, the solution technique begins by holding the wave number constant, the corresponding roots of the frequency equation are then evaluated to provide initial loci on the dispersion curves. From these loci, dispersion curves are then drawn within a frequency range of interest using a process of root finding and extrapolation. Greater details of the solution technique and examples of it use can be found in the theses of Lowe [1992] and [Pavlakovic [1998]. The curves will be examined in phase velocity and group velocity projections as a function of frequency. The different modes will be labelled by a system adopted by Silk and Bainton [1962] where a mode is tracked by its type, here being either longitudinal L or flexural F modes. The first index refers to the circumferential order, which describes the number of wavelengths around the bar circumference and this relates to the integer value of n in the frequency equation. The second index is a counter variable that relates to the order of the root of the frequency equation. Since it is unlikely that the PUNDIT transducers with their piston like excitation could excite torsional waves, they will not be referred to. The excitability of other modes can be assessed by observing the mode shapes, which describe how the radial and axial displacements vary as a function of the bar radius r.

For the reference bar the phase and group velocity projections are shown in Fig. 4.4 and Fig. 4.5 respectively. The dispersion curves shown are in fact universal for all diameters since the x axis represents frequency times radius. The bulk velocities have been included on both Fig 4.4 and Fig. 4.5 for reference only; classically they are not considered to propagate along the bar. A brief description of the related displacements for the fundamental modes shown follows. Disperse can not solve for velocities at zero frequency but at approximately zero frequency, the axial displacements for the first longitudinal mode L(0,1) are shown as u_{z0} in Fig. 4.6. The graph is plotted for an arbitrary displacement as a function of distance from the centre axis.

The axial displacements are constant for near zero frequency, the propagating wave can be described as plane, being purely extensional and propagating at the bar velocity c_0 equal to $\sqrt{E/\rho}$. The corresponding radial displacements for the L(0,1) mode near zero frequency, shown as u_{r0} in Fig. 4.7, are zero. The axial and radial displacements for the points on the L(0,1) curve coincident with the centre frequencies of the 54kHz and 83kHz PUNDIT transducers are also shown in Fig. 4.6 and Fig. 4.7 respectively. Comparing the mode shapes for the different frequencies reveals that as the frequency increases the radial component of motion grows and the axial displacement along the bar axis decreases. At much higher frequencies the mode behaves as a Rayleigh wave where displacements are confined to the outer surface.

For the first flexural mode F(1,1) the axial and radial displacements at the three frequencies, zero Hz, 54kHz and 83kHz are shown in Fig. 4.8 and Fig. 4.9 respectively. Near zero frequency F(1,1) behaves as pure bending, while with increasing frequency the axial components increase. Again for the F(1,1) mode, at much higher frequencies the displacements are confined to the surface. It should be noted that the L(0,1) mode displacements are symmetric about the axis whereas the F(1,1) displacements are non-axi symmetric.

The main characteristic of interest is that above zero frequency all guided modes have complicated functions of radial and axial displacements. As a first approximation, the PUNDIT transducers can be assumed to vibrate in the axial direction only so that modes with predominately axial displacements will be more strongly excited. Higher order modes that can also exist within the frequency range of interest are also shown in Fig. 4.4 and Fig. 4.5. It can be seen that the phase velocities for the higher modes exceed the bar velocity c_0. As described previously, however, the phase velocity does not correspond to the transmission of energy, which is propagated at the group velocity. Fig 4.5 reveals that apart from the low frequency range of the L(0,1) all modes of interest propagate at less than the bar velocity c_0. This suggests that the calibrated value on the reference bar is not intended to relate to a guided mode.

4.3.4 Wave propagation in a finite length solid bar

Treating a bar as a bounded medium of infinite length showed that no modes propagate above the bar velocity c_0. Kolsky [1963] informs that several writers [Southwell 1941 p355 for example] have pointed out that in theory we could treat the bar in the same manner as an infinite medium where elastic waves propagate at the bulk velocities c_1 and c_2. Indeed Disperse [Lowe (1992)] uses the superposition of partial waves that propagate at the longitudinal c_1 and

shear c_2 wave velocities for the solution of the modal wave equations. A point disturbance that arises somewhere within a bar will excite dilatation and transverse waves, which spread out spherically from the source. At a certain point down the length of the bar, the arriving waves could be said to have travelled by a variety of routes, the earliest arrival corresponding to a wave propagating with the bulk longitudinal velocity down the most direct path, the axis, that has not interacted with the boundaries. Redwood [1960] states that from this approach clearly some part of the signal will arrive with a velocity c_1 in any finite bar. The parts of the wave that interact with the surface will give rise to reflected dilatation and transverse waves. These in turn will give rise to both types of wave as they are also reflected to give rise to guided waves. The amplitude of the unreflected wave will decrease inversely with the distance travelled. It follows that the greater part of the energy of the disturbance will travel with a velocity less than that for dilatation waves. In the limit, this agrees with the Pochammer-Chree analysis that assumes an infinite length of bar where the energy of the unreflected wave will have fallen to zero. It seems intuitive from this that if a point force is applied to the centre of a bar whose length is comparable to the radius, some energy will reach the other face at the dilatation velocity. For the PUNDIT transducers, excitation is in the form of a piston source, which could be said to apply a plane wave to the ends of the bar. Whether plane waves would propagate in the manner suggested for the point force is uncertain. For plane waves Bancroft [1941] suggests that where lateral motion is freely allowed the operative elastic constant will be *E*, whereas if it is inhibited the constant will be $(\lambda + 2\mu)$. Thus at low frequencies where plane waves can propagate, a dilatation wave will travel in the first case at the bar velocity, while in the second case at the longitudinal bulk velocity. The author is unaware of any general solution for wave propagation in a length of finite bar and so it will be assumed that this problem has yet to be substantially covered theoretically. Such a task is not the purpose of this investigation and so a finite element and experimental study will be performed to see if Bancroft's suggestions for plane waves can be verified.

4.4 Wave velocity extraction

It was noted earlier that in a dispersive system the wave phase velocity is a function of frequency. For a finite duration signal that comprises a range of frequency components the effect leads to distortion of the wave packet as it propagates. Common techniques such as comparing the time domain signal envelopes of the propagated signal with the input are not appropriate when assessing signal transit times in such a system. This section briefly describes the phase spectrum, instantaneous frequency and F ridge point wave velocity extraction techniques that will be applied to the finite element and experimental results. So as to not

distract too much from the aim of this chapter the techniques are covered in much greater depth in Appendix 1. The instantaneous frequency and the F ridge point technique have been developed by the author to complement the established phase spectrum method.

4.4.1 Phase Spectrum – Fourier Transform

The phase spectrum approach described by Sachse and Pao [1978] evaluates the phase velocity of a wave from the difference in the phase spectra of two signals that occur at different points along the passage of the wave. The technique for obtaining the phase velocity begins by first computing the FFT (Fast Fourier Transform) of the two time domain signals $u(t)$ and $v(t)$. The phase spectra $\phi(\omega)$ of each FFT is then found which will be a discontinuous function with values that vary from 0 to 2π (depending on the arc tan argument) which must be transformed into a continuous function. For a known path length z, at a given frequency ω, the difference in the phase is used to evaluate the phase velocity, which is given by

$$v_{ph}(\omega) = \frac{z\omega}{\phi_v(\omega) - \phi_u(\omega)} \qquad 4.42$$

Group velocity can be then be evaluated from equation 4.42 by differentiating frequency with respect to wavenumber.
In Appendix 1, the effectiveness of the phase spectrum technique is shown to be greatly reduced when the signal to noise ratio falls below 2:1, when more than one mode is present in a signal and where discontinuities exist in the time domain.

4.4.2 Instantaneous frequency - Hilbert transform

The technique briefly described here compares the time delay at which a value of instantaneous frequency occurs in two related signals to give the group velocity for a wave propagating at that frequency. A signal is said to be analytic [Ville (1948)] if its Fourier transform for negative frequencies is zero. An analytic signal $u_a(t)$ can be synthesised from a real time signal $u(t)$ by modifying the Fourier transform [Randall (1987)] where

$$U_a(\omega) = 0 \qquad \text{when } \omega < 0,$$
$$U_a(\omega) = U(\omega) \qquad \text{when } \omega = 0,$$
$$U_a(\omega) = 2U(\omega) \qquad \text{when } \omega > 0,$$

The inverse Fourier transform of $U_a(\omega)$ will be complex where the real and imaginary parts are related by the Hilbert transform. The analytic signal can be written in terms of modulus and phase as

$$u_a(t) = |u_a(t)|e^{i\phi(t)} \qquad 4.43$$

The rate of change of phase gives the instantaneous frequency ω_i given by

$$\omega_i(t) = \phi' \geq 0 \qquad 4.44$$

If the signal was a sinusoidal wave at a frequency ω then the instantaneous frequency ω_I would coincide with that frequency. When the signal comprises a number of sinusoidal waves of the same amplitude then the instantaneous frequency is the average of those frequencies. Thus the instantaneous frequency given by the analytic signal can be said to provide the average frequency that occurs in a signal at a given point in time.

Appendix 1 describes in greater detail a technique developed by the author that employs the instantaneous frequencies to extract group velocity, which is most suitable when applied to chirp type signals. To evaluate group velocity the first step is to compute the instantaneous frequencies $f_i\{u(t)\}$ and $f_i\{v(t)\}$ for an input signal $u(t)$ and output signal $v(t)$ respectively. At a frequency f_i on the $f_i\{u(t)\}$ curve the time delay dt_f to a similar point on $f_i\{v(t)\}$ is then found. For a given path length z, the group velocity $v_{gr}(f)$ as a function of frequency f is then obtained by

$$v_{gr}(f) = z / dt(f) \qquad 4.45$$

In Appendix 1, the effectiveness of the instantaneous frequency technique is shown to be reduced when the signal to noise ratio is low, where a signal consists of more than one mode and when discontinuities exist in the time domain. Additionally other than for chirp type signals determining the time delay becomes difficult unless the instantaneous frequencies for both signals are continually rising or falling.

4.4.3 F ridge points - Wavelet transform

The F ridge point technique briefly described here has been developed by the author. Group velocity is evaluated employing the emerging wavelet transform (WT) to locate the time when the maximum energy in a given frequency band occurs. Compared to the previous techniques mentioned, the study in Appendix 1 shows the F ridge point method to be much less sensitive to low signal to noise ratios and it also allows the investigation of complicated time signals that comprise multiple modes. The concept of the WT was formalised in a series of papers by Morlet et al [1982]. Since the introduction a seemingly exponential yearly increase in papers on the subject have been published on all manner of diverse uses. The original motive for the development of the WT [Goupillard et al (1984)] was to be able to transform a time signal and display the transform in such a manner that the contributions of different frequency bands could be analysed separately from each other. The representation is commonly known as time frequency analysis, where a one dimensional time signal is mapped into two dimensions of time and frequency. Wavelet functions $\psi(t)$ have a tapering or window operation applied to sinusoids so that they are located in time. Location in frequency is provided by the oscillatory nature of $\psi(t)$. However, frequency time analysis is not ideal since the uncertainty principle [Mallet (1989)] states that arbitrarily high precision in both time and frequency cannot be achieved.

From a given analysing wavelet ψ function a whole family of translated b and scaled a (related to frequency ω) versions are created by

$$\psi_{a,b}(t) = \frac{1}{\sqrt{a}}\psi\left(\frac{t-b}{a}\right) \qquad 4.46$$

The continuous wavelet transform (CWT) $Wv(a,b)$ of a function $v(t)$ is then given by the integral transform

$$W_\psi v(a,b) = \int_{-\infty}^{\infty} v(t)\overline{\psi_{a,b}(t)}dt = \int_{-\infty}^{\infty} v(t)\frac{1}{\sqrt{a}}\psi\left(\frac{t-b}{a}\right)db \qquad 4.47$$

Equation 4.47 describes the inner product of $v(t)$ with $\psi_{a,b}(t)$ or in other words the CWT evaluates the similarity between the wavelet and the signal, where the similarity is the frequency content. Thus the CWT coefficients refer to the closeness of the signal to the wavelet at the current scale. When a complex set of wavelets, such as a Morlet wavelet [Morlet et al (1982)] is applied to a signal the coefficients will themselves be complex. For a given scale a the modulus of the CWT gives the energy envelope of the signal as a function of

translation b. When the modulus of the complex coefficients are displayed in two dimensions of frequency time this display is known as a scalogram.

In the scalogram it is useful to observe the points in time-frequency where the maximum coefficients occur. When these peaks form a function of time or frequency they are known as ridge points [Mallet (1998)]. Abbate et al [1999] suggest that since the ridge points for this application are related to high concentrations of acoustic energy they are natural candidates for the characterisation of ultrasonic signals. Two straightforward processes can be employed to obtain ridge point functions. Firstly, if we stand on the time axis and look into the frequency domain the peaks in the CWT $Wv(b,f_i)$ will correspond to the instantaneous centre frequency f_i as a function of time b, which we shall call B ridge points. The instantaneous frequency given by the CWT identifies the centre frequency that occurs in a signal at a given point in time. This is a big improvement over the analytic signal technique where the average frequency was obtained. However, Appendix 1 shows that the technique is limited to higher scales (frequencies) where time location improves.

For non dispersive signals, the standard technique to measure time delays between two tone bursts is to compare the times at which the maximums in their signal envelopes occur. Similarly it is suggested by the author that the time delay between the maxima in the energy envelopes for two different signals can be compared. The time delay enables the evaluation of the group velocity of a given frequency band. To accomplish this we stand on the frequency axis at a given frequency and look into the scalogram, then the F ridge point will correspond to the time at which the scalogram is a maximum. For the F ridge point technique to be of use, any superimposed following modes or reflections should be of lower energy than the out going mode of interest. When this is the case if we stand on the frequency axis and look into the scalogram, the mountainous regions related to the CWT coefficients of the wave packet of interest will obscure the less significant following modes or reflections. Other than this straight forward case, Abbate et al [1999] and Veroy et al [1999] suggest that algorithms would be required to compare time delays between similar modes for the case when modes overlap in the time domain.

4.5 Finite element study

Numerical modelling was conducted using the finite element software FINEL [Hitchings (1997)] that has been developed in the Aeronautical Department of Imperial College. FINEL decomposes a problem into a finite number of small elements that when linked to together

form a mesh. The propagation of a disturbance through the mesh is solved by an explicit time marching scheme using basic equations of motion. By contrast the solution of the modal problem, by programs such as Disperse mentioned in the previous section, solve potential functions that exist for all time which influence the displacement field everywhere. As such FINEL has the ability to model the transient behaviour in a discrete geometry that Disperse cannot.

4.5.1 Finite element model description

The type of elements used for this work were four noded quadrilaterals for which displacements and stresses vary linearly between the corners. This type of element is often used for modelling plane stress, plane strain or axi symmetric solids. Taking advantage of the symmetry about the *x* axis, a uniform 2 dimensional oblong mesh that represented a cross section through the radius and along the axis of the bar was used. Fig. 4.10 shows a schematic of the finite element mesh approximation for the PUNDIT calibration bar. The oblong mesh was a 1280mm long, 25mm radius axi symmetric approximation using 512 by 10 square elements respectively. The bar length was chosen so that over the duration of the solution computation the fastest wave would not be reflected at the far end of the bar and interfere with the monitored out going wave.

FINEL uses an explicit time marching approach, which unlike implicit methods does not involve inversion of the large stiffness matrices that are commonly encountered. However the major disadvantage is that the explicit method is only conditionally stable. The parameters for stability are set out by [Alleyne (1991)]. For this work, the size of the elements was sufficiently small for there to be eight or more nodes per wavelength, where the wavelength was related to the Rayleigh wave. When such a criterion is met [Alleyne (1991)] states that the velocity error will be less than 0.5%. For stability the constraint is that no wave should be able to traverse more than one element within a given time step. For this work the time step was chosen to be typically 80% of the time taken for longitudinal bulk wave to propagate over the length of an element.

At one end of the mesh each node was excited by applying the same time varying displacement in the axial direction only. Modes with predominately axial displacements were therefore more strongly excited. For propagation of plane waves Bancroft [1941] suggests that where lateral motion is freely allowed the operative elastic constant will be *E*, whereas if it is inhibited the constant will be $(\lambda + 2\mu)$. To examine this, two solutions were computed, with different boundary conditions at the excitation end of the mesh. For case 1 lateral motion in the

y direction was freely allowed, while for case 2 lateral motion was inhibited. For the latter case, it would be expected that since elsewhere in the bar lateral motion is allowed, the phase velocity of the wave would be a function of the distance propagated. Free boundary conditions were used on the outside diameter of the bar. Consideration of flexural waves was not applicable due to the model being axi symmetric. Hanning windowed frequency modulated signals were used to enable the employment of the signal processing techniques that have been discussed in Appendix 1. The displacements at a number of the nodes along the central axis in the form of time traces in the in-plane direction only were stored for later signal processing. The frequency characteristics of the excitation were chosen so as to control the amount of energy available in the region of mode cut-off frequencies. To illustrate the effect of a cut-off mode, Fig. 4.11 shows the input chirp signals $u_{20}(t)$ and $u_{40}(t)$ that were applied to each node on the bar face, separated vertically for clarity, that have 20kHz and 40kHz centre frequencies respectively. Shown along with these are the monitored outputs at 100mm down the bar $v_{20}(t)$ and $v_{40}(t)$. The modulus of the frequency spectrum of $u_{20}(t)$ as shown in Fig. 4.12 has very little energy in the region of the L(0,2) cut off frequency which occurs at about 74kHz. By contrast there is relatively significant energy in the $u_{40}(t)$ input around the region of the cut-off frequency. The effect shown in Fig. 4.11 is that there is noticeable ringing in the time domain and in Fig. 4.12 a spike in the frequency domain is evident. Additionally shown in Fig. 4.12 is that if the cut-off frequency is significantly excited the finite element model predicts an increase in output energy which is not reasonable. Therefore choice of excitation characteristics requires some prior knowledge of mode phase velocities.

4.5.2 Finite element model results

Finite element results will be processed to obtain wave velocities by the three signal processing techniques described in Appendix 1. All three methods suffer from some limitations, there being no universal panacea to the problem. However, some combination of all three techniques should provide a full analysis. The excitation used for the first investigation was the 20kHz signal $u_{20}(t)$ as shown in Fig. 4.11. The bandwidth of this signal avoids significant excitation of the L(0,2) cut-off frequency, which was necessary to allow signal processing by the phase spectrum method. For case 1, lateral displacements along the bar were freely allowed. The phase velocities for the wave at the monitored points were evaluated using the phase spectrum method (see section A1.3), where $u(t)$ was the monitored signal at x=0mm and $v(t)$ the monitored signals shown in Fig. 4.13 at the points 0, 10, 20, 30, 40 and 50mm from the end of the bar. Fig 4.14 shows the evaluated phase velocities as continuous functions with the dispersion curve predicted by Disperse for L(0,1) shown as squares. The results show that up until almost one bar diameter from the end of the bar, the

phase velocity differs from the L(0,1) dispersion curve, with this difference being a function of frequency. After about one bar diameter away from the bar end the phase velocities of the monitored signals matched the dispersion curve. At low frequencies there is some indication of phase velocities above the bar velocity. This may be the case, or it could be an artefact that results from the effect of finite element approximations [Pavlakovic (1998)]. Additionally, the phase spectrum is sensitive to the chopping of seemingly innocuous long wavelength components out of the signal. When the model was repeated where only the node on the axis received excitation, very similar phase velocities were obtained. Thus where lateral displacements are freely allowed, the finite element model found no significant indication of the phenomena suggested by Redwood [1960] that for short enough path lengths some component of the guided wave travels at above the bar velocity.

The modelling was repeated for case 2 where lateral displacements on the bar end were inhibited. Avoiding monitoring under one bar diameter away from the bar end, the axial displacements in the x direction were monitoring at points 50, 100, 150 and 200mm from the end of bar as shown in Fig. 4.15. The evaluated phase velocities are shown as continuous functions in Fig 4.16 with the dispersion curve for L(0,1) shown as squares. It can be seen that compared to the dispersion curve, the phase velocity is a function of the distance from the bar end, but the difference is not a function of frequency. At short path lengths the wave propagates at near the bulk velocity such that the operative elastic constant will be $(\lambda + 2\mu)$. As the wave propagates further down the bar the phase velocity approaches the dispersion curve such that the operative elastic constant tends to E which agrees with Bancroft [1941]. Any deviation from a smooth curve again can be attributed to chopping the monitored signal. The finite element results suggest that for wave propagation in a bar, a wave of significant energy will only propagate above the bar velocity if some inhibition of lateral displacements is considered.

A comparison of the different signal processing techniques described in Appendix 1 used to evaluate the group velocity of a non trivial signal can be made by processing the model outputs when using an input signal $u_{40}(t)$ as in Fig. 4.11. For the model where lateral displacements are freely allowed it can be expected that the monitored signal will contain the L(0,1), L(0,2) and possibly the L(0,3) mode. For this case, the input signal $u(t)$ and monitored signal $v(t)$ at a distance from the end of x=150mm are shown in Fig. 4.17. For the monitored signal $v(t)$ there is evidence of ringing which is associated with the significant excitation of the L(0,2) cut off frequency. To enable signal processing by the phase spectrum method (see section A1.3) Fig. 4.17 also shows filtered versions of $u(t)$ and $v(t)$. These signals have been Gausian filtered in both time and frequency domain so that oscillations decay smoothly to zero within the duration of the window and the effect of exciting the cut-off frequency is removed. The filtered signals

will be used only for assessing group velocity by the phase spectrum method, where such filtering is necessary for meaningful results. Fig. 4.18 shows the useful range of the instantaneous frequency of signals $u(t)$ and $v(t)$ as obtained by the Hilbert transform technique (see section A1.4). At greater frequencies the ringing in the output due to excitation of the cut-off frequency greatly complicates the instantaneous frequency function so as to invalidate its use for the evaluation of group velocity. Fig. 4.19 shows the F ridge points (see section A1.5) of signals $u(t)$ and $v(t)$ as obtained by the wavelet transform, using a family of constant Q wavelets within the frequency range of f_{max}=120kHz and f_{min}=8kHz where the unscaled centre frequency was ω_0=2.8 rad/s. The centre frequency was chosen by trial and error, where typically a change in value of 10% has only a marginal effect. Fig. 4.20 shows the F ridge points (see section A1.5) of signals $u(t)$ and $v(t)$ as obtained by the wavelet transform, using a family of constant bandwidth wavelets which is analogous to the Short time Fourier transform (STFT) technique. For the STFT the frequency range varied between f_{max}=125kHz and f_{min}=10kHz and the use of an unscaled centre frequency of ω_0=2.2 rad/s was found to be appropriate. The results of evaluating the group velocity by the four techniques is shown in Fig. 4.21 along with the dispersion curves shown as dashed lines. For the filtered signals, extraction of the group velocity via the phase spectrum method proves to be the ideal, where excellent agreement with the L(0,1) dispersion curve can be seen. The range of frequency in this case is limited to up to 60kHz since the signal had to be low pass filtered otherwise results would have been meaningless. The Hilbert transform technique (see section A1.4) is the only method that identifies that some energy propagates above the bulk velocity and shows good agreement with the L(0,1) mode up to about 40kHz. However due the analytic signal being only loosely applicable at low frequencies, results in this region are unreliable. Similarly both the wavelet transform techniques (see section A1.5) cannot resolve velocity at the lowest frequencies due to the poor time location. The STFT method with its family of constant bandwidth wavelets picks up on the L(0,2) and L(0,3) modes, whereas the constant Q wavelets focus only on the L(0,1) mode. The reason is that these relatively narrow band STFT functions correlate better to the higher modes than the broader band constant Q wavelets. This highlights the necessity of choosing appropriate wavelet functions to analyse a given signal. For the PUNDIT reference bar simulation, none of the signal processing techniques have reliably identified energy propagating above the bar velocity in the finite element model.

By agreeing with dispersion curves the results from all three techniques suggest that the majority of the energy in the reference bar propagates as guided waves. All three signal processing methods used to extract wave velocities perform some degree of integration over a time window. They all perform some time/phase as a function of frequency analysis, and the uncertainty principle states that you can not have arbitrarily high precision in both. Thus if some energy does reach the monitoring point having propagated at the bulk velocity it must be

of relatively small energy and is therefore lost in the integration. The only way to identify whether some energy does propagate would be to observe the magnitude of the monitored signal in the time domain. No knowledge of the frequency content of the signal would be gained, only its location in time. This was achieved using the first quarter cycle of 40kHz centre frequency signals that are shown in Fig. 4.17. Up to the first quarter cycle the instantaneous frequency rises linearly for the input from 0 to about 22kHz which is shown in Fig. 4.18. For a point of given amplitude on the input $u(t)$ signal the time delay to a point of the same amplitude on the signal $v(t)$ that has propagated 150mm was obtained. Fig 4.22 shows the time delay between signals $u(t)$ and $v(t)$ as a function of signal amplitude. A zoom into the low amplitude results is shown in Fig 4.23. The time delays that correspond to the propagation of waves at the bulk and bar velocity are shown on both figures for comparison. A low energy component of the wave is identified to be propagating near to the bulk velocity. Beyond this arrival the time delay tends towards that for the bar velocity. This would tend to agree with the Hilbert transform results and suggests that the signal can only be identified in the low frequency region where its energy relative to other modes must be significant.

In conclusion, the finite element model has identified that energy will propagate above the bar velocity when lateral displacements are inhibited. When lateral displacements were freely allowed, at a distance greater than one diameter from the bar end the majority of the wave energy was observed to propagate as guided waves such that wave propagation could be considered classical. For simulation of wave propagation in the reference bar, the Hilbert transform technique (see section A1.4) developed by the author does indicate that a low frequency component propagates with sufficient energy to be recognised. However, an artefact of the technique in this region makes results unreliable. Some low level energy propagating above the bar velocity has been identified by observing the magnitude of the received signal in the time domain. An experimental study follows to confirm this.

4.6 Experimental study

For the time value on the PUNDIT calibration bar to be valid would require a wave to propagate within the bar at something near the bulk longitudinal velocity. The final section of this study is to apply the PUNDIT transducers to the bar and evaluate the signal transit time experimentally.

An experimental simulation of the threshold crossing method used by the PUNDIT was conducted. For the experimental signals, initially the 54kHz centre frequency narrow band PUNDIT transducers were coupled face to face by a thin film of grease. One transducer was

excited by the PUNDIT apparatus and from the other transducer the received signal averaged 500 times was taken to be the input signal $u(t)$. The transducers were then coupled to the calibration bar, excited by the PUNDIT apparatus, and an averaged signal $v(t)$ for propagation in the bar was obtained. The load presented to the transducers differs for the signals $u(t)$ and $v(t)$. Signal $v(t)$ can only then be considered to be a crude approximation of $u(t)$ that is delayed in time due to propagation down the length of the bar. A 54kHz disturbance propagating in aluminium at something like the bar velocity would have a corresponding wavelength of about 100mm, such that the signal wavelength will be of the same order as the length of the 153mm bar. Since the signal is narrow band the received signal after the first few cycles will consist of a superposition of the out going wave and reflections off the other end of the bar. Therefore only the first few cycles of the signals $u(t)$ and $v(t)$ are of interest which are shown in Fig 4.24. A horizontal line has been drawn to correspond to an arbitrary threshold. The time delay between when the input $u(t)$ crosses the threshold to when it is crossed by the signal $v(t)$ was obtained for values of threshold from the PUNDIT threshold value of 250μV to 3.5V which corresponds to the maximum amplitude of the first half cycle of the received signal. The time delay as a function of received signal amplitude is shown in Fig. 4.25 for which Fig. 4.26 shows a zoom of the low energy region. The horizontal lines drawn relate to propagation at the bulk and bar velocity. The time delay for a low energy component compares to the value of 25.8μs stamped on the reference bar which correspond to propagation of bulk waves. As the magnitude of the threshold increases so the time delay rises rapidly. This effect was described in chapter 3 when addressing the variation of signal transit times as a function of path length. In practice the magnitude of the received signal will depend on the acoustic coupling of the transducers to the reference bar. The amplitude of the transmitted pulse depends on the pressure exerted on the transducer, and the characteristics and thickness of the couplant medium [Canella (1974)]. Thus, if care is not taken when performing the calibration procedure, the amplitude of the received bulk wave could be reduced to below the magnitude of the PUNDIT threshold such that the apparatus does not recognise its arrival. A slower guided wave component of sufficient amplitude would then trigger the threshold resulting in an unreliable calibration of the apparatus.

A component propagating in the bar of sufficient energy has been recognised by threshold crossing but no information has been obtained on its frequency content. Only the phase spectrum technique (see section A1.3) has shown any reliability of evaluating phase or group velocities in the low frequency range of interest. The technique requires the signal to be compactly supported within the duration of the window and to have no interfering reflections. Unfortunately this is not possible for narrow band wave propagation where the wavelength is comparable to the length of the bar and the interference by the following reflected signal confuses the analysis.

To investigate further, the experiment was repeated, this time obtaining unaveraged signals of twice the duration as before. Without any filtering the signals were processed with the wavelet technique and after some low pass filtering it was possible to process using the Hilbert transform method (see section A1.4). The continuous wavelet transform (CWT) was applied to these signals so as to obtain the F ridge points (see section A1.5) which allows evaluation of the group velocity as a function of frequency of a signal. The instantaneous frequency of the filtered signals $u(t)$ and $v(t)$ obtained by the Hilbert transform technique are shown in Fig 4.27 where only the early portion of the functions can be used to evaluate group velocity since after that interference by the reflection off the bar end confuses the analysis. The F ridge points (see section A1.5) for the CWT method (within the frequency range of f_{max}=80kHz and f_{min}=20kHz where the unscaled centre frequency was set to ω_0=2.8 rad/s) for the raw signals $u(t)$ and $v(t)$ are shown in Fig 4.28. The evaluated group velocities for both the wavelet and Hilbert transform techniques are shown in Fig. 4.29. It can be seen that the analysis by either technique results in the plotting of a dispersion curve. For the Hilbert transform analysis the dispersion curve becomes unreliable beyond about 30kHz due to the interference of the reflection off the bar end in the signals. For frequency components below about 10kHz the technique indicates that the disturbance in the bar is propagating above the bar velocity which tends to the bulk velocity at the lowest frequencies. However, the Hilbert transform is unreliable in this frequency region so identification of such wave velocities cannot be presumed. The F ridge point CWT wavelet technique is not affected by the inclusion in the signal of the reflections since they are of lower energy than the out going signal. Within the 20kHz to 75kHz frequency range the CWT indicates that the majority of the energy of the disturbance is propagating as the L(0,1) mode. The wavelet transform cannot effectively evaluate the velocity of components below the 20kHz frequency since the uncertainty principle in this region leads to poor time location. However, the combination of the results from both techniques covers the frequency range of interest and suggests that over the length of the bar most of the energy of a disturbance propagates as a guided mode. The marginally lower velocities compared to the L(0,1) mode can be attributed to neglecting the extent of the slower velocity in the brass end caps when modelling using Disperse.

4.7 Conclusion

The PUNDIT apparatus calibration technique relies on setting the equipment to display a given time value when two transducers are coupled to the reference bar. The given time value was shown to relate to a wave that would have to propagate at a speed near to the bulk velocity.

This is contrary to classical assumptions where the bar would be considered to be a wave guide such that the fastest wave propagates at the bar velocity. However, it was noted that some researchers suggest that if a component of the wave propagates along the direct route (without interacting with the boundaries) then some energy will arrive that has propagated at the bulk velocity in any finite length of bar. Whether this component can be identified will depend on its energy relative to those that propagate as guided modes. An investigation was conducted which involved researching: the classical approximations for wave propagation in infinite bars, finite element modelling and experiments for wave propagation in finite bars, and an extensive evaluation of appropriate signal processing techniques which is presented in Appendix 1.

Wave propagation in a finite length of bar was modelled by a finite element axi symmetric approximation. Analysis of model results using the phase spectrum technique found that only if lateral deflections were inhibited would a component of the wave be identified to propagate above the bar velocity. When lateral displacements were freely allowed, at a distance greater than one diameter from the bar end, the wavelet and Hilbert transform signal processing techniques identified that the majority of the wave energy propagates as guided waves such that wave propagation could be considered to be classical. Controversially, when applying the time domain threshold crossing technique a component was identified to propagate at a velocity between the bulk and bar velocity. This technique provides ideal time location but no information is available regarding the frequency content of the component. Similarly, since the other signal processing techniques perform an integration to identify some frequency content, they loose information on time location. This stems from Heisenberg's uncertainty principle which states that simultaneous measurement of position and momentum is not possible. Likewise you cannot have arbitrary high precision when two operators do not commute such as frequency and time. It is for this reason that the problem is intractable.

Experimental studies were conducted to examine wave propagation in the actual calibration bar for a disturbance excited and received by the PUNDIT 54kHz narrow band transducers. Processing of results was complicated by superposition of reflections on the out going signal. Application of the F ridge point wavelet transform signal processing techniques to the experimental data found that most of the signal energy propagates as guided waves along the length of the bar. The F ridge point technique developed by the author was found to be particularly suitable for investigating experimental guided wave propagation in a finite length of bar since it ignores the presence of reflections in the monitored signal. Similar to the finite element analysis, simulation of the time domain threshold crossing technique identified a low energy component that propagates at the bulk velocity in the PUNDIT reference bar.

One application of the PUNDIT apparatus is to enable a comparative study of the velocity of sound in concrete. As such absolute values are not important, though the apparatus should still be calibrated with the reference bar so as to relate the velocity measurements of one test to another. It is recommended that if accurate measurement of the absolute value of velocity of sound in concrete is important, then care should be taken when coupling the transducers to the reference bar so as to maximise signal transmission to and from the bar. If not, the component travelling at the bulk velocity which is of relatively insignificant energy may be unlikely to trigger the threshold ahead of the slower much higher energy guided waves. This could result in incorrect calibration of the PUNDIT apparatus. Thus the calibration procedure used by the PUNDIT apparatus has been found to be dependent on effective coupling of the transducers to the reference bar.

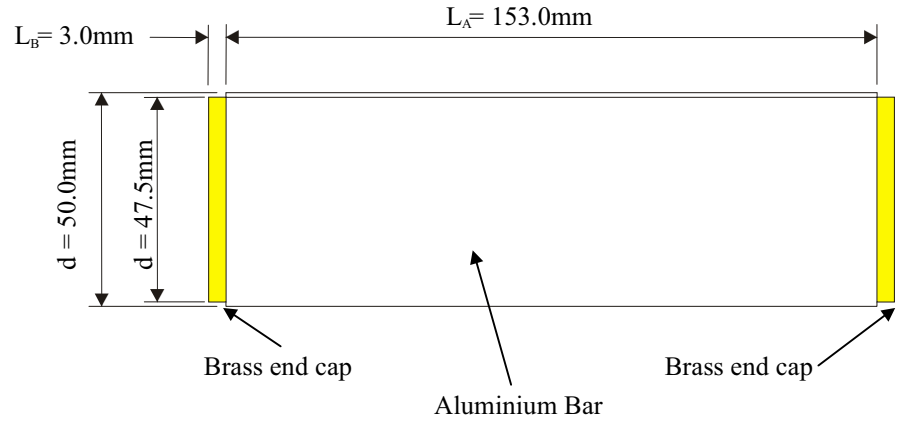

Figure 4.1. Pundit reference bar.

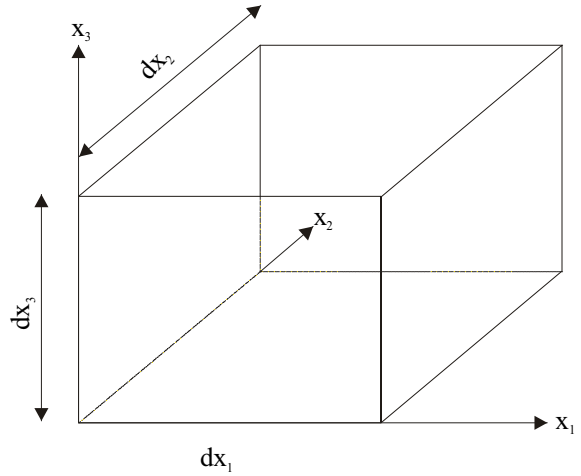

Figure 4.2. Elemental volume in Cartesian coordinates.

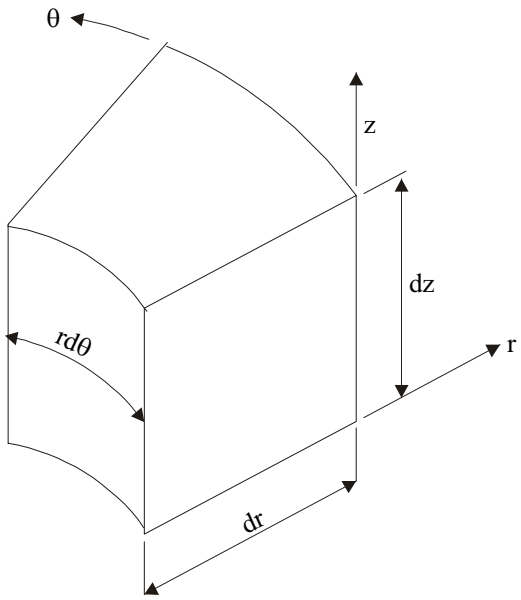

Figure 4.3. Elemental volume in cylindrical coordinates.

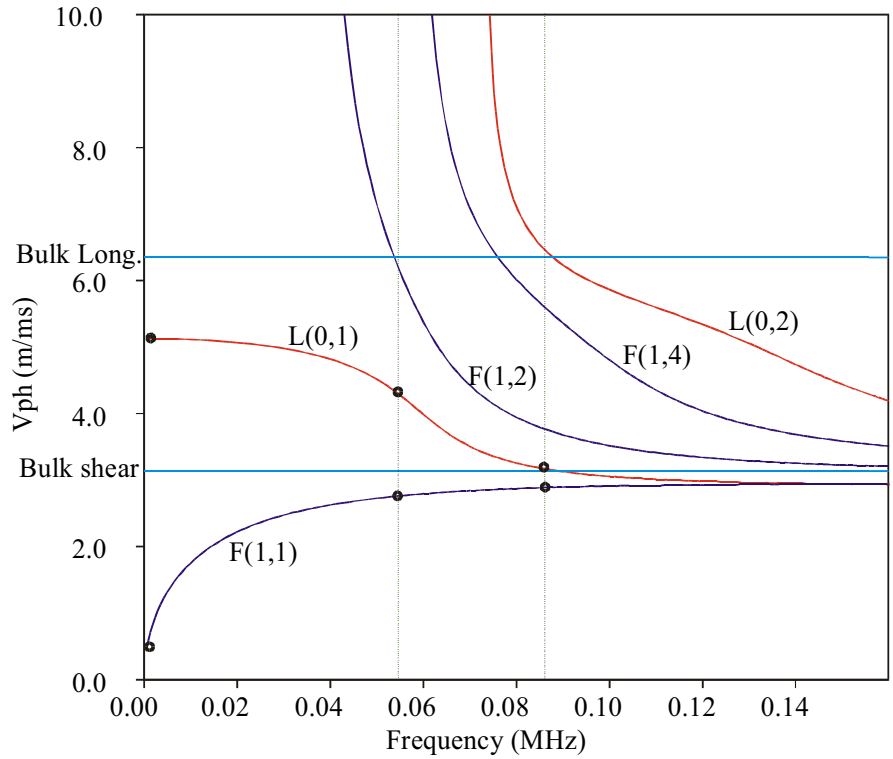

Figure 4.4. Phase velocity projection for 25mm radius aluminium bar.

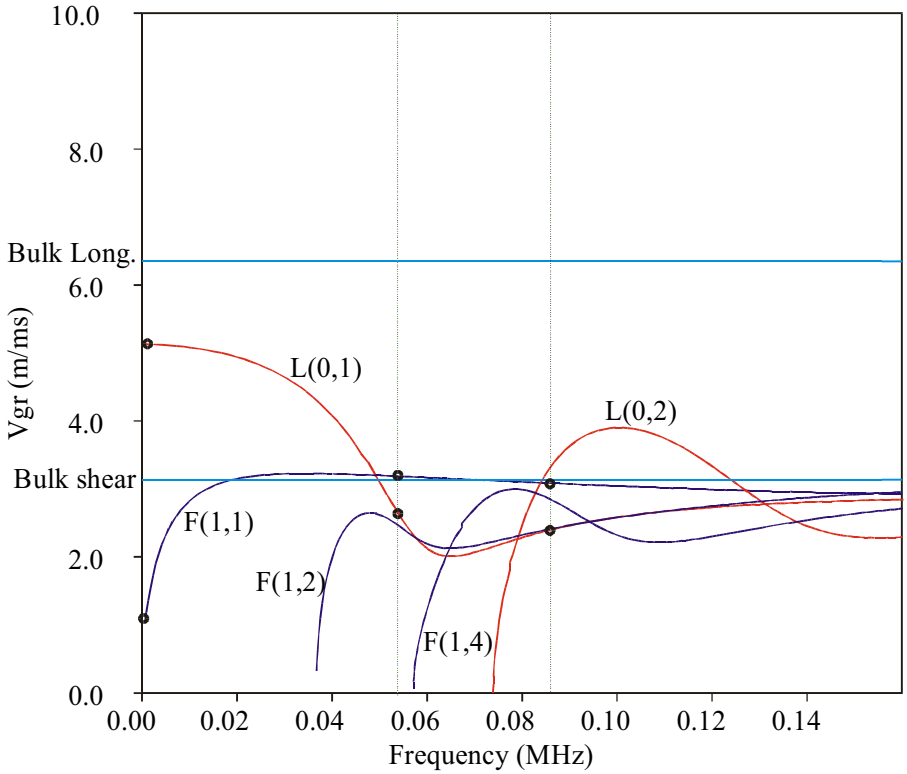

Figure 4.5. Group velocity projection for 25mm radius aluminium bar.

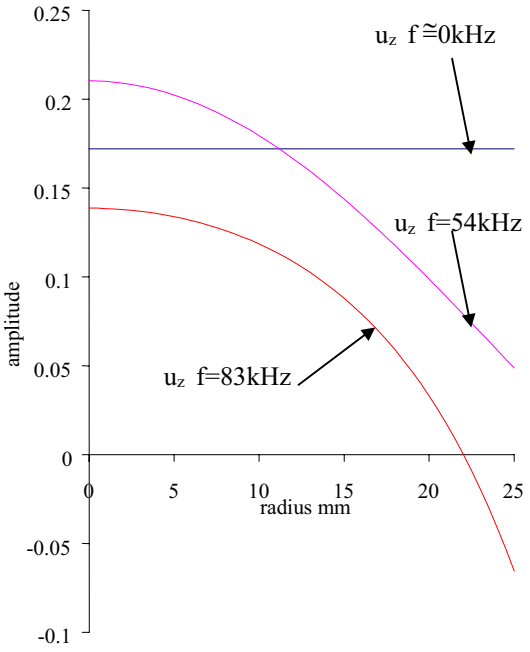

Figure 4.6. Axial displacements u_z for fundamental longitudinal mode L(0,1).

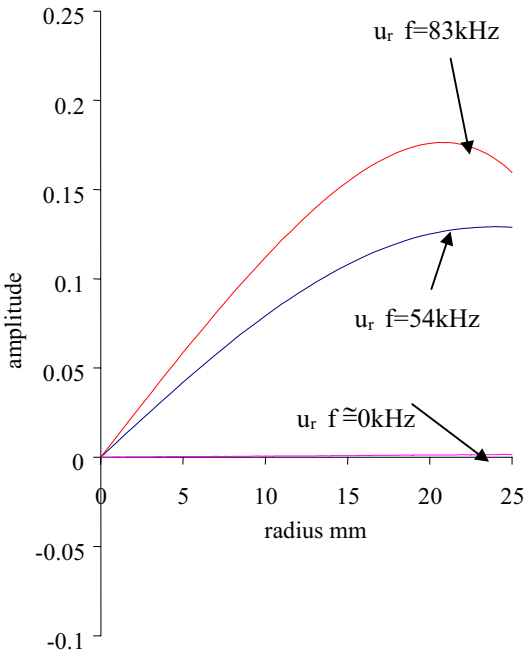

Figure 4.7. Radial displacements u_r for fundamental longitudinal mode L(0,1).

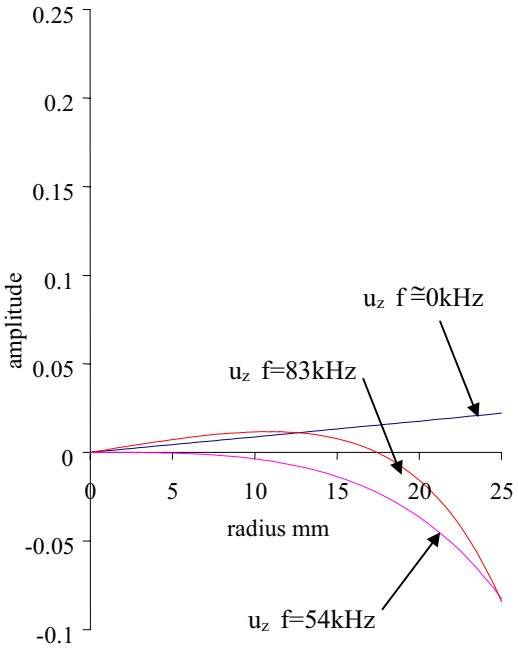

Figure 4.8. Axial displacements u_z for fundamental flexural mode F(1,1).

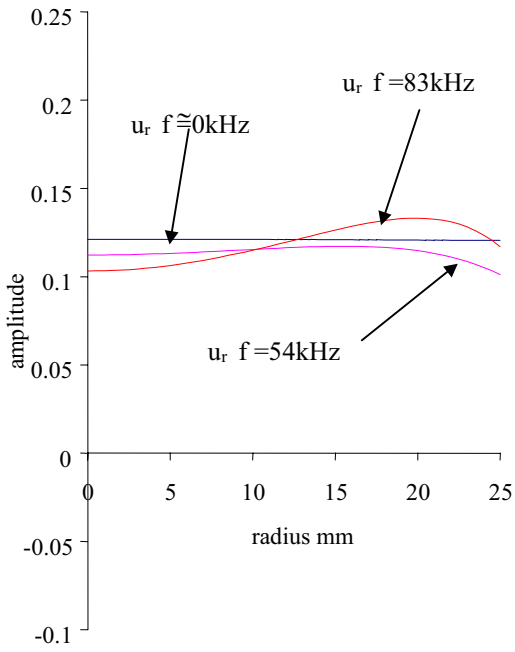

Figure 4.9. Radial displacements u_r for fundamental flexural mode F(1,1).

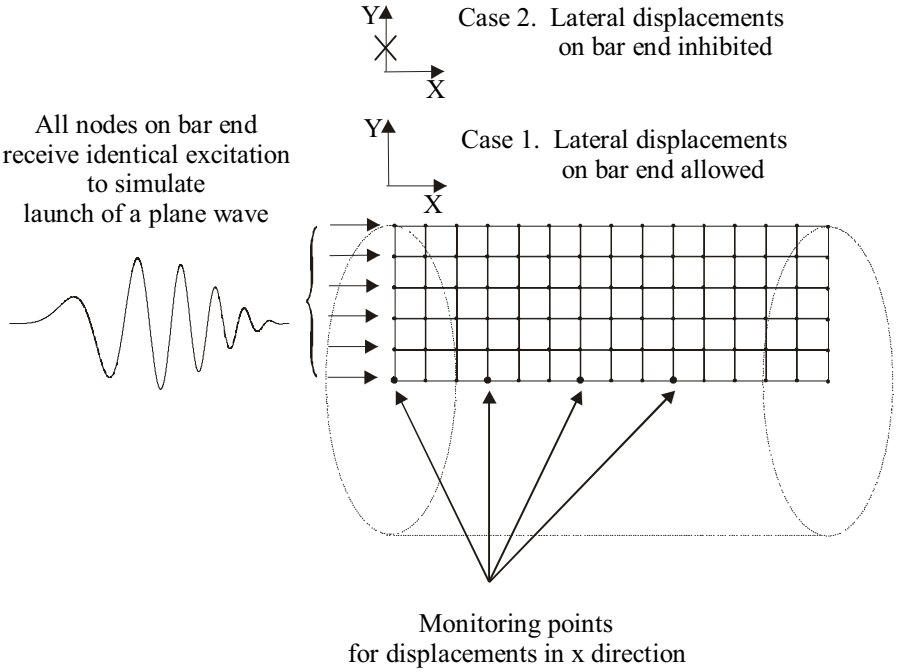

Figure 4.10. Schematic of oblong finite element mesh used to approximate wave propagation in Pundit calibration bar.

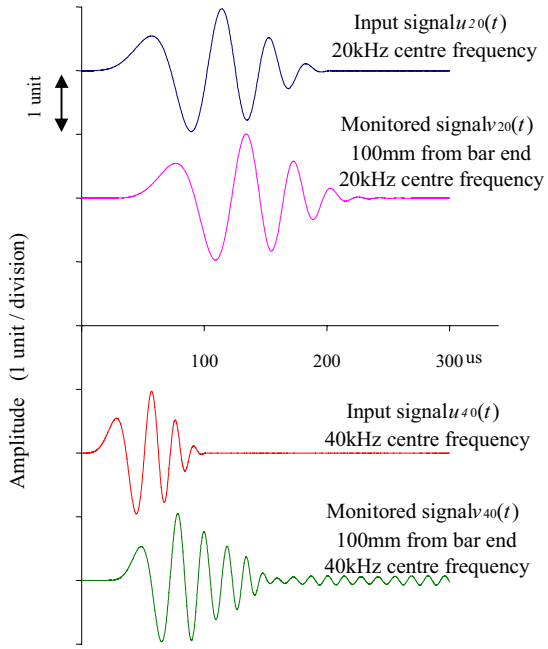

Figure 4.11. Example finite element model input and monitored signals. All separated vertically for clarity.

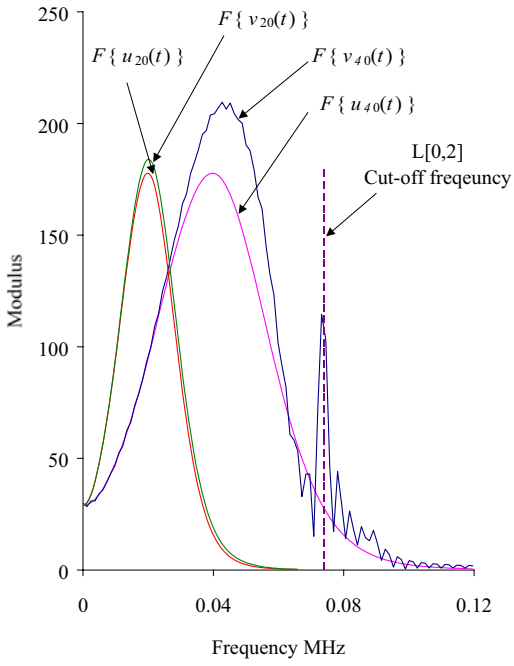

Figure 4.12. Frequency spectra of example finite element model input and monitored signals.

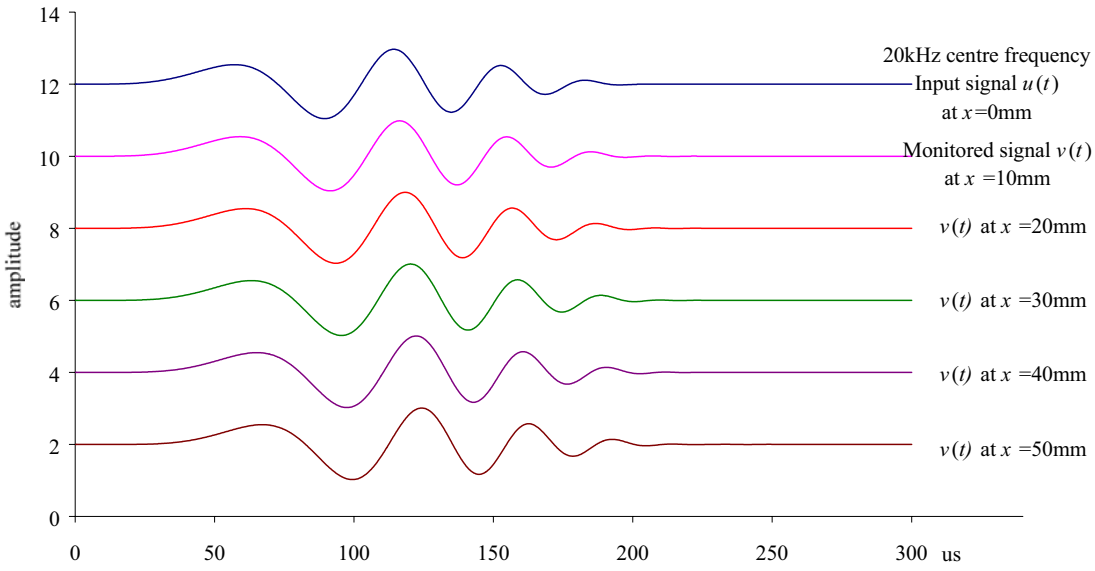

Figure 4.13. Input $u(t)$ and monitored signals $v(t)$ at centre of bar for finite element model of 50mm diameter aluminium bar where lateral displacements are freely allowed everywhere. All separated vertically for clarity.

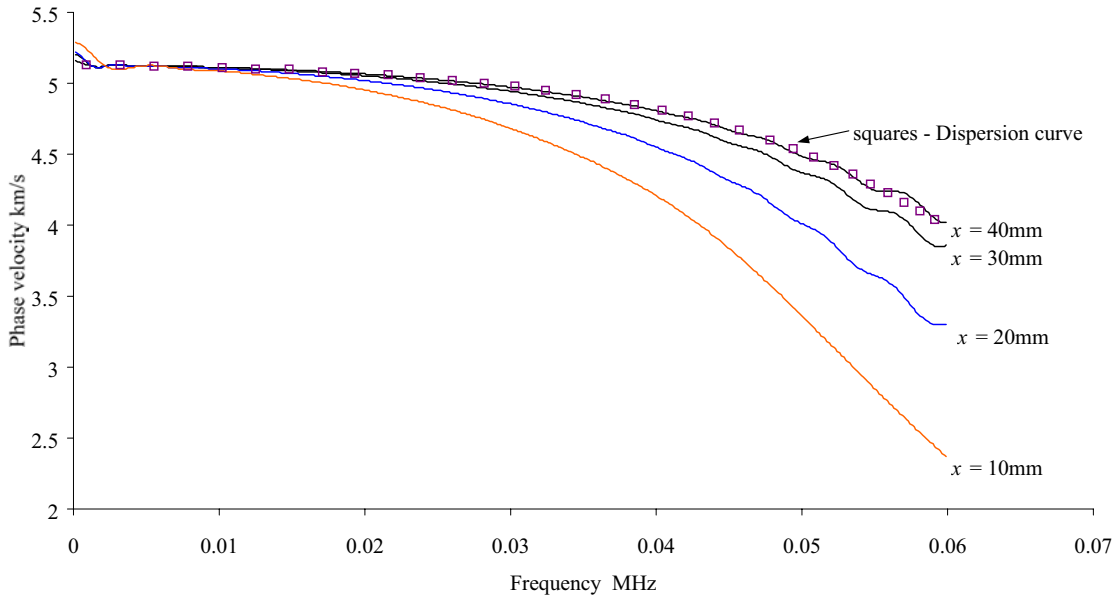

Figure 4.14. Phase velocity of monitored signals $v(t)$ relative to Input $u(t)$ (continuous functions) as shown in Fig. 4.13 shown along with dispersion curve for L(0,1) (squares).

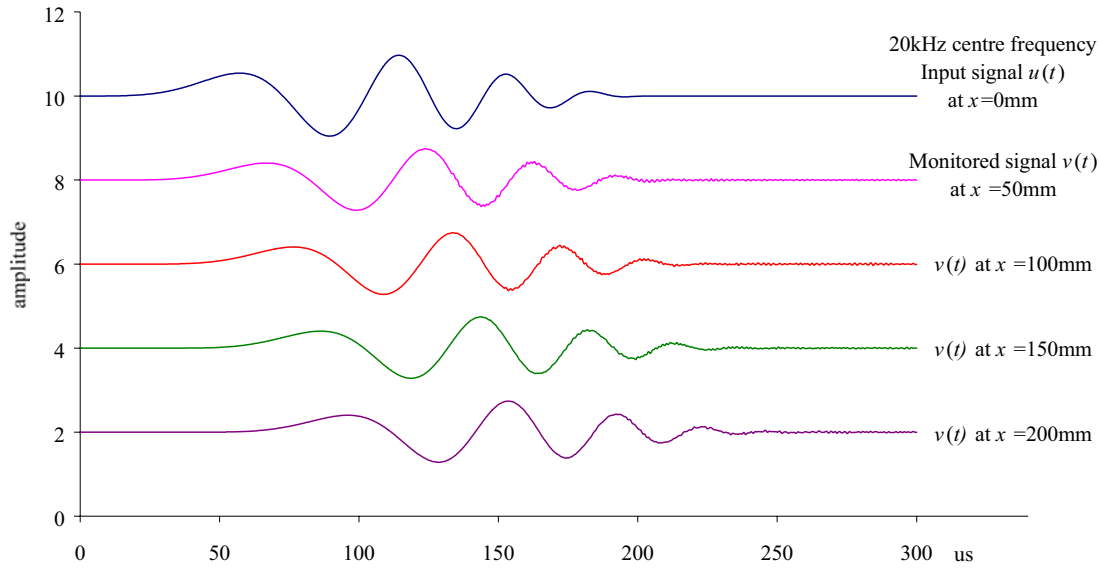

Figure 4.15. Input $u(t)$ and monitored signals $v(t)$ at centre of bar for finite element model of 50mm diameter aluminium bar where lateral displacements are inhibited on bar end. All separated vertically for clarity.

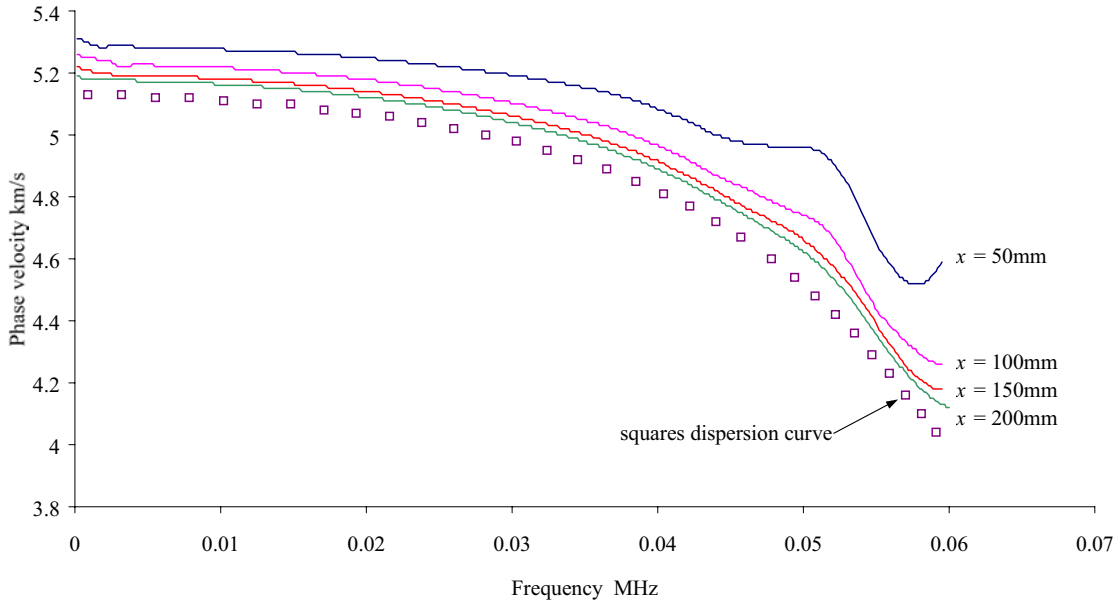

Figure 4.16. Phase velocity of monitored signals $v(t)$ relative to input $u(t)$ (continuous functions) as shown in Fig. 4.15 shown along with dispersion curve for L(0,1) (squares).

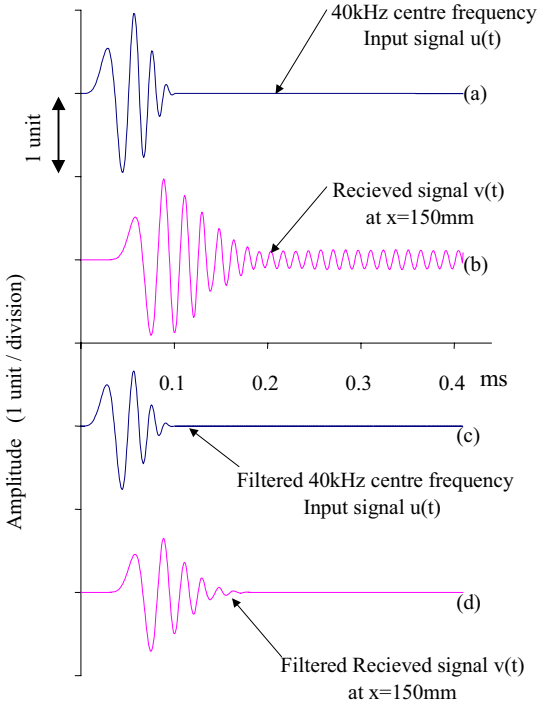

Figure 4.17. Finite element model input $u(t)$ and monitored signal $v(t)$ for the comparison of group velocity evaluation techniques. All separated vertically for clarity.

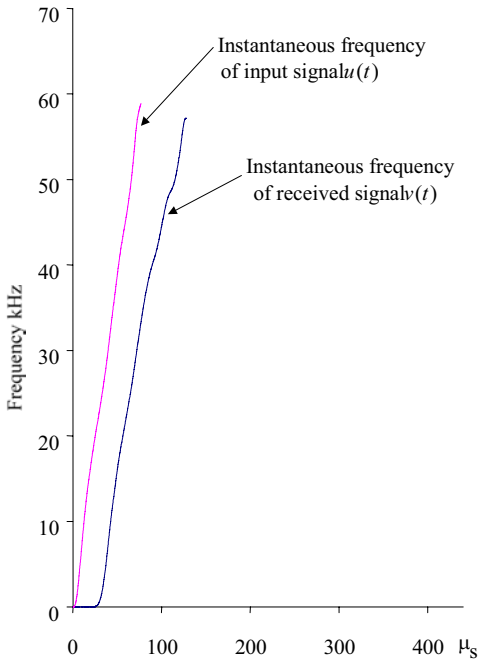

Figure 4.18. Instantaneous frequency of input $u(t)$ and monitored signal $v(t)$ in Fig 4.17 obtained by Hilbert transform technique.

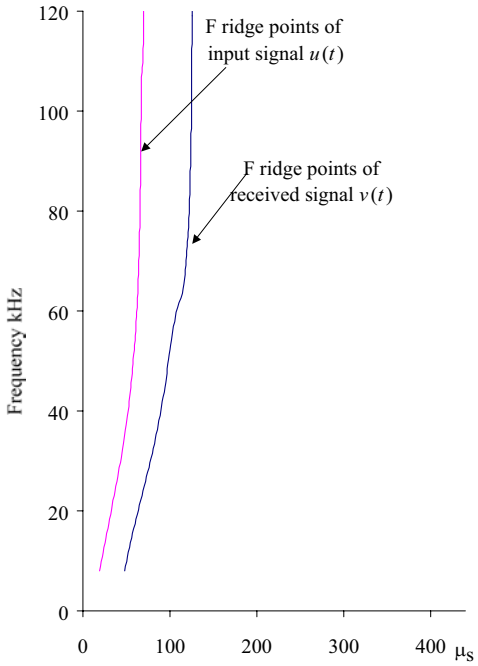

Figure 4.19. F ridge points of input $u(t)$ and monitored signal $v(t)$ in Fig 4.37 obtained by Constant Q wavelet transform technique with ω_0=2.8 rad/s.

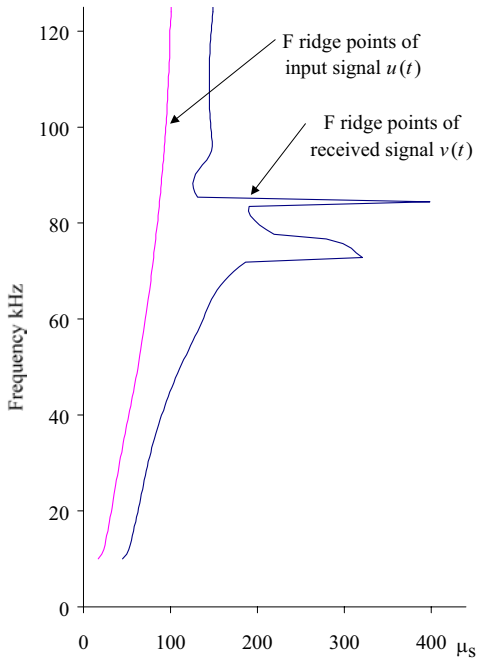

Figure 4.20. F ridge points of input $u(t)$ and monitored signal $v(t)$ in Fig 4.17 obtained by Constant bandwidth wavelet transform technique with ω_0=2.2 rad/s.

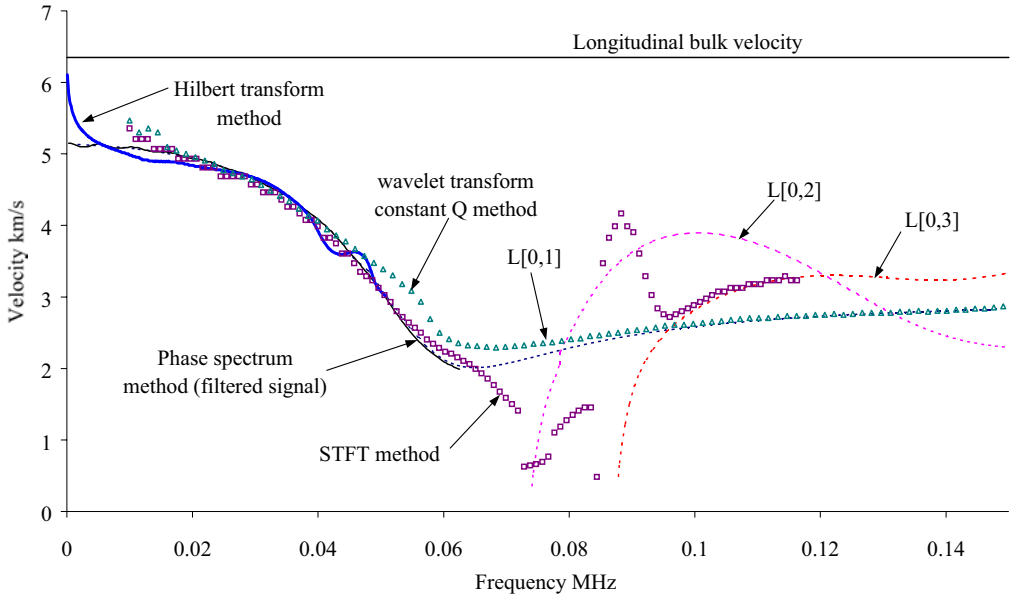

Figure 4.21. Comparison of results from different techniques used for extracting group velocity from the input $u(t)$ and monitored signal $v(t)$ shown in Fig 4.17 (with dispersion curves as dashed lines).

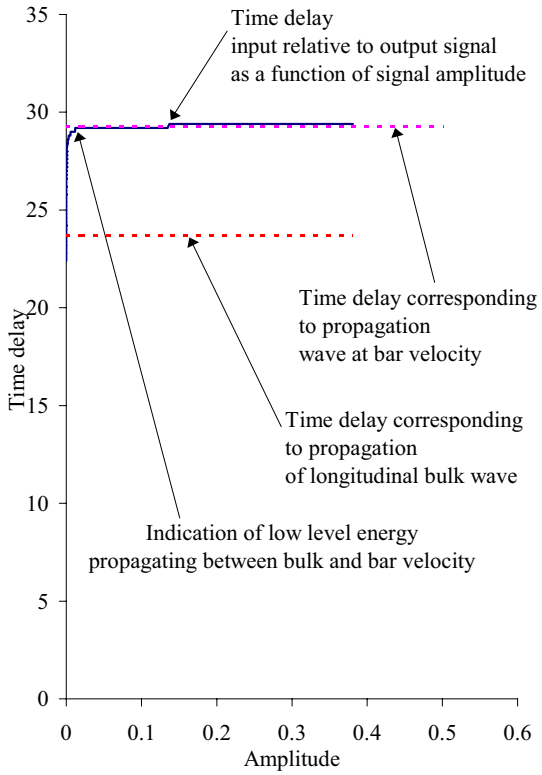

Figure 4.22. Time delay between finite element model input $u(t)$ and output $v(t)$ signal at 150mm from bar end as a function of signal amplitude. Dashed lines corresponding time delays for the bulk and bar velocity.

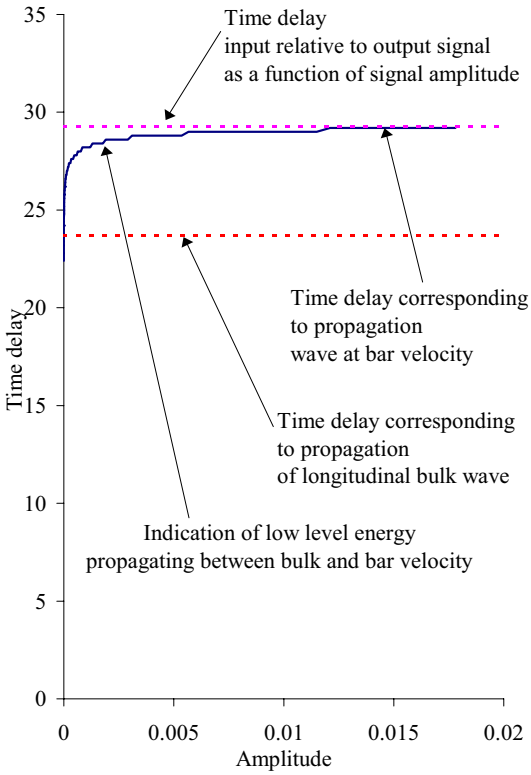

Figure 4.23. Zoom in of the time delay between for finite element model input $u(t)$ and output $v(t)$ signal as a function of threshold value.

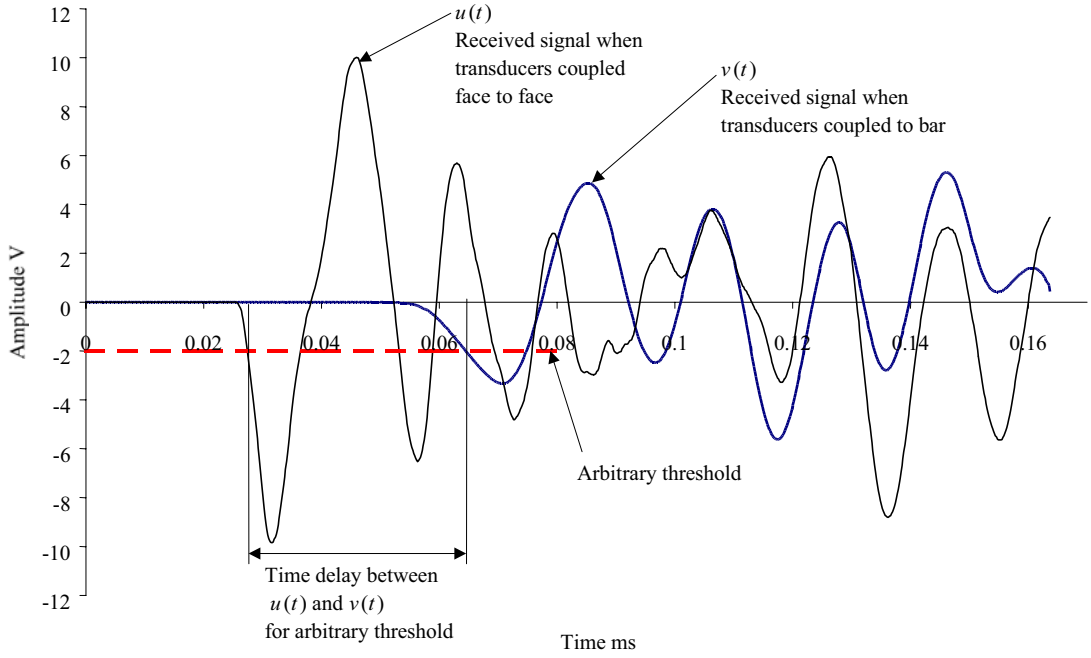

Figure 4.24. Experimental received signals for transducers coupled face to face (input $u(t)$) and transducers coupled to reference bar (output $v(t)$) for the evaluation of the time delay stamped on Pundit reference bar.

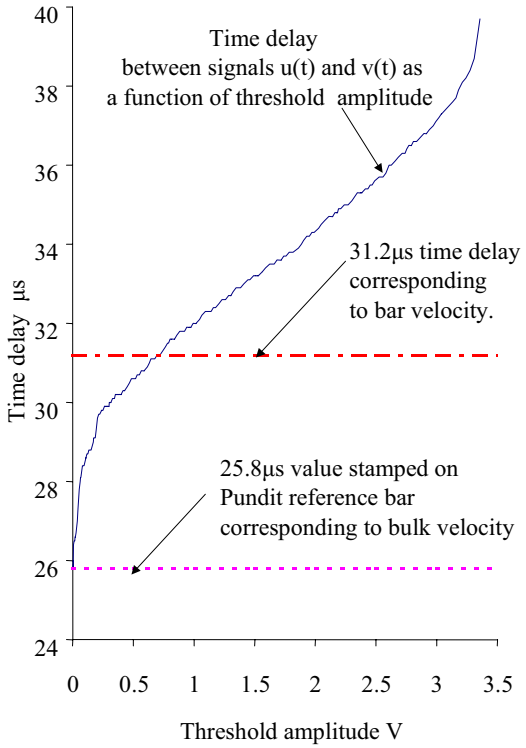

Figure 4.25. Time delay between experimental input $u(t)$ and output $v(t)$ signal as a function of threshold value.

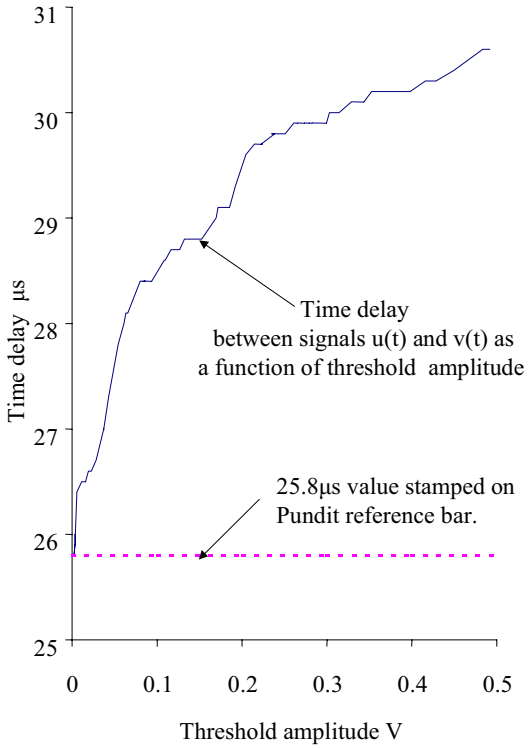

Figure 4.26. Zoom in of the time delay between experimental input $u(t)$ and output $v(t)$ signal as a function of threshold value.

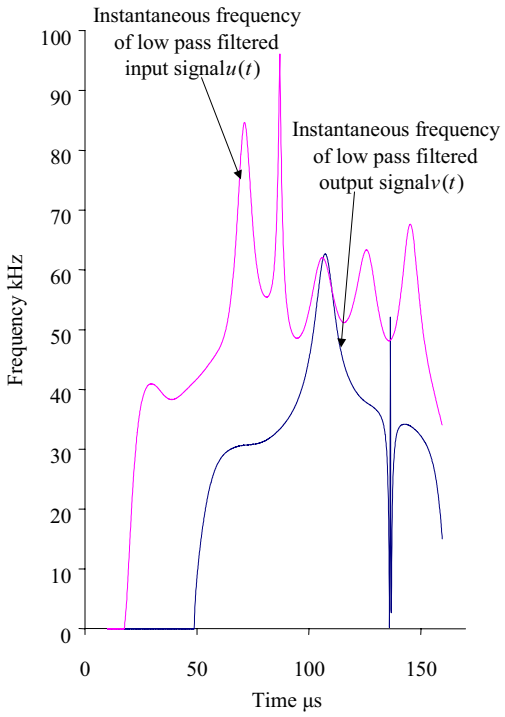

Figure 4.27. Instantaneous frequencies for low pass filtered experimental input $u(t)$ and output $v(t)$ signal evaluated by Hilbert transform method.

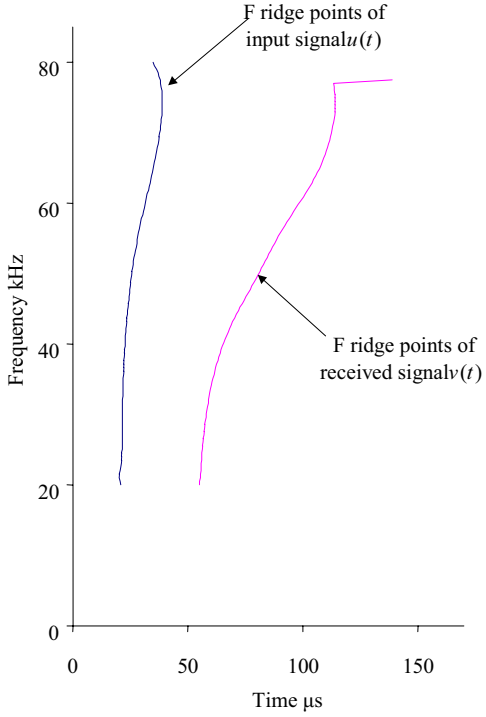

Figure 4.28. F ridge points for experimental unfiltered input $u(t)$ and output $v(t)$ signal evaluated by STFT transform where ω_0=1.9.

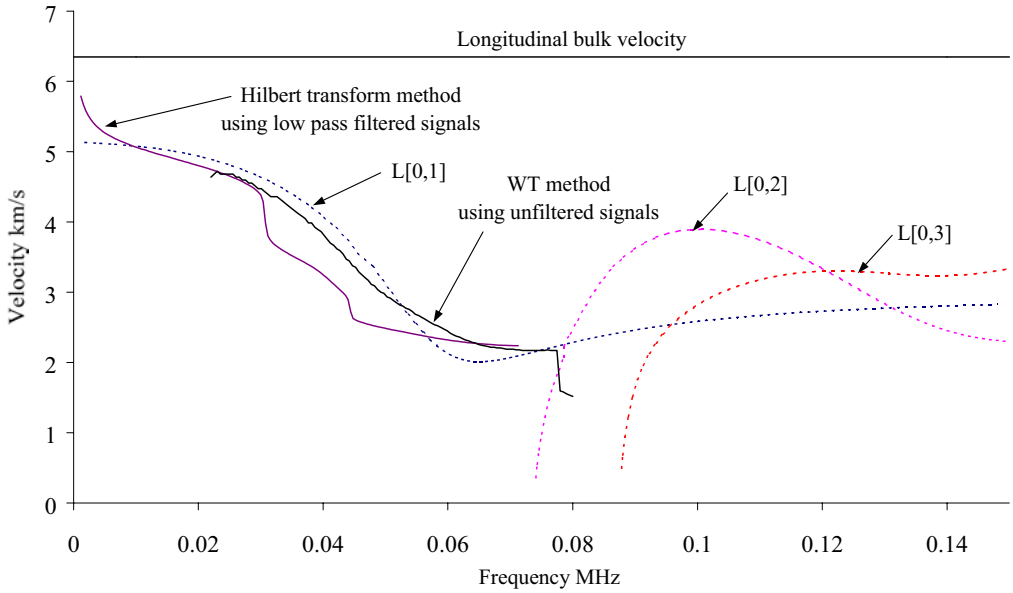

Figure 4.29. Experimentally evaluated group velocity of wave propagation in Pundit reference bar. Comparing Hilbert and WT transform techniques (with dispersion curves as dashed lines).

Chapter 5

Convenient coupling of transducers

5.1 Introduction

The most valuable use of the ultrasonic technique is to provide a relative assessment of concrete quality [Naik and Malhotra (1991)] and [Bungey and Millard (1996)] where an area is marked out on the structure and the velocity of sound is determined at the numerous grid points. The results are often plotted as a contour map where variations in pulse velocity aid the indication of problem areas. The application of standard ultrasonic transducers for such an inspection proves to be time consuming and messy due to the requirement that a viscous couplant be applied to each grid point. The purpose of the couplant is to fill the significant air gaps between the transducer face and rough test surface, which due to the impedance of liquids being higher than air, allows a much higher proportion of the wave energy to cross the interface. Higher viscosity couplants are generally recommended for rougher surfaces. The removal of such couplants after completion of tests is inconvenient. It is reported that it is difficult to achieve consistent coupling of ultrasonic transducer when testing concrete [Bungey (1991)]. Chapter 3 showed that the measured pulse velocity is affected by the magnitude of the received signal amplitude. The amplitude of the transmitted pulse depends on the pressure exerted on the transducer, the characteristics and thickness of the couplant medium, and the roughness of the surface under test [Canella (1974)]. There is thus an incentive to find alternative means of coupling transducers to a rough surface. In this work attention was focused on investigating solid coupling as an alternative to liquid coupling.

5.2 Possible coupling alternatives

For testing concrete surfaces a practical alternative to using a viscous couplant is to have some form of solid coupling. One idea reported is to use a fast setting mortar [Andrews and Hughes (1991)] between the face plate of the transducer and the concrete surface under test. The mortar sets in approximately 2 minutes developing sufficient strength to support a transducer. The effect is that more consistent coupling is achieved and signal transmission is improved due to the impedance of the mortar being a better match to concrete than a viscous coupling. However, the technique is certainly less convenient than using a viscous couplant when conducting a large number of tests on a grid. A more viable form of coupling that has been around for some years might be to couple with a compliant solid such as a rubber that conforms around the surface contours of the test surface as described by Dickson [1982].

Two common designs of rubber coupled devices are static and wheel probes. The static probe described by Billson and Hutchins [1993] has a rubber tip attached to the face of the transducer, which provides the coupling mechanism when the transducer is pressed against the test surface. For the wheel probe [Drinkwater and Cawley (1995)], the rubber is formed into a tyre, the tyre filled with a liquid, and the transducer is mounted on the wheel axis. For this design, modest coupling pressures allow satisfactory transmission of ultrasound, and enable rapid scanning of relatively smooth metal test surfaces. For concrete, rapid scanning of typically awkward profiles is not considered to be practical and so the design of a hand held rubber coupled transducer was envisaged to take one of three possible forms that are shown in Fig 5.1:

a) a flat pad bonded to the transducer face;
b) a profiled pad such as a hemisphere;
c) a liquid volume encapsulated by a thin flexible shell, to be termed a membrane (similar to the wheel probe concept but more flexible).

An alternative to rubber coupling is to have an indenter whose modulus is comparable to or higher than concrete. For a hard indenter efficient coupling would be achieved by increasing the pressure over the solid-solid interface. For the loads that could be applied by a hand held transducer such pressures necessitate that the contact area be relatively small. A possible device might be similar to the machined PZT conical transducers which have been developed at NBS [Proctor (1982)] for point source point receiver techniques. The point-like contact between a conical indenter similar to that shown in Fig 5.2a and the test surface is a means by which acoustic energy can be coupled efficiently. These transducers have been used by Evans [1997] for acoustic emission monitoring and by Hsu and Eitzen [1987] and Wu and Fang [1997] for determination of concrete slab Rayleigh wave velocities. However, for testing non conductive materials, the design would require a conducting foil between the conical tip and surface to complete the electrical earth. This would be impractical for numerous tests on the rough surfaces common to concrete structures. An alternative is to have a solid metal tip attached to the transducer face. Exponentially shaped transducers as show in Fig 5.2b are already commercially available (CNS Farnell, London) for testing difficult concrete profiles. These are not ideal devices since the low contact area made with the rough surface results in weak signal transmission. As such it is recommended [PUNDIT Operating Manual] and [Naik and Malhotra (1991)] that these transducers be used as receivers along with a standard transducer as a transmitter.

The feasibility of hard conical transducers was not investigated since their use is well documented. However, little additional effort would be required to allow contact models to predict the contact of conical indenters. Rubber coupled devices were researched since their use when testing concrete appears to be an original approach. The research involved a number of stages which will be described in this chapter in the chronological order in which they were tackled. For background the characteristics of concrete roughness and ultrasonic transmission through a dry rubber concrete interface were first investigated. With these findings in mind contact models were then derived to enable design optimisation of a hand held device. Prototype devices were made and tested. Model predictions and experimental results were compared to address the feasibility of dry rubber coupling transducers to concrete. Finally the option of smearing the rubber with water to improve coupling was investigated.

5.3 Characteristics of rubber concrete contact

Prior to the modelling and evaluation of various solid coupling designs an investigation was conducted into the characteristics of concrete surface roughness and transmission through a rubber-rough surface interface. The investigation would allow familiarisation with rough surface data and enable the choice of the parameters that the contact model will solve.

5.3.1 Concrete surface roughness characteristics

There are a large range of surface finish possibilities for a concrete structure that could be considered when addressing the feasibility of solid coupling of transducers. When conventionally coupling ultrasonic transducers the viscosity of the couplant recommended increases with surface roughness. Where the surface roughness is significant it is recommended [PUNDIT Operating manual] that some kind of surface preparation such as filling the surface with a quick setting mortar be performed. Adequately flat surfaces not requiring preparation will generally be those that had been in contact with metal or wooden shuttering during hydration or where an exposed surface was carefully floated flat prior to hydration. It would be expected that the use of a solid coupled device would apply only to surfaces not requiring preparation. Thus the characteristics of very rough surfaces or visually pleasing designs will not be considered.

When modelling contact of rough surfaces, the topography is often approximated by distributions of idealised asperities for which contact behaviour is well known [Greenwood and Williamson (1966)]. The major disadvantage of this technique is that the deformed shape of the surfaces, particularly where there is no contact can not be predicted. An alternative is to use the measured topography directly in a numerical contact model [Webster and Sayles (1986)] where the data could also be approximated by sine wave or statistically generated functions. The profile of a rough surface $u_{(r)}$ can be obtained by drawing a stylus over the surface and recording the vertical displacements at suitable intervals. Application of statistical methods reduces the data to height and wavelength parameters to describe the spatial structure of the surface [Whitehouse and Archard (1970)]. For the height considerations, the centre line average (*CLA*) or (R_a) has been used [Drinkwater (1995)], and is defined as the mean vertical departure of the profile from the centre line , where the average roughness is given by

$$R_a = \frac{1}{L}\int_0^L \left|u_{(r)}\right| dr \qquad 5.1$$

where the requirement for the centre line is

$$\int_0^L u_{(r)} dr = 0 \qquad 5.2$$

A statistically more meaningful measure of average roughness is the root mean square or standard deviation σ of the height from the centre line [Johnson (1985)] given by

$$\sigma^2 = \frac{1}{L}\int_0^L u_{(r)}^2 dr \qquad 5.3$$

The relationship between σ and R_a depends on the nature of the surface. For a sine wave profile

$$\sigma = \left(\pi / 2\sqrt{2}\right) R_a \qquad 5.4$$

and for a Gaussian random profile

$$\sigma = \left(\pi / 2\right)^{1/2} R_a \qquad 5.5$$

Additionally for a sine wave the amplitude A is related to the R_a by

$$A = R_a \pi / 2 \qquad 5.6$$

Substituting equation 5.6 into equation 5.5 provides the relationship between the statistical random data and the amplitude of an equivalent sine wave as

$$A = \sigma (2/\pi)^{-1/2} \qquad 5.7$$

These relationships enable the height distributions of a real rough surface to be modelled by a sine wave or Gaussian random distribution. It has been found [Johnson (1985)] that many real surfaces exhibit a height distribution that is close to the Gaussian probability function given as

$$\phi(u) = \sigma^{-1}(2\pi)^{-1/2} \exp\left(-\frac{u^2}{2\sigma^2}\right) \qquad 5.8$$

where $\phi(u)$ denotes the probability that the height of a particular ordinate lies between u and $u + du$. The probability that the height of an ordinate is greater than u is given by the cumulative probability function which is given as

$$\Phi(u) = \int_u^\infty \phi(u')du' \qquad 5.9$$

When plotted on normal probability paper, data that follows a Gaussian distribution will fall on a straight line whose gradient gives a measure of the standard deviation. To develop statistical data for the numerical contact model of i=1 to N data points, the author found that the following algorithm manipulates a set of random numbers so as to force a Gaussian distribution given by

$$y_i = 2n^{-1/2} \sum_{a=1}^{a=n} (x_a - n/2) \qquad 5.10$$

For each data point i a set of random numbers are generated, where it was found by experiments that a good distribution was possible when the number of random numbers n

used was $n>3N$. The magnitude of a generated random number R_a can vary between $1> R_a>0$. Depending on the magnitude of a random number R_a the corresponding value of x_a is given as $x_a=1$ when $R_a<0.5$ and $x_a=0$ when $R_a>0.5$. Having generated n random numbers, the corresponding values of x are integrated to give the amplitude of the function y_i. This processes is repeated for all data points and when completed some form of sampling or fitting of cubic splines can be applied to the function y so as to smooth it out.

For wavelength or spatial parameters the correlation length β^* is often used [Sayles (1982)] which is defined as the wavelength β when the autocorrelation function has decayed to some fraction of its peak, where the value $1/e$ has been used [Drinkwater (1995)]. The autocorrelation function $R(\lambda)$ over the range $\pm N/2$ is given as

$$R(\beta)=\frac{1}{N}\int_{-N/2}^{N/2}u(r)u(r+\beta)dr \qquad 5.11$$

The surface slope σ_m parameter that forms part of the plasticity index which indicates whether deformation is predominately elastic or plastic [Johnson (1985)] gives some indication of the smoothness or roughness of a surface, which is given as

$$\sigma_m=\frac{\sigma}{\beta*} \qquad 5.12$$

5.3.2 Real rough concrete surfaces

Surface texture was measured using a Talysurf surface profilometer using a ball end stylus. The equipment draws a stylus over a sample length of the surface, and digitises the vertical displacements at suitable intervals. The slope of the sample surface is removed from the data by finding a straight line (or arc for circular components) from which the mean square deviation is a minimum. The apparatus stores the trace from which the height σ and wavelength β^* parameters that describe the surface are calculated. The sample interval for this work was 50μm and for 501 samples gave a sample length of 25mm. Data is affected by variables such as sampling interval, sample length, stylus size and instrument response for example. The extent to which these variables affect such data is not considered in this work. Sampling intervals and stylus were chosen by reference to texts [West et al. (1987)] and [Whitehouse and Archard (1969)].

Surface	Standard deviation σ (μm)	wavelength β* (mm)	Rms. slope σ_m
Metal shuttering	14.1	0.17	0.083
Timber shuttering	98.7	2.75	0.036
Floated	33.1	2.1	0.016

Table 5.1 Surface roughness parameters of sample concrete surfaces.

Three differing surfaces were considered for this work that could be said to represent the range of concrete surfaces for which no preparation is required prior to ultrasonic testing. Sample blocks were obtained where the surfaces had been in contact with metal or wooden shuttering during hydration or had a floated finish. The profilometer traces of these surfaces are shown in Figs. 5.3a through to 5.3c. The statistical parameters that refer to these surfaces are shown in Table 5.1. The surface that had been in contact with metal shuttering during hydration had the lowest values of σ and β^* and largest value for the surface slope σ_m. This relatively flat surface had an appearance similar to a medium grade sandpaper. By contrast the surface that had been in contact with timber shuttering during hydration appeared much coarser with greater values of σ and β^*. This surface would be considered borderline as to whether any surface preparation should be required prior to conventional ultrasonic testing. The floated surface had a relatively small value for σ and a large wavelength β^*, giving the lowest surface slope σ_m resulting in the surface feeling smooth to touch. This surface could not be said to be typical for a floated finish, but it was taken to represent perhaps the smoothest concrete surface that might be encountered. The data from these three sample concrete surfaces will be used throughout this chapter for modelling. Experiments will be conducted on the actual surfaces in the vicinity of where the measurements were performed.

5.3.3 Ultrasonic transmission across an interface

The efficiency of ultrasonic coupling can be measured by the proportion of the signal that is transmitted or reflected at the interface. For conventional liquid coupling of transducers the transmission coefficient is related to the acoustic impedances of the couplant and the structure the signal radiates into. Additionally it can be shown [Canella (1974)] that the signal transmission is a strong function of couplant thickness unless the thickness is small. For grease couplant applied to concrete this effect can be neglected if the couplant thickness is less than about 0.5mm. The classical analysis considers the interaction of a normally incident plane wave with a plain boundary between two infinite media [Pialucha (1992)].

For convenience the normal incidence transmission coefficient is derived here following a similar approach to Kendal and Tabor [1971].

Consider the cylindrical bar shown in Fig 5.4a of cross sectional area A_o where materials of acoustic impedance Z_1 and Z_2 are connected perfectly at the interface x=0. The boundary conditions at the interface are that the pressures should be balanced and that the displacements be continuous giving

$$P_i + P_r = P_t \tag{5.13}$$

and

$$y_i + y_r = y_t \tag{5.14}$$

The normal pressures of the incident, reflected and transmitted waves as a function of time t and distance propagated x can be given respectively as

$$\begin{matrix} P_i e^{i(wt-k_1 x)} \\ P_r e^{i(wt+k_1 x)} \\ P_t e^{i(wt-k_2 x)} \end{matrix} \tag{5.15}$$

where the wave number k is the ratio of frequency ω over velocity c given as

$$k_n = \frac{\omega}{c_n} \tag{5.16}$$

the bar velocity c which is related to Young's modulus E and the material density ρ by

$$c_n = \sqrt{\frac{E_n}{\rho_n}} \tag{5.17}$$

from which the acoustic impedance is given as

$$Z_n = c_n \rho_n \tag{5.18}$$

For a linear system Hooke's law relates the pressures to the displacement by

$$P = -E \frac{\delta}{\delta x} y \tag{5.19}$$

which in terms of the displacement is written as

$$y = -\frac{1}{E}\int P dx \tag{5.20}$$

Substituting equation 5.20 into the displacement boundary condition given in equation 5.14 and applying the pressures given in equation 5.15 gives

$$\frac{1}{E_1}\left[\int P_i e^{i(wt-k_1x)}dx + \int P_r e^{i(wt+k_1x)}dx\right] = \frac{P_t}{E_2}\int P_t e^{i(wt-k_2x)}dx \tag{5.21}$$

which upon integration gives

$$\frac{1}{E_1}\left[\frac{P_i e^{i(wt-k_1x)}}{-ik_1} + \frac{P_r e^{i(wt+k_1x)}}{ik_2}\right] = \frac{P_t}{E_2}\frac{e^{i(wt-k_2x)}}{-ik_2} \tag{5.22}$$

At the interface, by setting x=0, allows the factorisation of the exponential terms such that equation 5.22 reduces to

$$P_i - P_r = P_t\frac{E_1k_1}{E_2k_2} \tag{5.23}$$

Substituting equation 5.13 and equation 5.18 into equation 5.23 gives

$$2P_i = P_t\left(1+\frac{Z_1}{Z_2}\right) \tag{5.24}$$

The normal transmission coefficient T_p for the perfect interface is the ratio of transmitted over incident pressure, which from equation 5.24 gives the classical solution as

$$T_P = \frac{2Z_2}{Z_1+Z_2} \tag{5.25}$$

Now consider an imperfect interface at x=0 as shown in Fig. 5.4b where the rough faces of two cylindrical bars of cross sectional area A_o are loaded against each other. The transmission across the interface is not only dependent on the acoustic impedances of the

two materials but also on the degree of contact. From friction studies, the true area of contact A_t can be considered as the sum of the points where the atoms on one face are within atomic distances of the atoms of another. For dry coupled interfaces the areas not in contact are described as air gaps. For transmission across steel interfaces Kendal and Tabor [1971] have shown that where the surfaces are separated by more than 10nm the transmission of a 200kHz signal across the air gap is insignificant. It is for this reason that some form of liquid couplant, with much higher impedance to air, is often used to fill the air gaps to allow a significantly greater proportion of the signal energy to transmit across the interface. The true area of contact will be a function of the material properties, applied load, the geometry of the surfaces and the way the individual asperities deform. To predict the transmission across an imperfect interface we will follow Tattersall [1972] and Baik and Thompson [1984]. The derivation begins by firstly considering the static case where the application of a stress σ results in the closure of the interface, the relative displacement of two points in the far field on opposite sides of the interface can be given as

$$\frac{\Delta}{2} = \frac{1}{2}\left(\Delta_P + \Delta_I\right) \qquad 5.26$$

where Δ_P is the displacement for a perfect interface and Δ_I represents the deformation in the vicinity of the imperfect interface. It follows that we could approximate the interface by a spring of stiffness per unit area (N/m^3) given by

$$k = \frac{\sigma}{\Delta_I} \qquad 5.27$$

which when used to join the faces of the two bars together will reproduce the static displacement. For the dynamic case, if the signal wavelength is large compared to the individual contact areas then the dynamic response is said to be related to the static response. This approach commonly known as the Quasi static model (QSM) where the spring stiffness for the QSM is again given by equation 5.27, and it may also have a mass term [Baik and Thompson (1984)] in order to include the inertial effects. The roughness of concrete surfaces is characterised by large wavelength relative to height parameters, such that the non contacting areas can be approximated as a planar array of cracks. Baik and Thompson [1984] have shown that for signal wavelengths which are large compared to such planar type defects the mass term is negligible. Additionally, for low frequencies Angel and Achenbach [1985] have shown that the QSM shows good agreement with other more rigorous models. The QSM implicitly assumes [Yalda-Mooshabab et al. (1992)] that contacts are close

enough to each other such that the depression due to one contact effects the state of neighbouring contacts. By considering that the contacts interact with one another, then following Kendal and Tabor [1971] the contacts can be lumped together such that the interface can be approximated as a constriction between the two bars as shown in Fig 5.4c. Consequently, if P_t is the pressure of the wave transmitted from left to right this exerts a force P_tA_0 on the interface and a displacement in that direction of P_tA_0/S. The stiffness S in this case has the more familiar units of force per unit displacement (N/m) and is related to equation 5.27 by

$$\frac{S}{A_0} = k \tag{5.28}$$

The boundary conditions for the imperfect interface are again that there should be equal pressures at the interface

$$P_i + P_r = P_t \tag{5.29}$$

However, due to the deformation in the vicinity of the constriction the displacements are discontinuous at the interface such that the boundary condition is given as

$$y_i + y_r = y_t + P_t \frac{A_0}{S} \tag{5.30}$$

The solution for the normal incidence transmission coefficient for the imperfect interface is solved by the same procedure as for the perfect interface. Substituting equation 5.20 into equation 5.30 and arriving at a similar position to equation 5.23 we get

$$\frac{P_i}{Z_1} - \frac{P_r}{Z_1} = \frac{P_t}{Z_2} + P_t \frac{i\omega A_0}{S} \tag{5.31}$$

Substituting the boundary condition equation 5.29 into equation 5.31 and rearranging as the ratio of transmitted pressure over incident gives

$$T_I = \frac{2Z_2}{(Z_1 + Z_2) + \dfrac{i\omega Z_1 Z_2 A_0}{S}} \tag{5.32}$$

If the stiffness k is substituted for S/A_0 this gives the standard representation attributed to Tattersall [1972], but the form of equation 5.32 is preferred since it will prove useful later. A spring stiffness of zero would approximate a slack interface for which the magnitude of equation 5.32 would be zero. A perfect interface would be approximated by an infinitely stiff spring which would result in a negligible imaginary term reducing equation 5.32 to equation 5.25. The efficiency of an interface can be given by the fractional transmission, which is the ratio of the transmission for an imperfect interface over that for a perfect one given by

$$T_f = \frac{T_I}{T_P} \qquad 5.33$$

Substituting equation 5.32 and equation 5.25 in equation 5.33 gives

$$T_f = \frac{1}{1 + \dfrac{i\omega Z_1 Z_2 A_0}{S(Z_1 + Z_2)}} \qquad 5.34$$

For low values of transmission where $|ix| >> \left(T_f^{-1} - 1\right)$ the modulus can be approximated by

$$\left|T_f\right|_{<0.3} \approx \frac{S(Z_1 + Z_2)}{\omega Z_1 Z_2 A_0} \qquad 5.35$$

Thus it follows that for low levels of contact the classical solutions predict that transmission across an imperfect interface will be proportional to the interfacial stiffness. It also follows from equation 5.35 that transmission is inversely proportional to frequency.

5.3.4 Experimental rubber concrete contact

This section describes an investigation conducted to examine the characteristics of ultrasonic transmission through a rubber-rough surface interface. The aim was to assess the degree of contact that would be made for loads that could be applied by hand, and to verify if the quasi static model QSM was appropriate for this type of contact. For the experiments transducers were rubber coupled to two different surfaces: a concrete block which had the floated concrete surface as shown in Fig 5.3c, and an aluminium block to which some medium grade sandpaper was bonded. The floated concrete surface represented perhaps the smoothest surface that might be encountered when testing concrete, and the sandpaper

bonded onto aluminium represented the metal shuttered concrete surface as in Fig 5a but without the inhomogeneity of concrete. A schematic of the experimental set up for tests on the concrete block is shown in Fig 5.5. Immersion type 40mm diameter 200kHz centre frequency transducers were used. The receiving transducer throughout all experiments was bonded to the underneath of the block.

To examine the degree of contact that might be expected and how this might vary as a function of applied load, initially the transmitter was grease coupled to the upper surface of either specimen, using a medium viscosity water pump grease. The transmitter was excited with a 150kHz 5 cycle tone burst and a reference signal for grease coupling was obtained. The transmitter was removed, and the test surface was degreased with a solvent. A thin layer of grease was then smeared over the transmitter face and a degreased 40mm diameter 2mm thick silicon rubber disc was then applied. The transmitter was then dry rubber coupled to the rough test surface and weights of up to 3.5kg were added in increments of 0.5kg to the back face of the transducer so as to load the interface and thereby increase the degree of contact. The transmitter was excited as for grease coupling and a signal for dry rubber coupling at a given applied load was received. The maximum amplitude of the received signal for dry coupling was then divided by that for grease coupling. The ratio was taken to represent the fractional transmission as given by equation 5.33 as a function of applied load.

Additionally an experiment was conducted to verify the frequency dependence predicted by the QSM. The transmitter was initially grease coupled to the upper rough surface. For the concrete sample, the transmitter was then excited with a 5 cycle tone burst, at centre frequencies of 100, 200 and 300kz to obtain reference signals for grease coupling over the frequency range of interest. For coupling to sandpaper the transmitter was only excited with a 220kHz 5 cycle tone burst. Dry rubber coupling was then achieved as done previously using a 1mm or 2mm thick 40mm diameter silicon rubber disc, where for these tests the total applied loads were 1.2kg, 2.2kg and 3.2kg (a load of 2kg being considered as typical that could be applied with a hand held device). The transmitter was then excited as for grease coupling, and signals for dry rubber coupling were obtained. The frequency spectrum (over a reasonable band width) of the received signal for rubber coupling was then divided by that for grease coupling. The ratio was taken to be the fractional transmission given by equation 5.33 as a function of frequency. To verify the prediction given by equation 5.32 that the transmission coefficient is inversely proportional to frequency, a single value of the interfacial stiffness was chosen such that the modulus of equation 5.32 could be compared to the experimental results.

5.3.5 Experimental results for rubber concrete contact

Fig 5.6a and Fig 5.6b show the experimentally evaluated fractional transmission as a function of applied load results for rubber floated concrete and sandpaper coupling respectively. For a 2kg load that could be applied by hand the fractional transmission would be expected to be in the region of 0.15 to 0.015 (16dB to 36dB loss of signal strength) depending on surface roughness. It is apparent that over the range of loads considered the transmission is approximately a linear function of applied load for contact with both rough surfaces. The greatest signal transmission occurs not surprisingly for contact with the smooth floated concrete. The levels of transmission are within the range for which equation 5.35 is applicable, thus for low load rubber concrete contact we can make approximations that:

a) $T \propto W$, transmission is proportional to load (from Fig 5.6a and 5.6b)
b) $T \propto S$, transmission is proportional to interfacial stiffness (from equation 5.35)
c) from which it follows that $S \propto W$, interfacial stiffness is proportional to load.

An investigation performed by Kendall & Tabor [1971] suggests the following relationships between interfacial stiffness and applied load that depend on the contact characteristics:

i) For asperities that interact, if the number of contacts remain the same and the size of the asperities grow with increasing load then the stiffness will remain constant.
ii) If the number of contacts increases with load and the separation between contacts remains constant the stiffness will be proportional to $W^{1/3}$ and the overall deformation will be elastic.
iii) For isolated non-interacting contacts, if with increasing load the number of contacts remains the same but the size of the contacts increases the stiffness will be proportional to $W^{1/2}$ and the overall deformation will be plastic.
iv) If on the other hand an increase in load leads to an increase in the number of contacts but not their average size, then the stiffness is proportional to W.

The experimental results for rubber concrete contact would appear to fall into the last description. Greenwood and Williamson [1966] and Archard [1957] have shown that for contact of nominally flat surfaces where the deformation of each asperity is independent of its neighbours then the real contact area is proportional to the applied load. Thus for low load flat rubber-concrete contact we can add another two approximations in that:

d) $A_t \propto W$, real area of contact is proportional to load and
e) $T \propto A_t$, transmission is proportional to real area of contact (from approximations a to d)

The term non interacting contacts refers to where individual contacts are more than 3 to 4 diameters apart [Kendall & Tabor (1971)], or when the true area of contact is less than about one tenth of the apparent area of contact. For $T \propto A_t$ this would limit the fractional transmission to 0.1. Generally this will be the case for concrete type surfaces, the floated surface being thought of as the smoothest surface that might be encountered. However Haines [1980] has shown that for ratios of true over apparent area of contact of approximately 0.2, the effect of asperity interaction is small, thus allowing the approximation $T \propto A_t$ even for contact with the floated surface.

The experimental results for the transmission as a function of frequency are shown in Fig 5.7a and Fig 5.7b for contact with the floated and sandpaper surfaces respectively. For both sets of results an appropriate value of interfacial stiffness was chosen so as to compare the QSM characteristics of transmission being inversely proportional to frequency. It can be seen that these results do not exhibit the dependence on frequency that the QSM predicts. There is evidence in both sets of results of some periodicy but the mean transmission remains fairly constant over the range of interest. Many researchers have found that contact problems display similar frequency dependence which the QSM predicts, for example, [Wooldridge (1979)] contact of steel blocks, [Margetan et al. (1990)] contact of metal-metal bonds, [Tattersall (1972)] adhesion testing and more recently [Drinkwater et al. (1998)] aluminium-aluminium contact. All these results relate to problems with appreciably higher loads and smoother surfaces and hence greater contact areas than apply to our case. Drinkwater [1995] found that when rubber coupling to roughened aluminium surfaces, frequency dependence was only occasionally identified and then not to the extend the QSM predicts. In that work the degrees of contact satisfied the limits of the QSM. Yalda-Mooshabab et al. [1992] note that for the QSM to be applicable the asperities are considered to interact. Boström and Wickham [1991] have shown that when the ratio of true over apparent area of contact equals 0.1, this results in the model predicting an appreciable build up of energy at the interface which invalidates the model. It is thus apparent that the QSM is not applicable for low load rubber concrete contact on the grounds of the low areas of contact experienced and that contact areas do not interact. The author speculates that non interaction of contact zones contributes to the lack of the predicted frequency dependence. A thorough investigation into the reasons of lack of frequency dependence would distract from the aim of this chapter which was to investigate convenient coupling, thus it was decided to accept the contact characteristics obtained from the experimental results.

Having established that for low levels of contact $T \propto A_t$, transmission is proportional to real area of contact, without frequency dependence it follows from equation 5.35 that the fractional transmission is equal to the fractional area of contact given by

$$T_f = \frac{A_t}{A_0} \qquad 5.36$$

Thus to predict the efficiency of a given solid coupled device, models will be derived to solve for contact area as a function of applied load to enable the transmission as a function of applied load to be predicted.

5.4 Solid contact model

The design optimisation of a device to enable convenient coupling of transducers when inspecting concrete structures requires some form of contact modelling to predict the signal transmission for a given applied load. The simplest models approximate surface roughness by distributions of idealised asperities for which contact behaviour is well known [Greenwood and Williamson (1966)]. The major disadvantage of this technique is that the deformed shape of the surfaces away from the contact zones can not be predicted. This is particularly troublesome when predictions of interfacial stiffness are required. An alternative to this successfully adopted by Drinkwater [1995] was to model the deformations of a solid rubber coupled device pressed onto a rough surface by using a numerical elastic line contact model [Webster and Sayles (1986)]. The digitised rough surface data was obtained from real surfaces using a surface profilometer. The interfacial stiffness was determined from predictions of the change in the separation between contacting surfaces as a function of load, which was then applied to quasi static contact models [Baik and Thompson (1984)] to estimate reflection or transmission coefficients. For low load rubber-concrete contact it was shown in section 5.3 that the fractional transmission is a function of the fractional area of contact and that determination of interfacial stiffness was not necessary. However, the numerical modelling of real surfaces is preferred for this work since it is uncertain how one might model the contact characteristics with some distribution of idealised asperities. This work considers various axi-symmetric solid contact designs that would attach to the face of a cylindrical transducer. When modelling the contact of such devices with a rough surface, initial trials using three dimensional numerical solutions [West and Sayles (1987)] were found to take considerable computational time. Line contact is more suitable for modelling

contact of parallel rollers and assumes that the surface roughness is parallel. It was therefore decided to derive more appropriate models where the solid bodies and hence the surface roughness are assumed axi-symmetric in profile. A number of different solution techniques for solving numerical contact problems are given by Johnson [1985]. The author chose to derive an alternative iterative solution technique which though crude proves effective and simple to program. Solid contact models will be validated by comparing their solutions for contact with smooth flat surfaces with those of classical analytical solutions.

5.4.1 Contact model for a compliant solid pressed onto a rigid surface

The following assumptions will apply to all contact models described in this chapter. Strains are assumed small enough for linear elasticity to apply. Surface slopes are assumed small so that forces act normally to the surface. It is assumed that there is no tendency for one body to slide with respect to the other and hence only forces normal to the surface are considered. As with classical solutions, the concrete surface will always be considered as an infinite half space.

For rubber-concrete contact, since concrete is appreciably stiffer than rubber, the solution can be approximated by a deformable smooth surface brought into contact with a rigid rough surface. When modelling the contact of solid bodies we want to know what the surface deformations may be for a given load distribution. The simplest case relates a point force P acting on a semi-infinite elastic body as in Fig. 5.8. The solution for the gradient $\partial w / \partial r$ a distance z from the surface and a radius r from the origin O, is given by Timoshenko and Goodier [1982] as

$$\frac{\partial w}{\partial r} = -\frac{P(1+v)}{2\pi E}[2(1-v)r(r^2+z^2)^{-\frac{3}{2}} + 3rz^2(r^2+z^2)^{-\frac{5}{2}}] \qquad 5.37$$

where E is Young's Modulus for the compliant material and v is Poisson's ratio. The normal displacement w is obtained from equation 5.37 by integration

$$w_{(z,r)} = \frac{P}{2\pi E}[(1+v)z^2(r^2+z^2)^{-\frac{3}{2}} + 2(1-v^2)(r^2+z^2)^{-\frac{1}{2}} + C] \qquad 5.38$$

where C is a constant of integration. For a semi-infinite body $w=0$ when $z=\infty$, which gives $C=0$. Thus from equation 5.38 the solution for the normal surface displacement ($z=0$) on a semi-infinite body, a distance r from a point force is classically [Boussinesq (1885)] given as

$$w_{(r)} = \frac{P\ (1-\nu^2)}{\pi E r} \qquad 5.39$$

Axi-symmetric load distributions can now be modelled by the superposition of equation 5.39. The surface deformations due to the application of a ring load of radius b and intensity q per unit length as in Fig. 5.9 can be approximated by the superposition of equi-spaced point forces as in Fig. 5.10 of equal magnitude P given as

$$P = qbd\theta \qquad 5.40$$

The point force P can be considered to be applied over an elemental area da, such that its effect is equivalent to an applied pressure p given by

$$p = \frac{P}{da} = \frac{qbd\theta}{bdrd\theta} = \frac{q}{dr} \qquad 5.41$$

A general point $B(r,0)$ is a distance s from a point force located at A in Fig. 5.11. The length s is a function of r and θ, that is derived geometrically. One solution is

$$s_{(r,\theta)} = \sqrt{(b - r\cos\theta)^2 + (r\sin\theta)^2} \qquad 5.42$$

which is relevant for a point both inside and outside the boundaries of the ring load. Substituting equation 5.40 for P and equation 5.42 for r into equation 5.39, and summing the point forces gives the solution for the normal surface displacement w, at a distance r from the origin, due to the action of a single ring load of radius b, as

$$w_{(r)} = \frac{(1-\nu^2)}{\pi E} \int_0^{2\pi} \frac{qb}{\sqrt{[b - r\cos(\theta)]^2 + [r\sin(\theta)]^2}} d\theta \qquad 5.43$$

The solution for an axially symmetric load distribution $q_{(b)}$ is obtained by integrating equation 5.43 over the contact area, which in a form suitable for a numerical solution gives

$$w_{(r)} = \frac{2(1-\nu^2)}{\pi E} d\theta \sum_{m=0}^{M} \sum_{n=0}^{N} \frac{q_{(b)} b}{\sqrt{[b - r\cos(md\theta)]^2 + [r\sin(md\theta)]^2}} \beta \qquad 5.44$$

When discretised into N and M elements this gives

$$d\theta = \frac{\pi}{M} \qquad 5.45$$

and

$$b = \frac{a}{N}\left(n + \frac{1}{2}\right) \qquad 5.46$$

where a is the maximum distance from the origin considered and $a/N=dr$. As $r \rightarrow b$, equation 5.44 is unduly sensitive to the ratio a/N due to the singularity at $r=b$. For convenience a factor β was found by experimentation to make the solution robust for a range of dr: $\beta = \sqrt{\pi / N}$ for m=0 and M, and β=1 elsewhere. This introduces some approximation in the vicinity of this point but has little effect overall and so does not compromise the analysis. Finally equation 5.44 can be given in a simplified form as

$$w_{(r)} = \sum_{b=0}^{b=a} I_{(r,b)} q_{(b)} \qquad 5.47$$

where the matrix $I_{(r,b)}$ is known as the influence coefficients that describe the displacement at r due to a unit intensity ring load of radius b.

5.4.2 Contact model for indenter and surface of similar modulus

The hard indenter contact can be modelled by simple modification of the compliant contact model. Where the modulus of the indenter E_1 is comparable to the surface E_2, it is required that the ratio of $(1-\nu^2)/E$ in equation 5.44 is replaced by $1/E^*$ [Johnson (1985)] where

$$\frac{1}{E^*} = \frac{1-\nu_1^2}{E_1} + \frac{1-\nu_2^2}{E_2} \qquad 5.48$$

The solution of equation 5.44 now gives the combined deformations of the two materials. The deformation in either material is obtained through the strain relationship

$$\frac{w_1 E_1}{1-v_1^2} = \frac{w_2 E_2}{1-v_2^2} \qquad 5.49$$

5.4.3 Contact model for a soft disc of finite thickness backed by a rigid substrate pressed onto a rigid surface.

When modelling the contact for soft discs of finite thickness that are attached to the face of a transducer, we can approximate this by a soft material backed by a rigid substrate. For a finite thickness *h* of material, a general correction factor *k* is derived from the constant of integration given in equation 5.38. For a point force acting on the face of the disc, the displacement *w* a distance *h* from the disc surface is zero. Setting *w=0* at *z=h* and solving equation 5.38 for the constant of integration gives

$$C = -(1+v)h^2(r^2+h^2)^{-\frac{3}{2}} - 2(1-v^2)(r^2+h^2)^{-\frac{1}{2}} \qquad 5.50$$

Assuming the first term has much less effect than the second term and rearranging gives

$$C \approx -2(1-v^2)r^{-1}\left(1+\frac{h^2}{r^2}\right)^{-\frac{1}{2}} \qquad 5.51$$

Thus substituting equation 5.51into equation 5.39, for a body of finite thickness *h* the normal surface displacement is given by

$$w_{(r)} = \frac{k_{(r)} P\ (1-v^2)}{\pi E r} \qquad 5.52$$

where

$$k_{(r)} = 1 - \frac{1}{\sqrt{1+\frac{h^2}{r^2}}} \qquad 5.53$$

The only similar case found in the literature [Goryacheva (1998)] was that for a strip punch in contact with an elastic layer of thickness h that lies without friction on a rigid foundation. The solution for the surface displacements is given as

$$w(r)_{z=0} = \frac{2(1-\nu^2)P}{\pi E}\left[K\left(\frac{r}{h}\right)\right] \qquad 5.54$$

where the kernel is said to take the form

$$K(t) = \int_0^{+\infty} \frac{L(u)}{u}\cos(ut)du \qquad 5.55$$

where

$$L(u) = \frac{\cosh 2u - 1}{\sinh 2u + 2u} \qquad 5.56$$

An equivalent solution to equation 5.54 that uses the authors' function can be obtained by applying equation 5.53 to the classical line load solution given by Johnson [1985] such that

$$w(r)_{z=0} = \frac{2(1-\nu^2)P}{\pi E}\left[\ln\left(\frac{h}{r}\right)k_{(r)}\right] \qquad 5.57$$

The authors' function that corrects for a finite thickness of material can then be validated by comparing equation 5.54 with equation 5.57. The comparison between the surface displacements for a rigid backed punch given by equation 5.54 and equation 5.57 as a function of the non dimensional distance r/h from the application of a line load are shown in Fig. 5.12. It can be seen that both functions agree satisfactorily which validates equation 5.53 for modelling of the deformations of a finite thickness strip punch. There is no reason to suspect that the same good agreement would not occur if an axi symmetric correction function had been found to compare with the authors' function. Therefore the function $k_{(r)}$ was included in the integral of equation 5.44 when modelling axi symmetric contact for a finite thickness material.

5.4.4 Numerical solution of contact model.

When modelling contact of rough surfaces, little is known about either the displacements $w_{(r)}$ or the load distribution $q_{(b}$ and so the solution of equation 5.47 is normally indeterminate. Various numerical methods have been developed to solve such problems [Johnson (1985)]. An iterative procedure that uses a matrix inversion technique is described by Webster and Sayles [1986] for the numerical solution of line contact numerical models. The following describes a simple to program alternative procedure developed by the author which was adopted for the solution of all cases in this work. In this example it is used for solving the deformations of a soft hemisphere pressed onto a rigid wavy surface.

The arbitrary profiles of the two bodies are shown in Fig. 5.13 where a function $g_{(r)}$ describes the wavy surface and $v_{(r)}$ describes the profile of the hemisphere such that it initially sits on top of the wavy surface. The hemisphere is then given a rigid body displacement δ (which enables the solution; it has no physical meaning) such that the overlap is described by a function w' where

$$w'_{(r)} = g_{(r)} - \left(v_{(r)} - \delta\right) \qquad \left(g_{(r)} \geq v_{(r)} - \delta\right) \qquad 5.58$$

and

$$w'_{(r)} = 0 \qquad \left(g_{(r)} \leq v_{(r)} - \delta\right) \qquad 5.59$$

For the example the overlap function $w'_{(r)}$ is shown in Fig. 5.14. An initial load distribution of $q_{(b)}$ is then assumed as a seed (a uniformly low value seems best) and a first estimate of the deformations $w_{(r)}$ is obtained by equation 5.47. The function $q_{(b)}$ is then adjusted for the next iteration n+1 by

$$q_{(n+1,b)} = q_{(n,b)}\left(1 + \frac{w'_{(b)} - w_{(n,b)}}{w_{(n,b)}}\right) \qquad 5.60$$

where $w'_{(b)}$ acts like an attracter and division by $w(n,b)=0$ is avoided. The result of equation 5.60 is then substituted back into equation 5.47 for the next estimate of $w_{(r)}$ as shown in Fig. 5.14. Iterations are repeated until the solution converges to a desired level. The effect of iterating by equation 5.60 is that the magnitude of $q_{(b)}$ approaches zero for non contacting points and is positive for contacting points. For the hemisphere example, after a number of

iterations the solution converged to a load distribution $q_{(b)}$ that is shown in Fig. 5.15 along with a displacement function $w_{(r)}$ shown in Fig. 5.16.

The displacements $w_{(r)}$ and the rigid body displacement $\left(v_{(r)} - \delta\right)$, both shown in Fig. 5.16 are added together to provide the deformed final profile of the hemisphere $u_{(r)}$ as shown in Fig. 5.17 given by

$$u_{(r)} = \left(v_{(r)} - \delta\right) + w_{(r)} \qquad 5.61$$

From Fig. 5.15 the total load F is obtained from

$$F = \sum_{0}^{a} q_{(b)} 2\pi b \qquad 5.62$$

From Fig. 5.17. the true area of contact A_t is obtained by the summation

$$A_t = \int 2\pi r dr \quad \text{for} \quad \left(u_{(r)} \le g_{(r)}\right) \qquad 5.63$$

5.4.5 Convergence of numerical solution.

The convergence of the solution for the hemisphere-wavy surface contact example was investigated. Normalised by the values after 10000 iterations, the predicted load given by equation 5.62 and the predicted true contact area given by equation 5.63 as iterations increase are shown in Fig. 5.18. and Fig. 5.19. respectively. The load converges rapidly, whereas the contact area converges more slowly. This is because after any number of iterations there is still some overlap of the surfaces of the two bodies, which makes the contact area appear larger for insufficient iterations. Thus convergence should be assessed by observing the contact area as a function of number of iterations. The following technique was found to aid the indication of adequate solution convergence. The idea is to obtain a prediction for the contact area using a different method and compare this to the estimation obtained by equation 5.63. When the two values agree the solution can be said to have converged. Deriving the technique begins by obtaining the overlap ratio $c_{(r)}$ of the rough surface profile $g(r)$ over the final profile $u_{(r)}$ given as

$$c_{(r)} = \frac{g_{(r)}}{u_{(r)}} \qquad 5.64$$

For the example of the hemisphere pressed onto the wavy surface shown in Fig 5.17, the function $c_{(r)}$ is shown in Fig. 5.20, where a line has been drawn at $c_{(r)} = 1$. Ideally the function $c_{(r)}$ would vary from zero to unity, where for contacting points $c_{(r)} = 1$. However since after a number of iterations the hemisphere may still overlap the wavy surface, more realistically as in Fig. 5.20, the overlap function varies from near zero to just over unity. If the line is drawn at $c_{(r)} = x$ as in Fig. 5.21, then a function $CA_{(x)}$ that describes how the contact area varies with x can be plotted. Referring to Fig. 5.21, for a given value of x the contact area is established by:

for $c_{(r)} \geq x$ and its previous neighbour $c_{(r-dr)} \geq x$ then the contact area at r is given by

$$A_{(r)} = 2\pi r dr \qquad 5.65$$

for $c_{(r)} \geq x$ and it previous neighbour $c_{(r-dr)} < x$ then by interpolating a point onto the line the elemental contact area at r-dr is given by

$$A_{(r-dr)} = 2\pi r dr \frac{c_{(r)} - x}{c_{(r)} - c_{(r-dr)}} \qquad 5.66$$

for $c_{(r)} \geq x$ and its subsequent neighbour $c_{(r+dr)} < x$ then by interpolating a point onto the line the elemental contact area at r+dr is given by

$$A_{(r+dr)} = 2\pi r dr \frac{c_{(r)} - x}{c_{(r)} - c_{(r+dr)}} \qquad 5.67$$

for all other conditions $A_{(r)}$=0. The total contact area CA for a given x is

$$CA_{(x)} = \int_0^a A_{(r)} dr \qquad 5.68$$

Around convergence the function $CA_{(x)}$ will be near zero for x>1 and then rise rapidly about x=1. Thus for insufficient iterations completed, the value at x where the greatest rate of

change occurs in the function $CA_{(x)}$ will coincide with the indicated contact area. This can be established by locating the maximum differential coefficient approximated by a central finite difference scheme given by

$$\frac{dCA_{(x)}}{dx} \approx \frac{CA_{(x+dx)} - CA_{(x-dx)}}{2dx} \qquad 5.69$$

Fig 5.22 shows the function $CA_{(x)}$ and the differential of $CA_{(x)}$ for the hemisphere example after 1000 iterations. Vertical lines are drawn to indicate the apparent contact area for x=1 and that which coincides with the maximum differential. For the hemisphere contact example, Fig 5.23 shows a comparison between the apparent contact area given by equation 5.63 and the indicated contact area given by equation 5.68 (where both are normalised by the contact area at 10000 iterations) as a function of the number of iterations completed. It can be seen that the two techniques of establishing the contact area converge on each other as the solution converges. This technique to indicate convergence is perhaps a little too complicated to be practical, however it was used to determine solution convergence throughout this work.

The investigation into solution convergence found that although the iterative technique given by equation 5.60 is a rather crude forward difference type equation it adequately enables the solution of the contact model. Other kernels that have not been investigated might prove to be more effective, but in any case solution time using a PC is not prohibitive.

5.4.6 Validation of solid contact model.

To confirm the accuracy of the solid body models a series of case studies were performed in line with procedures given for validating a 2D line contact model [Webster & Sayles (1986)]. Results from the contact models for various profiles of indenters in contact with a flat semi infinite body were compared to classical contact solutions.

The pressure distribution p_r for a smooth sphere of Young's Modulus E in contact with a rigid flat infinite half space can be shown to be of the form [Johnson (1985)]

$$p_r = p_o \sqrt{1 - \left(\frac{r}{a}\right)^2} \qquad 5.70$$

where a is the radius of contact, and the pressure at the origin p_o is related to the normal displacement u_z a distance r from the origin by

$$u_z = \frac{\left(1-\nu^2\right)}{E}\frac{\pi p_o}{4a}\left(2a^2 - r^2\right) \tag{5.71}$$

from which at the origin

$$u_z = \frac{\left(1-\nu^2\right)\pi a p_o}{2E} \tag{5.72}$$

For a conical indenter of angle α in contact with a smooth infinite half space the pressure distribution can be shown to be [Johnson (1985)]

$$p_r = \frac{E^* \cot\alpha}{2}\cosh^{-1}\left(\frac{a}{r}\right) \tag{5.73}$$

where E^* is the combined Modulus of the cone and surface as from equation 5.48.

The pressure distribution for a flat disc of radius a which can be approximated by the solution for a punch is given by [Johnson (1985)]

$$p_r = \frac{p_o}{\sqrt{1-\left(\frac{r}{a}\right)^2}} \tag{5.74}$$

where the normal displacement u_z which is independent of r is given by

$$u_z = \frac{\left(1-\nu^2\right)\pi a p_o}{E} \tag{5.75}$$

The following figures display the pressure distribution comparisons between the authors' axi-symmetric models for a set 2000 iterations and classical contact;

For a flat rubber disc of radius 25mm pressed onto a flat rigid half space, Fig 5.24 shows the predicted pressure distributions which are normalised by p_o, the pressure at $r=0$ from the classical solution, for

a) the solution by equation 5.44 (semi infinite body),
b) the classical solution for a punch given by equation 5.74,
c) for h/a=0.2 (finite disc thickness which is not treated by the classical solution) requiring the inclusion of equation 5.53 in equation 5.44

The pressure distribution of the author's model and the classical solution agree well for semi infinite bodies. When the disc thickness is finite (here 5mm), the effect of the function k is shown to increase the nominal pressure by a near constant factor.

For a spherical rubber device in contact with a flat rigid surface**,** Fig 5.25 shows the predicted pressure distributions which are normalised by p_o, the Hertzian solution pressure at $r=0$, for

a) the solution by equation 5.44,
b) the Hertzian contact solution given by equation 5.70.

The pressure distributions for both cases agree well. Additional iterations reduce the tapering off of the pressure distribution near the maximum contact radius.

For a conical indenter pressed onto a stiffer flat half space whose modulus is fours times greater than that for the cone**,** Fig. 5.26 shows the predicted pressure distributions which are normalised by the classical solution pressure near $r \approx 0$ (since at $r=0$, $p=\infty$), for

a) the solution by equation 5.44 (modulus corrected for by equation 5.48),
b) the classical solution given by equation 5.73.

The pressure distributions for the authors and the classical solutions again show good agreement.

In conclusion, following a similar technique to Webster & Sayles [1986], validation has shown that the authors axi symmetric models agree with comparable classical solutions for contact with smooth flat surfaces. Application of the model for contact with real rough surfaces will be dealt with in section 5.6.2.

5.5 Membrane contact model.

A schematic of a prototype membrane coupled device designed by the author is shown in Fig. 5.27. During assembly, water is pumped into the fixture via a control valve until the membrane bulges out to the desired initial deflection. The membrane shoe fits onto the face of a standard transducer, to provide a hand held device that is pressed onto the concrete surface under test. The problem of solving the membrane rough surface contact mechanics is not so straight forward as for solid contact. Johnson [1985] reports that the complex structure of tyres do not lend themselves well to analytical treatment, relying instead on simple one dimensional models to describe the main features of behaviour. A search found some modelling of tyres and inflatables, most relying on finite element computations. Notwithstanding this, a simple axi symmetric model was pursued that could utilise the iterative solution technique described in chapter 5.4.4. The procedure adopted by the author was to first derive a simplified model to determine the contact radius of a membrane when pressed onto a flat surface. This simplified model will allow the evaluation of the effect of large displacements of a membrane and the effect of the encapsulated constant volume of liquid, which are both expected to be non linear. This model was a combination of the classical solution for small deflections of circular plates that was modified for large deflections and includes a derived function that corrects for the volume of liquid remaining constant. Having addressed the non linearities in isolation a numerical membrane contact model could then be derived for modelling contact with rough surfaces. The stages that combine to form the complete model were:

1) Classical bending solution for a uniformly loaded circular plate with clamped edges with approximation for tension component
2) Function to account for constant volume
3) Membrane model - contact with a flat surface
4) Determining tension approximation from experiments
5) Membrane model - contact with a rough surface

In order to derive a simple physically dependable model some detail had to be excluded. A form of calibration of the model was therefore required to account for this. Experimental results of load as a function of contact radius for contact by various membrane designs with a smooth flat surface were obtained. These results were compared to model predictions to determine simple functions required to calibrate the membrane models.

5.5.1 Large deflections of a uniformly loaded circular plate

Consider first a circular plate of radius *a* shown in Fig 5.28, where deflections are small compared to the thickness of a plate the strain in the middle plain and therefore the tension component can be neglected. The slope of the deflected surface of the plate a distance *r* from the centre, due to a uniform pressure distribution *p* is given as [Timoshenko and S. Woinowsky-Krieger (1959)]

$$\frac{dw}{dr} = \frac{pr^3}{16D} + \frac{C_1 r}{2} + \frac{C_2}{r} \qquad 5.76$$

and integrating gives the deflection *w* at *r* as

$$w = \frac{pr^4}{64D} + \frac{C_1 r^2}{4} + C_2 \ln\frac{r}{a} + C_3 \qquad 5.77$$

where C_1, C_2, & C_3 are constants of integration to be solved by the boundary conditions, *a* is the plate radius and *D* is the flexural rigidity of the plate given as

$$D = \frac{Eh^3}{12\left(1 - v^2\right)} \qquad 5.78$$

where E is Young's Modulus of the material, *h* the thickness and v Poisson's ratio. For the case of a plate clamped at the edges the slope must be zero at *r*=0 and *r*=*a*. Hence simultaneously from equation 5.76, $C_2 = 0$ and thus $C_1 = -\frac{pa^2}{8D}$. It follows that $C_3 = -\frac{pa^4}{64D}$ since the deflection at the clamped edge (radius *a*) is zero. Substituting these values for the constants of integration into equation 5.77 gives

$$w_{(r)} = \frac{p_i}{64D}\left(a^2 - r^2\right)^2 \qquad 5.79$$

and

$$w_{(0)} = \frac{p_i a^4}{64D} \qquad 5.80$$

where $w_{(0)}$ shown in Fig 5.27 is the central displacement at r=0. Substituting equation 5.80 into equation 5.79 gives the profile of the membrane as a function of the radius as

$$w_r = w_0\left(1-\frac{a^2}{r^2}\right)^2 \qquad 5.81$$

For large deflections the stretching on the middle plain due to the tension N should be considered. Bending equations are modified to account for this where one method described by Timoshenko and S. Woinowsky-Krieger [1959] is valid for deflections of the order of one plate thickness. For v=0.3 a corrected version of equation 5.80 for the maximum deflection is given as

$$w_{(0)} = \frac{p_i a^4}{64D}\left(1+0.488\frac{w_{(0)}^2}{h^2}\right)^{-1} \qquad 5.82$$

where it is assumed that deformed profile is still given by equation 5.81. Where $w_0/h >> 1$ a power-series approach has been used [Hencky (1915)]. When modelling large displacements of uniformly loaded circular membranes the membrane deformations are described by a dimensionless displacement W which is given as

$$W(\rho) = q^{1/3}\sum_0^\infty a_{2n}\left(1-\rho^{2n+2}\right) \qquad 5.83$$

where a_{2n} are the coefficients of a power series, $W=w/a$, $\rho=r/a$ and $q=pa/(Eh)$. At the centre of the membrane where ρ=0 and for a Poisson's ratio of v=0.4, the power-series has been solved by the coefficients given by Fichter [1997] with the result that

$$\frac{w_0}{a} = 0.625q^{1/3} \qquad 5.84$$

from which in a form similar to equation 5.82 gives

$$w_{(0)} = \frac{p_i a^4}{64D}\left(0.65\frac{w_{(0)}^2}{h^2}\right)^{-1} \qquad 5.85$$

For a typical membrane coupled device $w_0/h >> 2$ will be the case such that equation 5.85 is preferred to equation 5.82. The Timoshenko assumption that the profile of the deformed surface for large displacements is of the same form as for small displacements will be adopted for this work.

5.5.2 Deriving the constant volume function

A simple function was derived to account for how the internal pressure of the encapsulated liquid varies with deformation of the membrane due to the assumption that the liquid volume remains constant. The function was derived by equating the volumes given by classical bending solutions. For a given initial pressure p_i the membrane in Fig 5.29 deforms to a maximum central displacement w_0 at $r=0$. When the membrane is loaded by a force F onto a flat surface the internal pressure becomes p_d. Within the contact radius d the profile of the membrane is now flat as in Fig 5.30. To obtain a simple function it was assumed that the deformed profile of the membrane in Fig 5.30 is equivalent to the annular membrane in Fig 5.31. Due to the simplification of the problem, the pressure p_f on the deformable part of the annulus is assumed to differ from the actual internal pressure p_d by some function B such that

$$Bp_d = p_f = \frac{F}{\pi d^2} \qquad 5.86$$

The function B was obtained empirically and was expected to comprise a constant to correct for the approximation of the problem by the annular membrane, multiplied by some power of the ratio w_0/h similar to the bending solution correction for the tension component. To solve for the displacements of the annular membrane, the boundary conditions are that, the slope must be zero at $r=d$ and $r=a$ and the deflection is zero at $r=a$. Solving the constants of integration for equation 5.77 gives the deflections outside of the contact area w_f as

$$w_f = \frac{p_f}{B64D}\left[r^4 - 2r^2\left(d^2 + a^2\right) + 4d^2a^2 \ln r + 2a^2\left\{a^2 + d^2\left(1 - 2\ln a\right)\right\}\right] \qquad 5.87$$

Equating the initial and final volumes described by the profiles in equation 5.80 and equation 5.87 gives

$$B\int_{0}^{2\pi}\int_{r=0}^{a} w_i\,dr d\theta = \int_{0}^{2\pi}\int_{r=d}^{a} w_f\,dr d\theta + \pi w_{(d)} d^2 \qquad 5.88$$

where $w_{(d)}$ is the displacement at $r=d$. The solution of equation 5.88 in terms of the internal pressures factorises as

$$p_f = Bp_i \frac{a^6}{\left(a^2 - d^2\right)^3} \qquad 5.89$$

By setting the contact ratio α as

$$\alpha = d / a \qquad 5.90$$

equation 5.89 can be simplified to

$$p_f = p_i B C_v \qquad 5.91$$

where the constant volume function C_v is given as

$$C_v = \left(1 - \alpha^2\right)^{-3} \qquad 5.92$$

5.5.3 Membrane flat surface contact model

For contact with a flat surface, the load F applied to the supports required to flatten a membrane to a radius d as in Fig 5.30 is obtained by substituting the calibration parameter and constant volume effect given by equation 5.91 into equation 5.85 giving

$$F = BC_v \frac{w_{(0)} 64D}{a^4}\left(0.65\frac{w_{(0)}^2}{h^2}\right)\pi d^2 \qquad 5.93$$

For a given load F equation 5.93 will enable the design of a membrane that will give a desired radius of contact d. The function B will be obtained empirically.

5.5.4 Validating membrane flat surface contact model

The experimental set-up used to calibrate the membrane flat surface model is shown in Fig 5.32. A fixture was designed to clamp various rubber discs. Water was pumped into the assembly via a control valve until the membrane bulges out and the desired initial deflection w_0. A load F was applied by adding weights on the back face of the fixture and the radius of contact d the membrane made on the Perspex plate was visually noted. Experimental results for load as a function of contact radius were then compared to predictions from the contact model to determine the calibration parameter B.

A number of different membranes designs were tested so as to validate the model over the range of w_0/h =3.33 to 13. A 50mm diameter 1mm thick silicon rubber disc, E=1.1MPa (obtained by tensile test), was assembled in the fixture such that the initial central displacement w_0 was either 8.5mm, 10mm and 13mm. In the other extreme a 2mm thick natural rubber disc, E=1.5MPa (obtained by tensile test) with an initial central displacement w_0 of 7mm was used. The function B that calibrated equation 5.93 to agree with all the experimental data was

$$B = 2.76\left(\frac{w_0}{h}\right)^{-1.1} \qquad 5.94$$

Two of the experimental results along with the predictions given by the calibrated equation 5.93 are shown in Fig 5.33. The flat surface model can be said to have been validated. It follows that the non linearity of large displacements and the effect of the constant volume of liquid have been accounted for.

5.5.5 Membrane model - rough surface

The approach adopted for numerical modelling of membranes is similar to the previous solid contact models. Fig 5.34 shows a membrane whose profile is initially described by a known function v_r. The application of a rigid body displacement δ forces the membrane onto the rough surface such that the profile becomes a complicated unknown function u_r. For axi symmetry, the upward reaction from the surface at a point of contact can be modelled as the effect of a ring load applied to the membrane. Fig 5.35 shows the exaggerated membrane surface deformations due to the application of a single ring load of radius b and load

intensity q. The solution for the axi symmetric displacements w_r can be modelled by a superposition of such ring loads. To derive the governing equations, firstly consider the circular plate of radius a where the outer edge is clamped as in Fig 5.36. A circular knife edge of radius b applies a load of intensity q, such that the load $P = 2\pi bq$ is uniformly distributed. For small displacements the deflections $w_{(r)}$ for the outer portion of the plate are given by Timoshenko and S. Woinowsky-Krieger [1959] as

$$w_{(r)} = \frac{P}{8D\pi}\left[\left(a^2 - r^2\right)\frac{a^2 + b^2}{2a^2} + \left(b^2 + r^2\right)\ln\frac{r}{a}\right] \qquad 5.95$$

and for the inner portion,

$$w_{(r)} = \frac{P}{8D\pi}\left[\left(b^2 + r^2\right)\ln\frac{b}{a} + \frac{\left(a^2 + r^2\right)\left(a^2 - b^2\right)}{2a^2}\right] \qquad 5.96$$

where D is the flexural rigidity. For large displacements the tension component N as given in equation 5.85 can be included in equations 5.95 and 5.96 by substituting the flexural rigidity D for D_N given as

$$D_N = 0.65\left(\frac{w_0}{h}\right)^2 D \qquad 5.97$$

When the knife edge ring load is applied to the clamped plate in addition to global deformations due to bending and tension there will be some local deformation within the vicinity of the applied load. Libai and Simmonds [1998] provide the idea that the "correct" displacements can be obtained by including the Boussinesq solution for the deformations on a semi infinite body. The application of a ring load on to a clamped edge rubber disc would then result in the axi symmetric deflections $w_{(r)}$ given by a superposition of the bending solutions as in Fig 5.36 and solid body solutions as in Fig 5.37, which would result in the dimpled profile as in Fig 5.38. We can get some idea of what the relative magnitude of these dimples will be by approximating the solid body displacements by those that would arise when a rigid flat punch is pressed onto soft surface. When the membrane is in contact with a flat surface the radius of contact is d. Within the contact area the nature of contact is assumed to be similar to that of a flat semi infinite punch of radius d. For a contact pressure p the surface displacements w_p of the punch which are constant over the radius r=0 to d are given as

$$w_p = \frac{\left(1-\nu^2\right)\pi dp}{E} \qquad 5.98$$

Substituting equation 5.78 into equation 5.98 gives

$$w_p = \frac{h^3 \pi dp}{12D} \qquad 5.99$$

For a membrane of radius a loaded by a uniform pressure p, the central displacement w_o (Fig 5.29), is obtained from equation 5.95 calibrated by the function B given as

$$w_0 = \frac{a^4 p}{64BD_N} \qquad 5.100$$

The ratio between the displacement for the punch given by equation 5.99 over that for the membrane given by equation 5.100 gives the relative displacement as

$$m_d = \frac{w_p}{w_0} = \frac{16}{3}\frac{\pi h^3 BD_N}{a^3 D}\frac{d}{a} \qquad 5.101$$

where $d/a=\alpha$ is the contact ratio from equation 5.90. Typical dimple magnitudes m_d for $\alpha=0.5$ for the membranes considered are:

Silicon rubber 25mm radius w_o=10mm and h=1mm 1.5%

Natural rubber 25mm radius w_o=7mm and h=2.1mm 5.3%

Since the magnitude of the solid body deformations compared to the bending deformations given by the approximation are shown to be relatively small then we need not be concerned about their effect on equations of equilibrium.

Thus the solution for the membrane deformations $w_{(r)}$ due to an axi symmetric load distribution $q_{(b)}$ will be the superposition of the bending equations 5.95 or 5.96 (modified to account for tension by equation 5.97 and including the calibration term B from the flat surface model given by equation 5.113) with the solid body equation 5.43. The square root of the constant volume function C_v given by equation 5.92 is applied to the superposition (and is to also be included in the iterative technique described in section 5.5.6) which was found the most suitable way of including it. Integrating the superposition of bending and

solid body equations over the membrane radius a gives the rough surface membrane contact model for $r > b$ as

$$w_{(r)} = \left\{ \frac{A}{4BD_N} \sum_{n=0}^{N} q_{(b)} \left[\left(a^2 - r^2\right) \frac{a^2 + b^2}{2a^2} + \left(b^2 + r^2\right) \ln \frac{r}{a} \right] + \right.$$

$$\left. \frac{2(1-v^2)}{\pi E} d\theta \sum_{m=0}^{M} \sum_{n=0}^{N} \frac{q_{(b)} b}{\sqrt{\left[b - r\cos(md\theta)\right]^2 + \left[r\sin(md\theta)\right]^2}} \beta \right\} \frac{1}{\sqrt{C_v}} \qquad 5.102$$

and for $r < b$

$$w_{(r)} = \left\{ \frac{A}{4BD_N} \sum_{n=0}^{N} q_{(b)} \left[\left(b^2 + r^2\right) \ln \frac{b}{a} + \frac{\left(a^2 + r^2\right)\left(a^2 - b^2\right)}{2a^2} \right] + \right.$$

$$\left. \frac{2(1-v^2)}{\pi E} d\theta \sum_{m=0}^{M} \sum_{n=0}^{N} \frac{q_{(b)} b}{\sqrt{\left[b - r\cos(md\theta)\right]^2 + \left[r\sin(md\theta)\right]^2}} \beta \right\} \frac{1}{\sqrt{C_v}} \qquad 5.103$$

When discretised into N and M elements this gives

$$d\theta = \frac{\pi}{M} \qquad 5.104$$

$$b = \frac{a}{N}\left(n + \frac{1}{2}\right) \qquad 5.105$$

and

$$dr = \frac{a}{N} \qquad 5.106$$

The parameter A is a function required to calibrate the model and is to be determined by comparison to results given by the flat surface model. Equations 5.102 and 5.103 can be shown in simplified form as

$$w_{(r)} = \sum_{b=0}^{b=a} I_{(r,b)} q_{(b)} \qquad 5.107$$

where the matrix $I_{(r,b)}$ is known as the influence coefficients that describe the displacement at r due to a ring load of radius b of unit intensity.

Examples of the form of the influence coefficients $I_{(r,b)}$ for a 7mm radius unit ring load applied to a silicon rubber membrane of 25mm radius w_o=10mm and h=1mm and natural rubber membrane of 25mm radius w_o=7mm and h=2.1mm membrane are shown in Fig. 5.39 and Fig. 5.40 respectively. The individual contribution to the influence coefficients given by the bending and solid body solutions are also shown.

5.5.6 Rough surface membrane model – numerical solution of equations

The solution of a given membrane contact problem proceeds in a similar way to the solid contact model in section 5.4.4. The membrane will be given a rigid body displacement, and the overlap between the displaced membrane and rigid surface will be used in an iterative procedure to solve for the displacements and loads. It is suggested by Johnson [1994] that for tyre modelling the contact width of the deformed profile will relax to about 20% less than the value established for the overlap. Similarly when modelling membranes, it was found that where the central displacement was no more than half the membrane radius (w_o<0.5a) that modelling of membrane contact was limited to a contact radius of about α=0.5. A solution to this problem is to increase the initial profile of the membrane by multiplying it by some fraction of the constant volume function C_v. The most appropriate fraction was found to be $\sqrt{C_v}$ since for this case when the solution converged the resulting contact radius was close to the value obtained by the overlap. Over the range of contact ratios considered (0.35 to 0.70) this effect enabled the rough surface model to be calibrated by a simple function that was independent of the contact radius. Since $\sqrt{C_v}$ will be a factor in the profile of the membrane then it was for this reason that $\sqrt{C_v}$ was used in the influence coefficients equations 5.102 and 5.103 so that the product would be C_v.

As an example of how the solution of the rough surface model proceeds, consider a rough surface to which the membrane is to be in contact with that is described by some function g_r which at some point has a maximum magnitude G. The unloaded membrane of radius a and displacement w_0 as shown in Fig. 5.41 just sits on the rough surface. The profile of the membrane v_r is given by

$$v_{(r)} = w_{(0)} - w_{(0)}\left(1-\frac{r^2}{a^2}\right)^2 + G \qquad 5.108$$

The membrane is then given a rigid body displacement δ such that it bisects the rough surface at a radius $r=d$ as shown in Fig. 5.41. Substituting δ for v_r and r for d in equation 5.108 gives an estimation of the contact ratio α_i as

$$\alpha_i = \frac{d}{a} = \left(1-\sqrt{\frac{w_0-\delta}{w_0}}\right)^{\frac{1}{2}} \qquad 5.109$$

The constant volume function is then accounted for in the initial profile of the membrane. Applying the square root of the constant volume function to equation 5.108, the adjusted profile of the membrane v_r that includes the C_v function is given as

$$v_{(r)} = w_0 - w_{(0)}\left(1-\frac{r^2}{a^2}\right)^2 \sqrt{C_v} + G \qquad 5.110$$

For the example the arbitrary profiles of the membrane v_r and the wavy surface g_r are shown in Fig 5.42. To enable the solution, the membrane is then given the rigid body displacement δ as shown in Fig 5.42 such that the overlap is described by a function w' where

$$w'_{(r)} = g_{(r)} - \left(v_{(r)} - \delta\right) \qquad \left(g_{(r)} \geq v_{(r)} - \delta\right) \qquad 5.111$$

or

$$w'_{(r)} = 0 \qquad \left(g_{(r)} \leq v_{(r)} - \delta\right) \qquad 5.112$$

For the example the overlap function w' is shown in Fig 5.43. An initial load distribution of $q_{(b)}$ is then assumed as a seed (a uniformly low value seems best) and a first estimate of the deformations $w_{(r)}$ is obtained by equation 5.107. The function $q_{(b)}$ is then adjusted for the next iteration n+1 by equation 5.60. For the membrane example, after a number of iterations the solution converged to a load distribution $q_{(b)}$ that is shown in Fig. 5.44 along with the displacement function $w_{(r)}$ shown in Fig. 5.45. Adding the displacements $w_{(r)}$ and the rigid body displacement $\left(v_{(r)} - \delta\right)$ together (both shown in Fig. 5.45) provides the deformed final

profile of the membrane $u_{(r)}$ as shown in Fig. 5.46. From Fig. 5.44 the total load is obtained by equation 5.62 and from Fig. 5.46 the contact area is obtained by equation 5.63. Convergence of the solution is monitored by the technique discussed in section 5.4.5.

5.5.7 Calibrating the rough surface membrane model

Calibration of the rough surface model was performed by using it to model contact with a flat smooth surface, solving for load as a function of contact radius and then comparing the results to those obtained using the already verified flat surface membrane contact model. Calibration would be achieved by finding some function to fit the parameter A in equations 5.102 and 5.103. It was expected that any difference by the rough surface model predictions would be due to the technique of estimating the contact ratio α in equation 5.109. Different methods of including the constant volume function were tried. All required some initial guess of what the final contact ratio would be. The technique chosen was the one that had the least undesirable effect and for which a simple function would account for any deviation from flat surface model results.

The calibration function A was determined by initially setting it to unity and plotting the ratio of the load predicted by the rough surface model over that predicted by the flat surface model required to deform a membrane to a contact ratio α. A number of cases were investigated in order to establish the calibration of the model over a range of membrane sizes, flexibility and degree of contact.

Examples of the ratios of the load predicted by the rough surface model over predictions by the flat surface model are shown in Fig. 5.47. The results shown are for a silicon rubber 1mm thick w_0=10mm and a natural rubber 2.1mm thick w_0=7mm membrane for contact ratios in the range α=0.35 to 0.75. Over the α=0.35 to 0.70 contact range the difference between the rough surface and flat surface model solutions is fairly constant. Above the contact ratio of 0.7 the difference starts to climb rapidly. This is due to there being greater significance in the difference between the converged result and initial estimation of the contact ratio. As such the constant volume function becomes dominant at higher contact ratios. It is not intended to use the model at contact ratios above 0.7 such that over the range of interest the approximate constant difference between the two solutions allows a function to be found that is independent of contact radius. It was found that the difference between the two solutions for a range of membranes could be adequately approximated by function

$$A = 2\left(\frac{a^2}{w_0 h}\right)^{0.22} \qquad 5.113$$

Fig. 5.48 shows the ratios of the load predicted by the calibrated rough surface model (where equation 5.113 is applied to equations 5.102 and 5.103) over that given by the flat surface model for the two membranes considered. Good agreement between the predictions by either model can be seen.

In conclusion, the rough surface membrane contact model has been validated for contact with smooth flat surfaces. Development of such a contact model would be a very difficult problem unless approached by the kind of simplified derivation adopted by the author. Leaving some of the details out allowed most of the physical behaviour to be described. The necessary calibration was achieved by comparing model predictions to those from the flat surface model which had been validated against experimental results. A desirable simple calibration function which was independent of contact radius was obtained.

5.6 Feasibility of dry rubber coupling transducers when testing concrete

An experimental study was conducted to examine the feasibility of dry coupling to a concrete surface using a hand held rubber disc or membrane coupled device. Tests were carried out by coupling transducers to the rough concrete surfaces described in chapter 5.3.2. The performance of dry coupling was given by the transmission ratio which was expressed by comparing the transmission through a rubber interface to that for grease coupling. Model predictions were compared to experimental results.

5.6.1 Obtaining experimental data

The experimental set-up for rubber disc coupling was as shown in Fig. 5.49. A 150mm by 150mm square by 300mm long 8mm aggregate concrete block with both smooth floated and steel shuttered surface finishes was obtained. The transducers used were of 32mm diameter with a 250kHz centre frequency. To avoid superposition of the received signal by reflections off boundaries broad band signals are desirable which was achieved by exciting these transducers well off centre frequency at 150kHz with a 5 cycle tone burst. The receiving transducer was always bonded to the lower surface of the concrete block. Initially the

transmitter was grease coupled to the upper rough surface. The maximum amplitude of the received signal for grease coupling was recorded. The upper rough surface was then cleaned with a solvent and allowed to dry. Various rubber discs were then used to solid couple the transducer to the rough surface. Weights were added to the back face of the transducer so as to load the interface. For a given applied load, the maximum amplitude of the received signal for solid coupling was then divided by that for grease coupling to provide the fractional transmission.

For membrane coupling a fixture was designed to hold the same 250kHz immersion transducer as shown in the schematic in Fig 5.50. Silicon or natural rubber discs were clamped in the fixture. The fixture was assembled underwater, and during assembly, the transmitter was pushed down into the fixture and then clamped when the membrane had bulged out to the desired initial deflection. The use of different rubbers, thickness and initial deflections enabled a variety of membrane designs to be tested. The procedure for obtaining the experimental data was the same as for rubber disc coupling.

5.6.2 Comparing model predictions to experimental data

Experimental results are plotted for fractional transmission as a function of applied load and compared to model predictions to assess the feasibility of rubber disc coupling. For experimental results the transmission ratio is taken as the maximum amplitude of the received signal for solid coupling over that for grease coupling. Model predictions took the predicted fractional transmission (see section 5.3.5) to equal the ratio of the predicted true area of contact over the area of the transducer face. Model predictions are obtained by giving the rubber device a rigid body displacement, running the program until the solution converges and obtaining load and contact area parameters. The device is then given a larger rigid body displacement and the program is rerun from the beginning. It is preferable to solve over a desired load range, since predictions for load were shown to converge much faster than contact area. By running the program for sufficient iterations the range of rigid body displacements required to provide predictions over a desired range of loads can be obtained.

The experimental results shown in Fig. 5.51 are for various thicknesses of silicon and natural rubber discs in contact with the steel shuttered concrete surface. It is evident that the results display linearity between signal transmission and applied load. There is little difference between the performance of the rubber discs. In general it appears that softer, thicker rubber

discs couple marginally better than thinner, stiffer discs. This is what would be expected since for a given load a stiffer material would conform less to a surface. Additionally for rubber backed by a rigid substrate, thinner material behaves as if stiffer, which is explained by the function derived in section 5.4.3 that corrects for a finite thickness of material. For a 2kg load that could be applied by hand, dry coupling of transducers results in about a 36dB loss in signal strength compared to grease coupling. The model predictions shown in Fig. 5.52 agree well with the experimental results which goes some way towards validating the argument given in chapter 5.3.5 that signal transmission is proportional to the true contact area for low load rubber-concrete contact. One reason for any difference between the magnitude of model predictions and experimental results could be attributed to the approximation of the rough surface by a discretised set of data. Here, predicted transmission is generally greater than for experimental results which suggest that the discretised surface topology is of longer wavelength than the actual surface tested (i.e. the discrete sampling of the surface topology has acted as a low pass filter). Due to the approximation of the surface topology by discrete data, the experimental results are smoother, since for a small change in load there will be a small corresponding change in contact condition due to the greater number of contacts made or lost. Frequency dependence was not considered for model predictions since the experimental investigation described in chapter 5.3 found it to be negligible for this type of contact.

Fig. 5.53 shows the experimentally measured transmission for coupling with various thicknesses of silicon and natural rubber discs to the floated concrete surface. It is clearer here that transmission improves for thicker softer rubber than for the contact results with the shuttered surface. The results suggests that it is reasonable to assume linearity of transmission as a function of applied load up to a fractional transmission of about 0.2. This would agree with the findings of Haines [1980] and is a major part of the transmission being proportional to contact area argument that relies on contact zones being considered to act in isolation. For the 2kg load, dry coupling of transducers results in about an 18dB loss in signal strength compared to grease coupling. The magnitude of the model predictions shown in Fig. 5.54 agree well with the experimental results. As with experimental results, predictions show some evidence that a variation in device rubber type or thickness effects the degree of contact. By comparing the predictions for coupling to the shuttered surface to those of the floated surface, the model clearly displays the difference in the degree of transmission that one could expect when coupling either of these surfaces. Thus overall the performance of the solid contact model is very satisfactory.

The experimental results shown in Fig. 5.55 are for various membranes in contact with the shuttered concrete surface. The variable w_o refers to the initial bulge of the membrane and h represents the thickness of the rubber. The dashed line is the 1mm thick silicon rubber disc experimental results taken from Fig. 5.51 to emphasise the advantage in using a membrane. Here for a 2kg load a possible 6dB increase in transmission ratio for a membrane over that for disc coupling can be expected. Comparing the model predictions in Fig. 5.56 with the experimental results reveals good agreement but not to the same extent for solid contact modelling. It is difficult to describe what effect a change in membrane design has on coupling characteristics from these results alone.

To investigate what the effect of varying membrane design parameters, when coupling to the floated surface only silicon rubber membranes were tested, since solid coupling showed that soft rubbers would couple better than hard rubbers. The experimental results shown in Fig. 5.57 are for 2mm thick silicon rubber membranes in contact with the floated concrete surface. The dashed line is the 2mm thick silicon rubber disc experimental results taken from Fig. 5.53 to emphasise the advantage in using a membrane. As with coupling to the shuttered surface, the results again suggest that a 6dB increase in transmission can be expected when coupling with the membrane. This effect is most likely due to the membrane being more compliant than a rubber disc. Comparing the model predictions in Fig. 5.58 with the experimental results reveals good agreement. Both experimental results and model predictions are characterised by a steeper initial rise in fractional transmission for an increase in applied load when compared to rubber disc coupling. For membrane devices the transmission then flattens off with increasing loads where the membrane with the lowest initial deflection w_0 has the lowest and flattest signal transmission for increased loads. This is because the contact radius becomes greater than the radius of the transducer, thus some of the applied load is wasted on making contact outside of the ultrasonic beam. It is thus important to design the membrane such that at around the desired applied load the deformed membrane makes a contact radius of the same order as the transducer radius. Overall the general characteristics of membrane contact have been adequately predicted.

The experimental results shown in Fig. 5.59 are for 1mm thick silicon rubber membranes in contact with the floated concrete surface. Again, the membrane with the lowest initial deflection w_0 has the lowest and flattest signal transmission for increased loads. If levels of transmission were sufficient then this effect could be exploited to achieve consistent coupling. Comparing the results to the ones for the 2mm thick membranes in Fig 5.57, reveals that the stiffer 2mm membranes generally couple better than 1mm membranes. This effect is duplicated in the model predictions shown in Fig 5.60. The effect was not as

expected, since intuitively it was thought that a thinner membrane, such as a balloon, would be the most appropriate design. To try to understand the cause, Fig 5.61 and Fig 5.62 show the predictions for a 0.75mm and 1.5mm thick membrane respectively coupled to a simple surface. The case is rather simplified but it does show that for thinner, more flexible membranes, the membrane will simply touch a greater number of peaks as the load is increased. For the thicker, more rigid membrane, the deformed membrane will make contact with less peaks, but bed down more, resulting in a potentially higher true area of contact for the same applied load. This effect can also be explained by examining the approximation for local deformations given by equation 5.101. In the form of equation 5.101 any increase in flexural rigidity due to an increase in thickness h or ratio w_o/h, or the amount of contact α, increases the magnitude of the dimples which results in the membrane being able to support increasingly greater local deformations.

5.6.2 Discussing dry solid coupling of transducers

The degree of coupling made by a rubber coupled device is more dependent on the surface roughness than on the device design. Fig. 5.63 through to Fig. 5.66 show examples of predicted axi symmetric deformations of solid coupled devices loaded by 2kg onto rough concrete surfaces. Silicon rubber disc coupling onto the steel shuttered surface is shown in Fig 5.63. A zoom of part of the contact area is shown in Fig 5.64, which illustrates the low degree of contact made when coupling to this surface. Coupling to the floated concrete surface by a silicon rubber membrane is shown in Fig. 5.65. A closer look at how the membrane conforms with the rough surface is shown in Fig 5.66.

For dry rubber disc coupling to the shuttered concrete surface with a 2kg applied load, the experimental results and predictions suggest that a 36dB loss in signal strength per transducer can be expected. Thicker, softer rubber discs tend to couple marginally better to a rough surface. Membrane coupling of transducers was shown to improve transmission by about 6dB, where membrane design was more critical than for disc coupling. Softer, thicker, larger w_o (generally more rigid) membranes were shown to couple better, which was not what might have been intuitively expected. Results for the floated surface represent perhaps the smoothest surface that might be encountered, where the loss in signal strength per transducer was about 12dB to 18dB for membrane and rubber disc coupling respectively. When testing concrete, signal strength is at a premium due to the severe attenuation within the concrete. Thus the experimental results and model predictions suggest that it is unlikely

that dry coupling ultrasonic transducers to concrete is feasible except when testing over short path lengths or on smooth surfaces (similar to the floated surface).

Model predictions agreed well with experimental results. Greatest confidence is given to the results provided by the solid contact model. Its derivation was straight forward requiring no empirical functions for its calibration. A versatile function was derived to account for a finite thickness of rubber backed by a rigid substrate which was shown to agree with a dedicated function for contact by rollers. The modelling of membrane deformations was a far more difficult problem to undertake made more complex by the effect of the encapsulated volume of liquid. The iteration technique developed initially for the solid contact model was not so well suited to solving contact for the membrane model. This is due to the much larger ratio of the magnitude of the surface roughness over the overlap function, such that the membrane model required about a 20 to 40 fold greater number of iterations than the solid contact model to converge. Due to the difficulties involved in developing the membrane model it was encouraging that predictions were found to agree so well with experimental results. The agreement of the solid contact model predictions with experimental results goes a long way in validating the argument that for low load rubber concrete contact the signal transmission is proportional to the true area of contact.

For dry coupling of transducers, membrane coupled devices were shown to provide improved signal transmission over rubber disc coupling. Additionally it was found that for a membrane device the signal transmission flattened off more appreciably than when disc coupling at higher loads. It follows that since the transmission is proportional to contact area, a membrane device can conform better to a rough surface and provide more consistent coupling over a range of loads. Thus in conclusion, membrane devices are preferred to discs when dry solid coupling ultrasonic transducers to rough concrete surfaces.

5.7 Wet membrane coupling of transducers

Although the transmission across a dry coupled interface is not sufficiently strong for most practical applications, the use of rubber coupled devices may still be attractive when wetted just with water. This is possible because the void volume at the interface is very much smaller that it would be without the rubber, so very little water is needed and furthermore it does not need to be viscous in order to be retained. Therefore the inconvenience of grease coupling can still be avoided. For dry coupling of transducers, membranes were shown to potentially conform better to a concrete surface and provide a means of more consistent

coupling. Thus for the wet coupling investigation the use of membrane devices only will be considered. The rough surface membrane contact model was used to predict what volume of water would be required to fill the voids left when a membrane couple device is pressed onto a concrete surface. Modelling was only conducted with the timber shuttered, roughest concrete surface since a membrane would have to adequately couple to this surface. From these predictions, a prototype membrane shoe (similar to the schematic in Fig. 5.27) was designed to hold the PUNDIT 54kHz 50mm diameter transducers. Experiments were conducted to assess the relative signal strength and repeatability of wet membrane coupling compared to conventional grease coupling.

5.7.1 Predicting reduction in volume of couplant required

Varying h, the thickness of material, and w_0, the initial deflection, enabled the characteristics of different membrane device designs to be investigated. The thicknesses of silicon rubber considered were 0.75mm, 1.0mm and 1.25mm. For a given thickness, nominal values of w_0 were chosen by solving the flat surface model for the parameter w_0 for the applied load F=2kg and the contact ratio α =0.75. Additional designs were obtained by having membranes with a value of w_0 of ±20% off the norm. The rough surface membrane contact model was used to predict what volume of water would be required as a function of applied load to couple various 50mm diameter membranes to the timber shuttered concrete surface shown in Fig 5.3b (the roughest surface considered feasible to solid couple to without any prior surface preparation). The predicted volume, Vol, of couplant required to adequately couple the deformed membrane to the rough surface was obtained by subtracting the rough surface profile $g_{(r)}$ from the deformed membrane profile $u_{(r)}$ and integrating over the radius r given by

$$Vol = 2\pi \int_0^R (u_r - g_r) r dr \qquad 5.114$$

The maximum volume of water that could be conveniently applied to a membrane was thought to correspond to the amount that would be left on the membrane surface after it had been wiped over with a damp sponge. The mass of water that just coats a 50mm diameter membrane was found experimentally to be approximately 0.05mg which equates to a volume of 50μL. The predicted volume of grease required to conventionally couple a transducer to a rough surface was obtained by first finding the maximum height G of the

digitised surface $g_{(r)}$. The height G was then substituted for $u_{(r)}$ in equation 5.114 and the volume was then predicted by integrating over the radius of the transducer R.

Fig 5.67 through to Fig. 5.69 show the predicted volume of couplant required (or void volume) as a function of applied load. Ideally a design will lead to a void volume of less than 50μL for a load under 2kg and the void volume should reduce slowly for increased loads so as to permit consistent coupling. Additionally the initial deflection should be as large as possible. All the membrane designs show the characteristics of consistent coupling to some extent. The most promising design that satisfies these criteria is the 0.75mm thick membrane with an initial deflection of 7.5mm to 10mm as shown in Fig. 5.67. A comparison between the remaining void volume when the optimum membrane is loaded by 1.5kg and a transducer sitting on the timber shuttered surface is shown in Fig. 5.70. A membrane shoe using the optimum membrane dimensions was designed to hold the PUNDIT 54kHz transducers (similar to the schematic in Fig 5.27) to enable some experiments to be conducted to assess the performance of wet membrane coupling.

5.7.2 Experimental investigation into the performance of wet membrane coupled devices.

A 250mm diameter 300mm long 5mm aggregate concrete block was obtained. The block had been cast in a cylindrical steel mould where the end of the block that was open to the air during hydration had a very rough floated finish. An area of this end was ground flat onto which a standard PUNDIT 54kHz transducer was bonded which would act as the receiver. The other end had been in contact with a rough timber board during hydration and had a very similar appearance to the surface in Fig 5.3b. To this end the transmitting transducer would be either grease or wet membrane coupled. The investigation entailed coupling the transmitting transducer by either technique a total of ten times to the rough surface, and recording the received signal each time. From either set of data the mean signal amplitude was obtained and this was plotted along side the maximum and minimum received signal amplitudes received. Presenting the results this way gave some idea of the consistency of coupling and enabled comparison of the signal transmission between conventional and wet membrane coupling.

Fig 5.71 and Fig. 5.72 show the maximum, mean and minimum received signals for the 10 repeat tests for conventional grease and wet membrane coupling respectively. A horizontal line has been drawn to represent the magnitude of the PUNDIT threshold. Comparing the

mean signal for conventional grease coupling with that for wet membrane coupling reveals that the transmitted signals are generally of the same order of magnitude. Marginally greater transmitted signal amplitudes are obtained using the membrane device. The signal amplitude deviation from the mean is marginally less for the membrane device which suggests that it should allow more consistent coupling. Conventional grease coupling to the concrete surface requires more effort to ensure a minimum amount of grease is used and the couplant is not contaminated by grit. It is also uncertain whether there are any air pockets once the transducer is coupled to the surface. By contrast, with the membrane device since the rubber and film of water are squashed into the voids, too much or contaminated couplant has little effect on the degree of coupling.

Since the PUNDIT apparatus uses a threshold crossing technique to determine signal arrivals, more consistent signal amplitudes will result in more consistent measured signal transit times. Thus this brief investigation has highlighted that wet membrane coupling of ultrasonic transducers can offer a significant improvement over conventional grease coupling when inspecting concrete structures.

5.8 Conclusion

Conventional grease coupling of ultrasonic transducers to a concrete surface is inconvenient, inconsistent and time consuming. An investigation was carried out to research possible alternative methods of coupling the transducers. It was thought that a rubber coupled device might improve the inspection technique.

Three concrete surfaces were considered that were thought to represent the range of surfaces that a transducer might be coupled to without the need for prior surface preparation. The topology of the sample concrete surfaces was digitised so as to describe them by height and wavelength parameters.

Experiments were then carried out on these surfaces to investigate the characteristics of signal transmission through a rubber rough surface interface. Experimentally it was found that the signal transmission was a weak function of frequency and that the transmission was proportional to the applied load. It was thus argued that the signal transmission was proportional to the true area of contact for a low load rubber-rough surface interface.

Models were derived to predict the surface deformations of solid coupled devices when pressed onto a rigid rough surface and hence estimate signal transmission through the interface. Considerable saving in computation time and simplification of derivations was achieved by considering the devices and hence the surface roughness to be axi symmetric in profile. A simple to program, iterative solution technique was derived to solve such contact problems. Solid contact model predictions agreed well with comparable classic solutions for contact of profiled bodies with flat surfaces. The membrane contact model was validated against experimental results.

Predictions and experimental results for signal transmission across a rubber-concrete interface found that a membrane device can offer a 6dB increase in transmission over disc coupling. For coupling to a concrete surface that had been in contact with steel shuttering during hydration a 30dB loss in signal strength per transducer could be expected. Since concrete surfaces are often rougher than this and signal strength is at a premium when testing concrete it is unlikely that dry rubber coupling of transducers would prove feasible, except when testing short path lengths or smooth concrete surfaces (such as the floated surface on which some tests were conducted).

Although the dry rubber coupling of transducers proves not to be practical, the membrane devices may appear to be attractive when wetted just with water, which avoids the inconvenience of grease coupling. Coupling with a thin film of water was shown to be possible because the void volume at the interface is very much smaller that it would be without the rubber. Unlike dry coupling, the signal transmission for a wetted membrane device was shown to be of similar magnitude to a grease coupled transducer. Additionally repetitive tests found that the membrane technique resulted in more consistent coupling. The chapter that follows this one investigates further the performance of wet membrane coupling of transducers which has shown potential to improve the ultrasonic inspection of concrete structures.

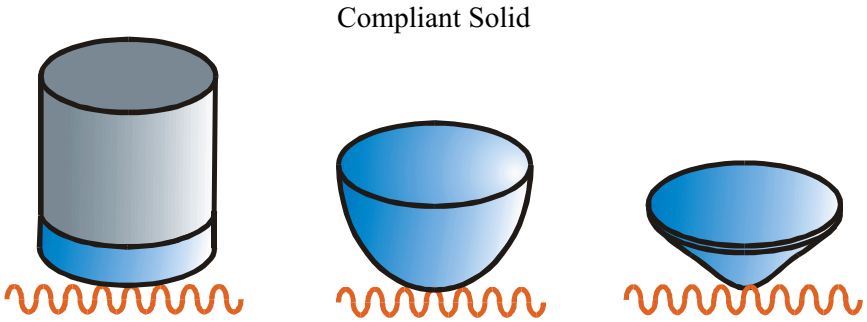

Figure 5.1. Various compliant designs for the solid coupling of ultrasonic transducers.

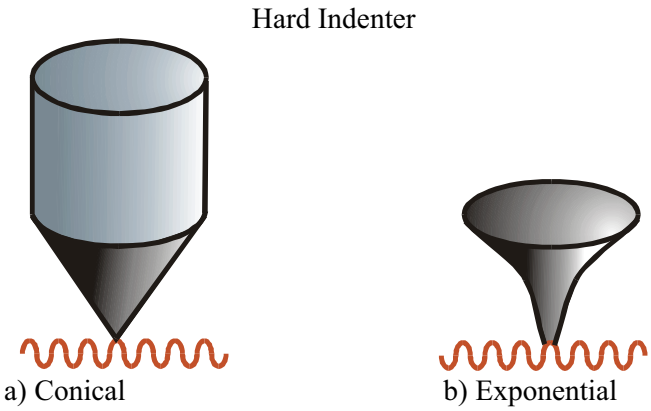

Figure 5.2. Indenter designs for the solid coupling of ultrasonic transducers.

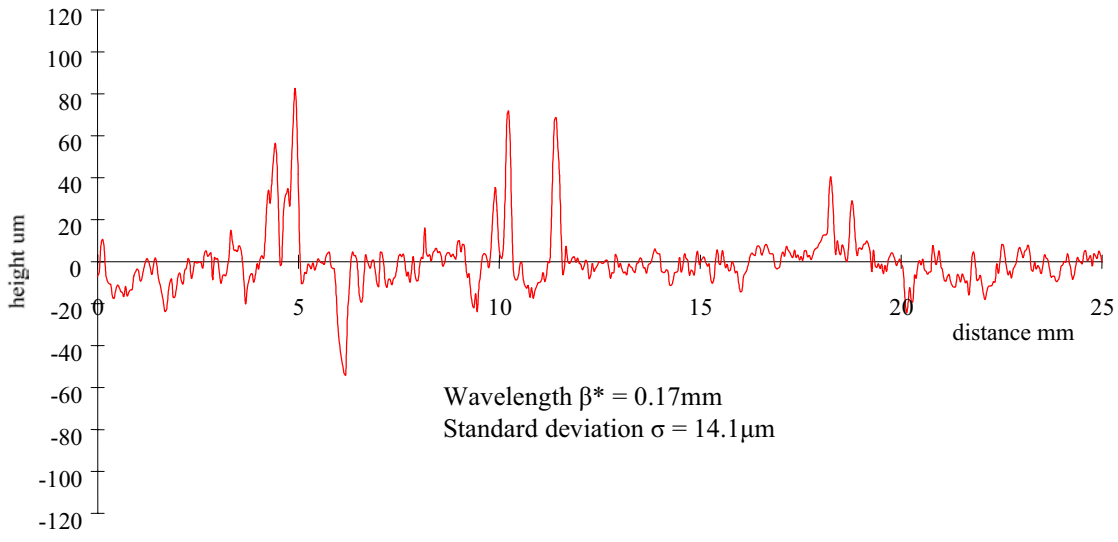

Figure 5.3a. Topography of sample concrete surface which had been in contact with metal shuttering during hydration.

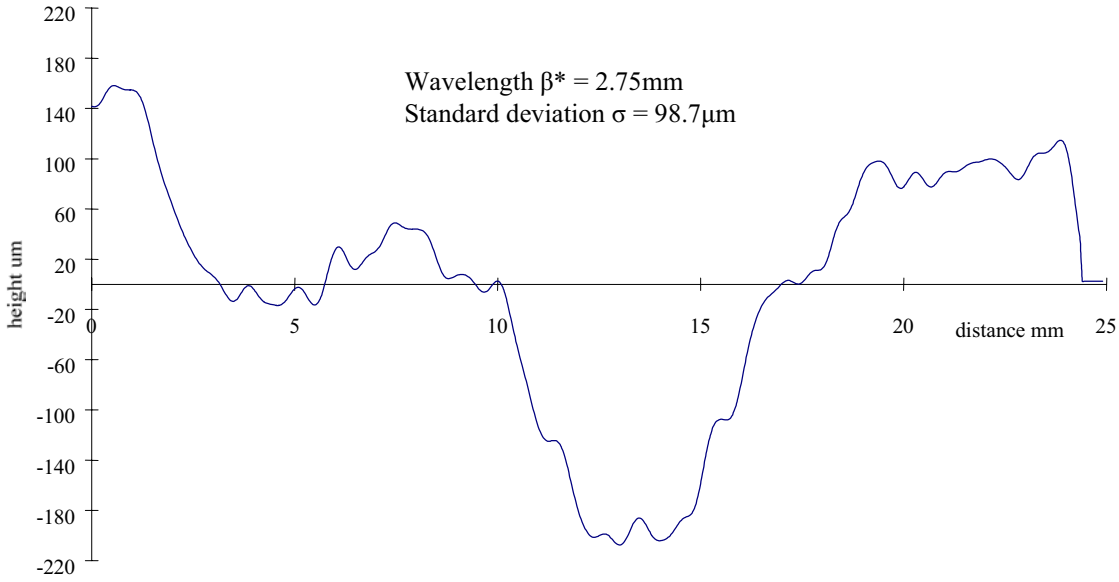

Figure 5.3b. Topography of sample concrete surface which had been in contact with timber shuttering during hydration.

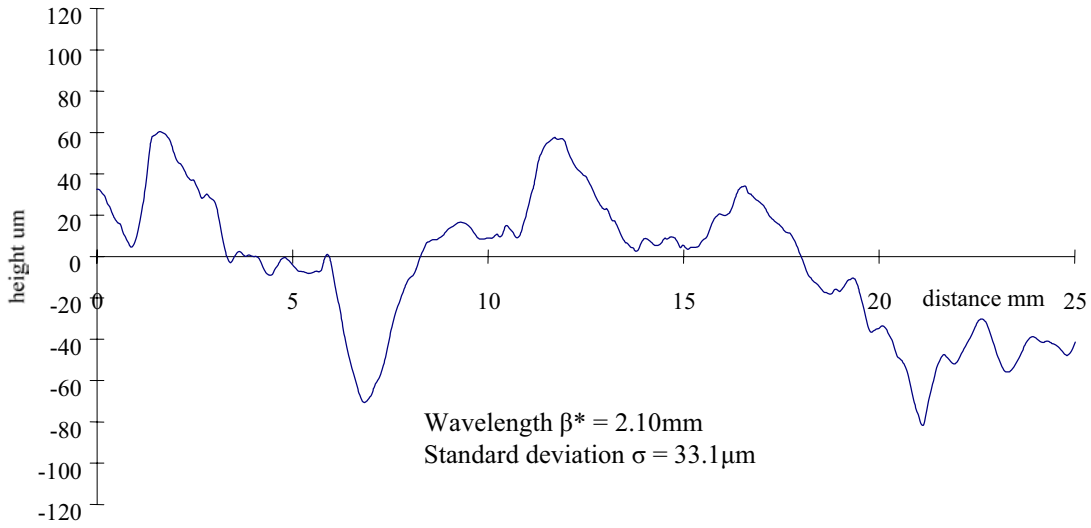

Figure 5.3c. Topography of sample concrete surface which had been floated prior to hydration.

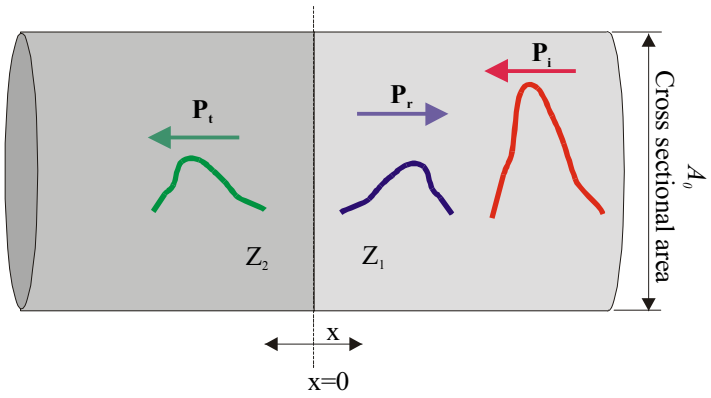

Figure 5.4a. Ultrasonic transmission across a perfect interface.

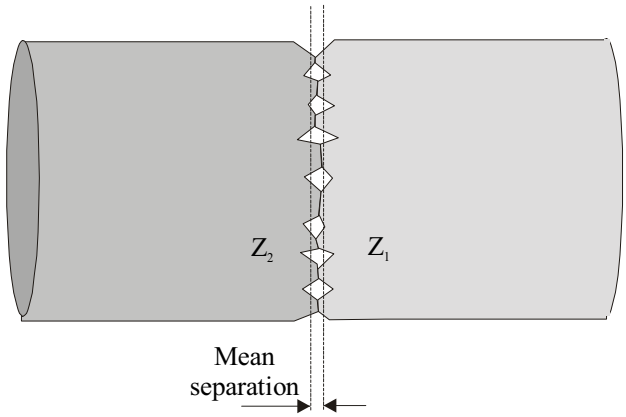

Figure 5.4b. Contact of an imperfect interface.

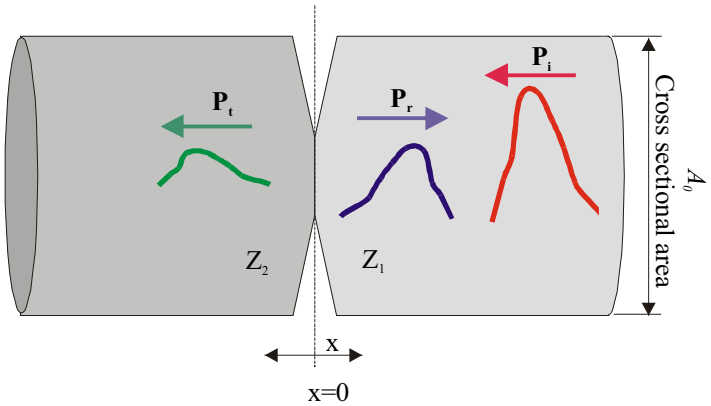

Figure 5.4c. Ultrasonic transmission across an imperfect interface approximated as a constriction.

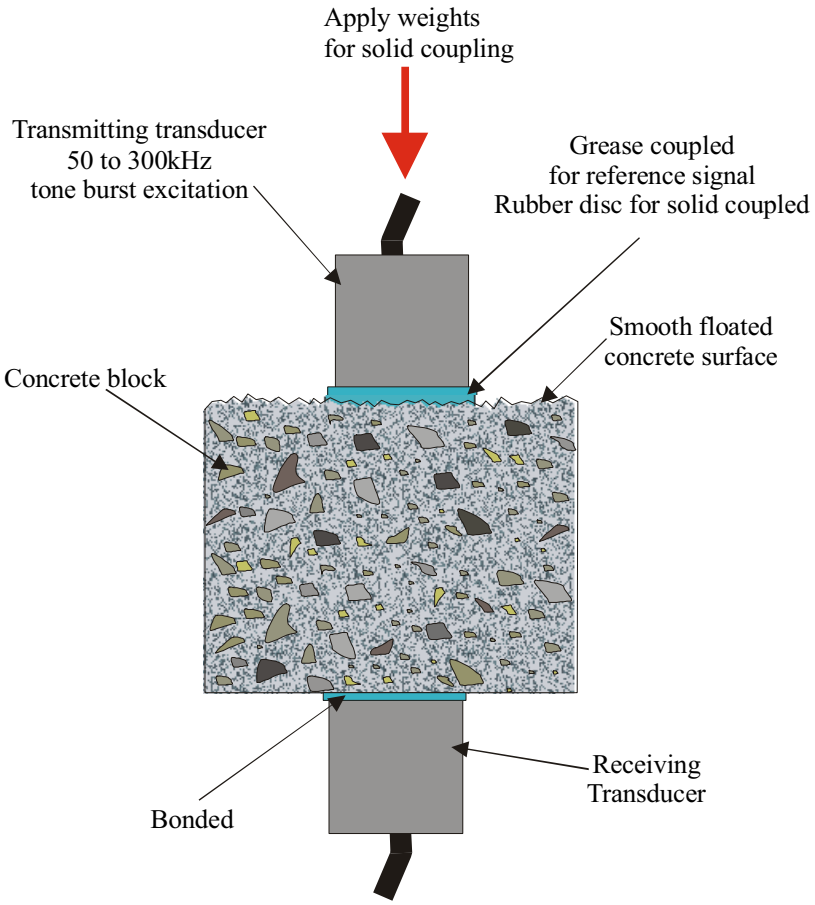

Figure 5.5. Experimental set up to investigate the characteristics of ultrasonic transmission across a rubber concrete interface.

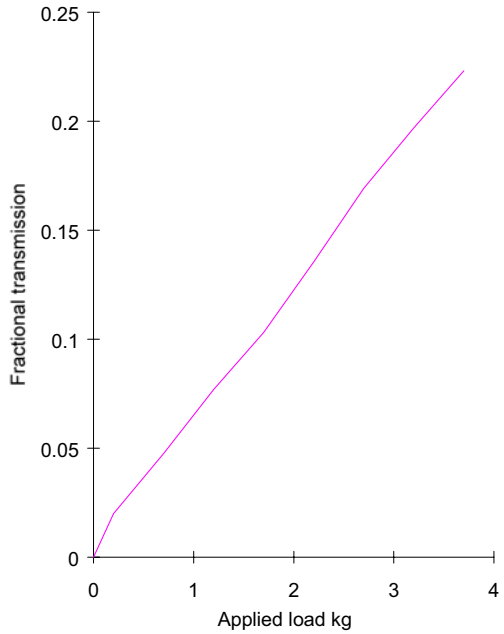

Figure 5.6a. Fractional transmission as a function of applied load, for 2mm thick silicon rubber floated concrete surface interface.

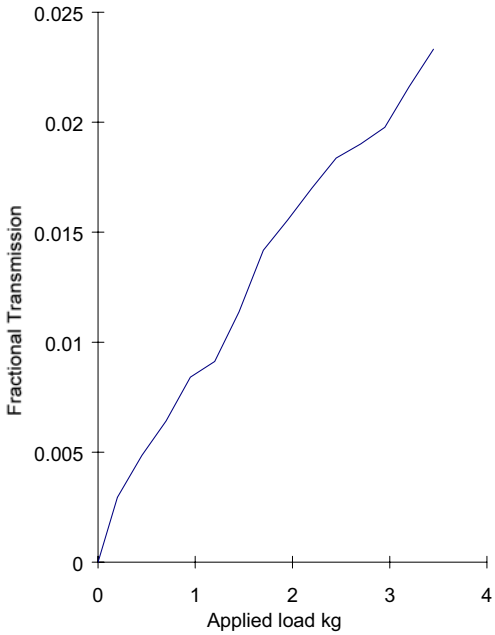

Figure 5.6b. Fractional transmission as a function of applied load, for 2mm thick silicon rubber medium sandpaper interface.

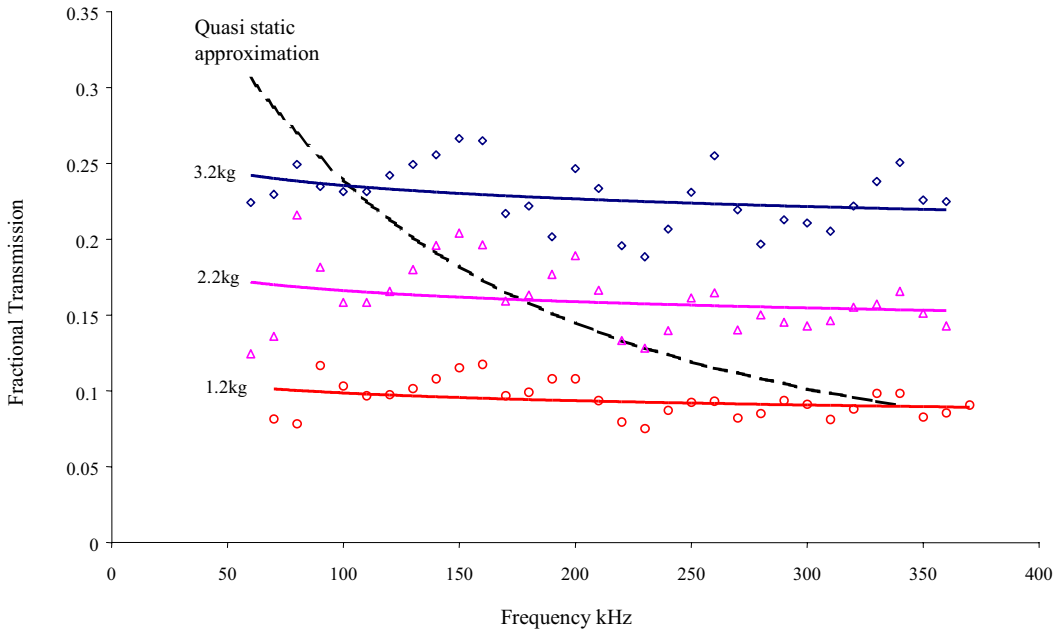

Figure 5.7a. Measured fractional transmission as a function of frequency for a 1mm thick silicon rubber disc floated concrete surface interface at 3.2kg (◊), 2.2kg (Δ), 1.2kg (o) applied loads. Best-fit curves (solid lines) and quasi-static prediction (dashed line) for comparison.

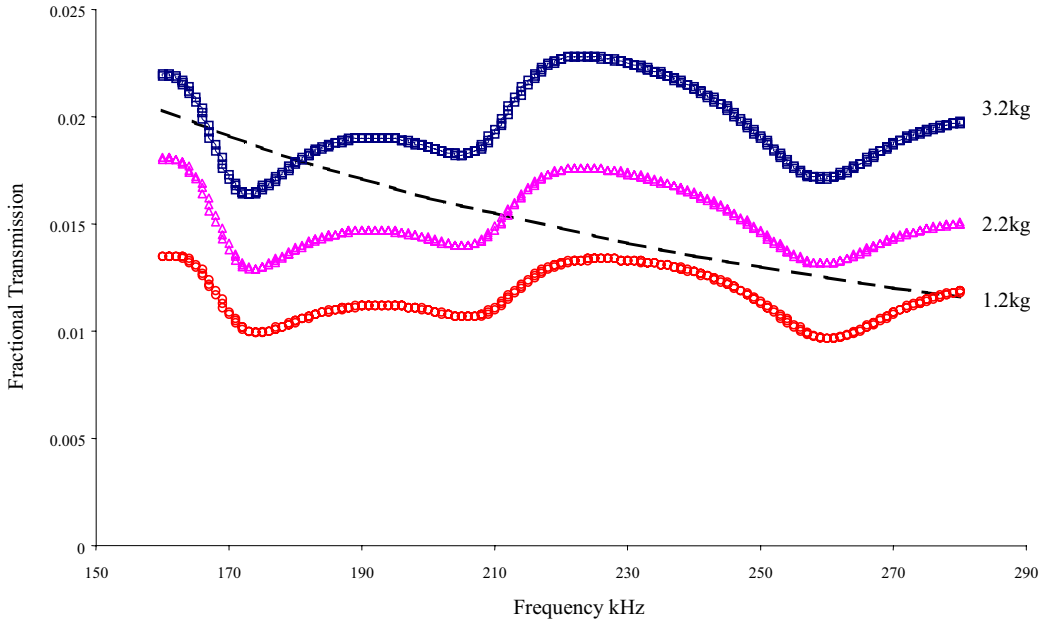

Figure 5.7b. Measured fractional transmission as a function of frequency for a 1mm thick silicon rubber disc-sandpaper interface at 3.2kg (◊), 2.2kg (Δ), 1.2kg (o) applied loads. Quasi-static prediction (dashed line) for comparison.

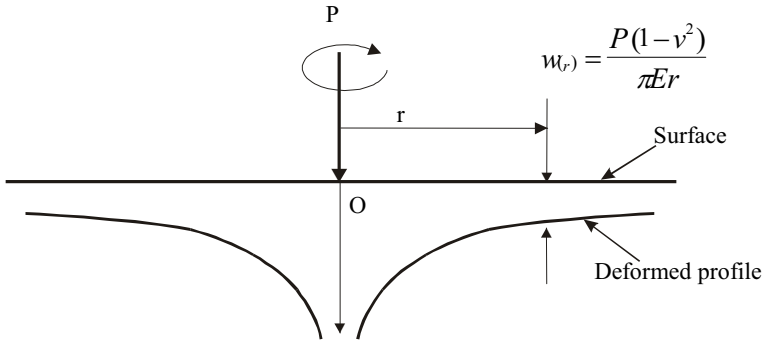

Figure 5.8. Surface displacement $w_{(r)}$ due to the application of a point force.

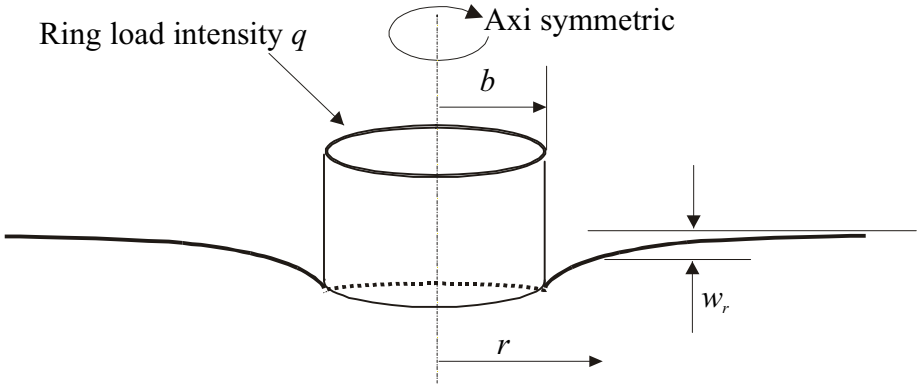

Figure 5.9. Surface displacement $w_{(r)}$ due to the application of a ring load.

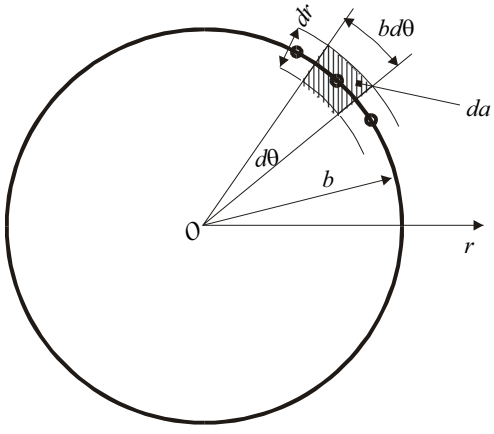

Figure 5.10. Ring load approximated by superposition of point forces.

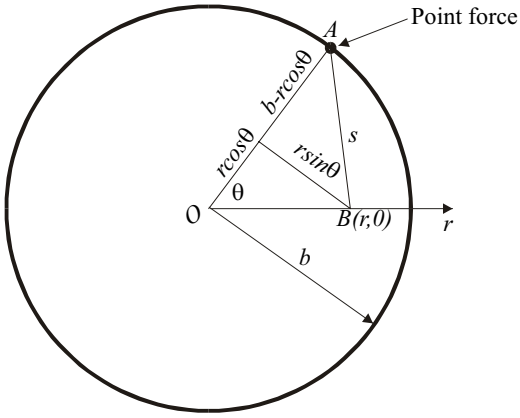

Figure 5.11. General point B a distance s from a point force at A.

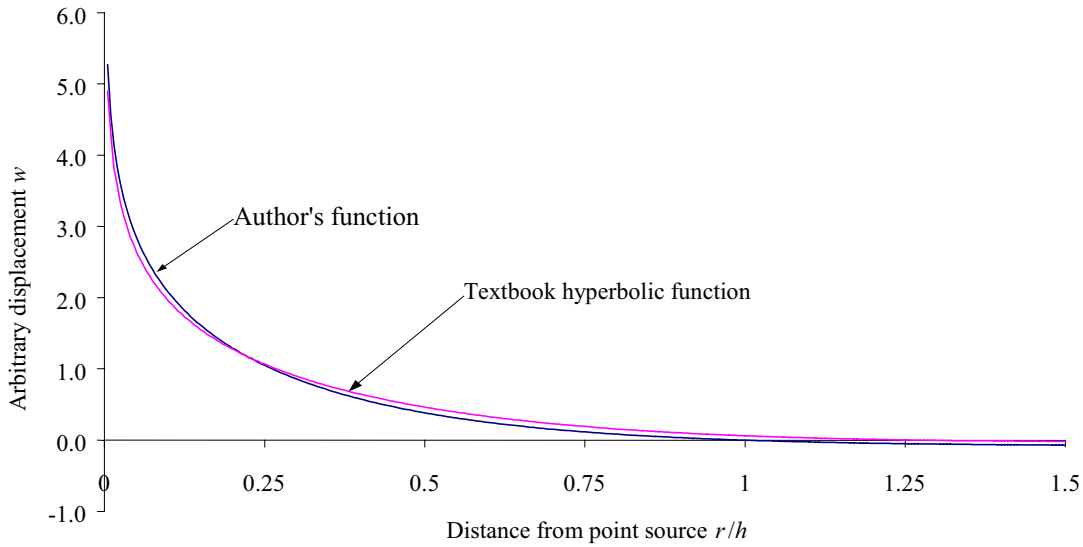

Figure 5.12. Arbitrary surface deformation for a point force applied to a finite thickness of material. Comparison between author's and textbook function.

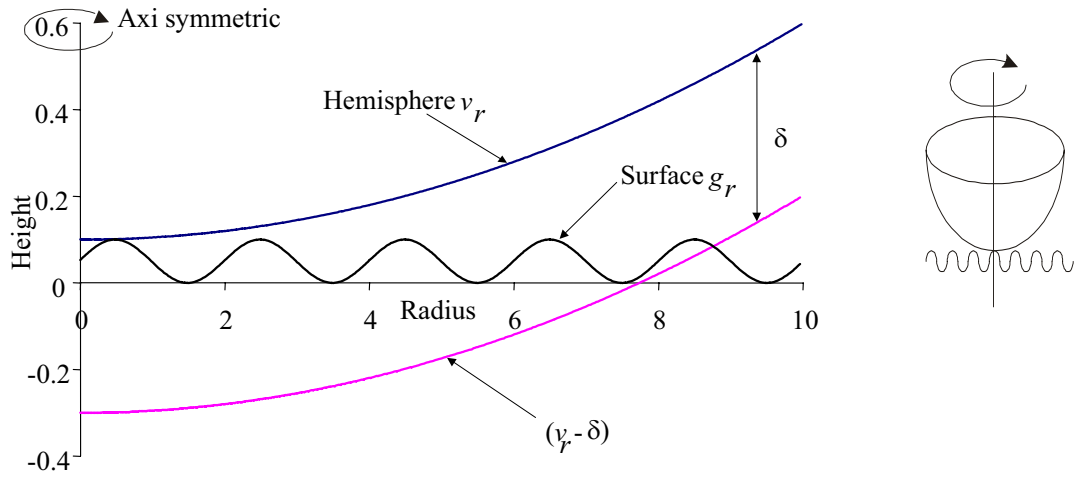

Figure 5.13. Hemisphere in contact with wavy surface.

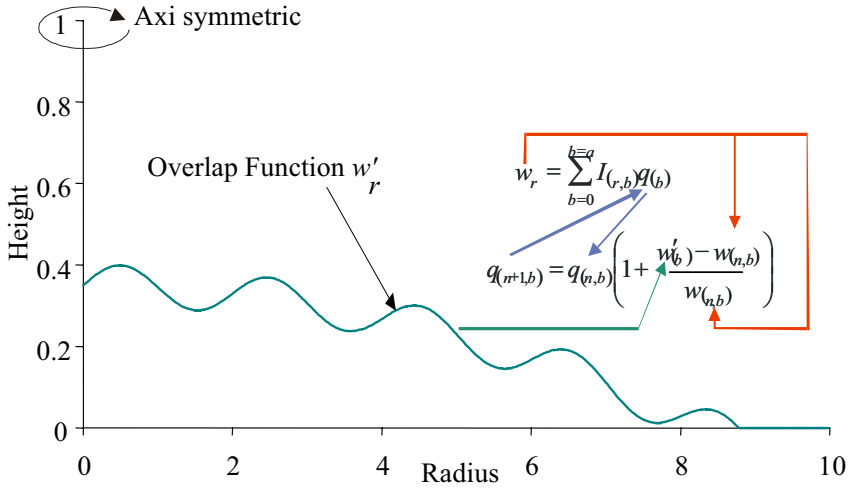

Figure 5.14. Solution iteration with overlap function.

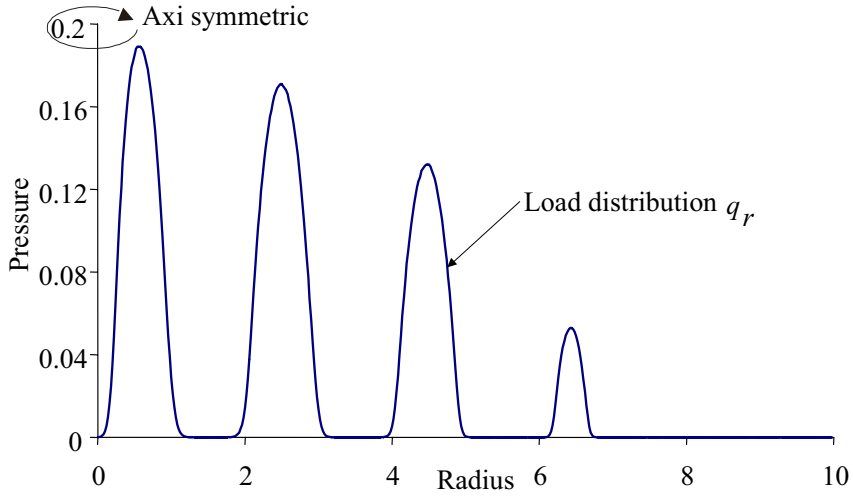

Figure 5.15. Converged contact load distribution for hemisphere example.

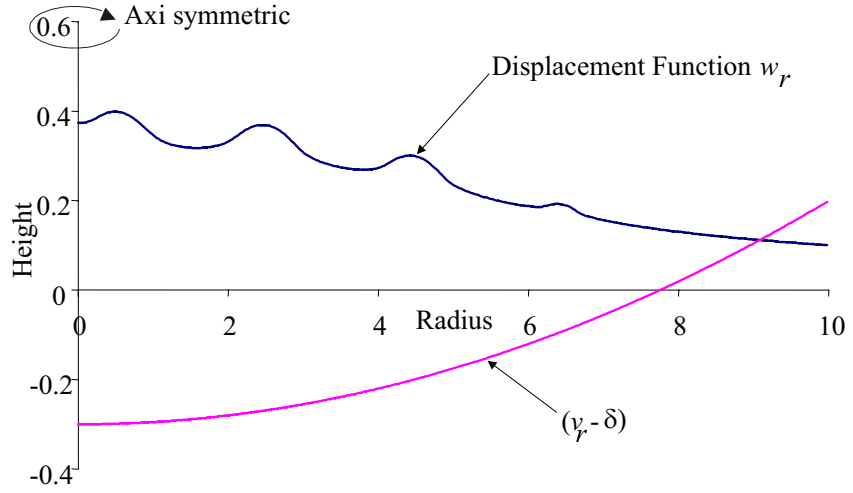

Figure 5.16. Converged displacement function along with rigid body displacement.

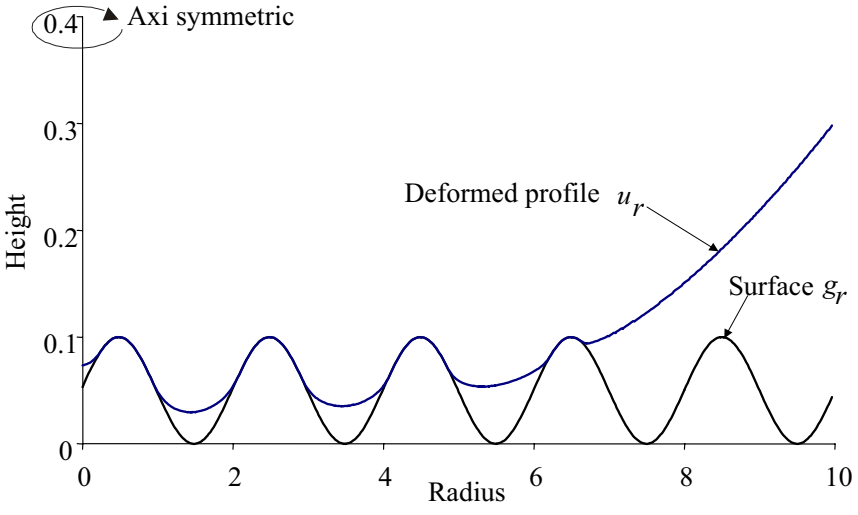

Figure 5.17. Converged contact solution for hemisphere example.

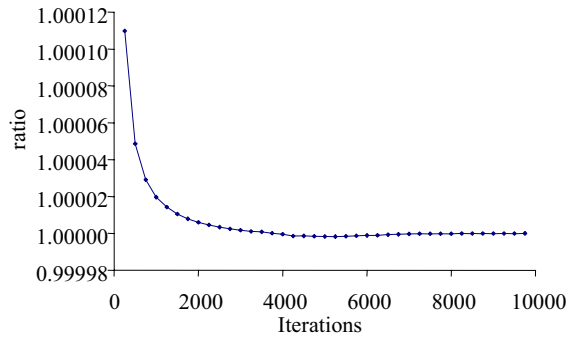

Figure 5.18. Solution convergence for load (normalised by value after 10000 iterations).

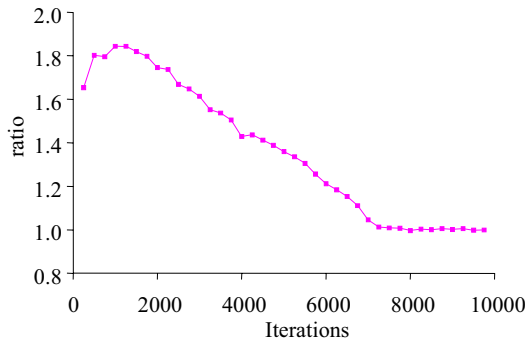

Figure 5.19. Solution convergence for area (normalised by value after 10000 iterations).

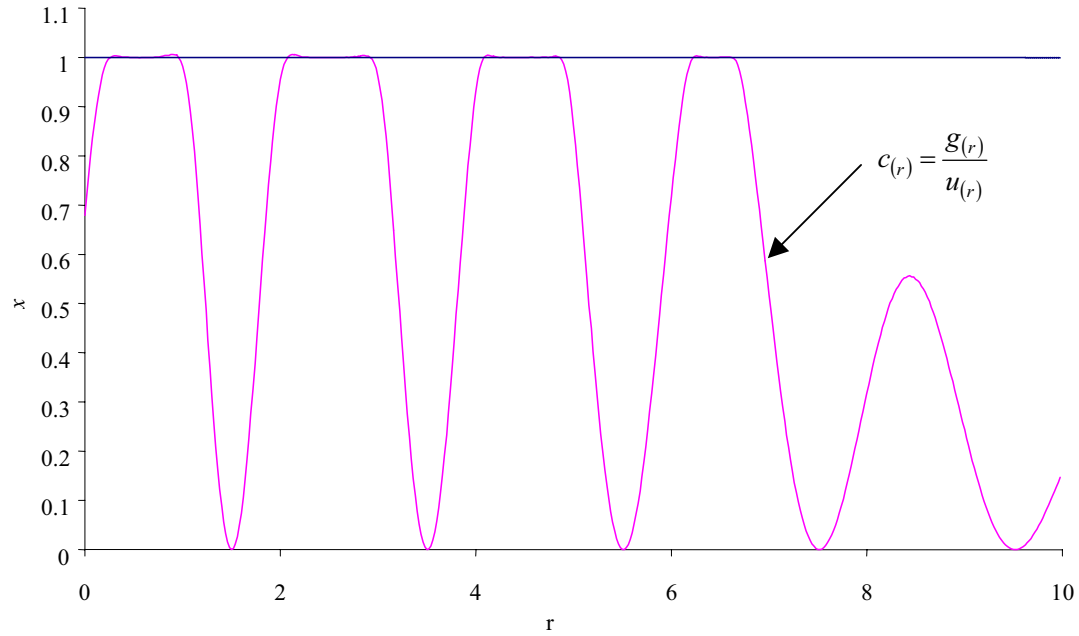

Figure 5.20. Overlap function $c(r)$ for hemisphere example after 1000 iterations, given by ratio of deformed surface of hemisphere $g(r)$ over wavy surface $u(r)$.

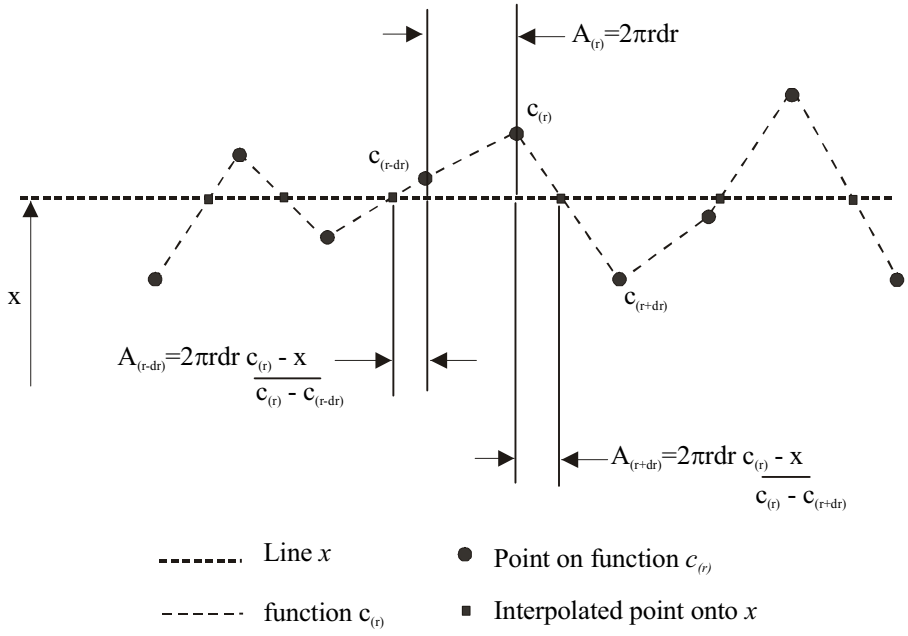

Figure 5.21. Determine the predicted contact area CA as a function of x.

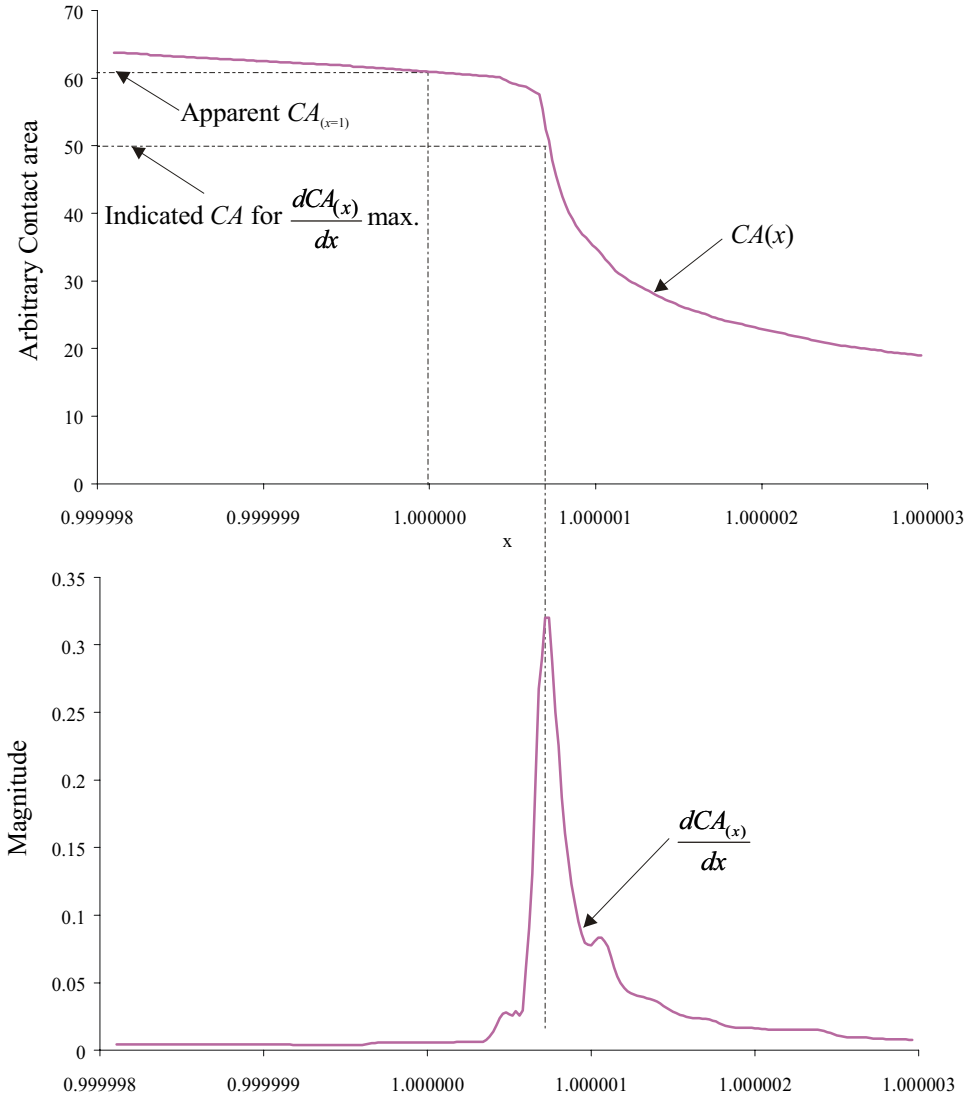

Figure 5.22. Monitoring solution convergence after 1000 iterations. Top, contact area $CA(x)$. Bottom, differential $dCA(x)/dx$.

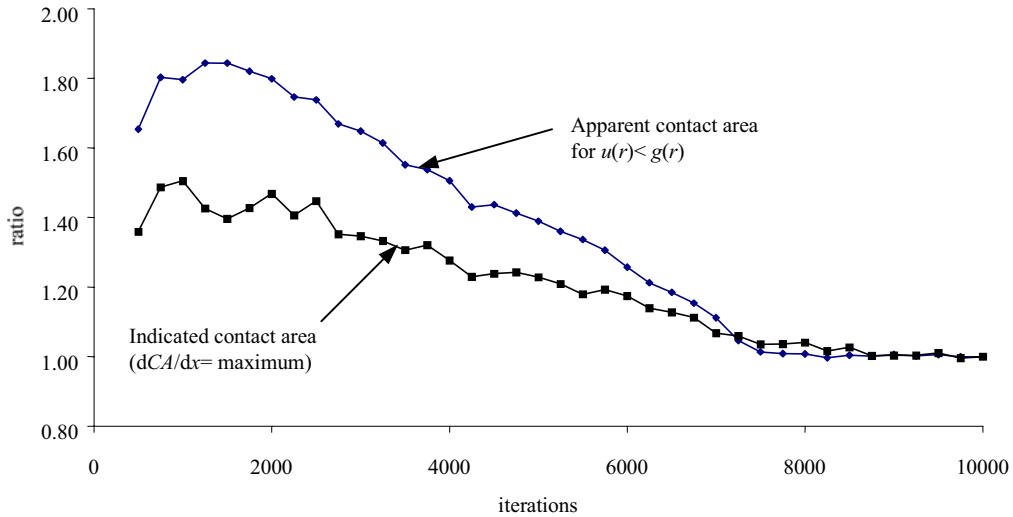

Figure 5.23. Monitoring solution convergence, comparison between apparent contact area for $u(r) < g(r)$ and indicated contact area for maximum dCA/dx.

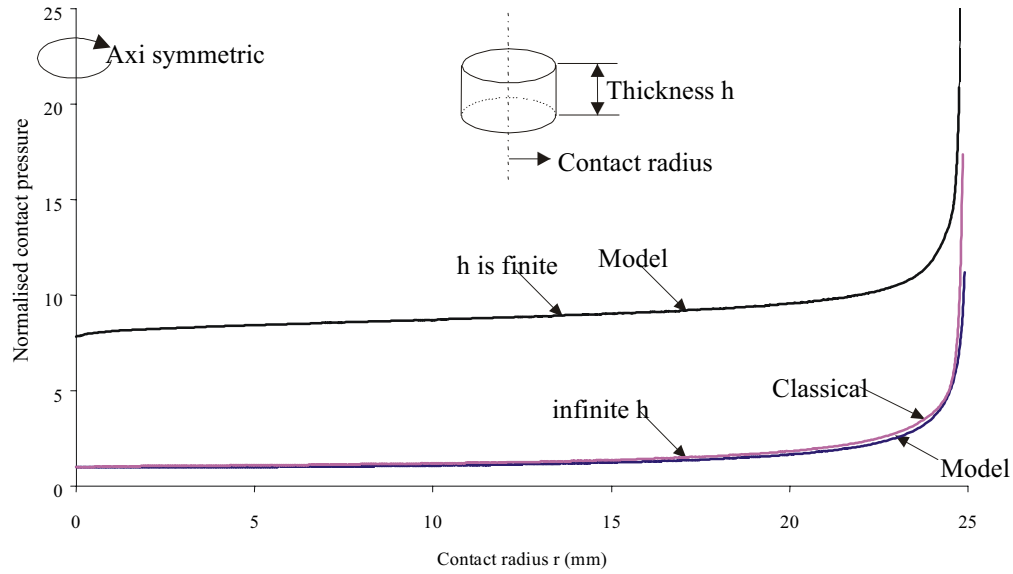

Figure 5.24. Comparison between model predictions and classical solution for a punch.

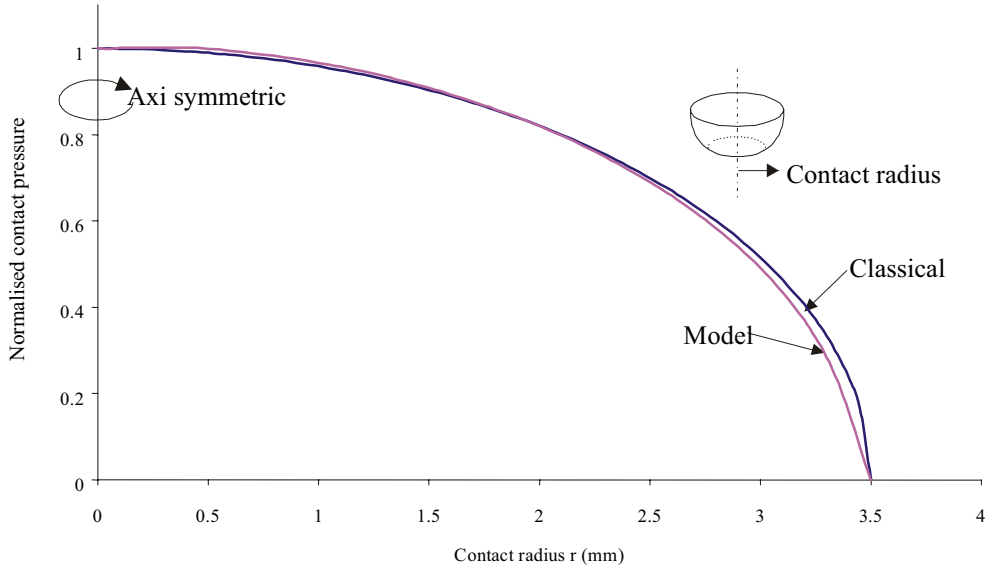

Figure 5.25. Comparison between model prediction and classical solution for a hemisphere.

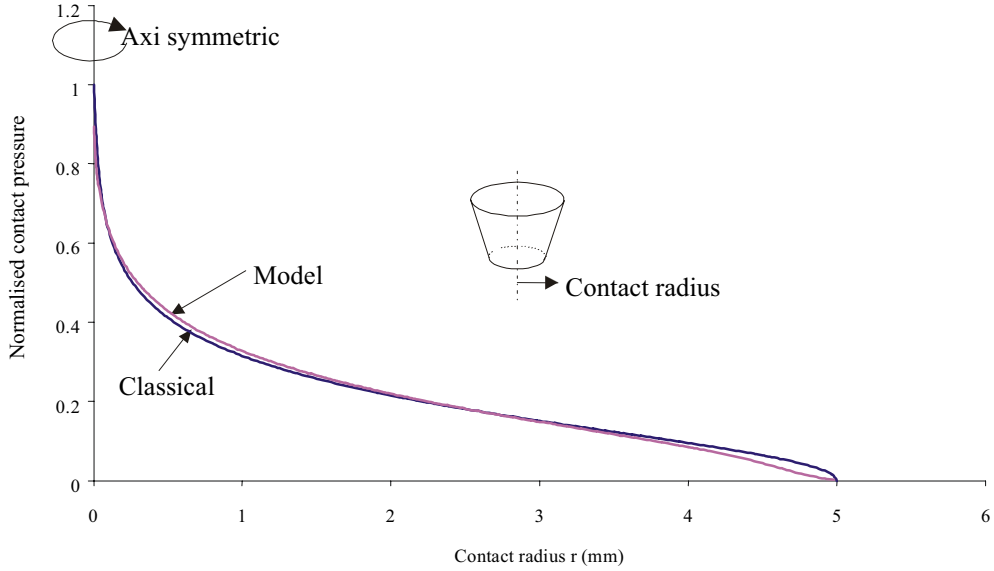

Figure 5.26. Comparison between model prediction and classical solution for a cone.

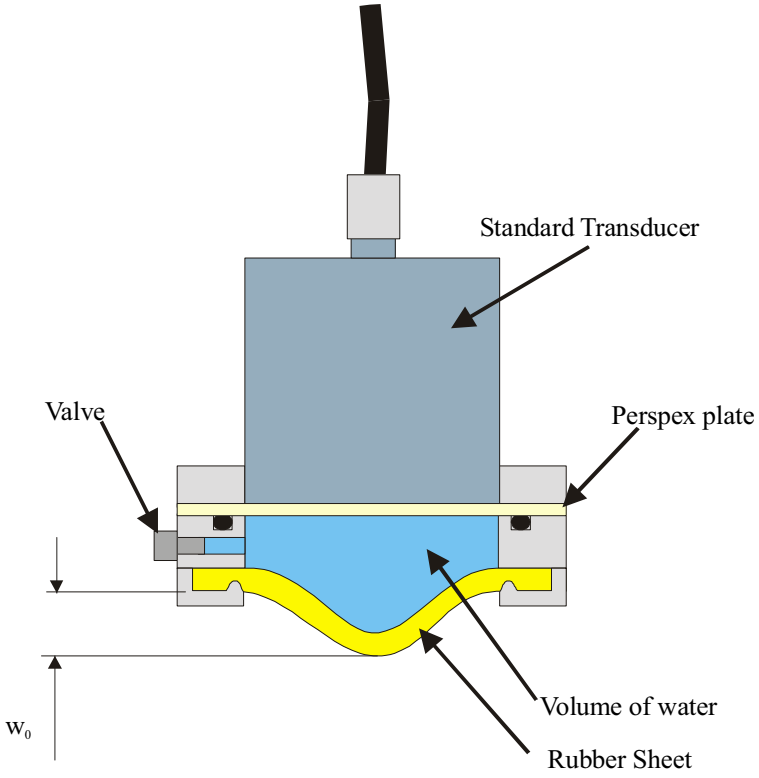

Figure 5.27. Schematic of membrane coupled transducer.

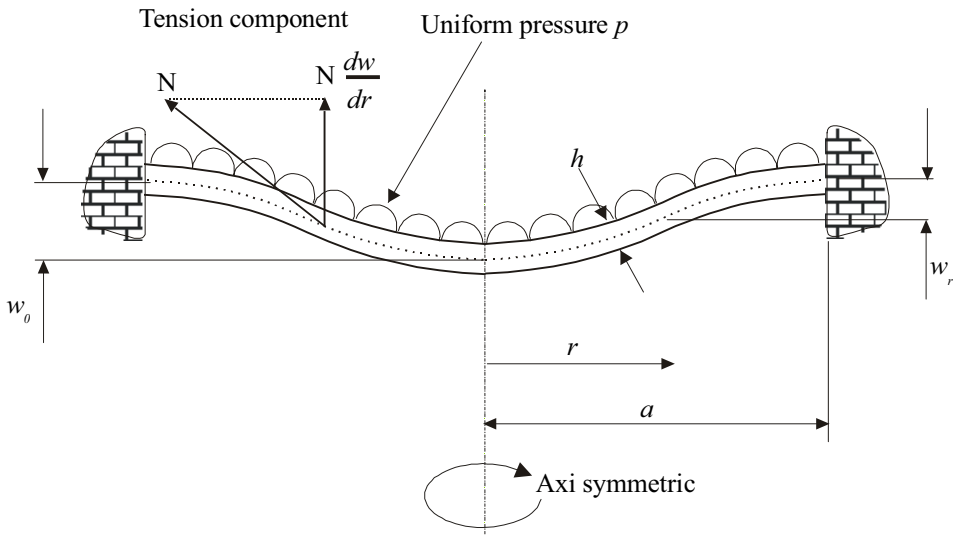

Figure 5.28. Deflections of a clamped circular plate due to a uniform pressure.

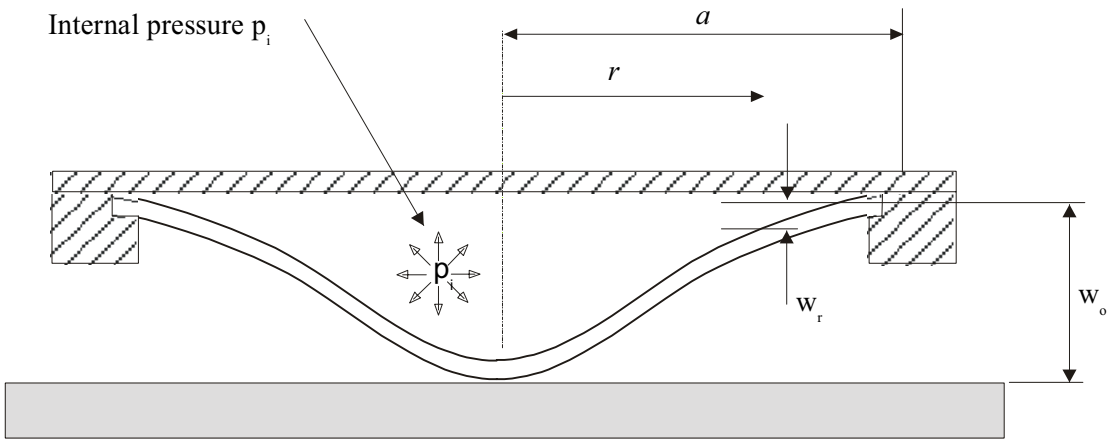

Figure 5.29. Membrane prior to contact.

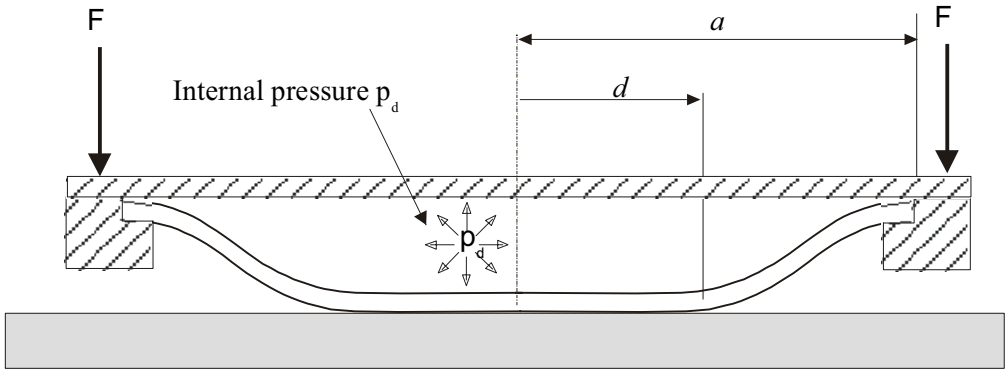

Figure 5.30. Membrane loaded by a force *F* onto a flat surface resulting in contact radius *d*.

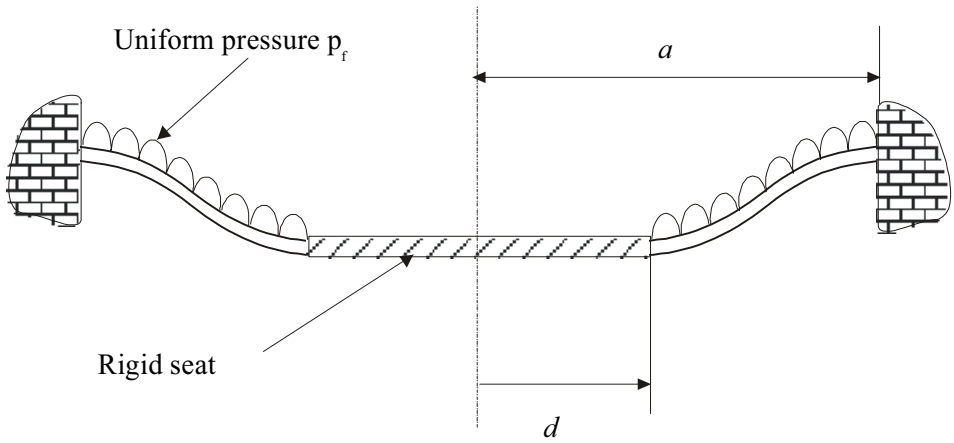

Figure 5.31. Approximation of Fig. 5.30 as a uniformly loaded annular diaphragm.

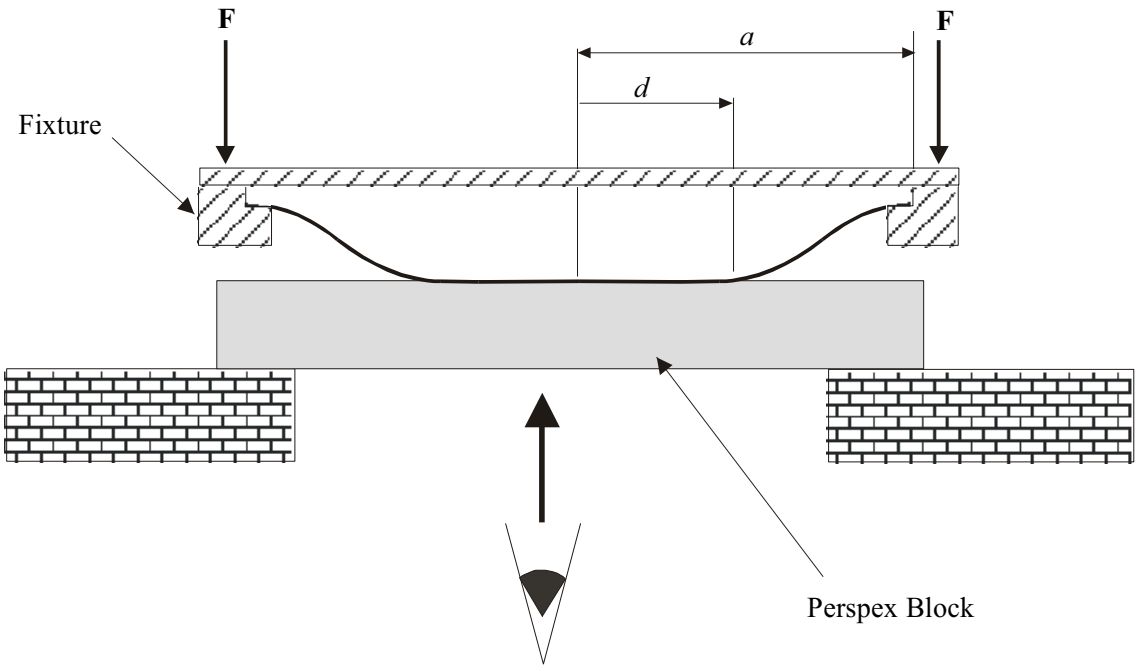

Figure 5.32. Experimental set up to calibrate flat surface membrane contact model. Observing the contact radius *d* as a function of applied load *F*.

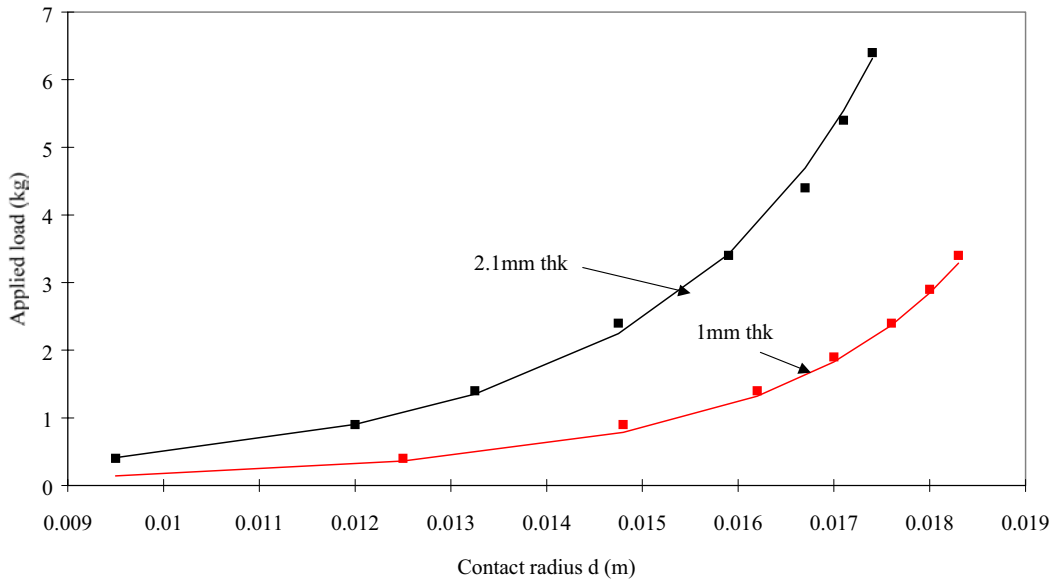

Figure 5.33. Calibration of flat surface membrane contact model. Model solution (solid lines) versus experimental results (squares) for 1 mm thick (w_o = 10mm) silicon rubber and 2.1mm thick (w_o = 7mm) natural rubber 50mm diameter membranes.

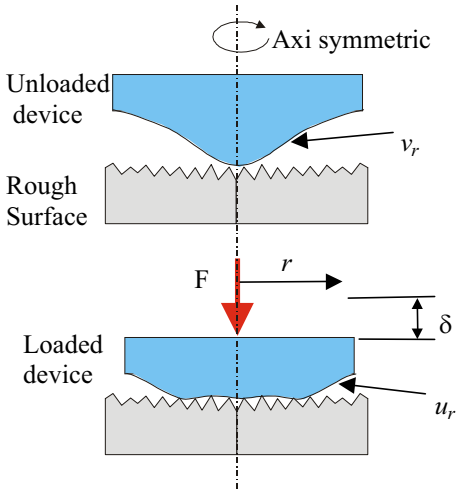

Figure 5.34 Membrane loaded onto a rough surface.

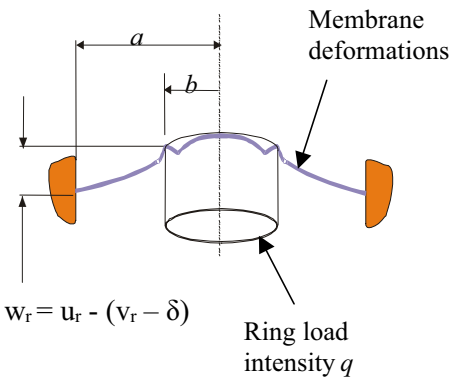

Figure 5.35. Membrane deformation. Upwards surface reaction approximated by a ring load.

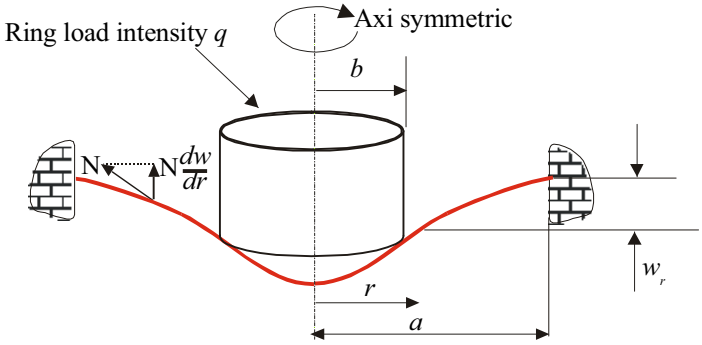

Figure 5.36. Global deformations of a clamped circular plate due to a ring load.

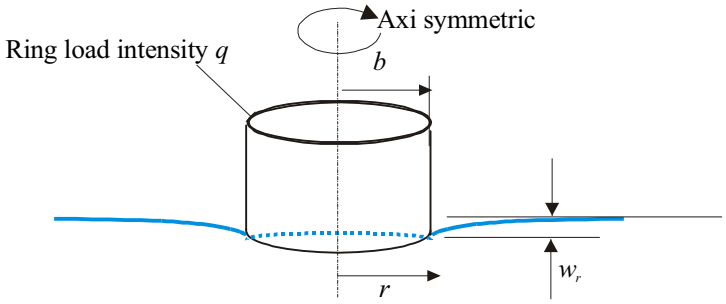

Figure 5.37. Surface deformations on a semi infinite body due to the application of a ring load.

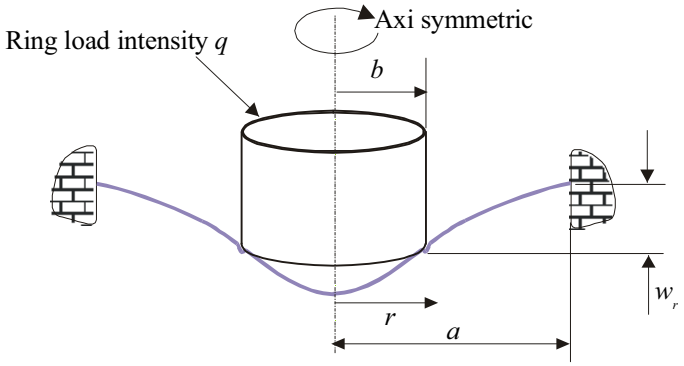

Figure 5.38. Superposition of Fig. 5.36 and Fig 5.37 to produce dimpled profile.

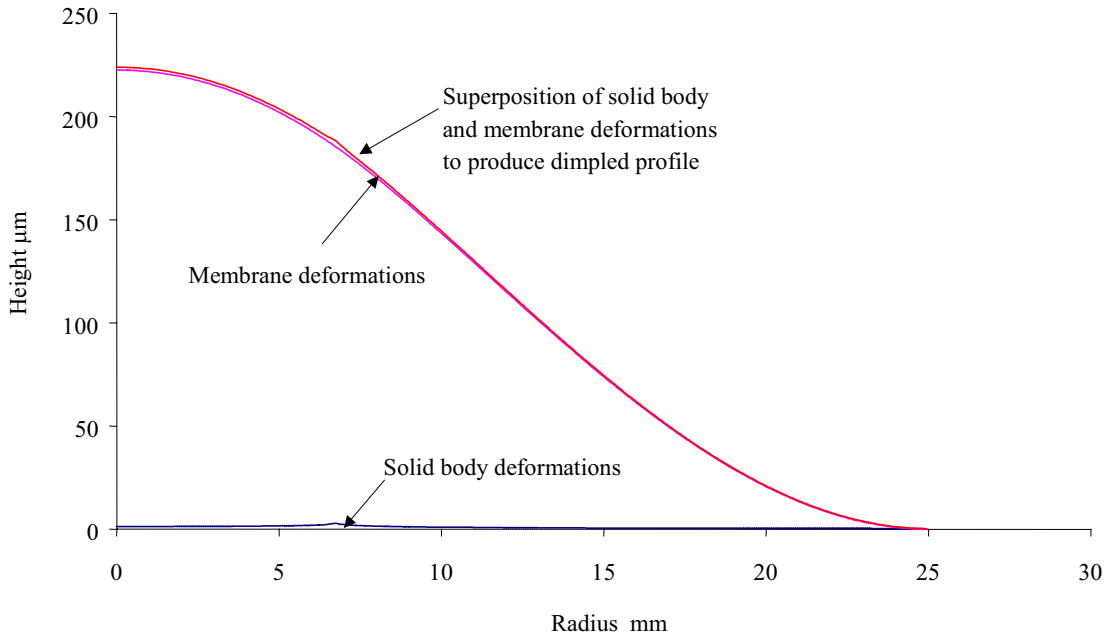

Figure 5.39. Membrane contact model influence coefficients for a 1mm thick, w_0=10mm, 25mm diameter silicon rubber membrane. The contribution given by the solid body and membrane deformations to the overall superposition are shown separately.

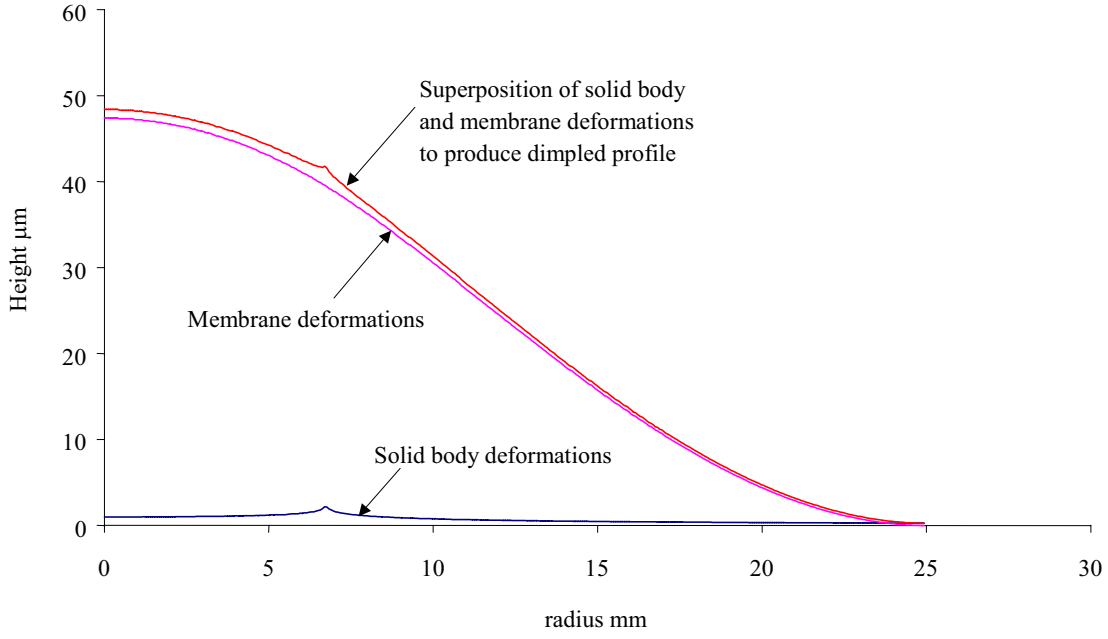

Figure 5.40. Membrane contact model influence coefficients for a 2.1mm thick, w_0=7mm, 25mm diameter natural rubber membrane. The contribution given by the solid body and membrane deformations to the overall superposition are shown separately.

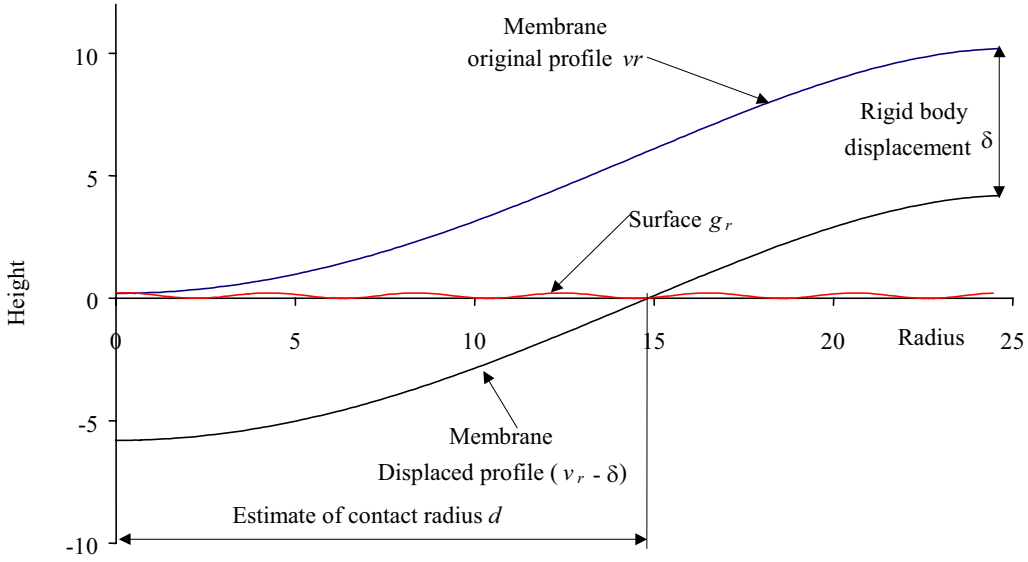

Figure 5.41. Membrane contact model solution. Determine contact radius from overlap of displacement membrane with rough surface.

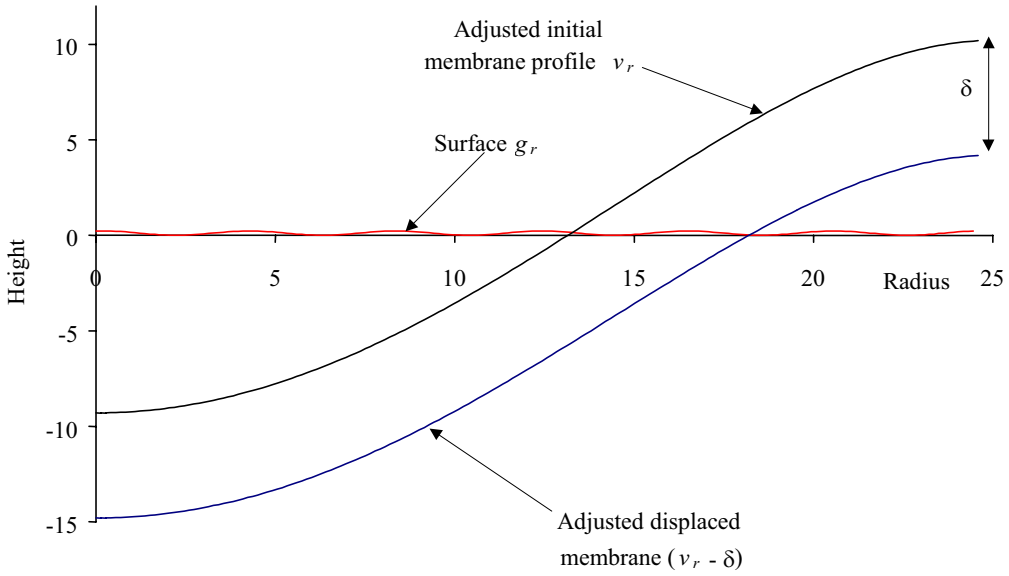

Figure 5.42. Adjusted initial membrane profile. Determine overlap function.

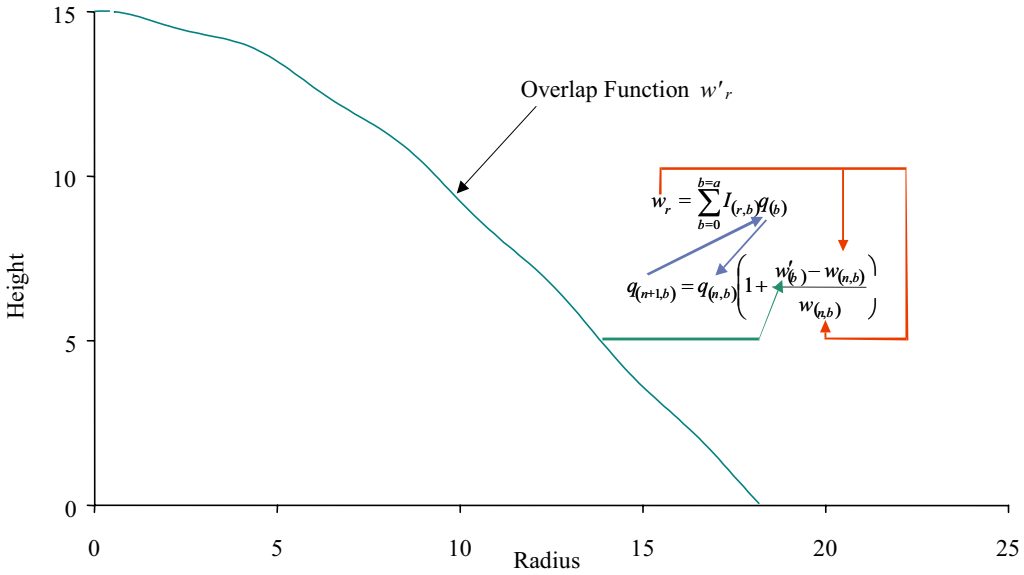

Figure 5.43. Solution iteration with overlap function.

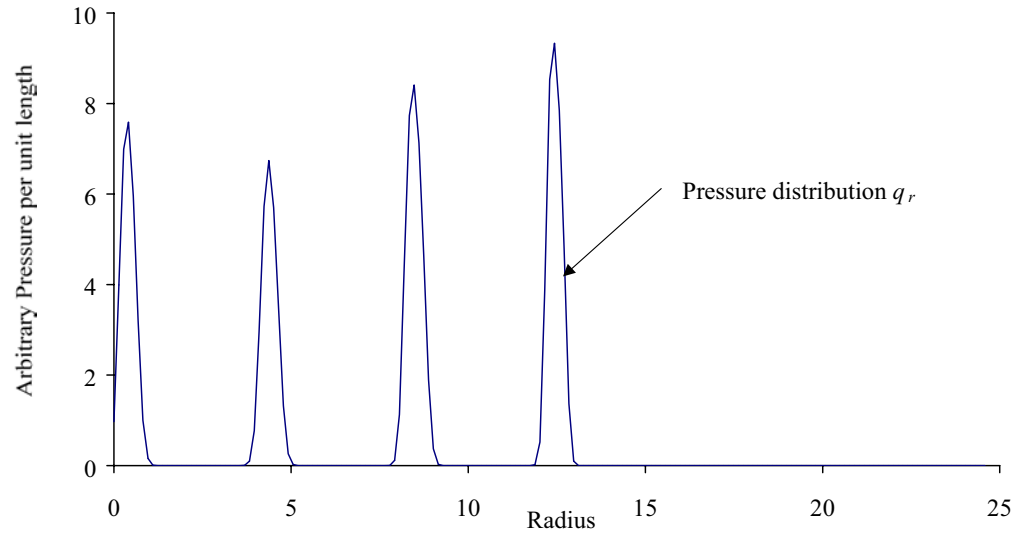

Figure 5.44. Converged contact load distribution for membrane example.

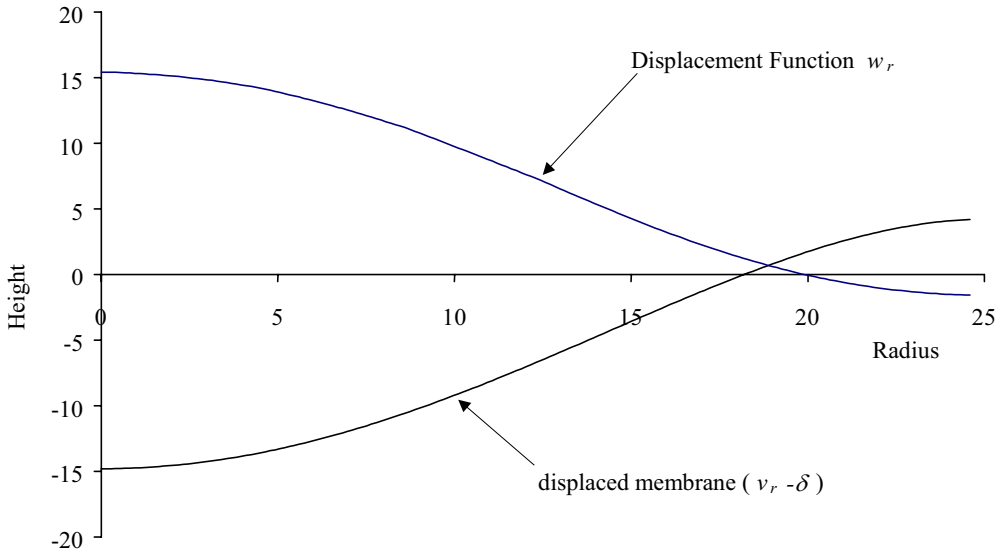

Figure 5.45. Converged displacement function along with rigid body displacement.

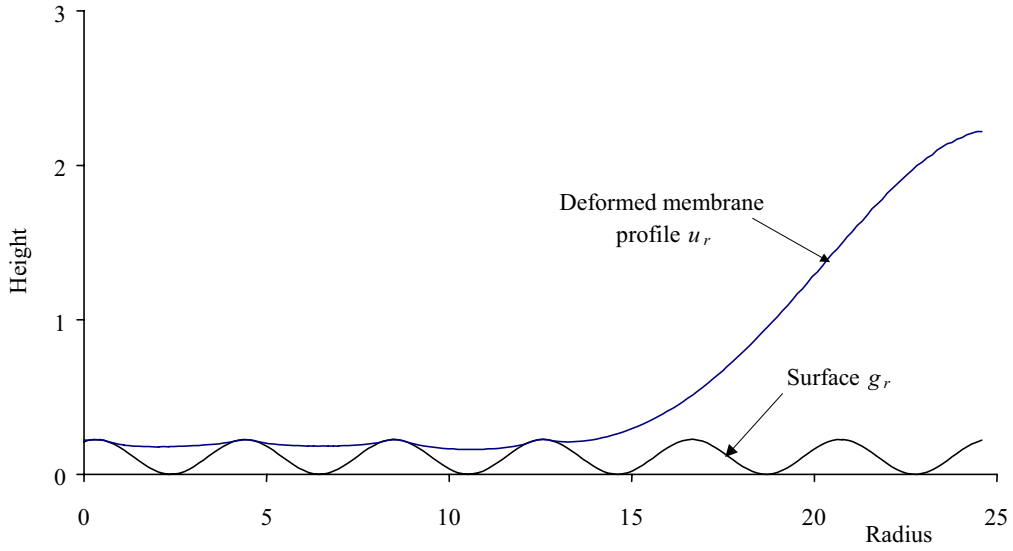

Figure 5.46. Converged contact solution for membrane example.

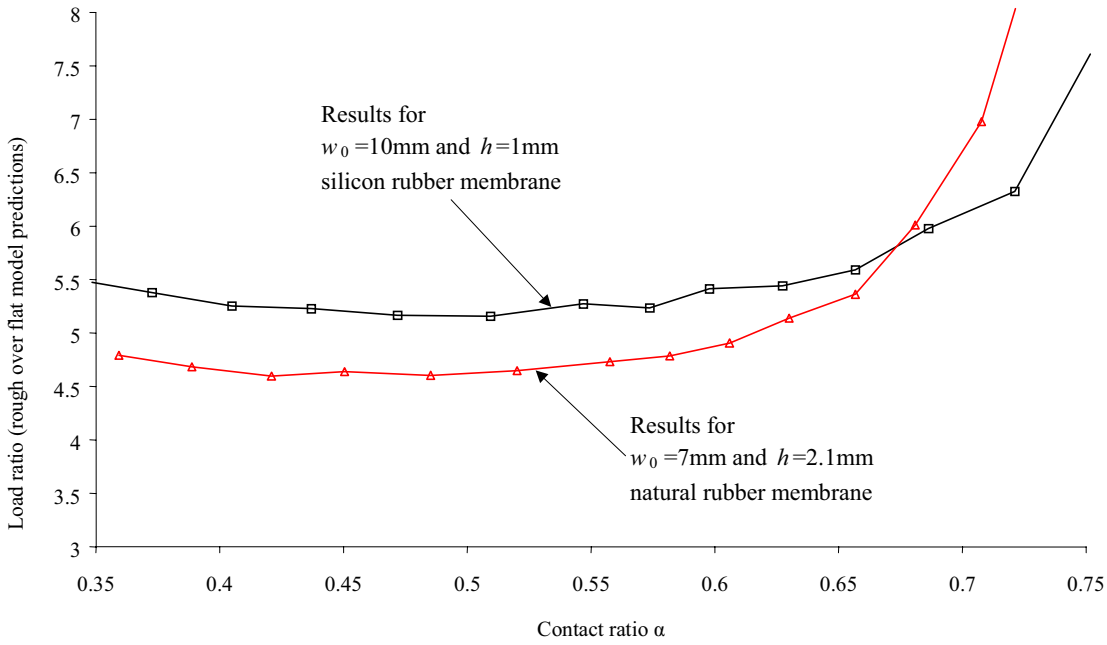

Figure 5.47. Difference between solutions given by the uncalibrated rough surface model and that given by the flat surface model for 1mm and 2.1mm membranes in contact with a flat smooth surface. Results plotted as the load ratio as a function of contact ratio.

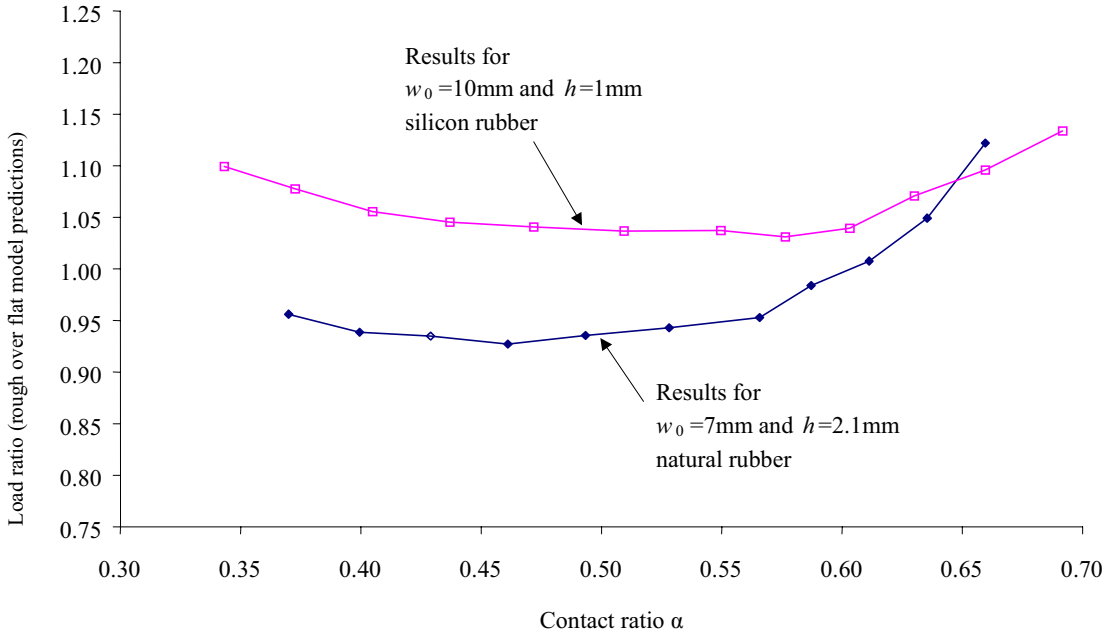

Figure 5.48 Difference between solutions given by the calibrated rough surface model and that given by the flat surface model for 1mm and 2.1mm membranes in contact with a flat smooth surface. Results plotted as the load ratio as a function of contact ratio.

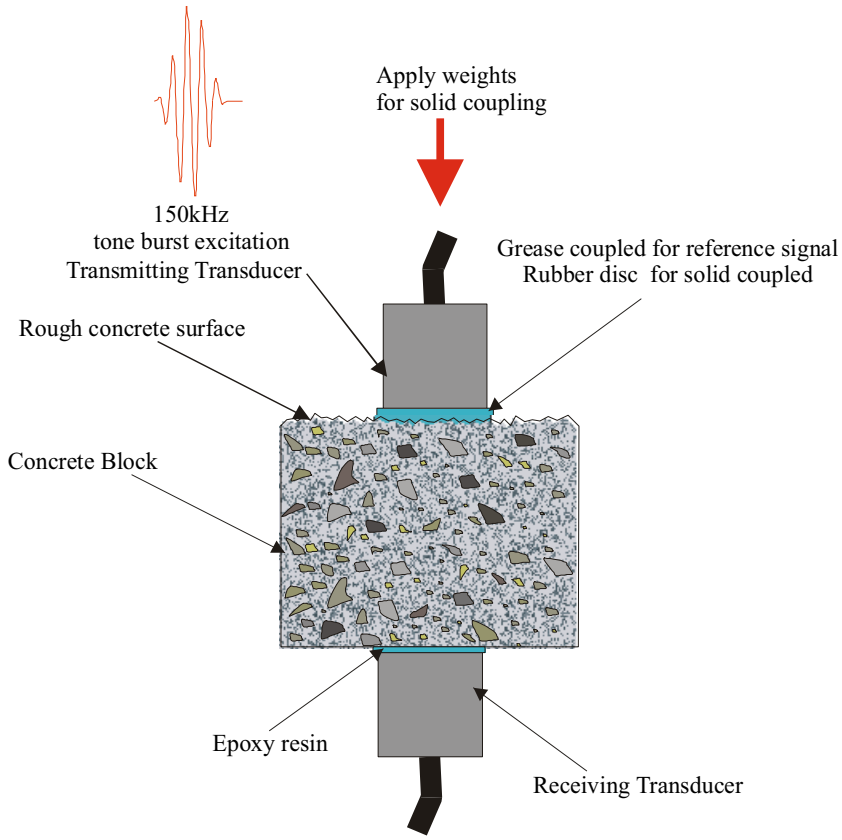

Figure 5.49. Experimental set up to investigate the feasibility of rubber disc coupling ultrasonic transducers to a rough concrete surface.

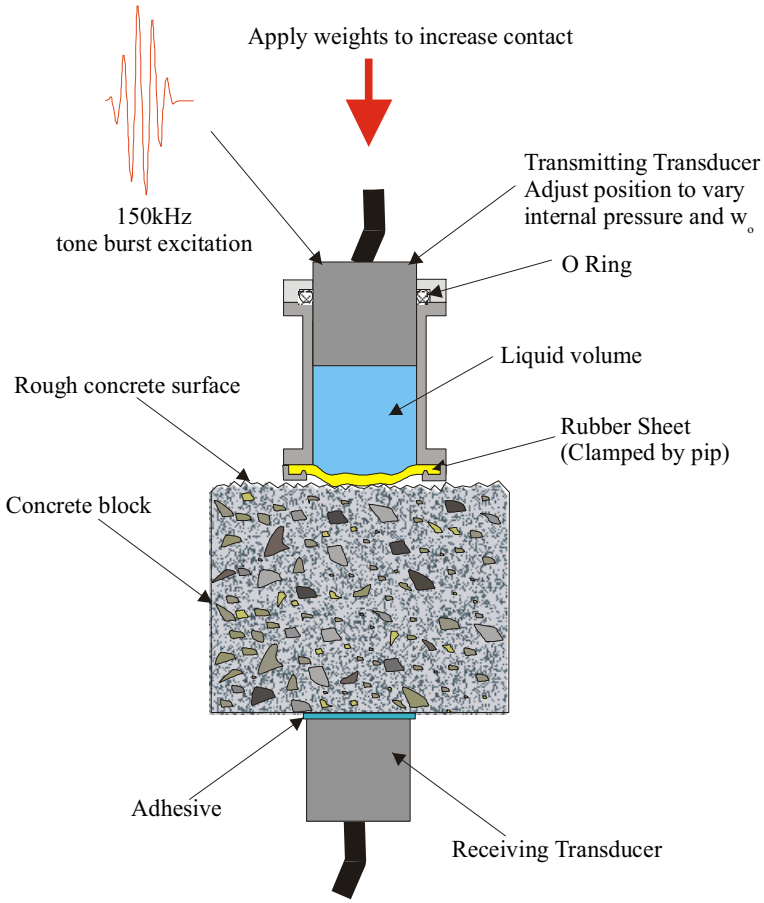

Figure 5.50. Experimental set up to investigate the feasibility of rubber membrane coupling ultrasonic transducers to a rough concrete surface.

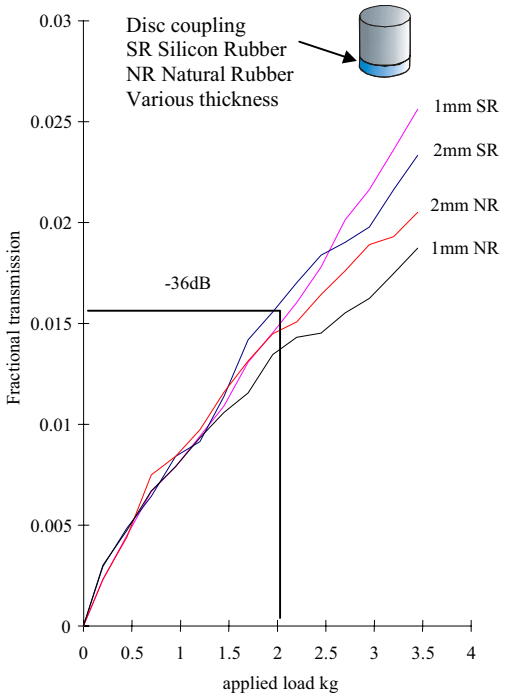

Figure 5.51. Measured transmission for dry rubber disc coupling to steel shuttered concrete surface.

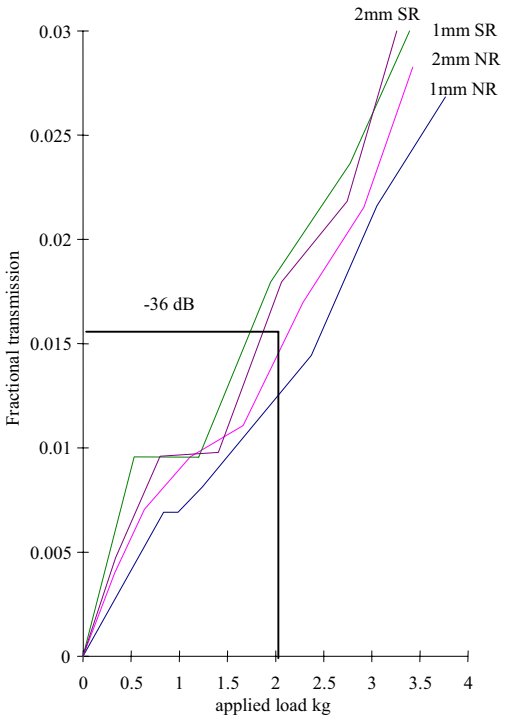

Figure 5.52. Predicted transmission for dry rubber disc coupling to steel shuttered concrete surface.

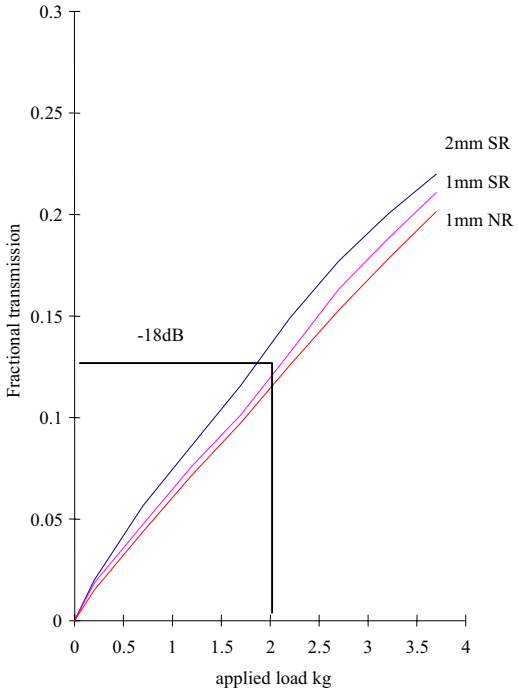

Figure 5.53. Measured transmission for dry rubber disc coupling to floated concrete surface.

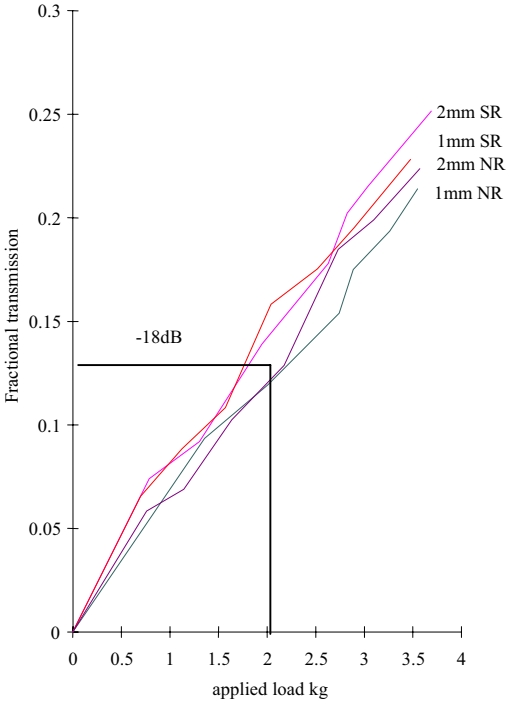

Figure 5.54. Predicted transmission for dry rubber disc coupling to floated concrete surface.

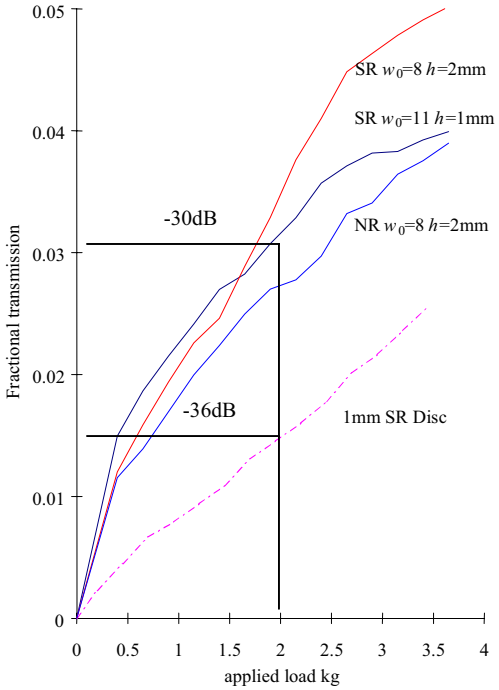

Figure 5.55. Measured transmission for dry membrane coupling to steel shuttered concrete surface. SR silicon rubber, NR natural rubber. 1mm experimental disc coupling for comparison.

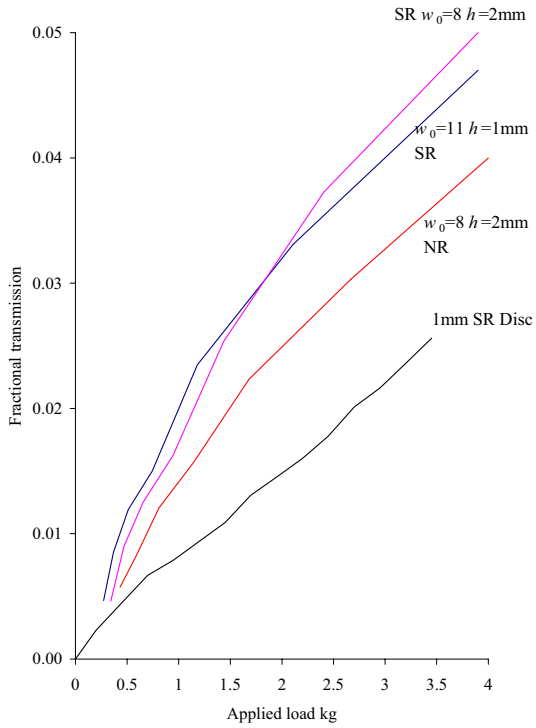

Figure 5.56. Predicted transmission for dry membrane coupling to steel shuttered concrete surface.

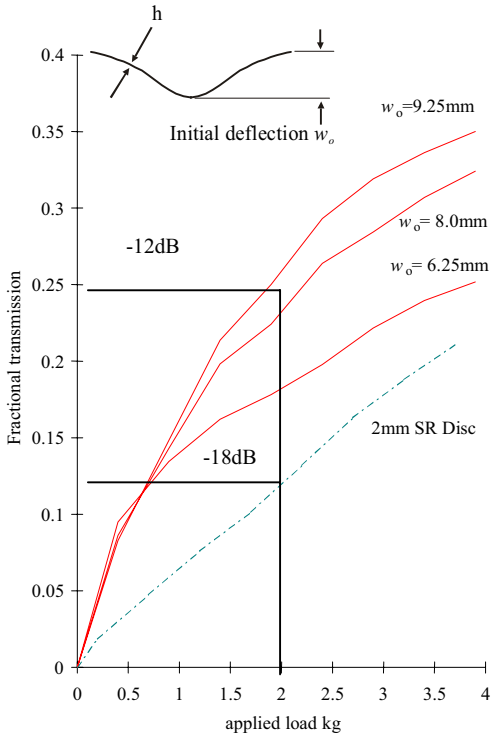

Figure 5.57. Measured transmission for various 2mm thick silicon rubber membranes coupled to floated concrete surface. 2mm experimental disc coupling for comparison.

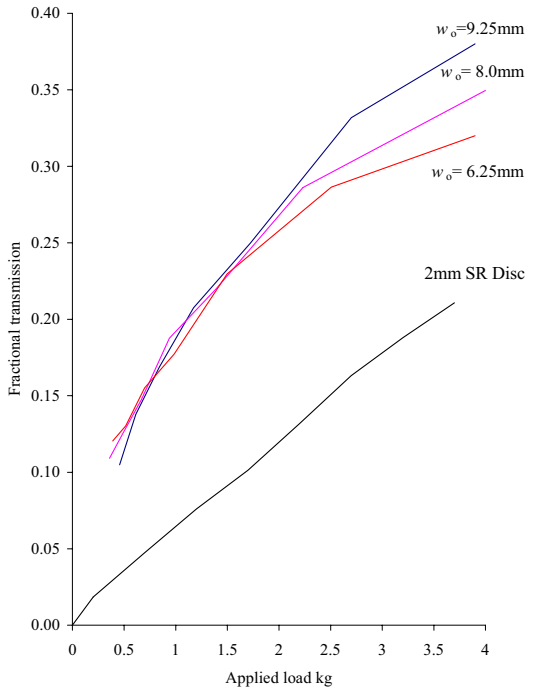

Figure 5.58. Predicted transmission for various 2mm thick silicon rubber membranes coupled to floated concrete surface.

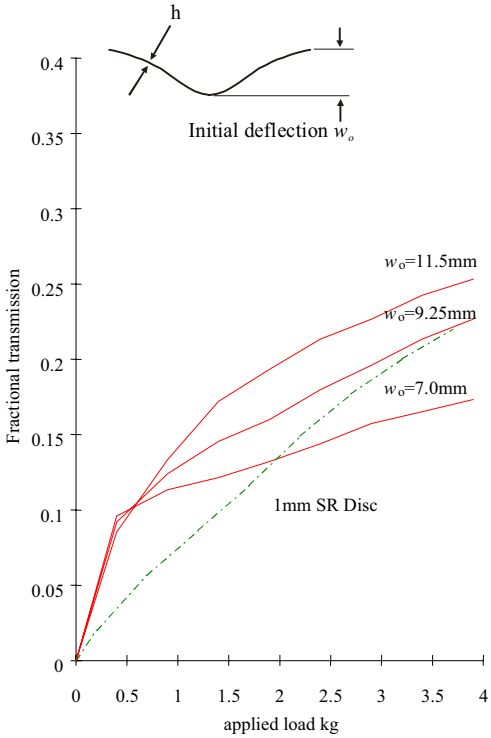

Figure 5.59. Measured transmission for various 1mm thick silicon rubber membranes coupled to steel shuttered concrete surface. 1mm experimental disc coupling for comparison.

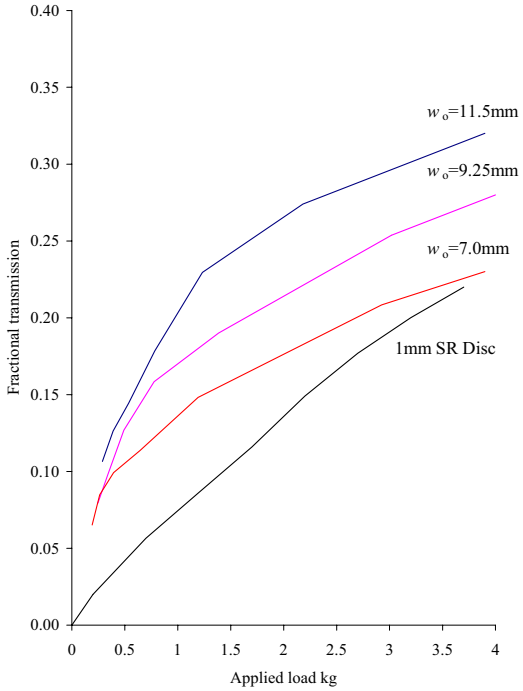

Figure 5.60. Predicted transmission for various 1mm thick silicon rubber membranes coupled to steel shuttered concrete surface.

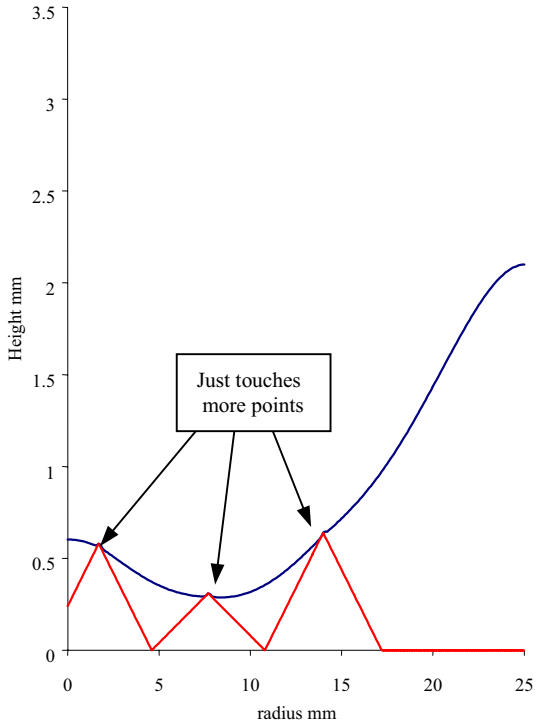

Figure 5.61. Deformation of a 0.75mm thick silicon rubber membrane loaded by 2kg onto a simple surface.

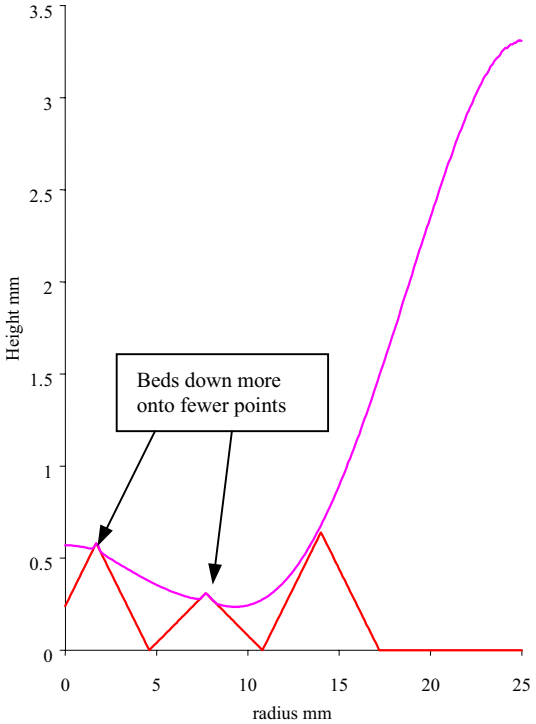

Figure 5.62. Deformation of a 1.5mm thick silicon rubber membrane loaded by 2kg onto a simple surface.

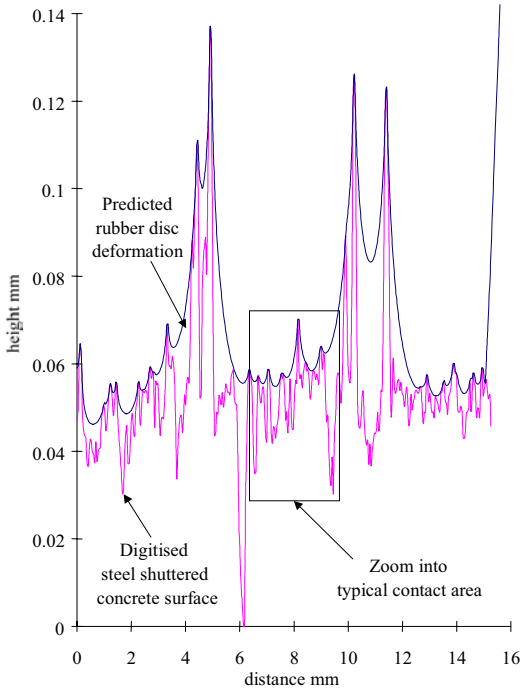

Figure 5.63. Predicted axi symmetric deformation of a 2mm thick silicon rubber disc loaded by 2kg onto a steel shuttered concrete surface.

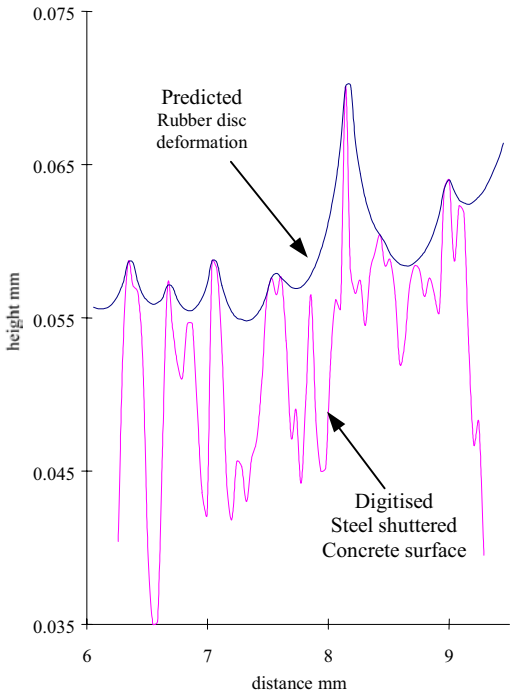

Figure 5.64. Zoom in of the typical contact area shown in Fig. 5.63.

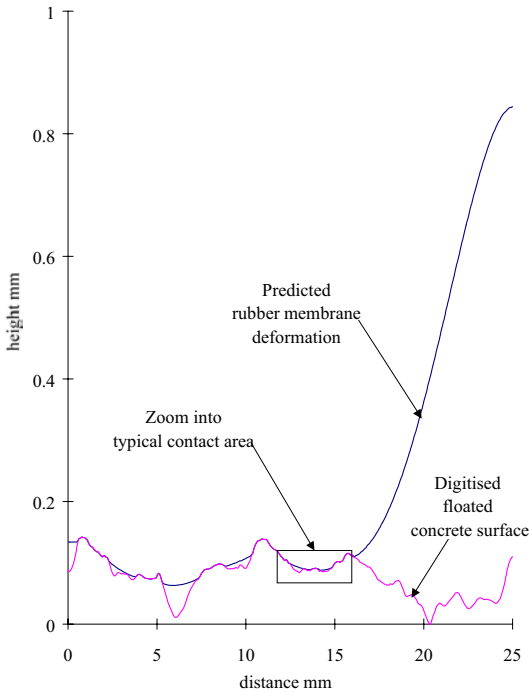

Figure 5.65. Predicted axi symmetric deformation of a 2mm thick silicon rubber membrane loaded by 2kg onto a floated concrete surface.

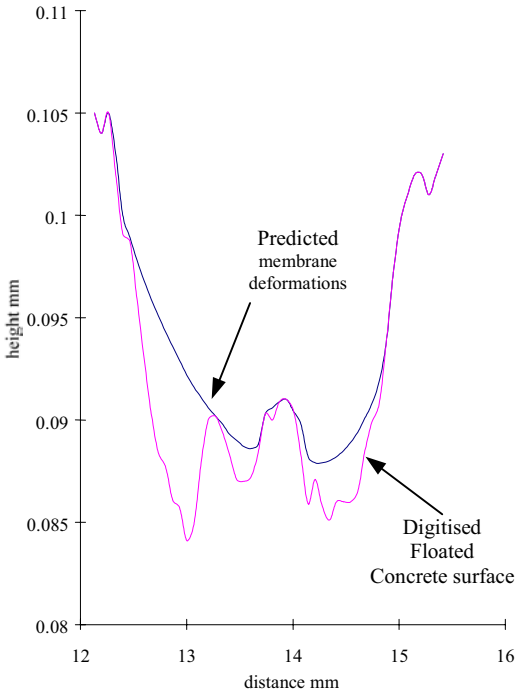

Figure 5.66. Zoom in of the typical contact area shown in Fig. 5.65.

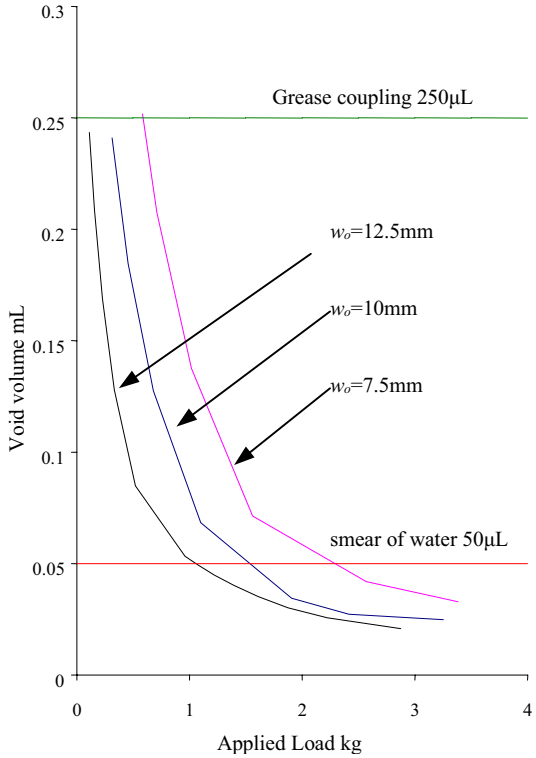

Figure 5.67. Predicted void volume as a function of applied load for 0.75mm thick silicon rubber membranes in contact with timber shuttered concrete surface.

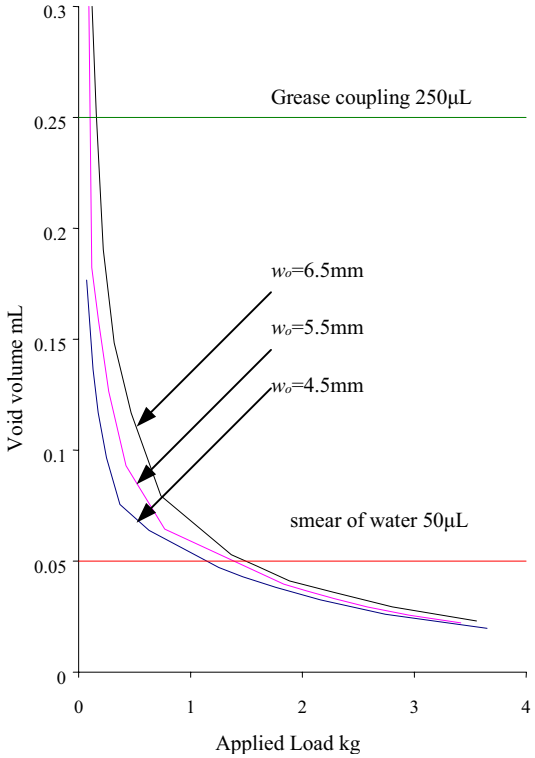

Figure 5.68. Predicted void volume as a function of applied load for 1.0mm thick silicon rubber membranes in contact with timber shuttered concrete surface.

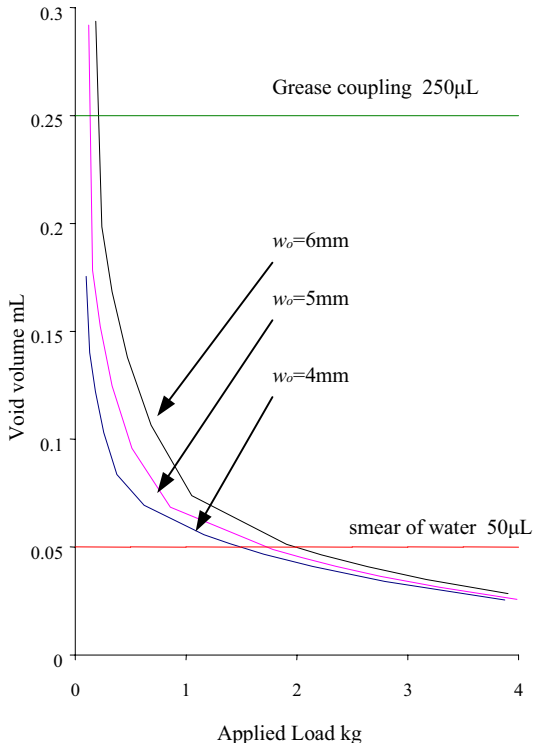

Figure 5.69. Predicted void volume as a function of applied load for 1.25mm thick silicon rubber membranes in contact with timber shuttered concrete surface.

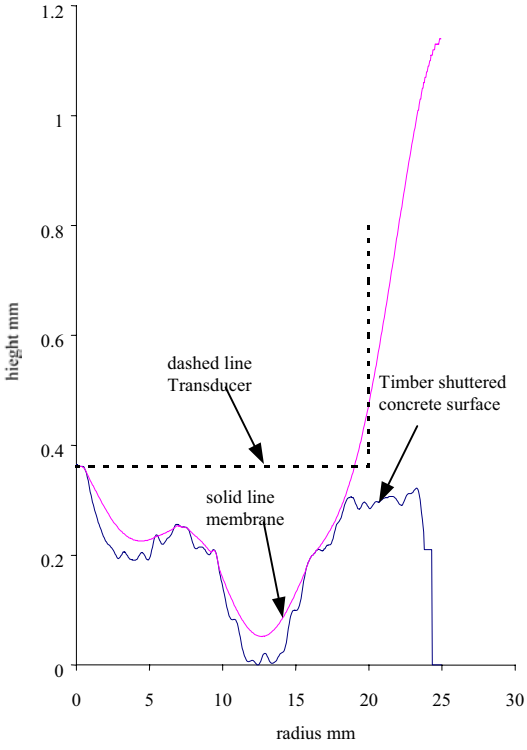

Figure 5.70. Comparing the void volume left by the optimum membrane loaded by 1.5kg and a transducer placed onto the timber shuttered concrete surface.

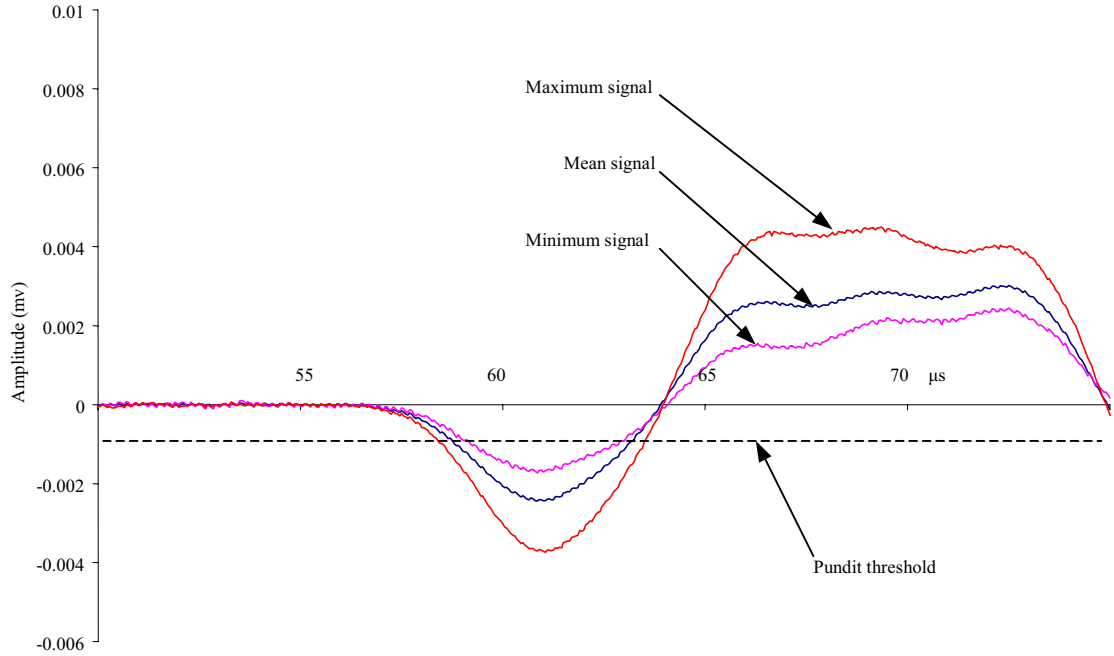

Figure 5.71. Conventional viscous coupling received signal amplitudes (x20dB) for 10 repeat tests on rough concrete surfaces.

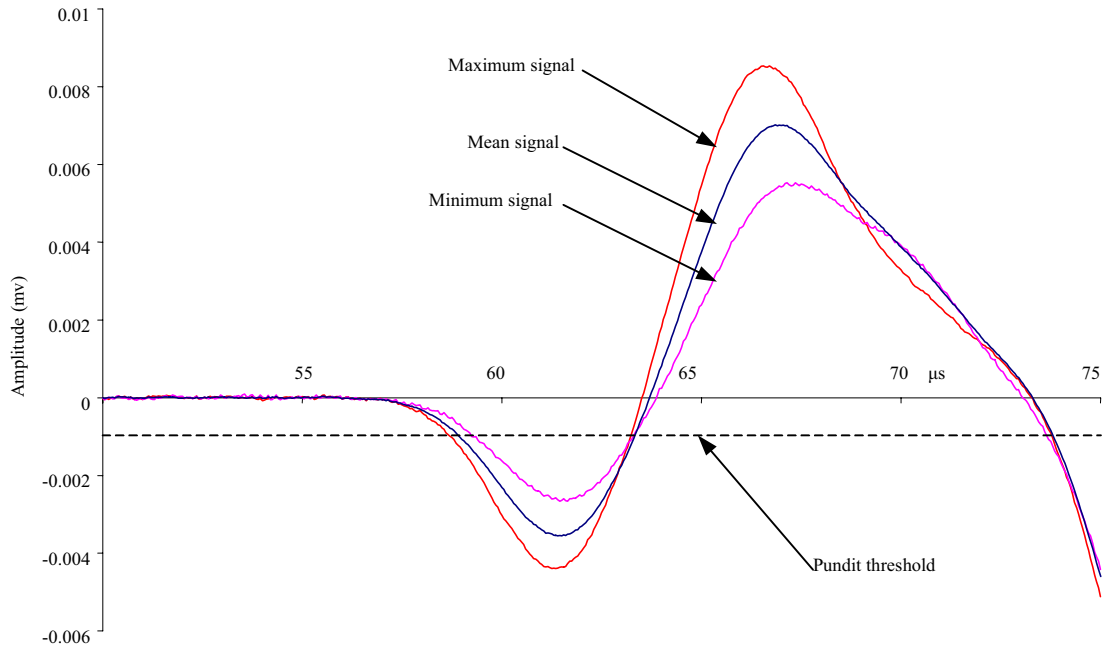

Figure 5.72. Wet membrane coupling received signal amplitudes (x20dB) for 10 repeat tests on rough concrete surfaces.

Chapter 6

Application – Wet membrane v Conventional coupling

6.1 Introduction

A popular method when performing the routine inspection of concrete structures is to find the velocity of sound in the concrete. A number of tests are often carried out on a grid marked out on the structure so as to construct a contour map of the velocity of sound. Such a map may often yield valuable information concerning variability of both material and construction standards [J.H. Bungey and S.G. Millard (1996)]. The application of the ultrasonic transducers requires that a liquid couplant, whose required viscosity depends on surface roughness, be applied between the transducer face and the concrete surface so as to fill the significant air gaps and thus facilitate signal transmission. Application of couplant to each grid point and the removal after testing proves both inconvenient and time consuming, hence the motivation to research alternative methods. It was suggested in Chapter 5 that ultrasonic inspection of concrete could be significantly be improved by solid coupling the transducers to the structure under test. Models were derived to predict the contact made by such devices so as to enable design optimisation. For a hand held device it was shown that only low levels of contact were made when dry rubber coupling the transducer. For most practical inspections this results in unacceptably low signal strengths. Alternatively an initial investigation found that by wetting a membrane coupled device with water, signal transmission was comparable to that for grease coupling and the received signal amplitudes were more consistent. This chapter reports on the application of wet membrane coupling, where its performance when inspecting a grid is compared to conventional grease coupling. Prototype membrane shoes were designed to fit to standard PUNDIT transducers. The derived membrane contact models were applied to optimise a membrane design.

6.2 Prototype membrane shoes

The design specification for a membrane shoe was that it should provide a means by which a standard ultrasonic transducer could be conveniently coupled to a concrete surface. The device should be robust, durable, compact and it should be straight forward to attach and retain the transducer requiring no force greater than can be applied by hand or special tools.

A general assembly of the prototype device is shown in Fig. 6.1 along with a photograph in Fig. 6.2. A commercial device would ideally do without most of the bulky aluminium body. Water was used as a liquid medium. The transducer is grease coupled to the Perspex plate whose acoustic impedance is well matched to water and the rubber membrane. Being transparent it allows inspection of the assembly for possible air bubbles. For the membrane, since the testing of concrete is conducted typically below 100kHz, the damping of the ultrasonic signal by the rubber is negligible. This allows selection of the membrane material from a wide range of compounds available. The material selected for the membrane was MOSITES 1453D high strength silicon rubber. A range of sample sheets of various thickness and surface finish were kindly supplied by Aerovac Systems (Keighly) Ltd, Keighly, West Yorkshire. M1453D is a high quality, high strength silicone rubber compound developed in the mid 1960s for aerospace applications. The material can withstand prolonged exposure to elevated temperatures and pressures and resist aggressive attack by a volatile liquid. The material has been used to manufacture inflatable pressure bags for applications were dimensional stability is important. These features may not be specifically required for exposure to civil engineering environments, but the material was selected for its durability characteristics. Additionally it is available with a textured fabric like surface finish, which was found to allow retention of the applied film of coupling water. Material properties of this rubber given by the supplier are shown in Table 6.1.

Physical Property	Value
Hardness	50 shore A
Tensile Strength	9.66Mpa
Elongation at break	650%
Modulus at 300% Elongation	1.75Mpa
Tear Strength	40Mpa
Specific Gravity	1.15

Table 6.1 Physical properties for MOSITES M1453D Silicon Rubber.

Component drawings for membrane shoes to suit the PUNDIT 54kHz and 83kHz transducers are shown in Appendix 2 in Fig. A2.1 and Fig. A2.2 respectively. The fixture is assembled underwater. The Perspex plate is secured onto the body by four counter sunk screws, squashing the rubber o ring. The silicon rubber disc is held in place by screwing down the clamp plate. The rubber deforms around the dimpled profile on the body face which provides a very effective means of securing the membrane under a pressure. Water is

pumped into the assembly via the control valve until the membrane bulges out to just above that which is desired. Finally, the membrane is allowed to deflate, letting out any air bubbles, and the control valve closed when the membrane reaches the desired initial deflection.

The experimental comparison described in this chapter used the PUNDIT 54kHz transducers. For these transducers a 50mm diameter rubber disc is used for the membrane, where the thickness h and initial deflection w_o are determined using the rough surface membrane contact model. The technique is described in detail in section 5.7. The selection was made by observing the predicted void volume left between the rubber and various rough surfaces when the membrane device is loaded by around 2kg. The void volume should be less than that which coincides with the volume of a smear of water applied to the membrane face. This requirement was predicted to be satisfied by having a silicon rubber membrane of 0.75mm thick and 10mm initial deflection. For this set up, Fig. 6.3 and Fig. 6.4 show the predicted volume of couplant as a function of applied load required to couple the device to the steel and timber shuttered surfaces respectively.

6.3 Experimental description

The purpose of the experiments was to assess the performance of wet membrane coupling of transducers compared to conventional grease coupling. Performance was measured as the time taken to complete the inspection of a complete grid, the degree to which the results were repeatable and the convenience of a technique.

For the comparison a 30mm spacing 10 by 10 position grid was marked out on two different concrete blocks. The flat block had been in contact with steel shuttering during hydration, photographs of which are shown in Fig 6.5a and Fig 6.5b. The surfaces were similar to the digitised surface shown in Fig. 5.3a being relatively flat with the appearance of a medium grade sand paper. It would conventionally be advised to viscous couple to this surface using a light grease. The rough surface block shown had two different surfaces. On one side the surface had a rough floated finish as shown in Fig 6.6a and Fig 6.6b. The other side had been in contact with timber shuttering during hydration, and is shown in Fig 6.7a and Fig 6.7b. This surface was similar to the digitised surface shown in Fig. 5.3b being perhaps borderline as to whether some prior surface preparation should be performed. On the rough surface concrete block the use of a stiffer grease would be recommended when conventional coupling.

For the tests, the PUNDIT equipment manufactured by CNS Farnell of London was used, which is the standard equipment used in the UK for through transmission testing of concrete. A detailed description of The PUNDIT apparatus and operation is given in Chapter 2. Fig. 6.8 shows a photograph of the PUNDIT apparatus and 54kHz transducers along side some prototype membrane shoes.

For either technique, the test involved measuring and recording the signal transit time at each of the one hundred grid points, and then repeating the inspection from scratch. As with through transmission testing of large structures, the co-operation of two operators was required. Conventional testing of concrete was conducted first. The viscous couplant used was Swafega, which is a jelly manufactured by Polycell, normally used for cleaning hands but often used when testing concrete structures. The couplant was applied to each grid point prior to testing. When testing numerous grid points, this method was found to be more convenient and less messy than when directly applying couplant to the face of the transducer as in Fig. 6.9. The time taken to apply the couplant to the complete grid was noted. The transducers were then coupled to each grid point and the signal transit time measured and noted. Discretion was used in that if the displayed measured signal transit time wandered off or was unrealistically low then transducers were uncoupled, couplant or water reapplied and the test was repeated. Prior to coupling to the next grid point the transducer face was wiped clean. The time taken to measure the signal transit times for the complete grid was recorded. The grid was then cleaned of couplant, for which the time taken was noted. The test procedure was then repeated for a new set of data. Following this, tests were conducted for the wet membrane technique. The transducers where coupled to the Perspex plate on the membrane shoes by smearing a light grease on the face of the transducer. Prior to coupling the device to each grid point the textured membrane was sprayed with water as in Fig. 6.10 and then the device was pressed onto the surface as in Fig. 6.11. The signal transit time was recorded, the membrane resprayed with water and the next grid point tested. As with conventional coupling the total time to test the complete grid was noted.

For each technique the percentage difference between the measured signal transit time for the initial and repeat test at each grid point was calculated. For visual interpretation of results, this difference was plotted as a 2D surface map. The mean value of the 2D surface map was taken to indicate technique repeatability.

6.4 Experimental results

The tests results for conventional coupling and wet membrane coupling to the flat surface concrete block are shown in Fig. 6.12a and Fig. 6.12b respectively. For each figure, the table on top shows the times that make up the test duration. Below this is shown a 2 dimensional surface map of the test area that indicates the signal transit time measurement repeatability. The time taken to completely inspect the 100 point grid by conventional means took a total of 28 minutes. One quarter of this time was attributed to applying the viscous couplant to the grid and then removing it after tests. By contrast the test duration when using the wet membrane coupled device was a total of 25 minutes. Greater time was required to inspect the grid since the membranes were sprayed with water in between tests whereas the couplant had already been applied to the grid for conventional coupling. The difference in the test duration for the two techniques is marginal, but with the membrane device, the freedom from the inconvenience and mess of applying and removing a viscous couplant was appreciated. The 2D surface plots reveal that there is a much greater difference between measurements for the initial and repeat tests for the conventional technique. The mean difference between the initial and repeat test given by the repeatability was found to be 0.9%. By contrast when using the membrane device, the repeatability improved by almost three fold to 0.33%. These results suggest that wet membrane coupling provides a means for more consistent coupling of ultrasonic transducers to concrete.

The tests results for conventional coupling and wet membrane coupling to the rough surface concrete block are shown in Fig. 6.13a and Fig. 6.13b respectively. The time taken to inspect the grid by conventional means took a total of 37 minutes. This was an additional 9 minutes when compared to the time for similar tests conducted on the flat surface block. The reason was that this surface was borderline as to whether prior surface preparation should have been performed. If the measured signal transit time at a grid point varied dramatically from the norm then the transit time was re-evaluated. Such intuition would normally be applied by operators when attempting to obtain reliable results. The time taken to inspect the grid using the membrane device was 27 minutes. Here, for the rougher concrete surface the membrane device offers a 27% improvement in inspection time. Comparing the 2D surface plots with those in Fig. 6.12 reveals that for the rougher surface the repeatability of both techniques has suffered. Conventional results varied by a mean of 1.56% which is above the 1% that the PUNDIT operation manual recommends. For the membrane device the repeatability is borderline, but is still an improvement over the conventional results.

6.5 Conclusion

The inconvenience of the present technique for ultrasonic inspection of concrete structures is caused by the requirement that a viscous coupling should be applied to each grid point. Application and removal of couplant proves to be messy and time consuming. As such the technique can often be unattractive to operators and those that specify such tests. Chapter 5 researched the feasibility of more convenient methods for coupling ultrasonic transducers. A simple answer would have been to solid couple the transducers to the concrete surface using a comparable material. However, modelling and experiments found that solid coupling of transducers was not feasible for most practical applications due to the low signal transmission. It was suggested that when a membrane device was wetted just with water that the signal transmission was comparable to conventional grease coupling when testing a relatively rough surface. This would still be more convenient than the handling of a viscous couplant. To investigate further, that chapter reported on the application of models to develop a prototype membrane device suitable for wet membrane coupling of standard PUNDIT transducers. In this chapter, the performance of the device was compared to conventional coupling when inspecting a one hundred point grid on two different concrete structures. The author recognised that the greatest improvement offered by the membrane coupling technique was that it was definitely less messy. Unlike an organised laboratory environment, the handling of viscous couplant around a concrete structure is a nuisance. It is very difficult to keep a tidy inspection area when applying couplant to a vertical surface. It is thus suggested that the wetted membrane devices should prove popular among operators. Measured signal transit times obtained by the membrane technique were shown to be more repeatable than when conventional viscous coupling the transducers. This was an unexpected bonus since the goal was to develop a device that would offer greater convenience. The improved repeatability of results was due to the membrane device coupling more consistently to a rough surface.

Application of research found that a wet membrane device offers a significant improvement over the current technique of viscous coupling transducers when ultrasonically inspecting concrete. The findings of Chapters 5 and 6 were conveyed at the QNDE international conference held in Montreal in July 1999 in the form of a presentation and poster. Prototype membrane shoes were exhibited and met with a warm response by interested conference attendees. Two papers were submitted for inclusion in the accompanying publication [Long et al. (1999)]. It is hoped that the findings of this work will be adopted as alternative practice whenever the convenience of concrete inspection, the time taken and the reliability of results are important.

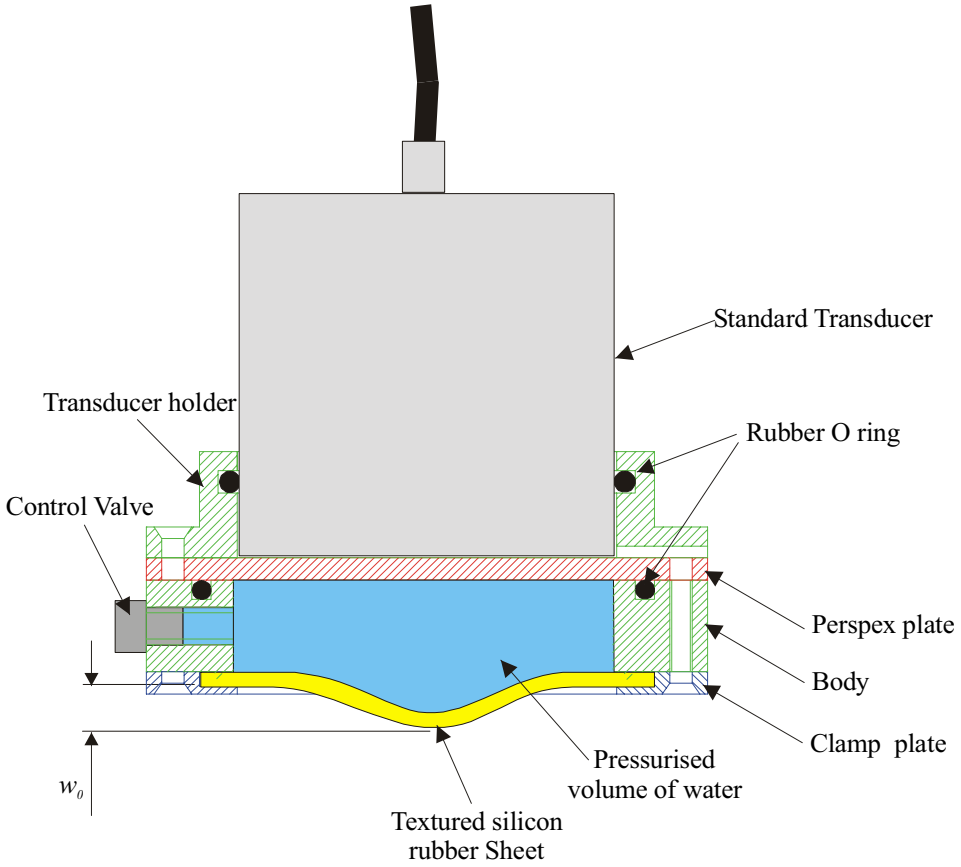

Figure 6.1 General assembly of prototype membrane shoe (not to scale).

Figure 6.2 Photograph of standard 54kHz transducer coupled to prototype membrane shoe.

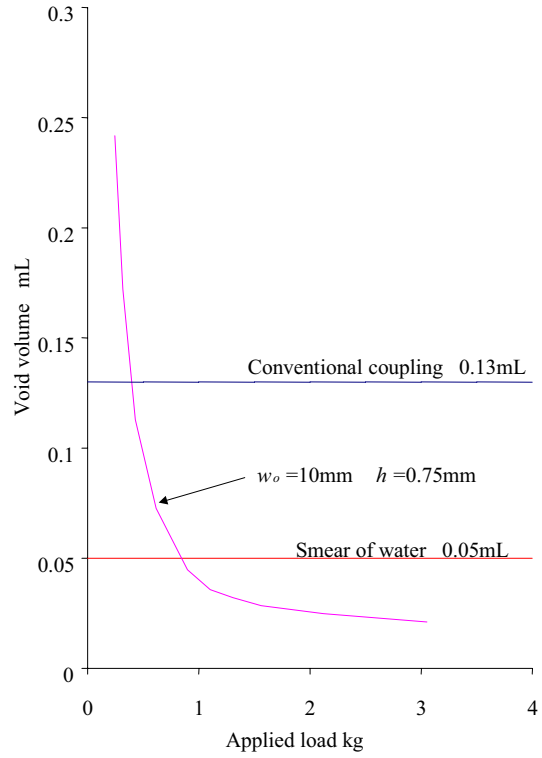

Figure 6.3. Predicted void volume as a function of applied load for optimum membrane design applied to steel shuttered concrete surface.

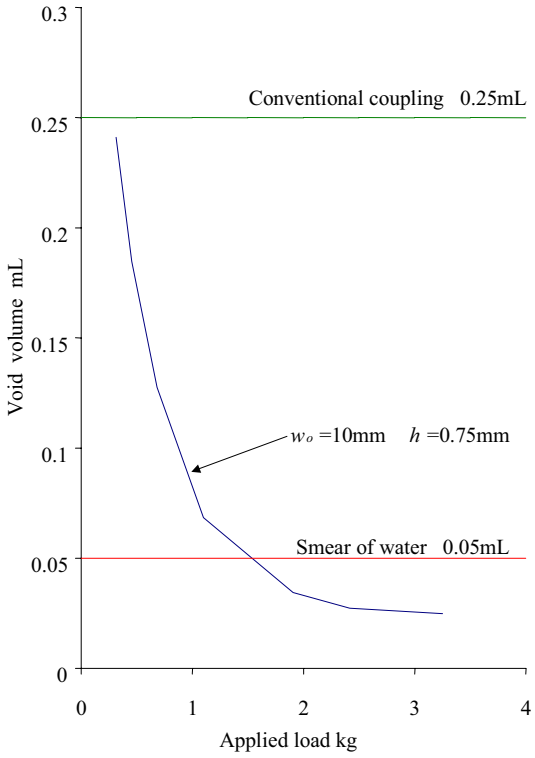

Figure 6.4. Predicted void volume as a function of applied load for optimum membrane design applied to timber shuttered concrete surface.

Figure 6.5a. Photograph of grid pattern marked out on the flat surface concrete block.

Figure 6.5b. Zoom in of flat surface concrete block.

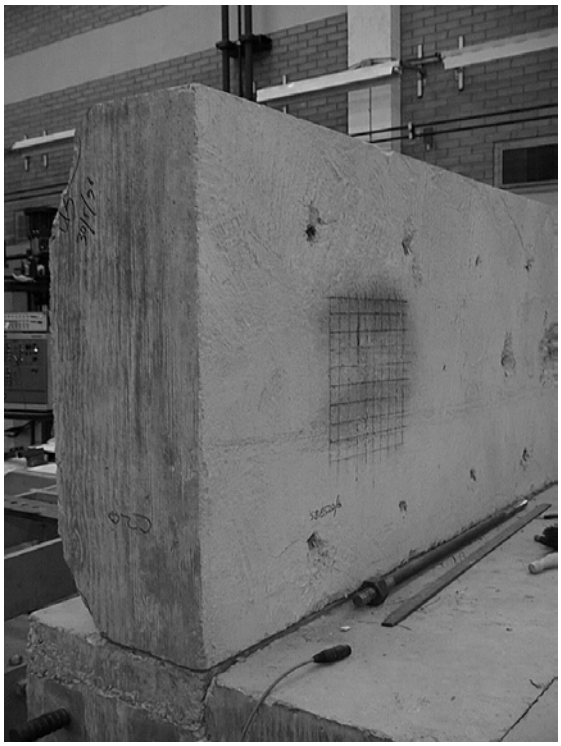

Figure 6.6a. Photograph of grid pattern marked out on the rough surface concrete block – floated surface side.

Figure 6.6b. Zoom in of floated surface.

Figure 6.7a. Photograph of grid pattern marked out on the rough surface concrete block – timber shuttered surface side.

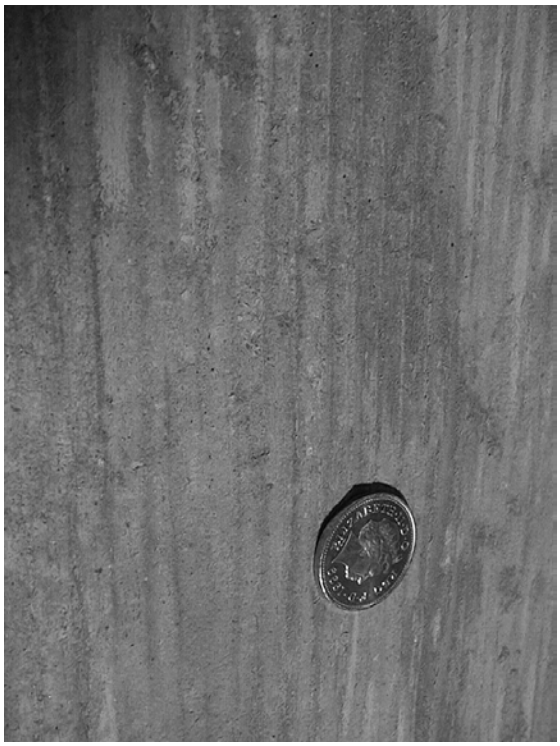

Figure 6.7b. Zoom in of timber shuttered surface.

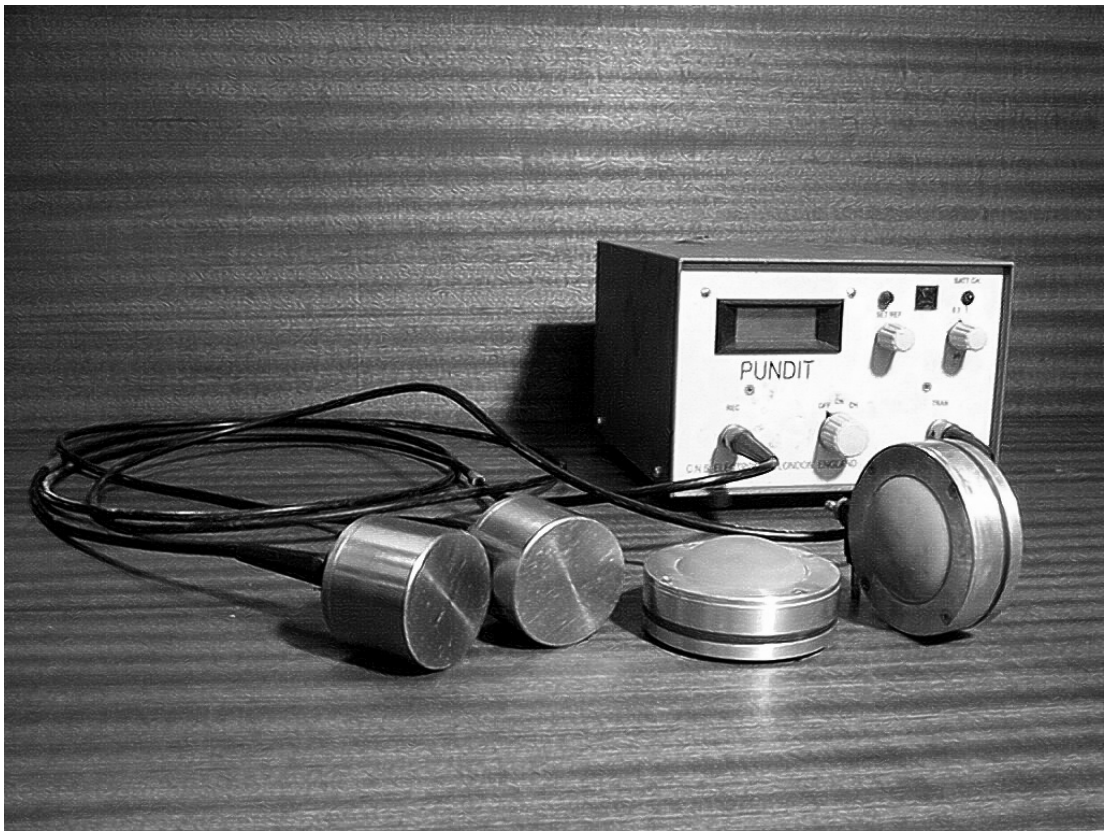

Figure 6.8. Pundit apparatus, 54kHz transducers and prototype membrane shoes.

Figure 6.9. Conventional coupling of transducers using Swarfega.

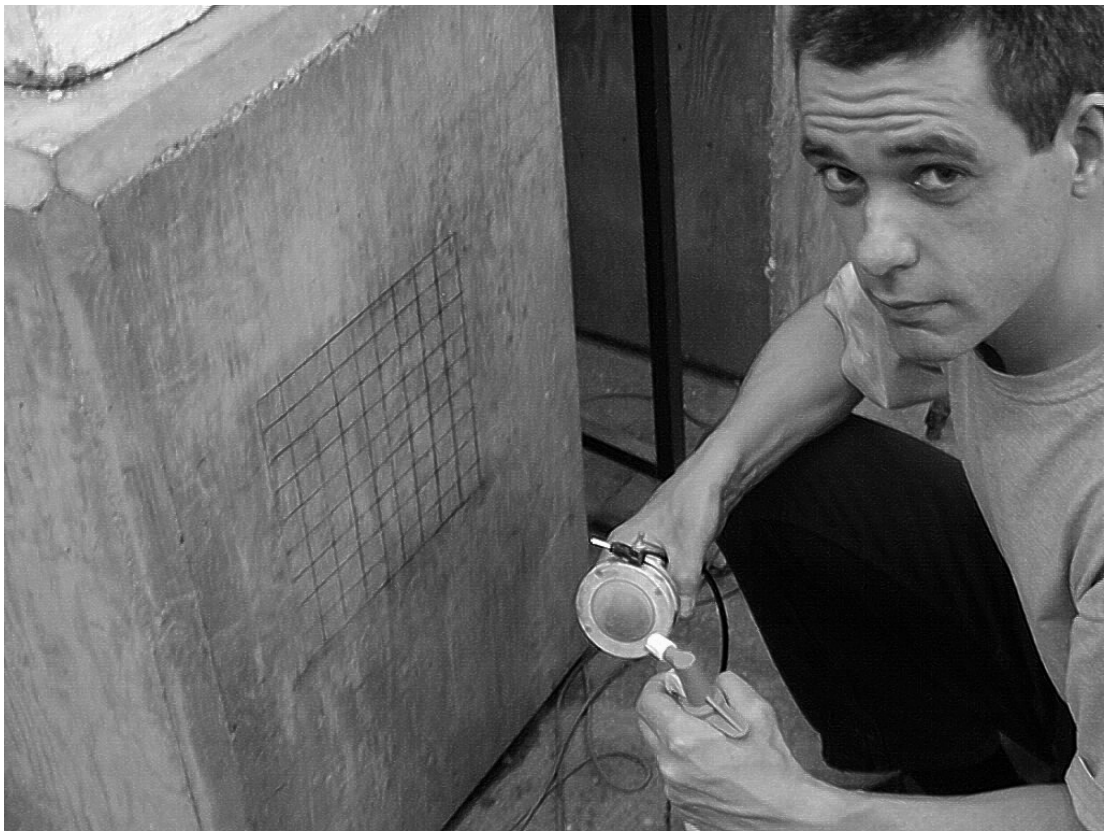

Figure 6.10. Film of water sprayed onto membrane shoe.

Figure 6.11. Application of membrane device to grid point on concrete block under test.

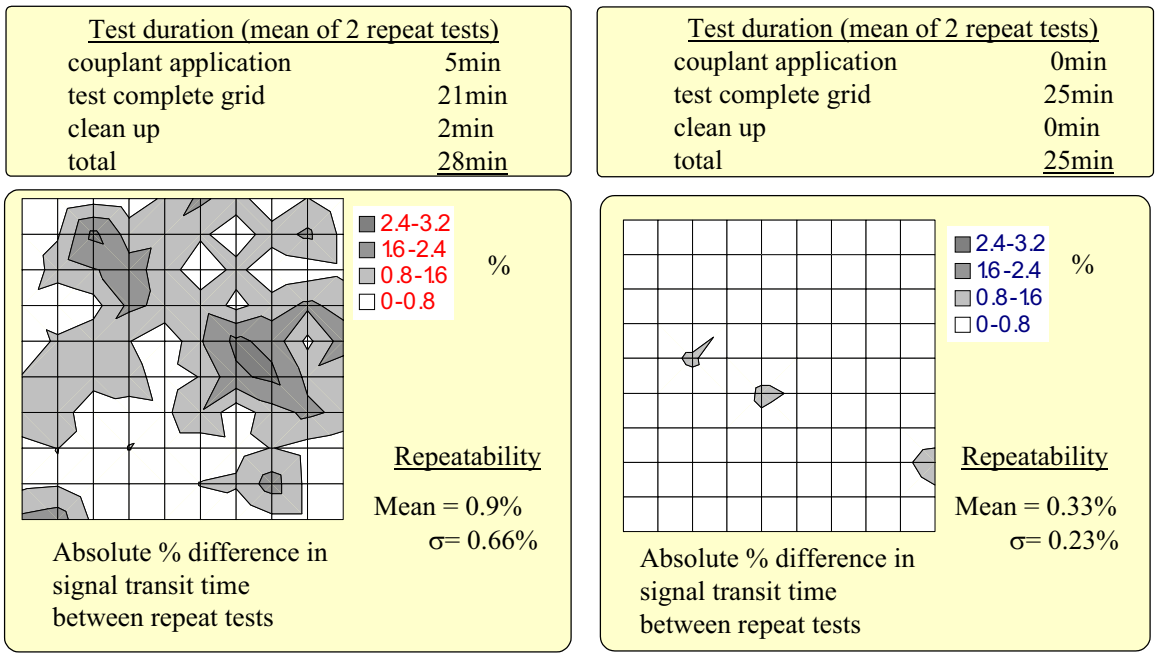

(a) (b)

Figure 6.12. Comparison of test duration and repeatability when testing flat shuttered concrete block. (a) conventional viscous coupling; (b) wet membrane coupling.

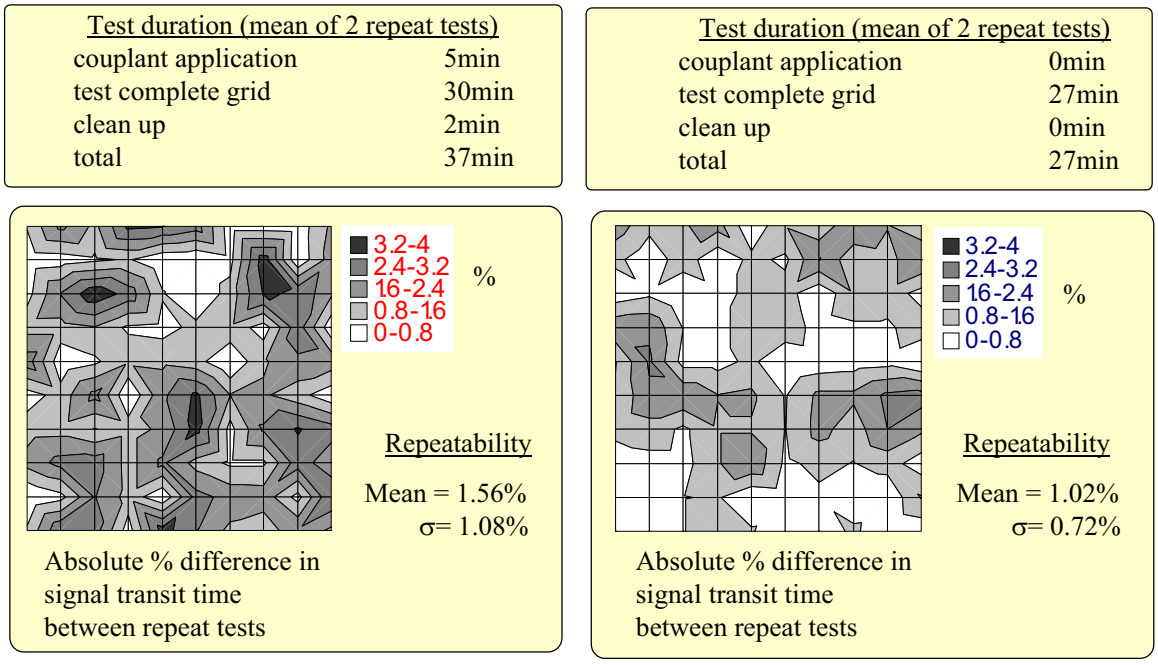

(a) (b)

Figure 6.13. Comparison of test duration and repeatability when testing rough surface concrete block. (a) conventional viscous coupling; (b) wet membrane coupling.

Chapter 7

Conclusions

7.1 Review of thesis

This thesis addressed some of the limitations of current commercial ultrasonic pulse velocity apparatus used for the routine inspection of concrete with the intention of improving the technique.

Chapter 2 identified concrete as a very versatile, potentially durable, complex composite material. In service it is exposed to a wide variety of environments and, because of its physical and chemical nature, it may deteriorate as a result. Once deterioration is apparent its classification and extent need to be appraised so that appropriate remedial action can be specified. Evidence is often required to identify the extent of internal voids and crack systems, as a result of inadequate workmanship. The long term monitoring of changes in material properties, crack systems and structural performance forms a necessary part of any maintenance program. Several diverse techniques for inspecting concrete quality or integrity were identified, each with its own particular advantages and limitations, there being no universal panacea. It was noted that at present civil engineering has the most confidence in the most destructive methods of test. For a non destructive test to be accepted would predominately require that its results are not ambiguous, costs involved with its use are low, and it should be convenient and rapid to employ. Ultrasonic pulse velocity testing was found to be well established and favoured for testing concrete uniformity. It is recognised for its relative speed of inspection and low cost. Resolving the limitations of the technique would make the technique more attractive to users and those that specify inspection requirements.

It is known that the measured pulse velocity varies with the path length tested for apparatus that uses threshold crossing to determine received signal arrivals. When the absolute value of the velocity in concrete is required, this anomaly can become significant. In Chapter 3 the factors that contribute to this anomaly were investigated. Signal losses due to beam spreading were predicted along with an experimental investigation to obtain functions that describe signal attenuation due to material properties. Commercial transducer and excitation characteristics were explored to model the pulse emitted from a transducer. From these studies the extent for the anomaly when testing various concrete mixes was predicted and a function has been derived to correct measurement errors.

Absolute values of measured pulse velocity are dependent on the reliability of the adopted technique used for calibrating the apparatus which is not so straight forward as it may seem. Calibration is achieved by coupling the transducers to a bar and setting the apparatus display to a time value stamped on the bar so as to remove the inherent time delay in the apparatus circuitry. The calibrated time value coincides with the time that a longitudinal bulk wave would take to propagate the length of the bar. However, being bounded the bar acts as a wave guide and so propagation of bulk waves cannot be assumed. To investigate this, chapter 4 reported on a finite element study that was carried out on wave propagation in a finite length of bar. To aid interpretation of data, an investigation of signal-processing techniques that were suitable for the evaluation of wave velocities in dispersive systems was carried out. A comparison of the techniques is presented in Appendix 1.

Commercial ultrasonic apparatus is predominately limited by the requirement that a viscous couplant should be applied between the transducer face and the surface under test so as to facilitate signal transmission. For an alternative, the solid coupling of transducers using a soft rubber was investigated in chapter 5. The topology of a range of concrete surfaces was surveyed. For rubber contact with such surfaces the characteristics of ultrasonic transmission across a low load interface was investigated experimentally. Numerical contact models were derived to predict the true contact area as a function of applied load that an axi symmetric body makes when pressed onto a real rough surface and thereby predict signal transmission. Such models enabled the design optimisation of a solid coupling device. A simple-to-program solution technique was developed to solve the contact model equations. Model predictions were validated against classical analytical solutions and experimental verifications. The performance of dry rubber coupling transducers to concrete was evaluated by employing a combination of experimental results and model predictions. Additionally the option of wetting a rubber membrane coupled device just with water was investigated, which still avoided the inconvenience of conventional viscous coupling.

The application of wet membrane coupling of transducers was discussed in chapter 6. Prototype membrane shoes to fit to standard commercial transducers were designed and optimised using the derived contact models. A comparison with conventional viscous coupling was conducted for the inspection of a 100 point grid on two different concrete blocks. The performance of a technique was gauged by the repeatability of results, the time to inspect the grid and time to prepare for and clean up after inspection.

7.2 Summary of findings

7.2.1 Correction of measured pulse velocity

The anomaly that measured pulse velocity varies with path length tested was attributed to the threshold crossing method employed by commercial apparatus to recognise the arrival of the received signal. As the signal amplitude decays with distance propagated due to beam spreading and material attenuation, the threshold was shown to cross by a later phase of the received signal.

Commercial transducers used for through transmission pulse velocity testing of concrete excite signal wavelengths greater than the diameter of the transducer which result in these transducers acting as a point source. Losses due to beam spreading can then be approximately as being inversely proportional to distance propagated.

The attenuation coefficient α for mortar and 5mm & 10mm aggregate concrete was experimentally determined. For wavelengths greater than 3 times aggregate size, the coefficient of attenuation for concrete was shown to be approximately a linear function of frequency.

The effect of the PUNDIT apparatus exponentially decaying excitation pulse applied to commercial narrow band transducers was investigated. The outcome was a near doubling of the expected period at the centre frequency of the first half cycle of the emitted signal and an approximate 90^{o} phase shift on the trailing part.

With these three findings in mind simple functions were derived to predict the modification of pulse shape with distance propagated in a concrete with a given aggregate size and thereby predict the variation in measured signal transit times. Predictions were shown to agree with the extent of the anomaly given by Bungey and Millard [1996] that a typical reduction in the measured velocity of 5% for path lengths between 3m to 6m can be expected. A function was derived to correct the apparatus displayed signal transit time, which would require monitoring of the amplitude of the received signal first half cycle which current standard equipment does not have the capacity for.

When the absolute value of pulse velocity in concrete is required, it is recommended that the correction function suggested in this thesis be adopted.

7.2.2 Evaluation of calibration procedure

Signal processing techniques suitable for the analysis of dispersive signals were explored. The phase spectrum method enabled determination of phase and group velocities as long as the signal was compactly supported within the sampled time window and the signal to noise ratio was above 2:1. The wavelet transform was found to be particularly valuable for the analysis of noisy signals or those that contain multiple dispersive modes. A technique was developed by the author around the wavelet transform to extract group velocity.

The phase velocity was extracted from axi symmetric finite element model results by the phase spectrum technique. It was found that no mode propagates with significant energy above the fundamental bar velocity in a finite length of bar unless some restriction is imposed on lateral displacements. Analysis of finite element and experimental results by the wavelet transform technique found that most of the energy of the propagating wave in the finite length calibration bar travels at guided wave velocities. A low energy level component was observed propagating at the bulk velocity when analysing the magnitude of experimental and finite element signals in the time domain. In practice, providing the transducers are effectively coupled to the reference bar, this component will be of sufficient magnitude to trigger the threshold in advance of slower higher amplitude guided waves.

This thesis recommends that when absolute values of pulse velocity are required, care should be taken to effectively couple the transducers to the reference bar so that the apparatus will trigger off the faster low level energy component travelling at the bulk velocity. If performing a comparative study where the path length is relatively constant, absolute values are not important. For this case, it is recommended that calibration of equipment is not necessary and neither is any correction for path length measured.

7.2.3 Convenient coupling of transducers

Solid coupling of transducers was investigated as an alternative to conventional grease coupling. For a rubber rough surface interface where only about 10% or less contact is made, it was found that transmission was only a weak function of frequency, which contradicted the established quasi static model. Additionally it was found that the transmission was approximately proportional to the load applied to the interface. From this study a relationship between signal transmission and true contact area was argued.

Axi symmetric models were derived as opposed to full 3D models which were found to take a considerable solution time, and established line contact models which are more suitable for the modelling of contact between parallel rollers. A simple-to-program iteration technique was developed, which though crude was shown to adequately solve contact model equations. The performance of solid coupling was taken to be represented by the fractional transmission, given as the ratio of the transmission for an imperfect interface over that for a perfect interface. Experimental results took the fractional transmission to equal the transmission for rubber contact over grease coupling. Model predictions took the fractional transmission to equal the predicted true area of contact over the transducer diameter. With this in mind solid contact model predictions were shown to agree very favourably with experimental results. This validates the models, as well as the argument that for fractional contact areas of about 10% or less the transmission across the interface is proportional to true area of contact. The membrane contact model was derived for which no similar numerical model is known. The derivation was not so straight forward as for solid body models, requiring some empirical data for calibration of the model. However, membrane model predictions were shown to adequately predict the range of signal transmission that might arise from a given design.

For a hand held device, the transmission across a dry coupled low load rubber disc interface was shown not to be sufficiently strong for most practical applications. Membrane coupling was shown to conform better to rough surfaces so as to offer up to 6dB increase in transmission by such devices. As an alternative to dry coupling, the option of wetting a membrane device with very little water was researched. Initial trials found that signal transmission for wet membrane coupling was comparable and more consistent than conventional viscous coupling of transducers.

Prototype membrane shoes were designed with the aid of the membrane contact model which was used to optimise the design such that only a smear of water need be applied to the membrane to adequately acoustically couple the device. A comparison with conventional viscous coupling was conducted for the inspection of a 100 point grid on two different concrete blocks. The performance of a technique was gauged by the repeatability of results, the time to inspect the grid, and time to prepare for and clean up after inspection. It was found that wet membrane coupling of transducers was more convenient, less messy and offered improved repeatability of results. It is thus recommended by this thesis that wet membrane coupling of transducers should be adopted as standard practice whenever an ultrasonic study of the uniformity of a concrete structure is carried out.

7.3 Recommended future work

7.3.1 Correction of measured pulse velocity

For the proposed correction functions to be adopted would require experimental data to confirm their acceptance. Such a task is not trivial, requiring a range of concrete blocks to be fabricated. For a range of blocks with different path lengths, the consistency of a given mix should not vary too greatly so as not to affect results.

7.3.2 Verification of calibration technique

Axi symmetric finite element models found that no mode propagates with significant energy above the fundamental bar velocity in a finite length of bar unless some restriction is imposed on lateral displacements. It would be worth investigating the more involved full 3D model to verify if this is still the case. This investigation is of use when addressing the topic, when is a bar a bar, or, at what length can a bar be considered long enough such that only the propagation of guided waves need be presumed. This study made no recommendations here, which leaves scope for future work.

7.3.3 Contact models

The solid body, axi-symmetric contact model derived in this thesis has a wide range of uses. Scope for its improvement would centre on speeding up the convergence of the iterative solution. The membrane contact model is perhaps limited by the requirement of empirical functions for its calibration. However, its use is not seen to be as popular as modelling of solid body contact and so the necessity for its improvement seems unlikely.

7.3.4 Convenient coupling of transducers

It is proposed that the design of alternative coupled devices for inspecting concrete has been effectively addressed in this thesis. Future work would centre on getting the technique to be included in recommendations BS 1881 published by the British Standards Institute.

Appendix 1

Signal processing for dispersive systems

A1.1 Introduction

This appendix describes in greater detail the signal processing techniques used by the author to extract wave velocities from the dispersive signals encountered in chapter 4. A dispersive system is where the phase velocity of a wave is a function of frequency. For a finite duration signal that comprises a range of frequency components the effect leads to distortion of the wave packet as it propagates. An established technique for extracting phase velocity is the phase spectrum method. Two techniques developed by the author are based on the Hilbert and the Wavelet transform for the extraction of group velocity. Individually the established and developed techniques all suffer from various limitations. However, their combination improves the analysis. The appendix first describes a set of simulated dispersive signals that each technique will be validated against. The established phase spectrum technique is then described followed by the derivation of the author's techniques.

A1.2 Simulated dispersive signals

A set of simulated dispersive signals was obtained from the finite element model discussed in section 4.4. For this application the model simulates wave propagation in a 50mm diameter 2m long aluminium bar by approximating the bar as an axi-symmetric finite element mesh. Being axi-symmetric the model does not simulate the propagation of flexural (non axi-symmetric) modes, which provides a useful simplification. The phase velocities for longitudinal wave propagation in an infinitely long bar can be described by the classical solutions given in section 4.3. Validation of the signal processing techniques described in this appendix will be conducted by comparing their extracted wave velocities to classical solutions. The extraction of wave velocities requires two signals that are related to each other. Here a signal $u(t)$ will represent the input axial displacements applied to one end of the bar and signal $v(t)$ the monitored axial displacements at some point along the length of the bar. Chirp signals will be used for the input which have the property that the instantaneous frequency increases as a function time t. For a linear chirp a carrier signal $u_c(t)$ of duration T with a centre frequency f_c can be described by the following function

$$u_c(t) = \sin(2\pi f_c t\tau) \qquad \text{A1.1}$$

where the time variable τ can be given as

$$\tau = \frac{f_c t}{k} = \frac{t}{T} = \frac{n}{N} \qquad \text{A1.2}$$

where k is the number of cycles completed within the duration T for $n = 0 \;\; to \;\; N$ discrete points. The time trace and modulus of the FFT (Fast Fourier Transform) of a carrier signal given by equation A1.1 are shown in Fig A1.1 and Fig A1.2 respectively. Here the amplitude modulation of equation A1.1 can be considered to be a rectangular window of duration T. Such a window will possess numerous spectral maxima which does not make for a smooth function in the frequency domain as seen in Fig A1.2. The frequency spectrum can be improved when the carrier $u_c(t)$ is amplitude modulated by a function such as a Hanning window $u_H(t)$, which is characterised by a smooth decay to zero amplitude, and is given by

$$u_H(t) = 0.5\left[1 - \cos\left(2\pi \frac{t}{T}\right)\right] \qquad \text{A1.3}$$

The product of the carrier signal given by equation A1.1 and the amplitude modulation given by equation A1.3 provides the desired input signal $u(t)$, which can be given as

$$u(t) = A[u_c(t) \times u_H(t)] \qquad \text{A1.4}$$

where A is a constant. The time trace and smooth frequency spectrum of a Hanning windowed linear chirp input signal are shown in Fig A1.3 and Fig A1.4 respectively. Such signals possess good low frequency content and are fairly broad band yet of relatively long duration (high time bandwidth product) which are ideal properties for signal processing.

Fig. A1.5 through to Fig. A1.16 show details of the three types of simulated signals that were constructed for the validation of the signal processing techniques. They are characterised by:

1) The bandwidth of the input signal at the bar end as shown in Fig. A1.5 and Fig. A1.6 is limited so as to predominately excite the fundamental L(0,1) mode. The early part of the monitored signal at 500mm from the bar end as shown in Fig. A1.7 and Fig. A1.8 will

then comprise solely the faster L(0,1) mode with the later portion a superposition of this and a number of slower modes. This was achieved by setting the centre frequency f_c of the input chirp signal to 40kHz;

2) Both signals the same as type (1) but with non-coherent noise added to both input and output as shown in Fig. A1.9 through to Fig. A1.12. This would simulate real life signals. Noise as is shown in Fig. A1.13, was provided by the function described in section 5.3.1 that forces a Gaussian distribution from a set of random data. Noise amplitude was set such that in the 20kHz to 60kHz frequency range the signal to noise ratio would be greater than 2:1 which is evident by comparing the FFT of the noise shown in Fig. A1.14 with the monitored signal FFT shown in Fig. A1.8.
3) Input same as type (1), but output being the superposition of the signal monitored at 250mm and the signal monitored at 750mm multiplied by –2 to simulate the presence of a reflection in the output as shown in Fig. A1.15 and Fig. A1.16.

A1.3 Phase spectrum by the Fourier transform

The established phase spectrum approach evaluates the phase velocity of a wave from the difference in the phase spectra of two signals obtained from different points along the passage of the wave. These two signals should be separated in time to allow evaluation of their individual phase spectra. If this is not the case then the alternative amplitude spectrum method [Pialucha et al (1989)] will provide discrete points on the dispersion curve. The technique is based around the Fourier transform and so assumes a signal to be periodic. As such the magnitude of the signal to be processed should decay away sufficiently rapidly (compact support) within the duration of the time window otherwise leakage of frequency components occurs. Another limitation of the technique is that only one wave packet should be present in the time signals. The phase spectrum of multiple wave packets will overlap and confuse the analysis. The phase spectrum method is briefly described here following a similar approach to Sachse and Pao [1978]. Consider a disturbance of finite duration that is generated at the location z=0, where the displacements for time $t \geq 0$ can be written as

$$u(0,t) = f(t) \qquad \text{A1.5}$$

The Fourier transform of this disturbance can be written as

$$U(0,\omega) = F(\omega) \qquad \text{A1.6}$$

The complex Fourier transform can be separated into its real and imaginary parts F_1 and F_2 respectively. The absolute value is then given as

$$\left|F(\omega)\right| = \left(F_1^2 + F_2^2\right)^{1/2} \qquad \text{A1.7}$$

such that the Fourier transform can be written in terms of

$$F(\omega) = \left|F(\omega)\right| \exp\left(-i\phi(\omega)_0\right) \qquad \text{A1.8}$$

where the phase spectrum $\phi(\omega)$ is given as

$$\phi(\omega) = \tan^{-1}\left[F_1(\omega) / F_2(\omega)\right] \qquad \text{A1.9}$$

If the pulse propagates a distance z then the Fourier transform of the $u(z,t)$ is given as

$$U(z,\omega) = F(\omega)\exp\left(-\alpha(\omega)z\right)\exp\left(-i\varepsilon(\omega)z\right) \qquad \text{A1.10}$$

where α is an attenuation parameter and ε the wave number, both being functions of the frequency ω. Substituting equation A1.8 into equation A1.10 gives

$$U(z,\omega) = \left|F(\omega)\exp\left(-\alpha(\omega)z\right)\right| \exp\left(-i\left[\varepsilon(\omega)z + \phi(\omega)_0\right]\right) \qquad \text{A1.11}$$

which gives the phase spectrum of the propagated pulse $\phi(\omega)_z$ as

$$\phi(\omega)_z = \varepsilon(\omega)z + \phi(\omega)_0 \qquad \text{A1.12}$$

which in terms of the wave number $\varepsilon(\omega)$ can be written as

$$\varepsilon(\omega) = \frac{\phi(\omega)_z - \phi(\omega)_0}{z} \qquad \text{A1.13}$$

Substituting equation A1.13 into equation 4.40 gives the phase velocity as

$$v_{ph} = \frac{z\omega}{\phi(\omega)_z - \phi(\omega)_0} \qquad \text{A1.14}$$

Alternatively we could consider the input to be described by the function $u(t)$ and the system the signal propagates in being characterised by the impulse response $h(t)$. The output signal $v(t)$ will then be the convolution of $u(t)$ with $h(t)$, thus

$$v(t) = u(t) * h(t) \qquad \text{A1.15}$$

By the convolution theorem it follows that

$$V(\omega) = U(\omega) \cdot H(\omega) \qquad \text{A1.16}$$

where $H(\omega)$ is the Fourier transform of $h(t)$. The frequency response function of the system is then obtained by

$$H(\omega) = \frac{V(\omega)}{U(\omega)} \qquad \text{A1.17}$$

Multiplying top and bottom of the RHS by the complex conjugate of $U(\omega)$ which is written as $U^*(\omega)$ we get

$$H(\omega) = \frac{V(\omega) \cdot U^*(\omega)}{U(\omega) \cdot U^*(\omega)} \qquad \text{A1.18}$$

which simplifies to

$$H(\omega) = \frac{1}{\left|U(\omega)\right|^2} G_{UV}(\omega) \qquad \text{A1.19}$$

where the cross spectrum $G_{UV}(\omega)$ is obtained from the individual Fourier spectra of the input and output given as

$$G_{UV}(\omega) = V(\omega) \cdot U^*(\omega) \qquad \text{A1.20}$$

The phase of the cross spectrum in equation A1.20 gives the phase difference between the input and output as a function of frequency which can be written as

$$\Delta\phi(\omega) = \angle G_{UV}(\omega) = \arctan\left(\frac{imag}{real}\right) \qquad \text{A1.21}$$

As an example the technique will now be applied to the straight forward case given by the simulated input and output signals shown in Fig. A1.5 and A1.7 respectively. If the output $v(t)$ had been reflected off a boundary at normal incidence the 180° phase difference could be corrected by multiplying the function by –1. Additionally, for real signals care should be taken when chopping or filtering signals in the time or frequency domain so as not to affect the phase spectrum. The technique for obtaining the phase velocity begins by first computing the FFT (Fast Fourier Transform) of $u(t)$ and $v(t)$. The phase difference $\phi(\omega)$ can then be computed from the phase of the cross spectrum. The computed phase spectrum $\phi(\omega)$ will be a discontinuous function with values that vary from 0 to 2π (depends on the argument used for the arctan computation) as shown in Fig A1.17 which must be transformed into a continuous function. At the point where the first discontinuity occurs and up to the second discontinuity 2π is then added to the function $\phi(\omega)$. From the second to the third discontinuity 4π is added to $\phi(\omega)$, and so on. The assembled continuous phase spectrum is shown in Fig A1.18. If a signal has little energy at certain frequencies, care should be taken in this region when assembling the continuous function, otherwise it is likely that the correction may be overlooked or 2π may well be unnecessarily added to the function. If there is an error in the continuous function at some frequency all subsequent phase values at higher frequencies will be subsequently affected. Referring to equation A1.14, the effect of such an error is reduced when $\Delta\phi(\omega) >> 2\pi$. This occurs when the product of propagation distance and frequency is large for which there are a relatively greater number of phase reversals. From the continuous phase spectra the phase velocity is then obtained by equation A1.14. From the phase velocity, the group velocity is obtained by equation 4.41 where the derivative can be solved by first fitting cubic splines to the phase velocity function, and then finding the differential of the splines.

The phase and group velocity curves that results from signals $u(t)$ and $v(t)$ are shown in Fig. A1.19 and fig. A1.20 respectively along with the relevant dispersion curves for the first three longitudinal modes evaluated by Disperse [Pavlakovic et al (1997)]. From zero to frequencies up to about 60kHz the extracted phase velocity agrees with the dispersion curve for the L(0,1) mode as shown in Fig. A1.19. The linear chirp signal proves to be an ideal signal for such a signal processing technique due to adequate energy at low frequencies and the smooth frequency spectrum. Above about 60kHz the extracted phase velocity becomes a cruder approximation. One reason for this that there was relatively little energy in the input

signal above 60kHz such that the results become increasingly unreliable. Additionally above the mode cut off frequencies of about 74kHz and 88kHz the input has also excited the L(0,2) and L(0,3) modes respectively. Since the signals represent axial displacements in the bar, at a given frequency above 74kHz the analysis will be dominated by which ever mode has the greatest axial displacements. This effect can be seen more clearly in the extracted group velocity shown in Fig. A1.20 which clearly shows up the existence of the first three longitudinal modes.

We now need to assess the technique for evaluation of phase velocity against the more demanding simulated signals. To simulate real life signals some noise was added to the input and output as shown in Fig. A1.9 through to Fig. A1.12. The extracted phase velocity for these signals is shown in Fig A1.21. Within the 20kHz to 60kHz frequency range the function adequately agrees with the L(0,1) mode. Outside this frequency range the extracted phase velocity becomes increasingly unreliable as the signal to noise falls below a ratio of 2:1. This is of particularly evident in the low frequency region where with reference to equation A1.14, errors in the continuous phase function have the greatest effect on the extracted phase velocity. The effect of errors that do occur in this region reduces further upstream as $\Delta\phi(\omega) >> 2\pi$. For such noisy signals, to acquire the group velocity would necessitate some smoothing of the extracted phase velocity function before its differential could be determined. Without having gone into too much mathematical rigour, it would appear that the phase spectrum method should be able to extract phase velocities from a set of signals over the frequency range where the signal to noise ratio is better than 2:1.

The final set of signals simulates the presence of a reflection in the output signal. This was obtained by dividing the monitored signal at 750mm by –2 and superimposing it on the signal monitored at 250mm form the bar end. It could also be considered that this simulates a signal with a signal to noise ratio of 2:1. The extracted phase velocity shown in Fig A1.22 is confused due to the overlapping of the spectra of the two wave packets present in the output signal. It would be impractical to determine the group velocity from such a function due to its oscillatory nature. The mean of the function follows the profile of the L(0,1) mode due to the dominance of the monitored signal at 250mm, which is twice the magnitude of the reflection. Thus it appears that over the frequency range where a signal is a superposition of a number of modes or wave packets the phase spectrum method is unlikely to provide any meaningful results unless the magnitude of the frequency components for one wave packet are at least twice that of any other.

A1.3 Instantaneous frequency by the Hilbert Transform

Audoin and Roux [1996] have estimated the time delay between two signals that corresponds to the asymptotic low frequency value by employing the Hilbert transform. The following section describes a technique developed by the author that uses the Hilbert transform to obtain the instantaneous frequencies from two related signals to enable extraction of group velocity. In the state of development presented the technique is limited to the analysis of signals for which the instantaneous frequency either continually rises or falls, such as is the case with linear chirp type signals. Since the introduction of the notion of the analytic signal [Ville (1948)] the Hilbert transform has been widely used in signal processing. The application of the Hilbert transform on normal real valued time signals enables them to be expressed as complex functions. This yields two useful properties, being the signal envelope and the instantaneous frequency, where the latter will enable the extraction of wave group velocity. To describe the technique, we begin by developing the analytic signal by following a similar approach to Randall [1987]. Consider a causal time signal where

$$u(t) = 0\,,\ t < 0 \qquad \text{A1.22}$$

meaning that there can be no output before the input is applied at time zero. The Fourier transform of this signal will comprise real and imaginary components

$$F\{u(t)\} = U(f) = U_R(f) + iU_I(f) \qquad \text{A1.23}$$

The Hilbert transform expresses the relationship between the real and imaginary parts of the Fourier transform by

$$U_R(f) = U_I(f) * \frac{1}{\pi f} \qquad \text{A1.24}$$

where the * represents a convolution. The Hilbert transform of a general frequency function $G(f)$ in the familiar form of the convolution integral can be written as

$$\mathrm{H}\{G(f)\} = \tilde{G}(f) = \frac{1}{\pi}\int_{-\infty}^{\infty} G(\phi)\frac{1}{f-\phi}\,d\phi \qquad \text{A1.25}$$

where the Hilbert transform is in the same domain as the original function. The Hilbert transform of a time function $u(t)$ is thus defined in the same way and is given as

$$\mathrm{H}\{u(t)\} = \tilde{u}(t) = \frac{1}{\pi}\int_{-\infty}^{\infty} u(\tau)\frac{1}{t-\tau}\,d\tau \qquad \text{A1.26}$$

or similar to equation A1.24 can be written as

$$\mathrm{H}\{u(t)\} = \frac{1}{\pi}u(t) * \frac{1}{t} \qquad \text{A1.27}$$

Here the sign function becomes useful where

$$\operatorname{sgn} t = \begin{cases} +1 & t > 0 \\ -1 & t < 0 \end{cases}$$

which has the Fourier transform of

$$F\{\operatorname{sgn} t\} = \frac{1}{i\pi f} \qquad \text{A1.28}$$

Recognising that a convolution in the time domain equates to a multiplication in the frequency domain results in

$$F\{\tilde{u}(t)\} = U(f)\cdot\{-i\operatorname{sgn}(f)\} \qquad \text{A1.29}$$

Hence the Hilbert transform of a time function can be obtained by multiplying positive frequency components by -i (a phase shift of -90^{o}) and negative frequency components by + i ($+90^{o}$). In the same manner as the relationship between real and imaginary frequency components was given in equation A1.24, we can apply the Hilbert transform to a real time signal to obtain a corresponding imaginary part. A complex time signal whose imaginary part is the Hilbert transform of the real part is known as an analytic signal given as

$$\overset{\triangledown}{u}(t) = u(t) + i\tilde{u}(t) \qquad \text{A1.30}$$

Similar to equation A1.8 the analytic signal can be written in terms of modulus and phase as

$$\overset{\nabla}{u}(t) = \left|\overset{\nabla}{u}(t)\right| e^{i\theta(t)} \qquad \text{A1.31}$$

where the envelope is obtained by

$$\left|\overset{\nabla}{u}(t)\right| = \sqrt{u^2(t) + \tilde{u}^2(t)} \qquad \text{A1.32}$$

and $\theta(t)$ is the instantaneous phase given by

$$\theta(t) = \tan^{-1}\left[\tilde{u}(t)/u(t)\right] \qquad \text{A1.33}$$

The rate of change of phase gives the instantaneous frequency, which in Hz is given by

$$f_i(t) = \frac{1}{2\pi}\frac{d\theta(t)}{dt} \qquad \text{A1.34}$$

For a sinusoidal wave, equation A1.34 coincides with the frequency. However, the instantaneous frequency of the sum of two ordinary waves is the average of their frequencies. Therefore the technique does not give the desired results for relatively noisy signals or where more than one signal or mode is propagating simultaneously. Additionally, the analytic signal is only simply applicable when the carrier frequency of a signal is greater than the highest frequency of the amplitude modulating window function [Randall (1987)]. This requires that the window function should be smooth so that higher frequency components decay rapidly. Also, since they are not oscillatory, window functions will have a predominant DC component, such that the carrier signal should not have comparable energy in this region. Fortunately, this is the case for the majority of ultrasonic signals encountered.

Equation A1.34 has similarities to equation 4.41, which gave the author the notion of using the instantaneous frequencies of a signal to extract the group velocity of a wave. As with the phase spectrum method, two signals $u(t)$ and $v(t)$ along the passage of the wave are required for the evaluation of group velocity. To enable individual processing, the signals should be separated in time if on the same time trace. A major limitation of the technique is that in order to compute the group velocity the signals should have the property that their

instantaneous frequencies increase with some function of time. Linear chirp signals given by equations A1.1 through to equation A1.4 were used which have the property that their instantaneous phase is a square function of time, and thus the derivative and hence instantaneous frequency is a linear function of time.

The technique will now be applied to the input $u(t)$ and output $v(t)$ signals shown in Fig. A1.5 and A1.7 respectively. The Hilbert transforms of signals $u(t)$ and $v(t)$ as obtained by equation A1.26 are shown in Fig. A1.23 and A1.24 respectively. The instantaneous phase of each signal is then computed by equation A1.33. The phase will be a discontinuous function with values that vary from 0 to 2π (depends on argument used for arctan computation) which must be transformed into a continuous function. This can be achieved in the same manner as was adopted for the phase spectrum technique described in the previous section. The continuous instantaneous phase of the input and output signal are shown in Fig. A1.25 and A1.26 respectively. From these functions the instantaneous frequency $f_i(t)$ for each signal is then determined by equation A1.34 where the derivative can be obtained numerically by the use of finite differences. The instantaneous frequencies $f_i\{u(t)\}$ and $f_i\{v(t)\}$ for the input and output signals are shown in Fig. A1.27 and A1.28 respectively. For a value of frequency f on the input $\mathrm{f_i}\{u(t)\}$ curve the time delay dt_f to a similar point on output $\mathrm{f_i}\{v(t)\}$ curve is then found as shown in Fig. A1. 29. Time delay measurement is straight forward so long as the instantaneous frequency increases or decreases continuously as a function of time. An illustration of the importance of this can be seen in Fig. A1.29, where beyond 0.2ms the instantaneous frequency becomes some kind of oscillatory function such that time delay measurement becomes unreliable. The group velocity $v_{gr}(f)$ as a function of frequency f is then obtained by

$$v_{gr}(f) = z / dt(f) \qquad \text{A1.35}$$

The group velocity curve extracted from signals $u(t)$ and $v(t)$ is shown in Fig. A1.30 along with the relevant dispersion curve for the L(0,1) mode evaluated by Disperse. Notice that at lowest frequencies the technique displays higher group velocities than the dispersion curve suggests. This is a typical artefact of the technique that occurs where there is some overlapping of the frequency spectra of the carrier and window functions that makes the analytic signal unreliable in this region. The irregularity beyond 40kHz frequencies is due to components of the L(0,2) or L(0,3) modes propagating faster than L(0,1) components which interferes with the analysis. Thus other than the trivial case of constant phase velocity, the

technique is only valid in a region where phase velocity continually falls or rises as a function of frequency.

Application of the technique to the noisy input and output signals shown in Fig. A1.9 through to Fig. A1.12 is not practical. For these signals the noise becomes so amplified in the instantaneous frequencies that evaluation of the time delay becomes unreliable. Thus the technique requires better than 2:1 signal to noise ratios. Finally the technique was employed on the output signal with the simulated presence of a reflection which is shown in Fig. A1.15 through to Fig. A1.16. The extracted group velocity is shown in Fig. A1.31 which should be compared with the one in Fig A1.30. For frequencies up to about 40kHz the extracted group velocities agree. The point in the signal shown in Fig. A1.15 where the simulated reflection was added corresponds to an instantaneous frequency of about 40kHz. The effect is that the extracted group velocity is confused for frequencies beyond 40kHz due to the overlapping of the two signals. Thus the presence of a reflection does not unduly affect the analysis over the portion of the signal where only the outgoing wave packet is present.

To be of some practical use the developed Hilbert transform technique would require the inclusion of some form of filtering in order to reduce undesirable effects when signals include significant noise, more than one mode or additional wave packets. The notion of evaluating group velocities by determining signal instantaneous frequencies was believed to be useful, such that the following section describes further development where the concept is applied to the wavelet transform.

A1.4 Ridge points by the wavelet Transform

The previous two signal processing techniques described are both susceptible to noise and are affected when multiple modes or reflections are superimposed on the same time trace. As an alternative a technique employing the WT was developed by the author to extract group velocity in a manner similar to the Hilbert transform technique which was described in the previous section. The wavelet transform (WT) discussed here will prove to be much less sensitive to noise and allow the investigation of complicated time signals. The concept of the WT was formalised in a series of papers by Morlet et al [1982]. Since the introduction a seemingly exponential yearly increase in papers on the subject have been published on all manner of diverse uses. Mathematically, significant work has been conducted [Meyer (1990)], [Mallet (1989)], [Daubechies (1988)] and [Chui (1992)]. Useful descriptions on the application to NDT and signal processing can often be found in related conference

proceedings and journals [Abbate et al (1999)] and [Moubarik et al (1993)] for example. It was found that [P. Kumar and E. Foufoula-Geogiou (1994)] gave a clear informative introduction before applying the technique to various geophysical data. Here the technique will be described without too much mathematical rigour in an attempt to convey its usefulness to NDT signal processing.

The original motive for the development of the WT [Goupillard et al (1984)] was to be able to transform a time signal and display the transform in such a manner that the contributions of different frequency bands could be analysed separately from each other. The representation is commonly known as time frequency analysis, where a one-dimensional time signal is mapped into two dimensions of time and frequency. This is not possible with the Fourier transform, where it is possible to go back and forth between frequency or time domains but never have information about the signal simultaneously in both domains. However, frequency-time analysis is not ideal since the uncertainty principle [Mallet 1989] states that arbitrarily high precision in both time and frequency cannot be achieved. Other time frequency representations for NDT applications like the short time Fourier (STFT) transform [Onsay and Haddow (1993)] and the Wigner-ville (WV) transform [Moubarik et al (1993)] have been compared to the WT. The WT is shown to be well adapted to localisation in time and frequency unlike the Fourier technique. The WV transform is not limited by the frequency time location, however, Prosser and Seale [1999] state that this advantage comes at the expense of computational complexity and the appearance of cross terms if the signal contains multiple frequency components that make interpretation of results very difficult.

Like the Fourier transform, the WT approximates a signal by a superposition of functions. Joseph Fourier discovered in the early 1800s that any periodic function can be expressed as an infinite sum of periodic complex exponential functions. The Fourier transform of a function $v(t)$, given as

$$V(\omega) = \int_{-\infty}^{\infty} v(t) e^{-i\omega t} dt \qquad \text{A1.36}$$

is a decomposition of the signal into complex exponential functions of different frequencies. The signal $v(t)$ is multiplied by an exponential term at some frequency ω and integrated over all time. If the result of this integration is high at a particular value of ω then the signal can be said to have a dominant spectral component of frequency ω. Since the integration is over all time, no matter where in time the component with a frequency ω appears, it will have the

same effect on the integration. Thus the Fourier transform evaluates the existence of a certain frequency but not where it is located in time. It follows then that if we want to locate features in time then the bulk of the integration should occur over a finite duration. To locate in time, wavelet functions $\psi(t)$ have a tapering or window operation so that they decay sufficiently fast, which is known as the property of compact support. Location in frequency will be provided by the oscillatory nature of $\psi(t)$ which to be an analysing wavelet must satisfy the admissibility condition that

$$\int_{-\infty}^{\infty} \psi(t)dt = 0 \qquad \text{A1.37}$$

Compact support and zero mean are just two characteristics of wavelets that can be satisfied by a whole myriad of functions. Having chosen an analysing wavelet ψ with its own properties we can create a whole family of related wavelets $\psi_{a,b}$ that are translated (b) and scaled (a) versions of ψ by

$$\psi_{a,b}(t) = \frac{1}{\sqrt{a}}\psi\left(\frac{t-b}{a}\right) \qquad \text{A1.38}$$

The normalisation $1/\sqrt{a}$ is chosen such that

$$\int|\psi_{a,b}(t)|^2 dt = \int|\psi(t)|^2 dt = 1 \qquad \text{A1.39}$$

for all scales a where $\psi(t) \equiv \psi_{1,0}(t)$, which implies that the wavelets have the same unit energy.

The continuous wavelet transform CWT of a function $v(t)$ is then given by the integral transform

$$W_\psi v(a,b) = \int_{-\infty}^{\infty} v(t)\overline{\psi_{a,b}(t)}dt = \int_{-\infty}^{\infty} v(t)\frac{1}{\sqrt{a}}\psi\left(\frac{t-b}{a}\right)db \qquad \text{A1.40}$$

Strictly speaking equation A1.40 describes the mapping of $v(t)$ in terms of time scale representation. Scale will be shown to be related to frequency when we come to describing the computation of the CWT. Equation A1.40 describes the inner product of $v(t)$ with $\psi_{a,b}(t)$ or in other words the CWT evaluates the similarity between the wavelet and the signal,

where the similarity is the frequency content. Thus the CWT coefficients refer to the closeness of the signal to the wavelet at the current scale. The inverse wavelet transform involves a two dimensional integration over scale *a* and translation *b* and is given by

$$v(t) = \frac{1}{C_\psi} \int_{-\infty}^{\infty} da \int_{-\infty}^{\infty} \frac{1}{a^2} W_\psi v(a,b) \psi_{a,b}(t) db \qquad \text{A1.41}$$

where the admissibility constant C_ψ depends on the choice of wavelet and is given by

$$C_\psi = \int_{-\infty}^{\infty} \frac{|\hat{\psi}(\omega)|^2}{|\omega|} d\omega < \infty \qquad \text{A1.42}$$

The CWT is also an energy preserving transformation (a type of Parseval's relationship for wavelets) that is

$$\int_{-\infty}^{\infty} |v(t)|^2 = \frac{1}{C_\psi} \int_{-\infty}^{\infty} \int_{0}^{\infty} \frac{1}{a^2} |W_\psi v(a,b)|^2 \, da db \qquad \text{A1.43}$$

In reality, for the analysis of sampled signals a discrete set of dilations and translations are considered that describe the discrete wavelet transform DWT. Choosing $a = a_0^m$ and $b = nb_0 a_0^m$ with a_0>1 with *m*,*n* as integers, generates from equation A1.38 a family of wavelets given by

$$\psi_{m,n}(t) = a_0^{-m/2} \psi\left(a_0^{-m} t - nb_0\right) \qquad \text{A1.44}$$

The exact reconstruction of *v*(*t*) from its WT is affected if discrete sequences are used since the inversion equation A1.41 is derived for continuous functions. Daubechies [1988] has shown that by setting a_0=2 and b_0=1, a set of orthonormal wavelets are constructed, (where the inner product of two different wavelets is zero and their integrals as in equation A1.39 are unity), which have excellent inversion properties. The integer *m* can then be thought of as an octave multiplier which results in a sparse set of orthogonal wavelets (where the inner product of two different wavelets is zero) with no redundancy. This would be ideal for the analysis of broad band signals such as those obtained in laser ultrasonics, however most ultrasonic signals rarely have frequency components occurring over more than a few octaves. As such the DWT with a dyadic basis (2^m) would generally provide too coarse a

representation for the recognition of NDT type features. A more appropriate representation can be achieved using suboctave divisions in the dyadic grid [Onsay and Haddow (1993)]. This results in a ideal dense time scale representation that aids interpretation of the WT at the expense of a lot of redundancy. Not being concerned about redundancy allows the use of Gaussian window functions, which are not orthonormal, but offer ideal time frequency localisation [Chui (1992)] and allow simple conversion from scale to frequency parameters. The Morlet wavelet is a Gaussian type function, which is defined by

$$\psi(t) = Ce^{-i\omega_0 t} e^{-\frac{t^2}{2}} \left(1 - \sqrt{2} e^{-\omega_0^2/4} e^{-\frac{t^2}{2}} \right) \qquad \text{A1.45}$$

where *C* is a constant to satisfy equation A1.39. The Fourier transform of equation A1.45 is given by

$$\Psi(\omega) = e^{-(\omega-\omega_0)^2/2} - e^{-\omega_0/4} e^{-(\omega-\omega_0)^2/4} \qquad \text{A1.46}$$

It is usual to have the unscaled centre frequency ω_0 greater than

$$\omega_0 = \pi \sqrt{\frac{2}{\ln 2}} \approx 0.85(2\pi) \qquad \text{rads/s} \qquad \text{A1.47}$$

which results in $\exp(-\omega_0^2/4) < 10^{-3}$, so that the second term in equation A1.46 can be neglected, such that equation A1.45 can be approximated by

$$\psi(t) = \pi^{-1/4} e^{-i\omega_0 t} e^{-\frac{t^2}{2}} \qquad \text{A1.48}$$

If ω_0<5 rads/s then wavelets described by equation A1.48 have a significant DC component. Most texts give equation A1.48 for the Morlet wavelet, where for their application signal reconstruction is not an issue. It was found useful to be able to have the option of ω_0<5 rads/s, which means that the desired filtering techniques would require the inversion process, thus equation A1.45 was used for this work. Equation A1.45 or equation A1.48 describe a complex wavelet ψ(t) possessing real and imaginary functions. A complex Morlet wavelet centred at time b = 0 is illustrated in Fig. A1.32 for an unscaled centre frequency ω_0=5 rads/s. From such a wavelet, a family of scaled and translated wavelets are obtained by applying equation A1.45 to equation A1.38. For a real Morlet wavelet where ω_0=3 rads/s,

scaled versions with zero translation for the octave multiples a =1, 0.5 and 0.25 are shown in the time domain in Fig. A1.33 with their Fourier transforms shown in Fig. A1.34. For a decrease in scale as seen in Fig. A1.33 the wavelet duration decreases, and the centre frequency and bandwidth of the wavelet increases as shown in Fig A1.34. This is the essential feature of the WT that is often highlighted at the start of most texts. That is that the WT is able to zoom in to analyse short duration features and zoom out to look at long duration features. The wavelet transform in this work will be displayed in frequency time, where the frequency plane is divided into equal intervals. This allows a more familiar representation than would be obtained in scale time where every scale or octave is subdivided by a constant number of suboctaves. We thus need to convert the scale parameter to its equivalent frequency. For the Morlet wavelet this is straight forward since the unscaled centre frequency of $\psi(t)$ is $\omega_0=2\pi f_0$ rads/s, thus when scaled by a the centre frequency ω_a is given as

$$\omega_a = \frac{\omega_0}{a} \qquad \text{A1.49}$$

This illustrates the constant Q nature of the CWT, where Q is related to the band width BW of a signal divided by the centre frequency ω_0 and so is given by

$$Q = \frac{BW_{\omega_0}}{\omega_0} \qquad \text{A1.50}$$

To obtain a desired family of wavelets, practically we would choose a range bounded by a maximum f_{max} (respecting Nyquist sampling theory) and minimum frequency f_{min} (respecting the wavelet duration) with which to analyse a signal. For a total N equi spaced frequencies, the corresponding scale at the n^{th} frequency is given by

$$a_n = \frac{f_0}{f_{\min} + \left(\frac{f_{\max} - f_{\min}}{N-1}\right)(n-1)} \qquad \text{A1.51}$$

At this point it will be useful to mention that if we had a family of wavelets that had constant bandwidth instead of constant Q then the CWT can be used to compute the STFT. This would require the duration of each wavelet governed by the windowing function to be a constant by having

$$f_{0n} = f_0 + \left(1 + \left(\frac{f_{\max} - f_{\min}}{N-1}\right)(n-1)\right) \qquad \text{A1.52}$$

Having covered sufficient background on wavelets we can now examine the characteristics of the CWT. All the following CWT will be applied to the simulated output signal first shown in Fig. A1.7. A Gray scale will be used for presenting the CWT where dark will relate to the higher positive magnitudes of the CWT coefficients. All wavelet sets will comprise 120 scaled wavelets that are derived from the unscaled mother wavelet. The Hilbert transform instantaneous frequency of the signal $v(t)$ will be included on frequency time (f,b) plots to help interpretation of the representations. To aid the understanding of the wavelet transform a comparison will be made between the CWT coefficients that result from using either real only or complex wavelets. For a family of real only Morlet wavelets, with an unscaled centre frequency of ω_0=7.5 rads/s, the coefficients of the CWT $Wv_r(f,b)$ are shown in Fig A1.35. It is rather difficult to relate any of the real only CWT representation to the signal $v(t)$ or the instantaneous frequency obtained by the Hilbert transform technique. This is because the real CWT is sensitive to phase, such that much of the similarity of the signal to the analysing wavelet will be lost if the two are 90^o out of phase. The representation is also complicated by the real CWT generating both positive and negative correlation coefficients. The square of the modulus of CWT coefficients $|Wv(f,b)|^2$ that result from a family of complex Morlet wavelets (ω_0=7.5 rads/s) are displayed in Fig. A1.36. This type of representation is commonly known as a scalogram [Hlawatsh (1992)] and describes the energy distribution of the signal. Comparing Fig. A1.36 and Fig. A1.35 it can be seen that the scalogram representation greatly improves the interpretation of the features of a signal when viewed in frequency time.

A closer examination of the CWT coefficients for a 37kHz real and a complex wavelet are shown in Fig. A1.39. The coefficients $v_{\psi f}(b)$ for the real wavelet are characterised by being an oscillatory function which can be considered to be the output of a band pass filter described by the wavelet $\psi_r(ft/f_0)$, when the input is $v(t)$ which is shown in Fig. A1.37. The band pass nature of the real wavelets is clearer when observing the FFT modulus of the real wavelet coefficients that are shown in Fig A1.40 which should be compared to the FFT modulus of $v(t)$ shown in Fig A1.38. Shown in Fig. A1.39 are the coefficients $|v_{\psi f}|(b)$ for the complex wavelet. Comparing the complex with the real coefficients reveals that $|v_{\psi f}|(b)$ represents the envelope of the band passed signal. For further appreciation the real and complex coefficients for 54kHz and 83kHz frequencies are shown in Fig. A1.41 through to Fig. A1.44.

Since a family of wavelets was shown to decompose a signal into its different frequency bands, it follows that for an orthogonal set of wavelets the relationship with the Fourier transform and the scalogram [Young 1992] is

$$\iint |Wv(\omega, b)|^2 \, d\omega db \equiv \int |V(\omega)|^2 \, d\omega \qquad \text{A1.53}$$

Even for a dense set of wavelets whose bandwidths overlap such that there is redundancy in the frequency domain, equation A1.53 remains a good approximation. This is verified in Fig A1.45 which shows the FFT of signal $v(t)$ and the frequency spectrum computed by the CWT for the unscaled wavelet centre frequencies of ω_0=3.8 and 6.3 rad/s. For the broad band set of wavelets (ω_0=3.8 rad/s), there is a lot of redundancy so the spectra appears smoother. For the set of narrower band wavelets (ω_0=6.3 rad/s) the profile of the spectra improves since the set tends towards orthogonality. Thus with narrower band wavelets you will get better identification of frequency components. However, since narrower band wavelets will be of longer duration there will be some degradation in the location of these frequency components in the time domain. This highlights that appropriate wavelets should be chosen and that because of the uncertainty principle, we have to settle for a trade off between frequency and time location.

Relating Parseval's theorem to equation A1.53 suggests that we can integrate over frequency to obtain the signal envelope given by

$$|\tilde{v}(b)| = \frac{1}{2\pi} \sqrt{\frac{1}{C_\psi} \int |Wv(\omega, b)|^2 \, d\omega} \qquad \text{A1.54}$$

Fig A1.37 shows the envelope of the input signal $v(t)$ evaluated by equation A1.54 for a set of wavelets where ω_0=7.5 rad/s, f_{min}=10kHz and f_{min}=120kHz. This is compared to the envelope obtained by the modulus of the analytic signal given by equation A1.32. The techniques show good agreement in the higher frequency region but both struggle to approximate the envelope for the early low frequency part of $v(t)$.

In the scalogram it is useful to observe the points in time-frequency where the maximum coefficients occur. When these peaks form a function of time or frequency they are known as ridge points [Mallet (1998)]. The coefficients at the ridge points can be shown to be sufficient alone to define the signal [Guillemain and Kronland-Martinet (1996)]. Abbate et al

[1999] suggest that since the ridge points for this application are related to high concentrations of acoustic energy they are natural candidates for the characterisation of ultrasonic signals. Two straightforward processes can be employed to obtain ridge point functions. If we stand on the time axis and look into the scalogram plot, the ridges in the CWT $Wv(b,f_i)$ will correspond to the instantaneous centre frequency f_i as a function of time b, which we shall call B ridge points. Fig. A1.46 shows the B ridge points of the CWT in Fig. A1.36. It is compared to the instantaneous frequency as obtained by the Hilbert transform method. For the CWT method, at low frequencies there is very poor frequency-time location since here the window width of the analysing wavelet is similar to the duration of the signal. As such it is not until the wavelet window duration corresponds to about half the signal duration that location is adequate. Since the CWT represents energy density, the ridge points can be used to evaluate wave group velocities. For the commonly encountered narrower band ultrasonic signals, the poor frequency-time location becomes an issue, which prevents the technique from providing useful results.

An alternative technique for extracting the group velocity from dispersive signals is suggested by the author. Similar to measuring time delays by the maximums in the time domain signal envelopes it is suggested by the author that we can use the energy envelopes as in Fig. A1.39 to evaluate the arrival time of a frequency component. This time we stand on the frequency axis and look into the scalogram plot, then the F ridge points will correspond to the time at which the most significant magnitude of a frequency component occurs. Fig A1.46 shows the F ridge points for the CWT in Fig. A1.36. It can be seen that there is now much better correlation in the low frequency region to the instantaneous frequency obtained by the Hilbert transform method. For the F ridge point technique to be of use for group velocity evaluation, any superimposed following modes or reflections should be of lower energy than the out going mode of interest. When this is the case if we stand on the frequency axis and look into the scalogram, the mountainous regions related to the CWT coefficients of the wave packet of interest will obscure the less significant following modes or reflections. Other than this straight forward case, Abbate et al [1999] and Veroy et al [1999] suggest that algorithms are required to compare time delays between similar modes for the case when modes overlap in the time domain.

For initial validation of the F ridge point technique, the group velocity was extracted from the straight forward input and output signals shown in Fig A1.5 and Fig. A1.7 respectively. Two suitable families of wavelets where chosen that would provide good results over the 10kHz to 100kHz frequency range. One set comprised of 120 relatively narrow band constant Q wavelets (CWT) using an unscaled centre frequency of ω_0=7.5 rad/s. The other

set comprised of 120 constant bandwidth wavelets (STFT) using an unscaled centre frequency of ω_0=2.2 rad/s. To extract the group velocity, the time delay dt_f between the F ridge points for the input and output signal is obtained in a similar manner to the Hilbert transform technique shown in Fig. A1.29. Group velocity is then obtained by equation A1.35. For the CWT and STFT analysis the extracted group velocities are shown in Fig. A1.47. Neither set of wavelets are able to extract the velocity for frequencies below about 10KHz since the wavelet duration in this region is greater than the duration of the signals which results in poor time location. From 10kHz to the L(0,2) cut off frequency the extracted group velocity from both sets of wavelets agrees with the Disperse prediction for the L(0,1) mode. Beyond about 70kHz where there is relatively little energy in the signal, what mode an analysis picks up on is related to the bandwidth and duration of the analysing wavelets. In this frequency region, the velocity obtained using the STFT follows the L(0,2) mode while that from the CWT tends to a mean of all modes present. When compared to the results from the Hilbert transform technique shown in Fig.A1.30 the F ridge point method proves a marked improvement. The technique was then applied to the noisy signals shown in Fig. A1.9 and Fig. A1.11. The extracted group velocity for these signals is shown in Fig A1.48. The extraction of group velocity for the noisy signals is relatively unaffected by the presence of noise. In the low frequency region, the choice of bandwidth for the STFT wavelets proves better choice than that for the CWT. Unlike the F ridge point technique, neither the Hilbert transform nor the established phase spectrum techniques were able to extract the group velocity from the noisy signals. Finally the F ridge point technique is applied to the input signal shown in Fig A1.5 and the output signal with the simulated reflection shown in Fig. A1.15. The extracted group velocity for these signals is shown in Fig A1.49. Here again a better choice of band width for the STFT has been made. The reason that the STFT set of wavelets gives better results over the complete frequency range considered is that its wavelets are more broadband for low frequencies giving improved time location and narrower banded for high frequencies giving improved frequency location. For the STFT wavelets the F ridge point technique gives much improved results compared to those from the Hilbert transform technique shown in FigA1.31. The established phase spectrum method was not able to extract the group velocities for these signals due to the severe oscillations in the extracted phase velocity shown in Fig. A1.22.

Before leaving the wavelet investigation, another use for the scalogram is signal enhancement, which is possible by filtering the signal in frequency time. The author initially presumed that a new technique was being developed but it was later discovered that it had already been reported [Moubarik et al (1993)]. The technique for filtering typical signals found in NDT begins by first computing the complex CWT and displaying this as a scalogram. Next all wavelet coefficients corresponding to an energy level smaller than say –

30dB are discarded and the signal is then reconstructed from the remaining coefficients by the inverse WT using equation A1.41. This energy thresholding in the time frequency domain acts locally on unwanted components unlike time domain averaging or frequency domain filtering which acts globally. To illustrate, Fig. A1.50 shows the scalogram where the coefficients 30dB down from the maximum of the scalogram shown in Fig. A1. 36 have been discarded. The inverse wavelet transform IWT is then performed to reconstruct the signal of $v(t)$. When performing the IWT, the coefficient C_ψ in equation A1.41 is assessed by evaluating the energy conservation given by equation A1.43. The reconstructed filtered signal and the Modulus of the corresponding FFT are shown in Fig. A1.51 and Fig. A1.52 respectively. The filtering process has removed the presence of the lower energy L(0,2) and L(0,3) modes without chopping out the higher frequency components belonging to the dominant L(0,1) mode. By being more selective rather than just filtering everything below 30dB down, the low frequency content of L(0,1) could have been protected.

A1.5 Conclusion

Signal processing techniques were investigated that might extract the wave velocities from the dispersive signals encountered in chapter 4. The established phase spectrum technique was described and two techniques developed by the author were presented. For validation of techniques a set of simulated signals obtained from a finite element model were constructed.

The phase spectrum technique provides the most reliable results for signals that are noiseless, and where only one wave packet propagates. Moving away from the ideal, the technique begins to struggle and group velocity evaluation from the extracted phase velocity becomes impractical.

A technique was developed by the author to extract group velocity from the signal instantaneous frequencies obtained via the Hilbert transform and analytic signal. The technique suffers if Hilbert transform of the signals to be analysed is not simply applicable. Additionally, similar to the phase spectrum technique it is unable to extract group velocities for noisy signals. However, where a slower wave packet is superimposed in the later portion of a signal the technique is still able to analyse the earlier uncontaminated portion.

As an alternative a technique was developed by the author that employed the wavelet transform. The so called F ridge point technique locates the time at which the most significant magnitude of a frequency component occurs. These times are compared for an

input and output signal and the difference gives the time delay and hence group velocity for that frequency component. The developed F ridge point method was shown to be much less sensitive to the presence of noise or other lower energy wave packets. Additionally, the technique does not suffer from the poor frequency time location that occurs with a similar technique reported by [Abbate et al 1999].

All three techniques investigated suffer from some limitations, there being no universal panacea. However, some combination of these methods should enable a complete analysis of dispersive signals such as those encountered in Chapter 4.

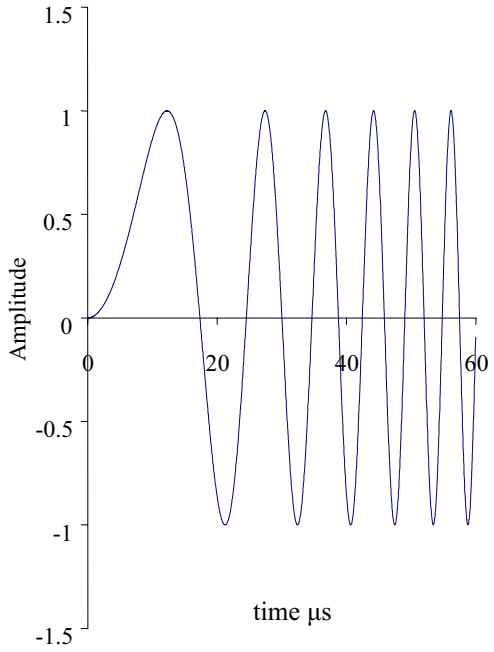

Figure A1.1. Example of a rectangular windowed linear chirp.

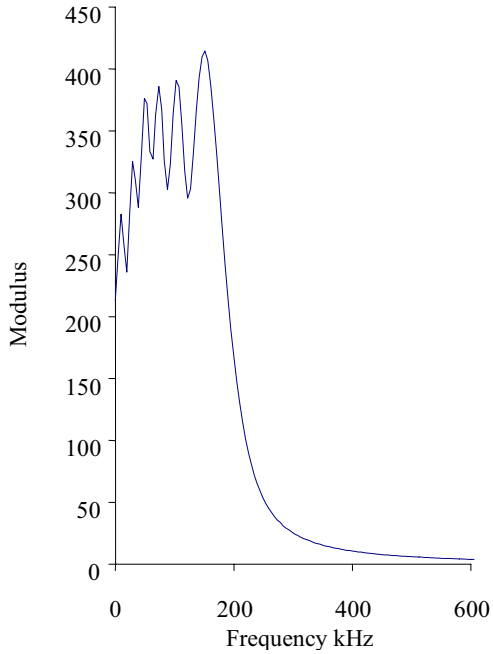

Figure A1.2. Modulus of FFT for rectangular windowed linear chirp.

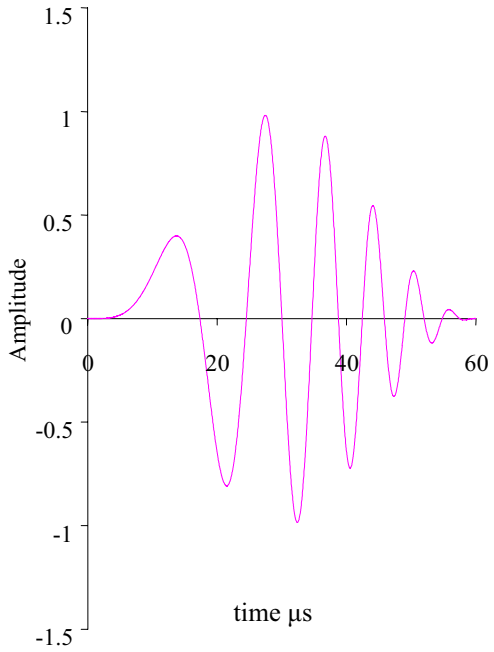

Figure A1.3. Example of Hanning windowed Linear chirp.

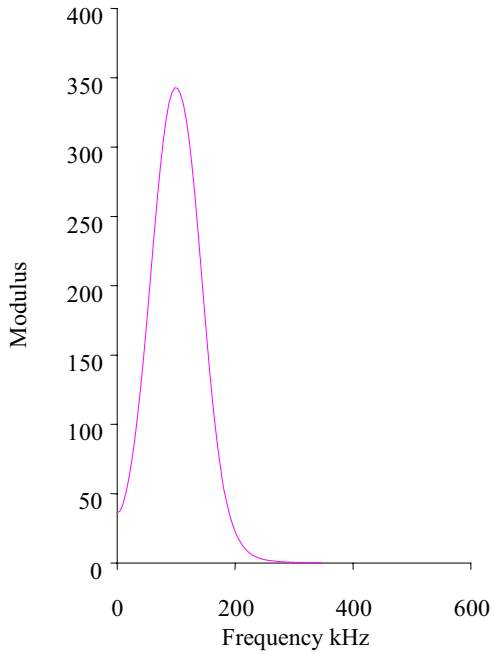

Figure A1.4. Modulus of FFT of Hanning windowed linear chirp.

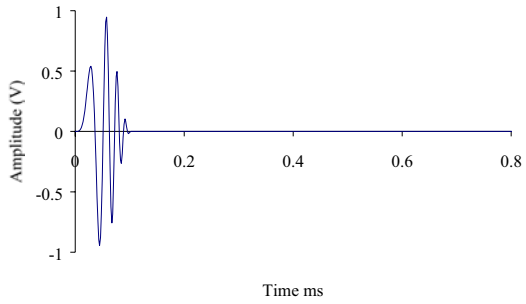

Figure A1.5. Input signal (f_c=40kHz) applied to bar end.

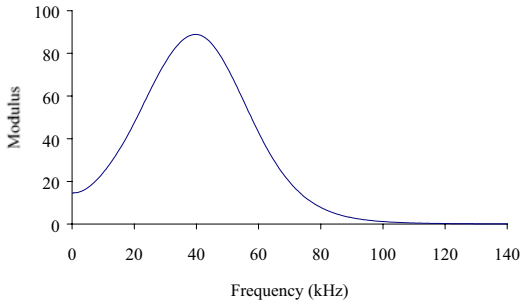

Figure A1.6. Modulus of the FFT of signal shown in Fig. A1.5.

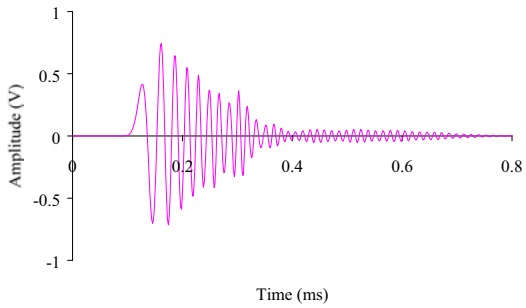

Figure A1.7. Signal (f_c=40kHz) monitored at 500mm from bar end.

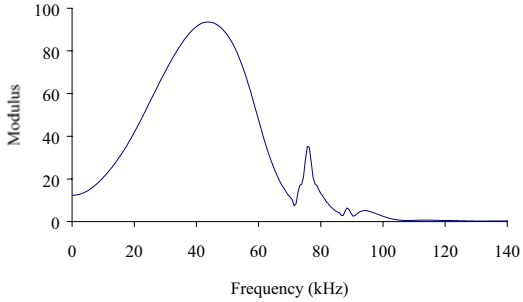

Figure A1.8. Modulus of the FFT of signal shown in Fig. A1.7.

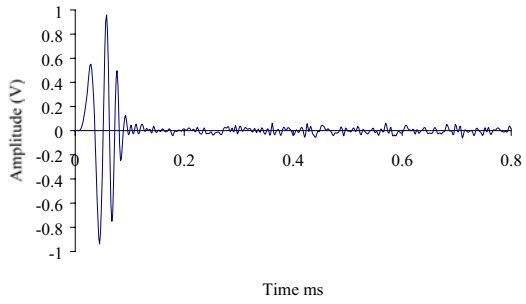

Figure A1.9. Input signal (f_c=40kHz) at bar end with added noise.

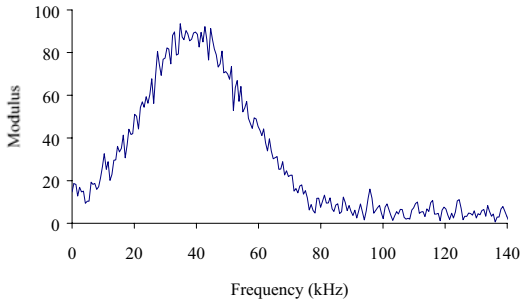

Figure A1.10. Modulus of the FFT of noisy signal shown in Fig. A1.9.

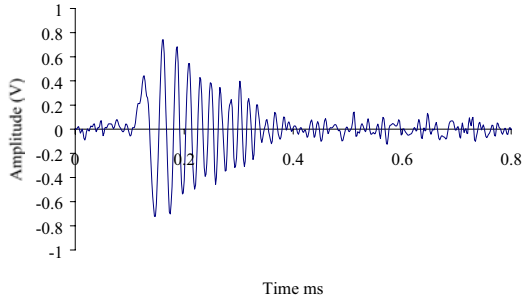

Figure A1.11. Signal (f_c=40kHz) monitored at 500mm from bar end with added noise.

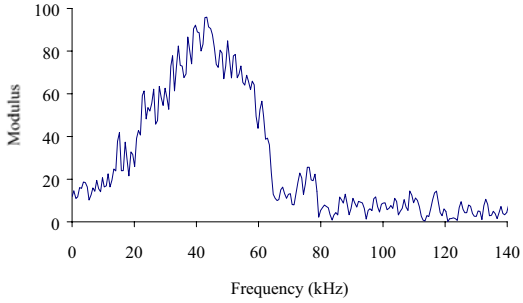

Figure A1.12. Modulus of the FFT of noisy signal shown in Fig. A1.11.

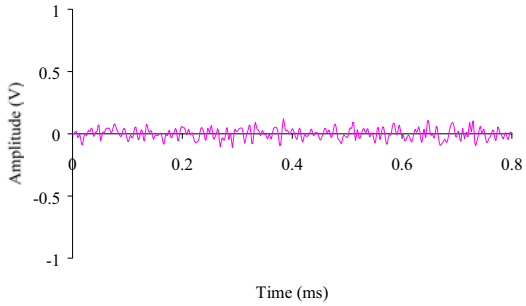

Figure A1.13. Noise content of output signal shown in Fig. A1.11.

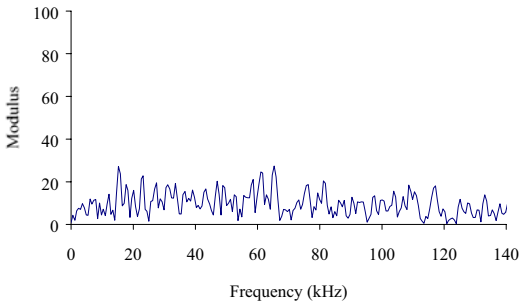

Figure A1.14. Modulus of the FFT of the noise content of signal shown in Fig. A1.11.

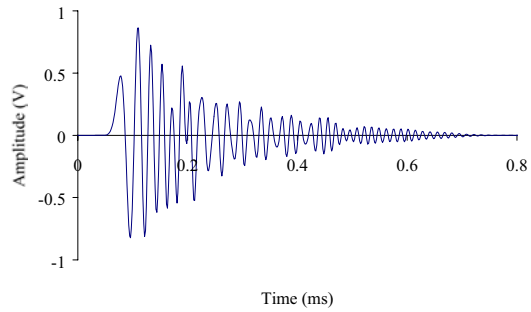

Figure A1.15. Signal (f_c=40kHz) monitored at 250mm from bar end with inverse of signal monitored at 750mm to simulate a reflection.

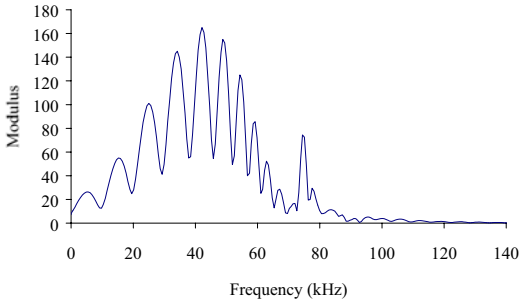

Figure A1.16. Modulus of the FFT of the signal shown in Fig. A1.15.

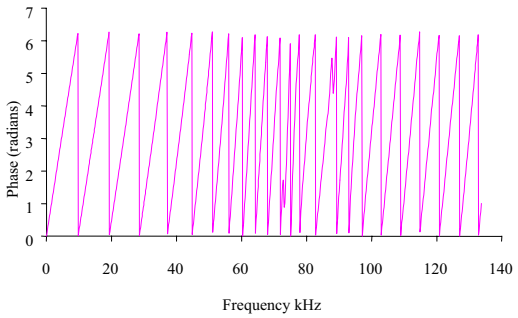

Figure A1.17. Phase spectra of the cross spectrum relative to the simulated signals shown in Fig A1.5 and Fig. A1.7.

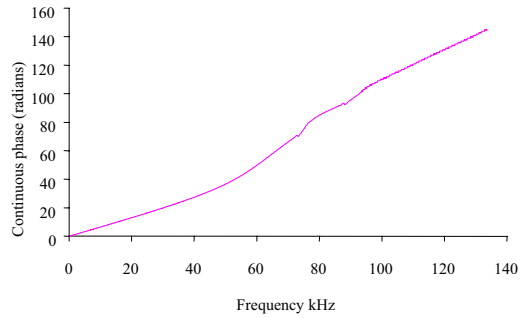

Figure A1.18. Assembled continuous phase spectra of that shown in Fig. A1.17.

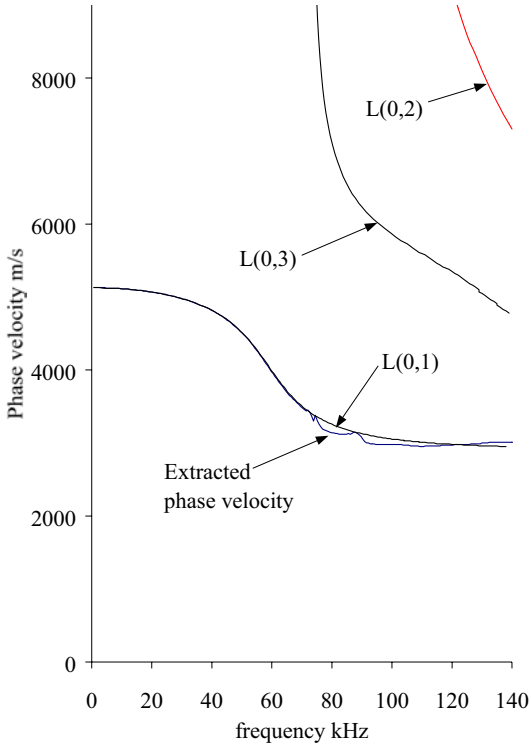

Figure A1.19. Phase velocity extracted from signals shown in Fig A1.5 and Fig. A1.7. Phase velocities for first three longitudinal modes predicted by Disperse.

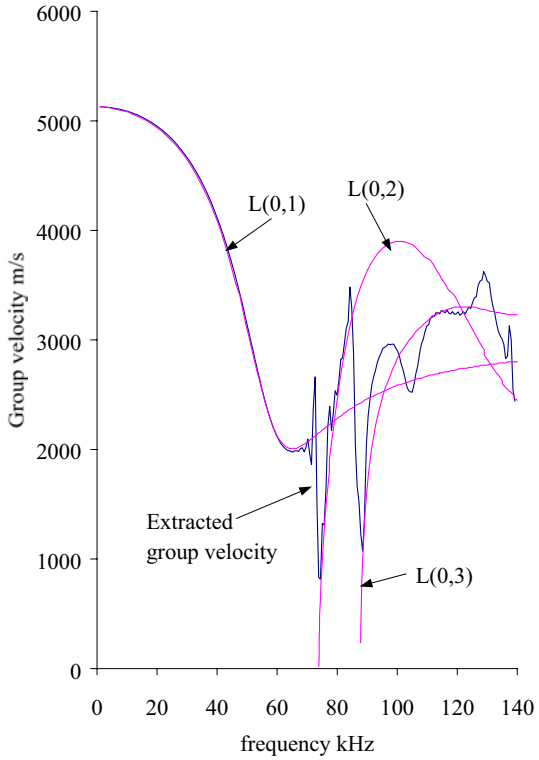

Figure A1.20. Group velocity extracted from signals shown in Fig A1.5 and Fig. A1.7. Group velocities for first three longitudinal modes predicted by Disperse.

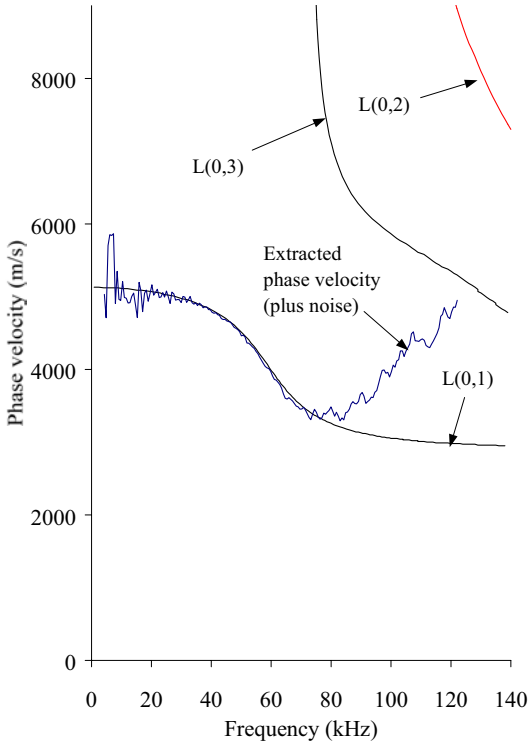

Figure A1.21. Phase velocity extracted from noisy signals shown in Fig A1.9 and Fig. A1.11 with phase velocities for first three longitudinal modes predicted by Disperse.

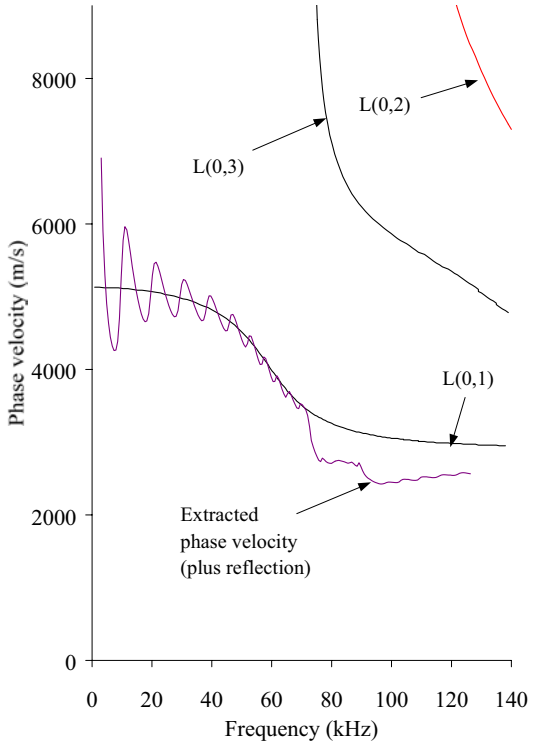

Figure A1.22. Phase velocity extracted from signals shown in Fig A1.5 and Fig. A1.15 with phase velocities for first three longitudinal modes predicted by Disperse.

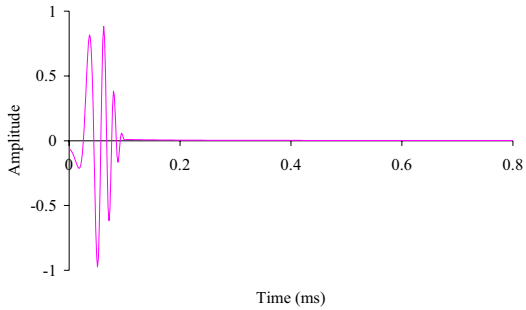

Figure A1.23. Hilbert transform of input signal shown in Fig. A1.5.

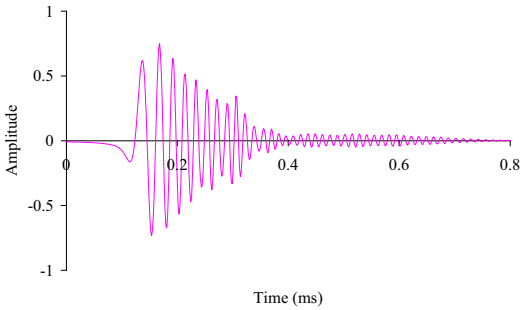

Figure A1.24. Hilbert transform of output signal shown in Fig. A1.7.

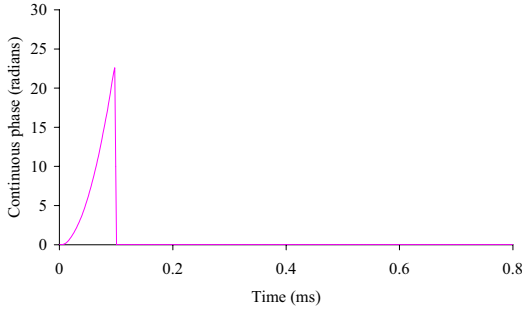

Figure A1.25. Continuous instantaneous phase of input signal shown in Fig. A1.5.

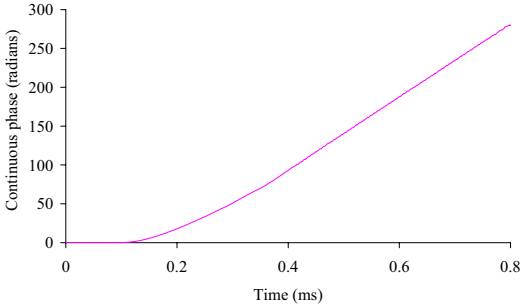

Figure A1.26. Continuous instantaneous phase of output signal shown in Fig. A1.7.

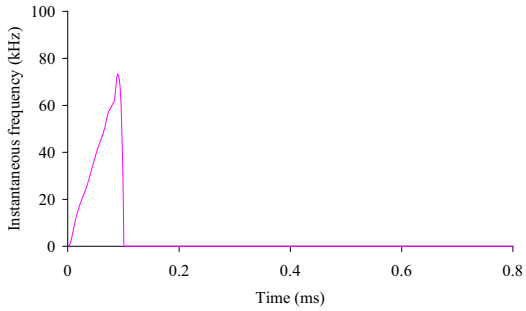

Figure A1.27. Instantaneous frequency of input signal shown in Fig. A1.5.

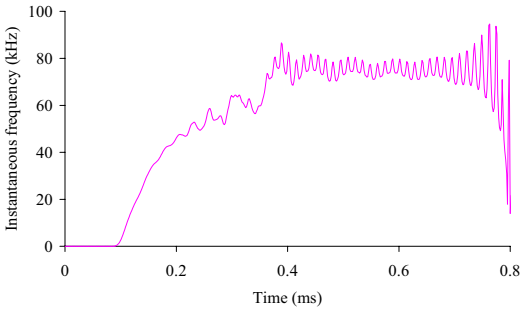

Figure A1.28. Instantaneous frequency of output signal shown in Fig. A1.7.

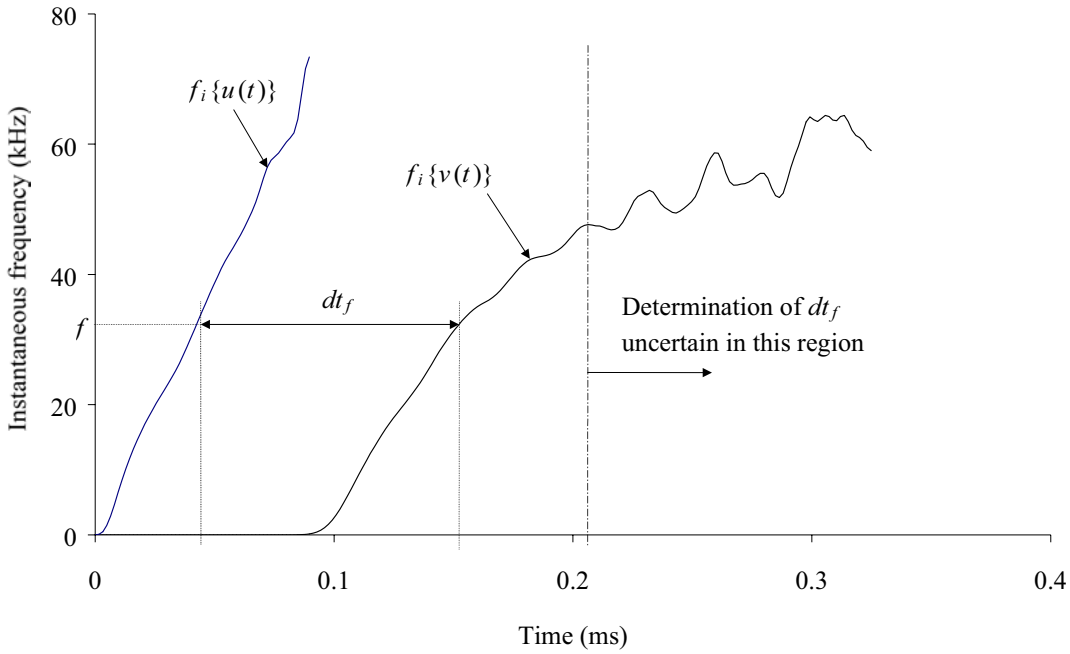

Figure A1.29 Evaluation of the time delay dt_f at frequency f from the instantaneous frequencies $f_i\{u(t)\}$ and $f_i\{v(t)\}$.

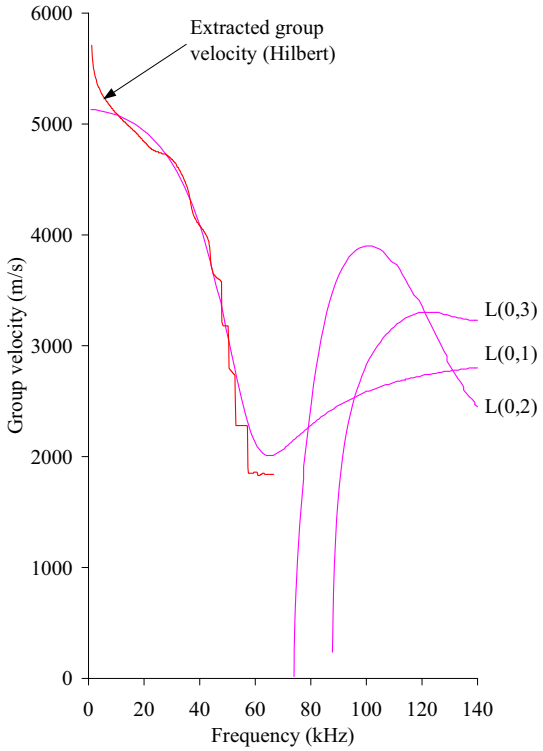

Figure A1.30. Group velocity extracted from signals shown in Fig A1.5 and Fig. A1.7 using the Hilbert transform technique. Group velocities for first three longitudinal modes predicted by Disperse.

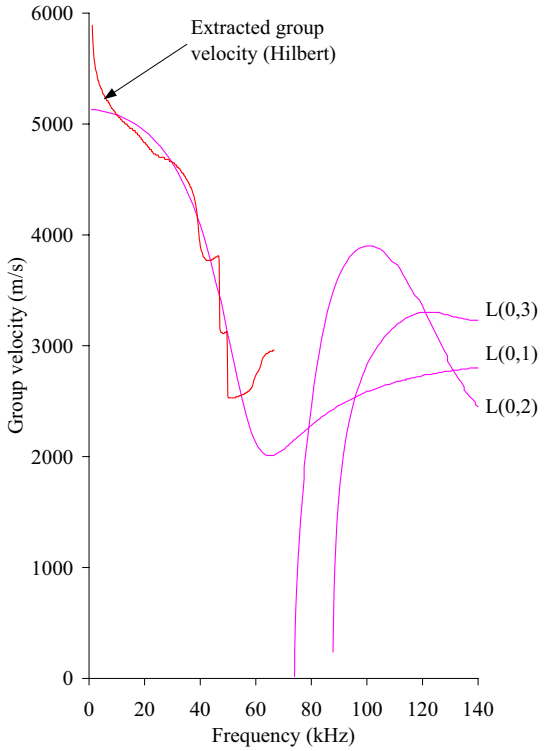

Figure A1.31. Group velocity extracted from signals shown in Fig A1.5 and Fig. A1.15 using the Hilbert transform technique. Group velocities for first three longitudinal modes predicted by Disperse.

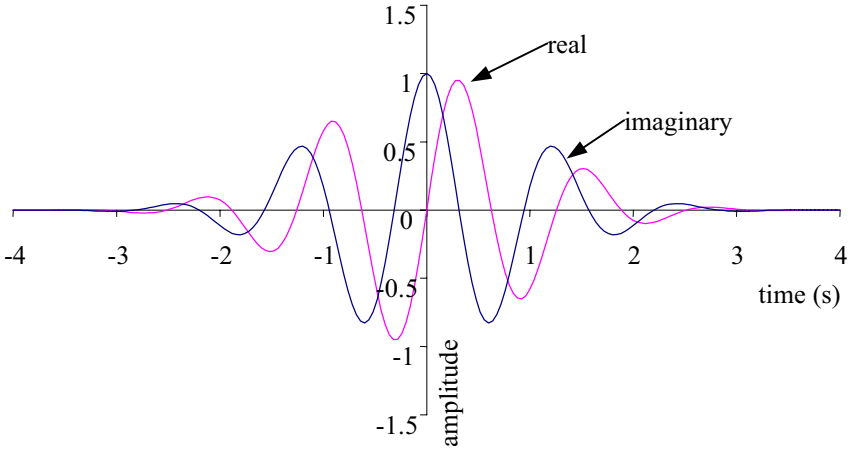

Figure A1.32. Real and imaginary Morlet wavelets for a=1 and ω_0=5.

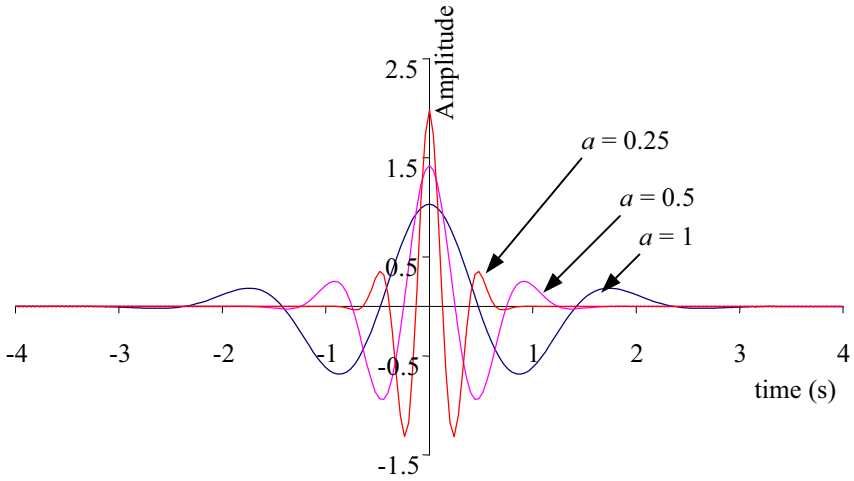

Figure A1.33. Time domain of real Morlet wavelets where ω_0=3 rads/s and translation b=0 for scales a=1, 0.5 and 0.25.

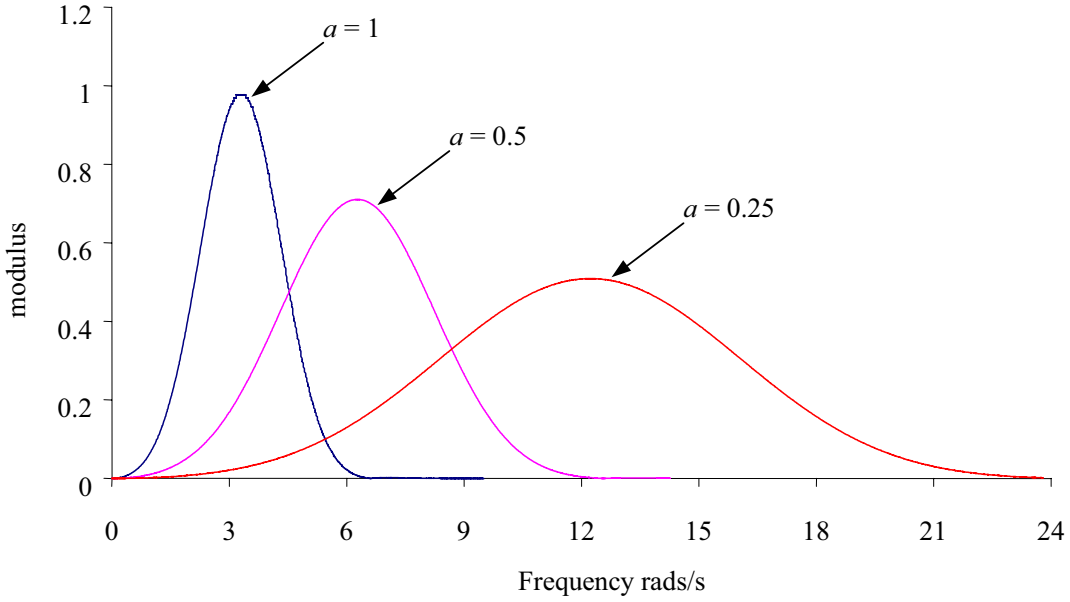

Figure A1.34. Modulus of FFT of real Morlet wavelets (ω_0=3 rads/s) for scales a=1, 0.5 and 0.25.

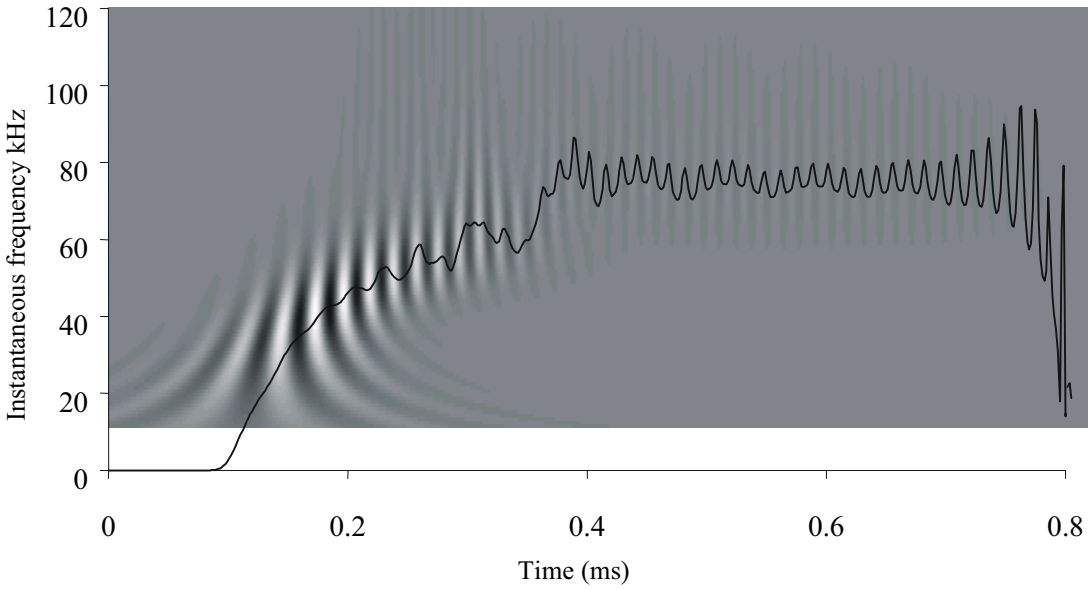

Figure A1.35. Coefficients of CWT of signal $v(t)$ using real only part of Morlet wavelets (ω_0=7.5 rads/s). Grey scale - grey zero, black max. negative, white max. positive. Hilbert transform instantaneous frequency included to help interpretation of representation.

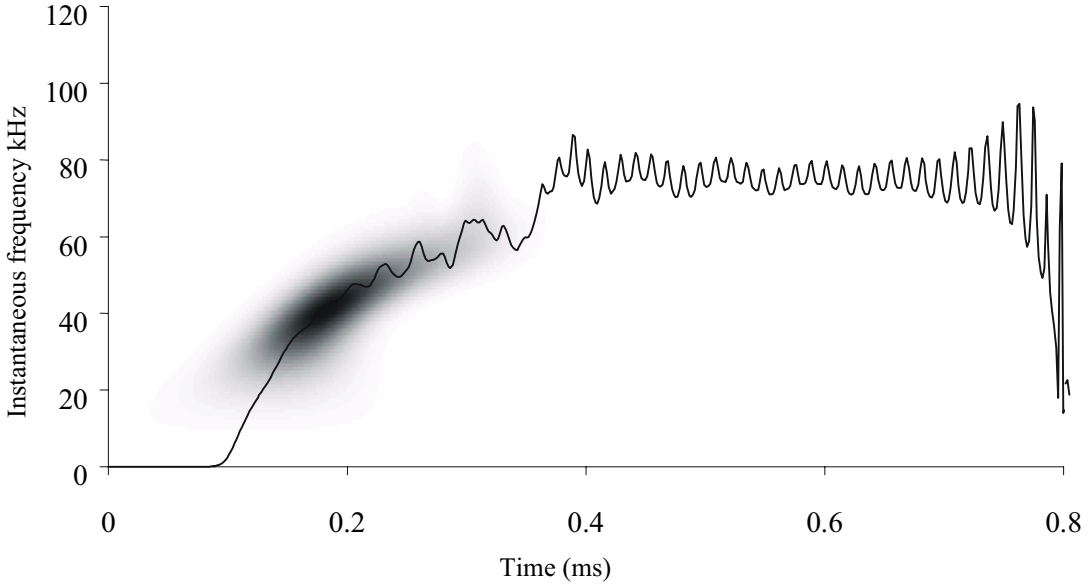

Figure A1.36. Scalogram (modulus of CWT) of $v(t)$ using complex Morlet wavelets (ω_0=7.5 rads/s). Grey scale- black max., white min. Hilbert transform instantaneous frequency included to help interpretation of representation.

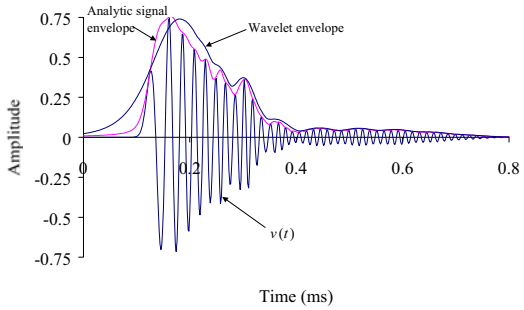

Figure A1.37. Monitored signal $v(t)$ first shown in Fig. A1.5 along with envelopes established from the Analytic signal and Wavelet transform.

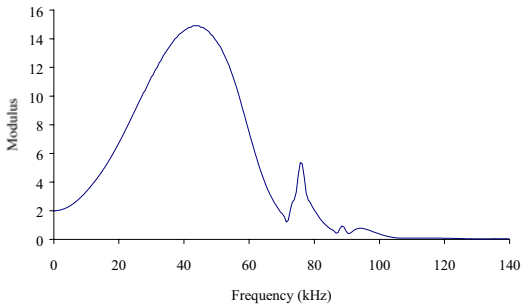

Figure A1.38. Modulus of the FFT of signal $v(t)$ shown in Fig. A1.37.

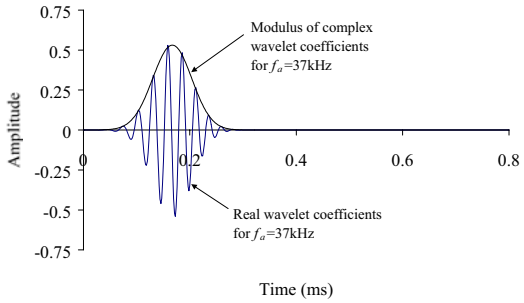

Figure A1.39. Wavelet transform coefficients (f_a=37kHz) of signal $v(t)$ for real (oscillatory function) and complex (envelope) Morlet wavelets.

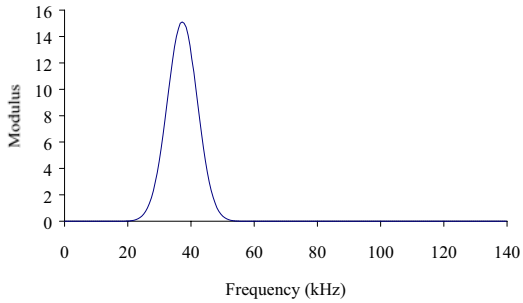

Figure A1.40. Modulus of the FFT for the real Morlet wavelet coefficients shown in Fig. A1.39.

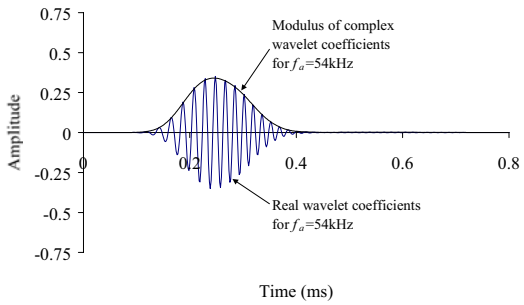

Figure A1.41. Wavelet transform coefficients (f_a=54kHz) of signal $v(t)$ for real (oscillatory) and complex (envelope) Morlet wavelets.

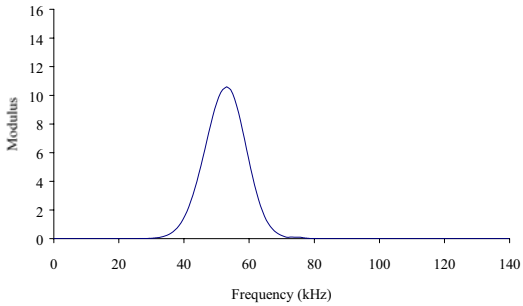

Figure A1.42. Modulus of the FFT for the real Morlet wavelet coefficients shown in Fig. A1.41.

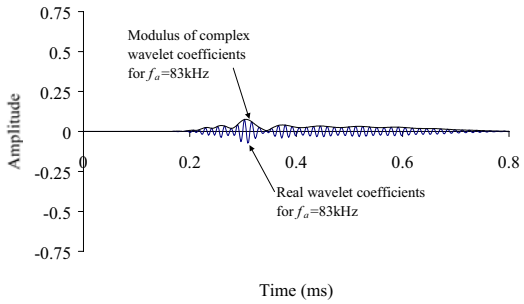

Figure A1.43. Wavelet transform coefficients (f_a=83kHz) of signal $v(t)$ for real (oscillatory) and complex (envelope) Morlet wavelets.

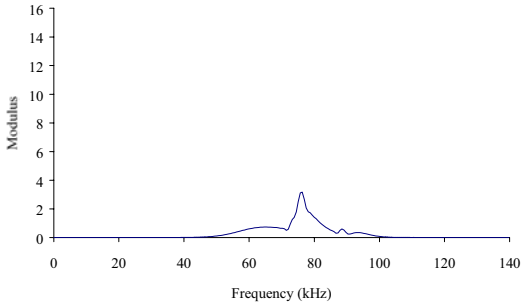

Figure A1.44. Modulus of the FFT for the real Morlet wavelet coefficients shown in Fig. A1.43.

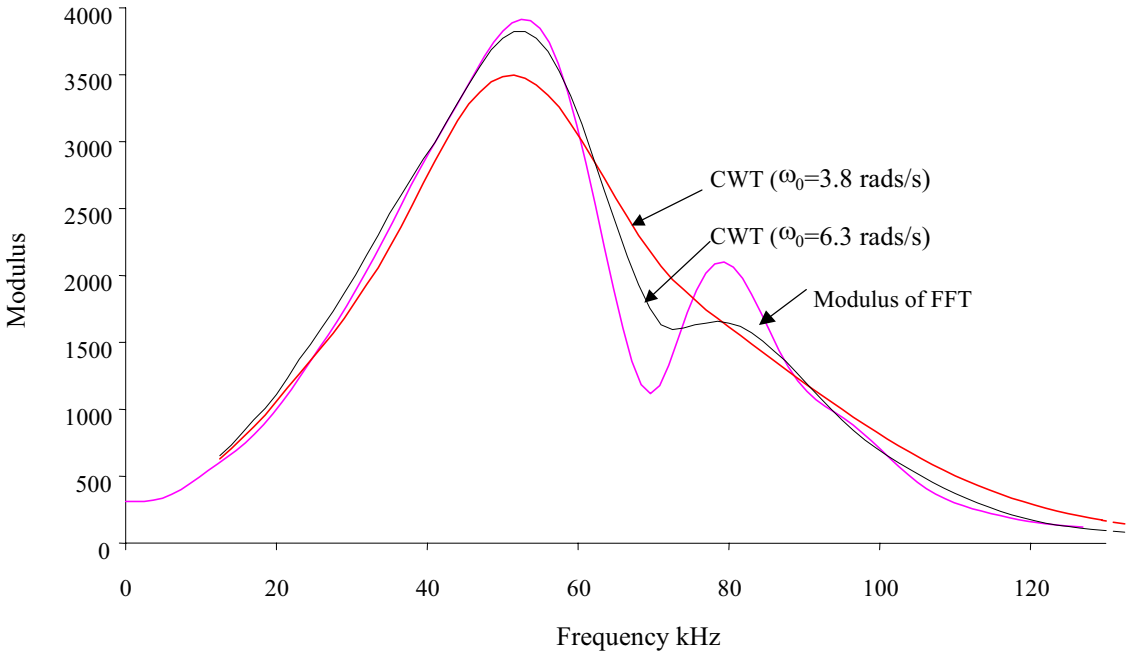

Figure A1.45. Comparison between the frequency spectra of $v(t)$ as obtained by FFT and CWT where ω_0=3.8 rads/s and 6.3 rads/s.

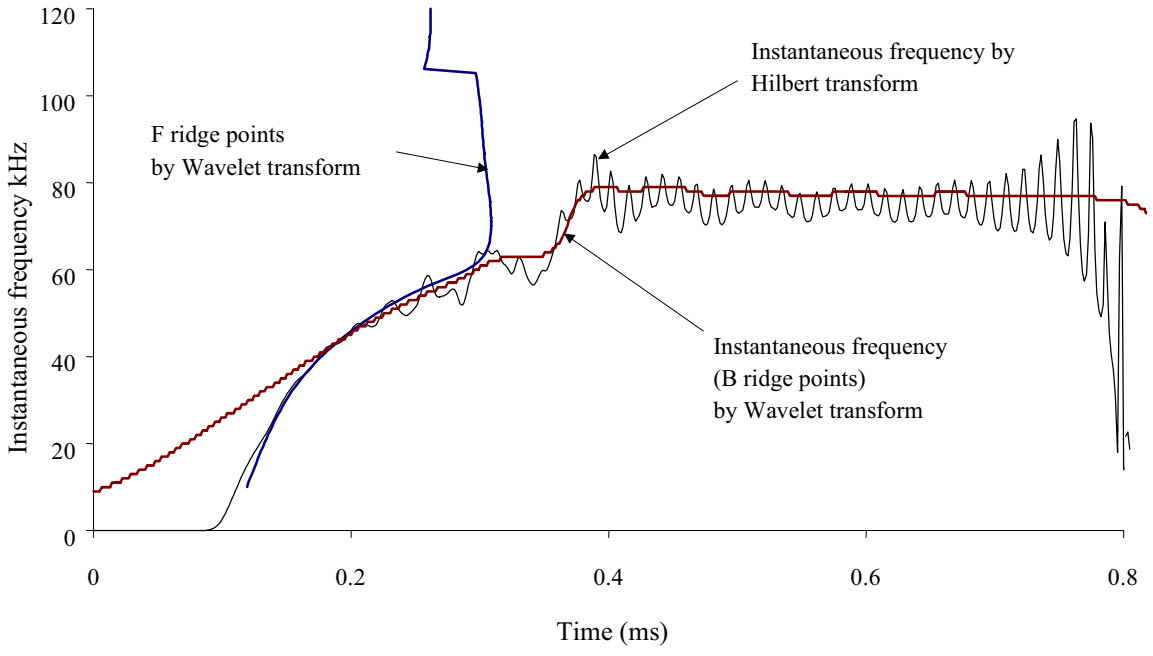

Figure A1.46 Comparison between: B ridge points of the CWT in Fig. A1.35 that represent the centre frequency of signal at a given point in time; the instantaneous frequency given by Hilbert transform; and the F ridge points of the CWT in Fig.A1.35 that represent the time at which the most significant energy of a frequency component occurs.

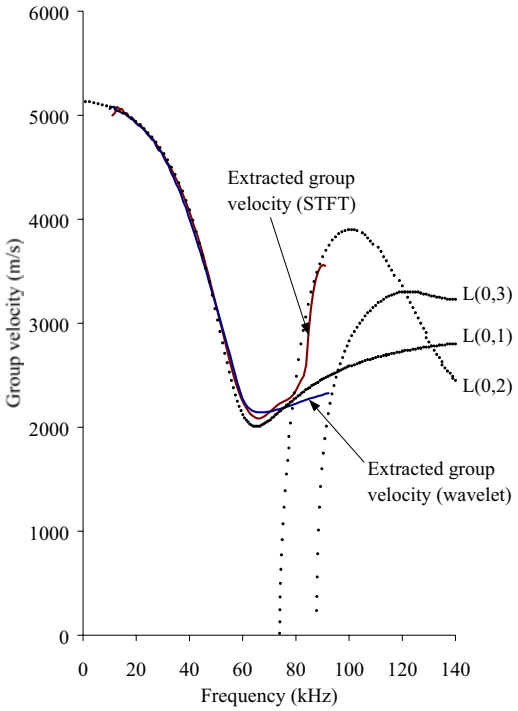

Figure A1.47. Group velocity extracted from signals shown in Fig A1.5 and Fig. A1.7 using the CWT and STFT technique. Disperse predictions for first three longitudinal modes shown as dots.

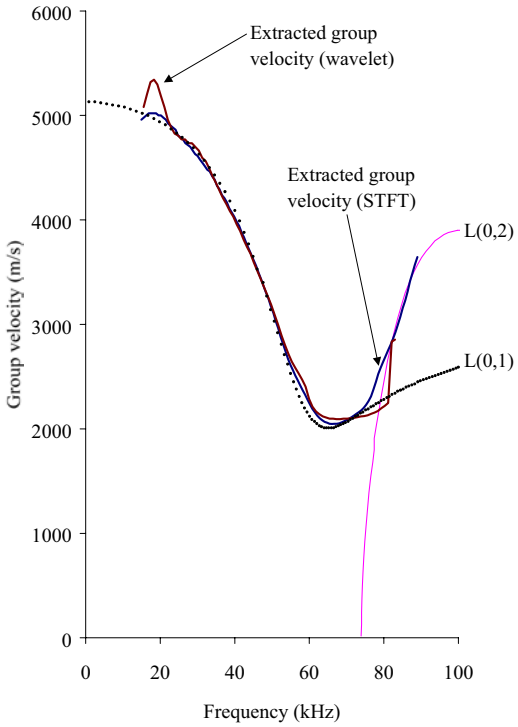

Figure A1.48. Group velocity extracted from the noisy signals shown in Fig A1.9 and Fig. A1.11 using the CWT and STFT technique.

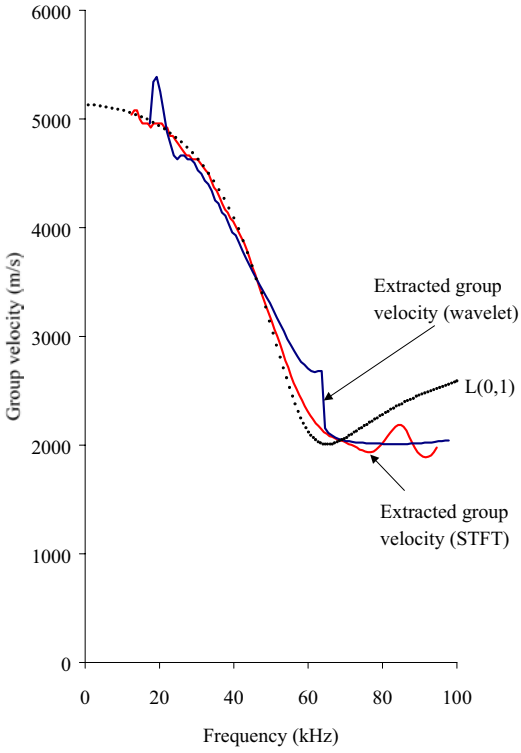

Figure A1.49. Group velocity extracted from the output signal with simulated reflection shown in Fig A1.15 using the CWT and STFT technique.

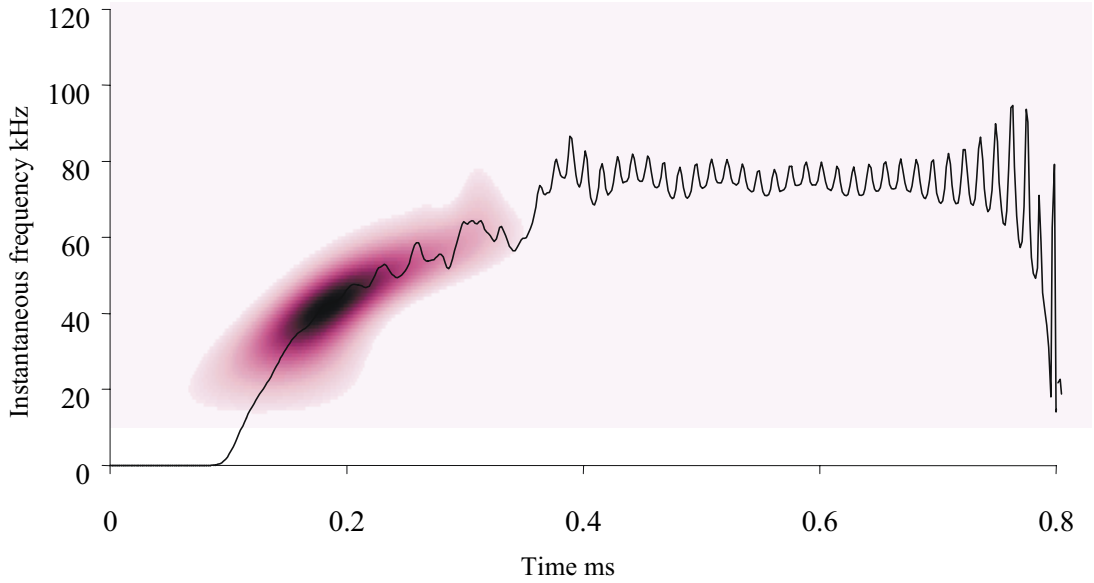

Figure A1.50. CWT shown in Fig. A1.36 with coefficients 30dB down from the maximum removed. Instantaneous frequency obtained by Hilbert transform shown to aid interpretation.

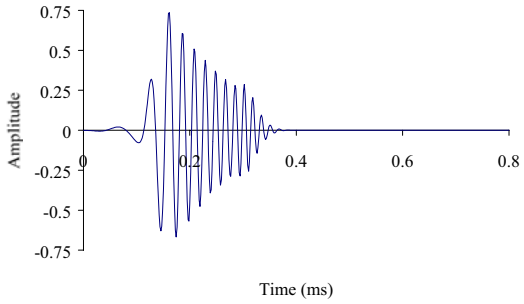

Figure A1.51. Inverse Wavelet transform coefficients of the energy filtered CWT shown in Fig A1.50.

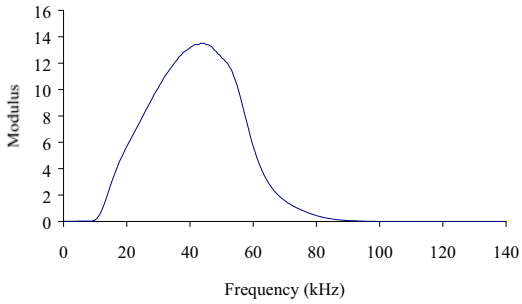

Figure A1.52. Modulus of the FFT for the energy filtered signal sown in Fig. A1.51.

Appendix 2

Component drawings for protype membrane shoes

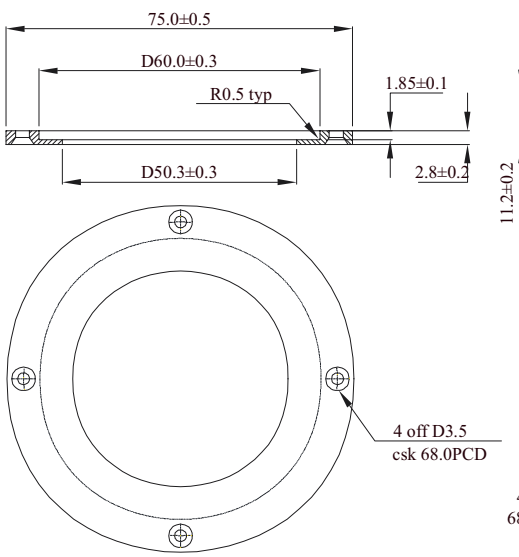

Figure A2.1a. Clamp plate
Aluminum. Alloy 1 off.

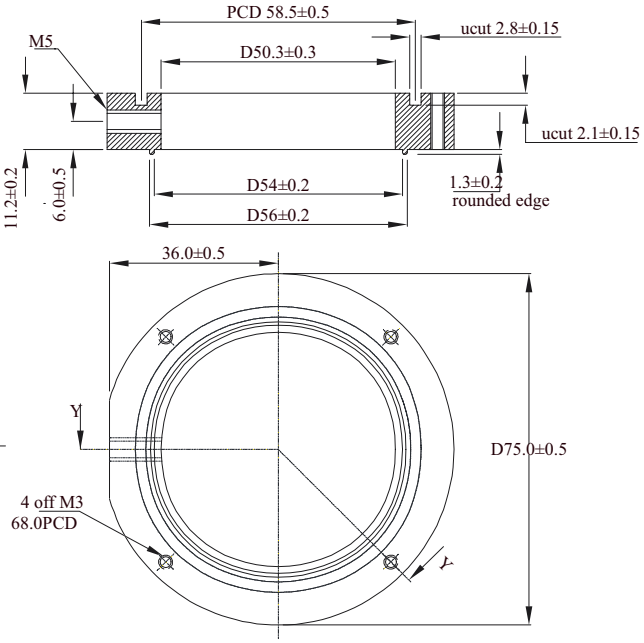

Figure A2.1b. Body.
Aluminum. Alloy 1 off.

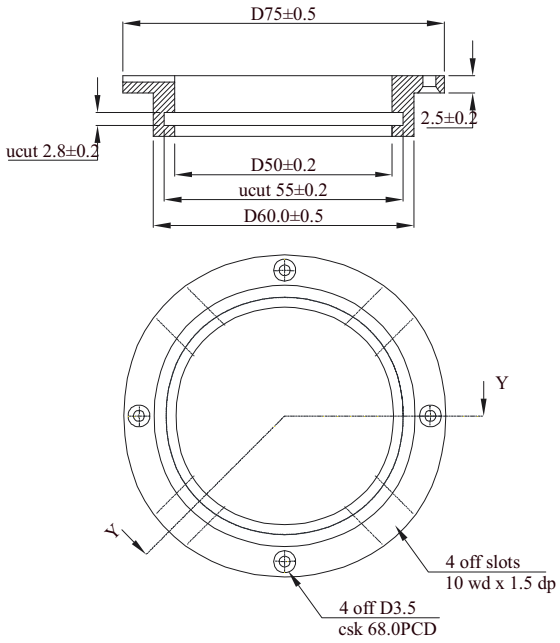

Figure A2.1c. Transducer holder
Aluminum. Alloy 1 off.

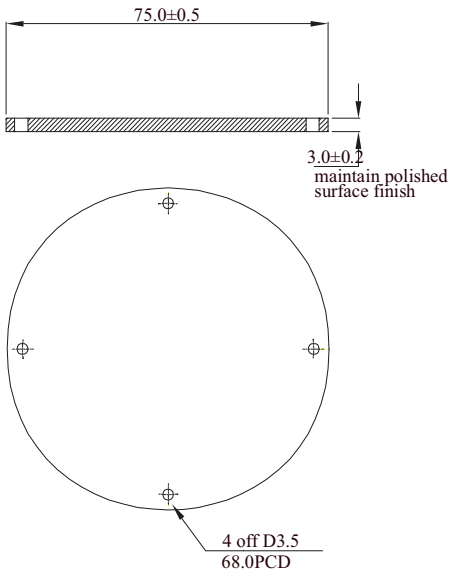

Figure A2.1d. Plate
Perspex 1 off.

Figure A2.1. Component drawings (not to scale) for prototype membrane shoes to fit the standard PUNDIT 54kHz transducers.

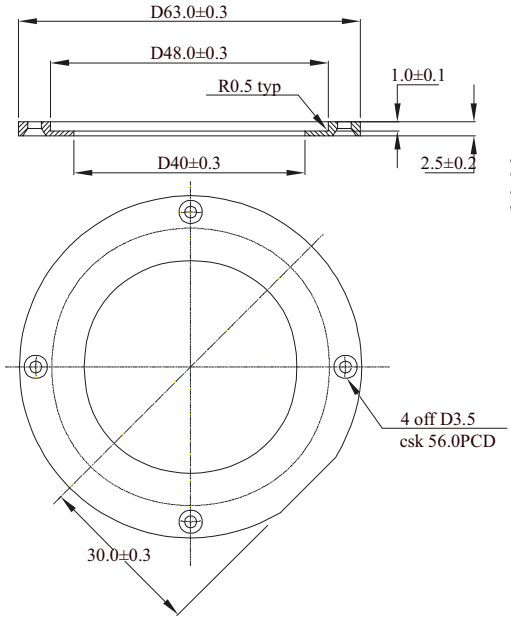

Figure A2.2a. Clamp plate
Aluminum. Alloy 1 off.

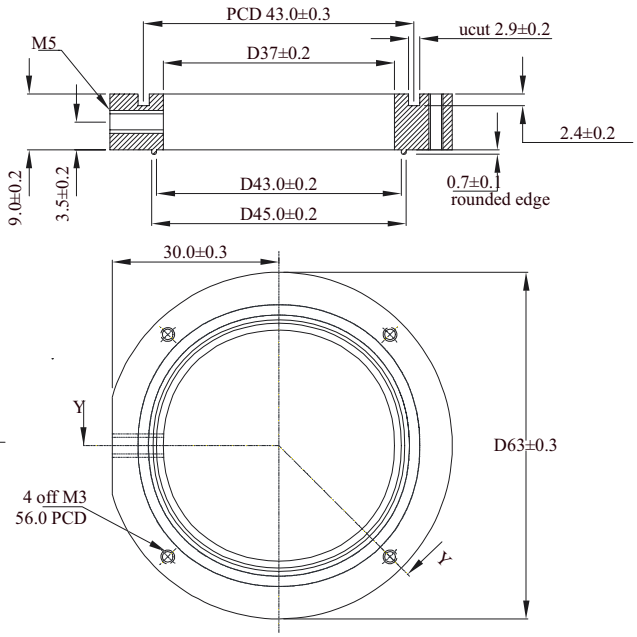

Figure A2.2b. Body.
Aluminum. Alloy 1 off.

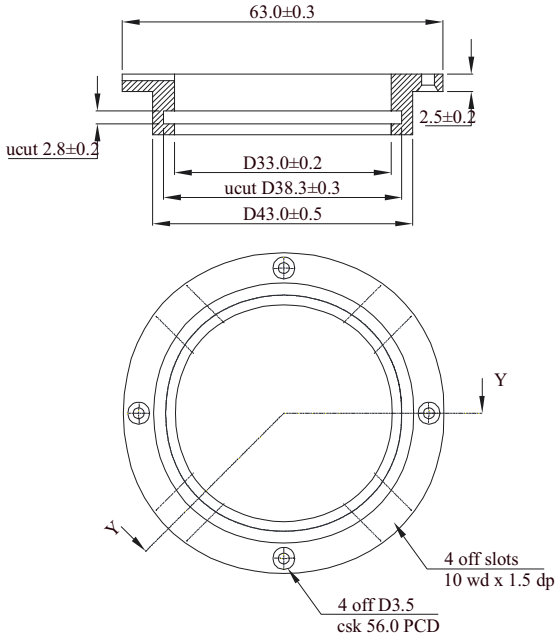

Figure A2.2c. Transducer holder
Aluminum. Alloy 1 off.

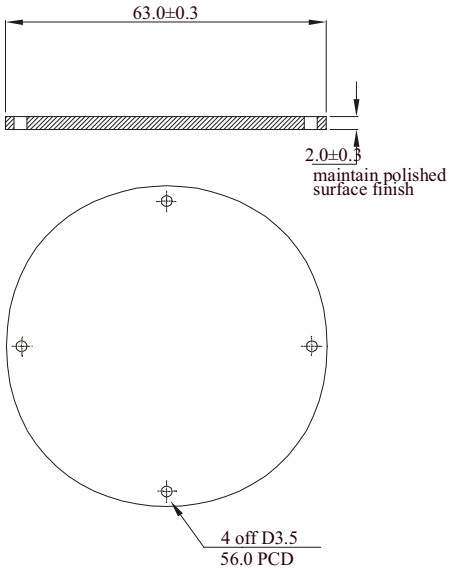

Figure A2.2d. Plate
Perspex 1 off.

Figure A2.2. Component drawings (not to scale) for prototype membrane shoes to fit the standard PUNDIT 83kHz transducers.

References

A. Abbate, D. Klimek, P. Kotidis and B. Anthony, "Analysis of Dispersive Ultrasonic Signals by the Ridges of the Analytic Wavelet Transform," in *QNDE* (D. Thompson and D. Chimenti, eds.), vol. 18, pp. 703-710, Plenum Press, New York, 1999.

B.T. Akhlaghi and W.H. Cogill, "Application of the free plate analogy to a single layered pavement system," *Insight* 36(7), pp.514-518, 1994.

B.T. Akhlaghi et al, "Analysis of pavements using an acoustic wave method -part 1," *Insight* 37(7), pp.531-535, 1995.

B. Audoin and J. Roux, "An innovative application of the Hilbert transform to time delay estimation of overlapped echoes," *Ultrasonics*, Vol. 34, No. 1, pp. 25-33.

ACI, *Specifications for structural concrete for buildings*, Amercian Concrete Institute, 1996.

D. N. Alleyne, The Nondestructive Testing of Plates using Ultrasonic Lamb Waves, Phd, Imperial College of Science Technology and Medicine, London, 1991.

D.R. Andrews and A.M. Hughes, "A novel ultrasonic transducer for inspecting concrete", IEEE Symposium on Ultrasonics & Ferroelectrics, Orlando, USA, 1991.

Y.C. Angel and J.D. Achenbach, "Reflection and transmission of elastic waves by a periodic array of cracks," *Journal of Applied Mechanics*, Vol. 52, pp. 33-41, 1985.

J.F. Archard, "Elastic deformation and laws of friction," Proceedings of the Royal. Society, Vol. A243, pp. 190-205, 1957.

ASTM C805, *Rebound number of hardened concrete*, American Society for Testing and Materials, Philadelphia.

ASTM D4788, *Determining the thickness of bound pavement layers using short pulse radar,* American Society for Testing and Materials, Philadelphia.

B. Auld, *Acoustic Fields and Waves in Solids*. Vol. 1. Stanford: Krieger publishing Company, 2nd ed., 1990.

J.M. Baik and R.B. Thompson, "Ultrasonic scattering form imperfect interfaces: a quasi-static model," Journal of non-destructive Evaluation, Vol. 4, pp. 177-196, 1984.

G. Ballard, GB Geotechnics, Cambridge, Private communication, 1996.

D. Bancroft, "The velocity of longitudinal waves in cylindrical bars," *Phys. Rev*. vol. 59, pp. 588-593, 1941.

D.R. Billson and D.A Hutchins, "Development of Novel Piezoelectric Ultrasonic transducers for Couplant-Free Ultrasonic Testing," *British Journal of Nondestructive Testing*, Vol. 35, pp. 705-708, 1993.

A. Boström and G. Wickham, "On the Boundary Conditions for Ultrasonic Transmission by partially Closed Cracks," *Journal of Nondestructive Evaluation*, Vol. 10, No. 4, 1991.

J. Boussinesq, " Application des potentiels a l'étude de l'équilibre et du mouvement des solides élastiques", Gauthier-Villars, Paris, 1885.

G. Bradfield and E. Gatfield, "Determining the thickness of concrete pavements by mechanical waves: directed beam method." *Concrete research,* 16(46): 49. 1964.

BS 1881: Part 201, *Guide to the use of non-destructive methods of test for hardened concrete*, British Standards Institution, London.

BS 1881: Part 203, *Recommendations for measurement of velocity of ultrasonic pulses in concrete*. British Standards Institution, London, 1986.

BS 1881: Part 205, *Recommendations for radiography of concrete*, British Standards Institution, London.

J.H. Bungey and S.G. Millard, *Testing of concrete structures*, Blackie Academic & Professional, London, 1996.

J.H. Bungey, "The validity of ultrasonic pulse velocity testing of in-place concrete for strength," *NDT International*, IPC press, pp296-300, 1980.

J.H. Bungey, “Ultrasonic testing to identify alkali-silica reaction in concrete.” *British Journal of NDT* , 33(5), pp. 227-231, 1991.

G. Canella, “The effect of couplant thickness in ultrasonic contact testing,” *British Journal of Nondestructive Testing*, pp.179-182, 1974.

H. L. R. Chen et al, “Impulse radar reflection waveforms of simulated reinforced concrete bridge decks.” *Materials Evaluation*, Dec. 94, pp. 1382-1388, 1994.

C. Chree, “The equations on an isotropic elastic solid in polar and cylindrical coordinates, their solutions, and applications,” *Trans. Cambridge Philos. Soc*., vol. 14, pp. 250-369, 1889.

C.K. Chui, *An Introduction to Wavelets, Wavelet Analysis and its applications*, Vol. 1, Academic Press, New York, 1992.

Concrete Society, *Concrete core testing for strength*, Technical Report 11, Concrete Society, London, 1987.

I. Daubechies, “Orthonormal bases of compactly supported wavelts,” *Commun. on Pure and Appl. Math*., Vol. XLI, pp. 901-996, 1988.

A.G. Davis et al. “Impact-echo and Impulse Response stress wave methods: Advantages and limitations for the evaluation of highway pavement concrete overlays.” *SPIE* 2946, pp. 88-96, 1996.

J.K. Dickson, *Dry coupling ultrasonic method of inspection on composite and metallic honeycomb panels on aircraft structure*, 10th World Conference on Non-destructive Testing, pp. 216-221, 1982.

B. Drinkwater and P. Cawley, “An ultrasonic wheel probe alternative to liquid coupling.” *Insight,* 36(6), pp. 430-433, 1994.

B.W. Drinkwater and P. Cawley, “An ultrasonic wheel probe alternative to liquid coupling,” in *QNDE* (D. Thompson and D. Chimenti, eds.), vol. 14, pp. 983-989, Plenum Press, New York, 1995.

B.W. Drinkwater, *The Use of Dry Coupling in Ultrasonic Nondestructive Testing*, Thesis for the degree of Doctor of Philosophy, University of London, 1995.

B.W. Drinkwater and P. Cawley, "The Practical Application of Solid Coupled Ultrasonic Transducers," *Materials Evaluation*, pp. 401-406, 1997

B.W. Drinkwater, R.S. Dwyer-Joyce and A.M. Robinson, "The use of ultrasound to investigate rough surface contact phenomena," in *QNDE* (D. Thompson and D. Chimenti, eds.), vol. 18A, pp. 1455-1462, Plenum Press, New York, 1998.

M.J. Evans, *The Use of Diffuse Field Measurement For Acoustic Emission*, Thesis for the degree of Doctor of Philosophy, University of London, 1997.

U. Ewert, V.A. Baranov et al, "Cross-sectional imaging of building elements using Cobalt radiation." *NDT&E International* 30(4), pp. 243-248, 1997.

C.A. Fairfield et al, "Radar measurement of density variations around an arch bridge." *Insight,* 37(11), pp. 871-874, 1995.

B. Fay, "Ultrasonic backscattering: fundamentals and applications," *Physical Acoustics*, Eds. O. Leroy, M.A. Breazeale, Plenum Press, New York, 1991.

W.B. Fitcher, Langley Research Center, Hampton, Virginia, NASA Technical Paper 3658, (1997).

J. Forrest, "In-situ measuring techniques for pile length". Port Hueneme, CA, Civil Engineering Laboratory, Naval Construction Battalian Center, 1977.

I.G. Goryacheva, *Contact mechanics in tribology*, (Kluwer Academic, Dordrecht,) p. 51, 1998.

P. Goupillaud, A. Grossmann and J. Morlet, "Cycle-octave and relatedtransforms in seismic signal analysis," *Geoexploration*, 23, pp. 85-102, 1984.

K.F. Graff, *Wave Motion In Elastic Solids* Ohio: Clarendon Press, Oxford, 1975

J.A. Greenwood and J.B.P. Williamson, “Contact of Nominally Flat Surfaces,” Proceedings of the Royal. Society, Vol. A295, pp.300-319, 1966.

P. Guillemain and R. Kronland-Martinet, *Proc. of IEEE, Special Issue on Wavelets*, Vol. 48, No. 4, pp. 561-585, April 1996.

N.F. Haines, “The theory of sound transmission and reflection at contacting surfaces,” CEGB Report RD/B/N4744, Berkeley Nuclear Labs, 1980.

M. S. A. Hardy and M.O. Gordon “Surface Penetrating Radar for the non-destructive evaluation of highway pavements”, Non-destructive testing of highway pavements, IEE, London, 1997.

R. Halmshaw, *Non-destructive testing*. London, Edward Arnold, 1987.

T.H. Havelock, *The Propagation of Disturbances in Dispersive Media* London: Cambridge University Press, 1914.

H. Hencky, “On the stress state in circular plates with vanishing bending stiffness,” *Zeitschrift für Mathematik und Physik*, vol. 63, pp. 311-317, 1915.

D. Hitchings, “FE77 user manual version 2.45”, Imperial College of Science Technology and Medicine, London, 1997.

F. Hlawatsch and G.F. Boudreaux-Bartels, “Linear and Quadratic Time-Frequency Signal Representations,” *IEEE Signal Processing*, 21, 50, April 1992.

S. Howkins, “Measurement of pavement thickness of concrete pavements by rapid and non-destructive methods”, National Co-operative Highway Research Program, Report 52, 1968.

N.H. Hsu and D.G. Eitzen, “Point Source/Point Receiver Ultrasonic Wave Speed Measurement,” in Ultrasonics International 87 Conf. Proc.

James Electronics Inc., *Instruction manual for model C-4899 V-Meter*, James Electronics Inc. Chicago, Illinois.

K.L. Johnson, *Contact Mechanics*, Cambridge University Press, Cambridge, 1985.

R. Jones, *Non-destructive testing of concrete*. Cambridge, Cambridge University Press, 1962.

M.C. Junger and D. Feit, *Sound, Structures, and Their Interaction*, MIT Press, 1986

T. Kay, *Assessment & Renovation of concrete stru*ctures, Longman Scientific & technical. New York, 1992.

G.W.C. Kaye and T.H. Laby, *Tables of Physical and Chemical Constants*, Longman, Harlow, 1995.

P. Kear and M. Leeming, "Radiographic inspection of post-tensioned concrete bridges." *Insight* 36(7), pp. 507-510, 1994.

K. Kendall and D. Tabor, "An ultrasonic study of contact between stationary and sliding surfaces," Proceedings of the Royal. Society, Vol. A323, pp. 321-340, 1971.

B. Koehler, G. Hentges, et al, "A novel technique for advanced ultrasonic testing of concrete be using signal conditioning methods and a scanning laser vibrometer." *NDT in Civil Engineering1997 conference proc.* Liverpool, pp.123-134, 1997.

H. Kolsky, *Stress Waves In Solids*. Dover Publications, New York, 1963.

M. Krause and H. Wiggenhauser, "Ultrasonic pulse echo technique for concrete elements using synthetic aperture." NDT in civil engineering 1997 Liverpool conference proc 8, 1997.

J. Krautkramer and H. Krautkramer, *Ultrasonic Testing of materials*, G. Allen & Unwin, 1969.

P. Kumar and E. Foufoula-Georgiou, "Wavelet Analysis in Geophysics: An Introduction," in *Wavelets in Geophysics* (P. Kumar and E. Foufoula-Georgiou, eds.), Academic Press, New York, 1994.

A. Libai and J.G. Simmonds, *The nonlinear theory of elastic shells*, Cambridge University press, pp 542, 1998.

Y. Lin et al. “Recent developments in the impact echo technique for non-destructive evaluation of concrete structures*.” 14th World Conference on Non Destructive Testing*, New Delhi, India, pp. 831-834, 1996.

R. Long, M. Lowe, and P. Cawley, “INVESTIGATION INTO CONVENIENT COUPLING FOR ULTRASONIC TRANSDUCERS WHEN INSPECTING CONCRETE STRUCTURES,” in *QNDE* (D. Thompson and D. Chimenti, eds.), vol. 19, pp., Plenum Press, New York, 1999.

R. Long, M. Lowe, and P. Cawley, “AN AXI SYMMETRIC NUMERICAL ELASTIC CONTACT MODEL FOR APPLICATION TO THE TRANSMISSION OF ULTRASOUND ACROSS A ROUGH INTERFACE,” in *QNDE* (D. Thompson and D. Chimenti, eds.), vol. 19, pp., Plenum Press, New York, 1999.

A.E.H. Love, *The Mathematical Theory of Elasticity*, Cambridge University Press, 4th ed., 1927.

M. Lowe, *Plate Waves for the NDT of Diffusion Bonded Titanium*. PhD, Imperial College of Science Technology and medicine, 1993.

V.M. Malhotra and N.J. Carino, *Handbook on NDT of Concrete*, Eds. V.M. Malhotra and N.J. Carino, CRC Press, Boston, 1991.

S. Mallat, “Multifrequency channel decomposition of images and wavelet models,” *IEEE Trans. on Acoustics, Speech and Signal Anal*., 37(12), pp. 2091-2110, Dec. 1989.

S. Mallat, *A Wavelet Tour of Signal Processing*, Academic Press, San Diego, CA, 1998.

L.E. Malvern, *Introduction To The Mechanics Of A Continuous Medium Michigan*: Prentice-Hall, New Jersey, 1969.

G. Mays, *Durability of concrete structures*, E & FN Spon, London, 1992.

Y. Meyer, “Ondolettes et applications,” *J. Annu. Soc. Math*., Soc. Francaise Math., Paris, France, pp. 1-15, 1990.

S. Mindess and J. Young, *Concrete*, Prentice Hall, New Jersey, 1981.

J. Morlet, G. Arens, E. Fourgeau and D. Giard, “Wave propagation and sampling theory-part 1: complex signal and scattering in multilayered media,” *Geophysics*, 47(2), pp. 203-221, 1982.

J. Morlet, G. Arens, E. Fourgeau and D. Giard, “Wave propagation and sampling theory-part 2: sampling theory and complex waves,” *Geophysics*, 47(2), pp. 2222-236, 1982.

S.E. Moubarik, D. De Vadder and P. Benoist, “Wavelets and Nondestructive Evaluation,” in *QNDE* (D. Thompson and D. Chimenti, eds.), vol. 12A, pp. 727-734, Plenum Press, New York, 1993.

E. Nagy and E. Landis, “Analysis of x-ray micro-tomographic images to measure work of fracture in concrete.” in *QNDE* (D. Thompson and D. Chimenti, eds.), vol. 16, pp 1761-1766, Plenum Press, New York, 1997.

T.R. Naik and V.M. Malhotra, “The ultrasonic pulse velocity method,” Chapter 7 in *Handbook on NDT of Concrete*, Eds. V.M. Malhotra and N.J. Carino, CRC Press, Boston, 1991.

S. Nazarian. and M.R. Baker, “Limitations and advantages of sonic and ultrasonic methods as tools for maintenance management of bridge decks and concrete slabs.” *SPIE* 2946, pp. 184-194, 1996.

A.M. Neville and J.J. Books, *Concrete Technology*, Addison Wisley Longman, 1990.

A.M. Neville, *Properties of Concrete*, John Wiley and Sons Inc. 1996.

T. Önsay and A.G. Haddow, “Comparison of STFT, Gabor and wavelet transforms in transient vibrabration analysis of mechanical systems,” *J. Acoust Soc. Am.* 3, 2290(A), 1993.

E.P. Papadakis, “The measurement of ultrasonic attenuation,” *Physical Acoustics* 19, pp107-155, 1990.

B. Pavlakovic, M. Lowe, D. Alleyne and P. Cawley, “Disperse : a general purpose program for creating dispersion curves,” in *QNDE* (D. Thompson and D. Chimenti, eds.), vol. 16A, pp. 155-192, Plenum Press, New York, 1997.

B. Pavlakovic, *Leaky Guided Ultrasonic waves in NDT*. PhD, Imperial College of Science Technology and medicine, 1998.

P.H. Perkins, *Repair, protection and waterproofing of concrete structures*, E & FN Spon, London, 1997.

PCA, *Design and control of concrete mixtures*, Portland Cement Association, 1994.

T. Pialucha, C.C.H. Guyott and P. Cawley, "Amplitude spectrum method for the measurement of phase velocity," *Ultrasonics*, Vol. 27, September, pp. 270-279, 1989.

T.P. Pialucha, *The reflection coefficient from interface layers in NDT of adhesive joints, PhD,* University of London, 1992.

J. Pochammer, "Ueber die Fortpflanzungsgeschwindigkeiten kleiner Schwingungen in einem unbergrenzten isotrpen Kreiscylinder," *J. f. d. reine und angewandte Math*., vol. 81, pp. 324-336, 1876.

S. Popovics et al, "Comparison of DIN/ISO 8047 (Entwurf) to several standards on determination of ultrasonic pulse velocity in concrete." International Symposium Non-Destructive Testing in Civil Engineering, Berlin, 1995.

J.S. Popovics and J.D. Achenbach, "Airport pavement NDE research at CQEFP." *SPIE* 2945, pp. 294-302, 1996.

T.M. Proctor, Jr. "An improved piezoelectric acoustic emission transducer," *J. Acoust. Soc. Am.* 71, pp. 1163-1168, 1982.

W.H. Prosser, M.D. Seale and B.T. Smith, "Time-frequency analysis of the dispersion of Lamb modes," *J. Acoust Soc. Am.* 105 (3), 2669, 1999.

PUNDIT 6, Operating manual, CNS Farnell, Manor Way, Borehamwood, Herts.

R.B. Randall, *Frequency Analysis*, Brüel and Kjær, 1977.

M. Redwood, *Mechanical Waveguides* London: Pergamon Press, Oxford, 1960.

J.L. Rose, *Ultrasonic waves in solid media*, Cambridge University Press, Cambridge, U.K. New York. 1999.

T. Saarenketo and M.K. Soderqvist "Ground Penetrating Radar applications for bridge deck evaluations in Finland." *Insight,* 36(7), pp. 496-501, 1994.

W. Sachse and Yih-Hsing Pao, "On the determination of phase and group velocities of despersive waves in solids," *J. Appl. Phys*. Vol. 49, No. 8, pp. 4320-4327, 1978.

R.S. Sayles, "The profile as a random process," in *Rough Surfaces*, Ed. T.R. Thomas, Longman Group Ltd, 1982.

M. Sansalone and N.J. Carino, "Impact echo: A method for flaw detection in concrete using transient stress waves," NBSIR 86-3452, National Bureau of Standards, September 1986.

M. Sansalone and N.J. Carino, "Stress wave propagation methods," *Handbook on NDT of Concrete*, Eds. V.M. Malhotra and N.J. Carino, CRC Press, Boston, 1991.

G. Schickert, "NDT in civil engineering in Germany." *Insight* 36(7), pp. 489-495, 1994

M. Schickert "Towards SAFT-Imaging in ultrasonic inspection of concrete." *International Symposium Non-Destructive Testing in Civil Engineering*, Berlin, 1995.

M.G. Silk, *Ultrasonic Transducers for Nondestructive Testing*, Adam Hilger Ltd, Bristol, 1984.

M. Silk and K. Bainton, "The propagation in metal tubing of ultrasonic wave modes equivalent to lamb waves," *Ultrasonics*, pp. 11-19, 1979.

R.V. Southwell, *Theory of Elasticity*. Clarendon Press, Oxford, 1941.

K.H. Stokoe and S. Nazarin, "Use of surface-waves method in pavement evaluation", Trans. Research Records, 1070, 1986.

H.G. Tattersall, "The ultrasonic pulse-echo technique as applied to adhesion testing," Journal of Applied Physics D: Applied physics, Vol. 6, pp. 819-832, 1973.

S. Timoshenko and J. Goodier, *Theory of Elasticity*, (Macraw Hill, New York, 1982).

S. Timoshenko and S. Woinowsky-Krieger, *Theory of plates and shells*, (Macraw Hill, New York, 2nd edition 1959).

H.N. Tomsett, "Nondestructive testing of floor slabs." *Concrete* , 8(3), pp. 41-42, 1992.

K. Veroy, S. Wooh and Y. Shi, "Analysis of dispersive waves using the wavelet transform," in *QNDE* (D. Thompson and D. Chimenti, eds.), vol. 18a, pp. 687-694, Plenum Press, New York, 1999.

J. Ville, "Theorie et Applications de la Notion de Signal Analytique," *Câbles et Transmissions*, Vol. 2a, pp. 61-74, 1948.

J. Waddell and J. Dobrowokski, *Concrete Construction Handbook*, Magraw-Hill, 1999.

J.P. Warhust et al, "Advanced Ground-Penetrating, Imaging Radar for bridge inspection." Lawrence Livermore National Laboratory , California, USA: 9, 1993.

M.N. Webster and R.S. Sayles, "A Numerical Model for the Elastic Frictionless Contact of Real Rough Surfaces," Trans. ASME Journal of Tribology, Vol. 108 No. 3 pp 314-320, 1986.

G. J. Weil, "Infrared thermographic techniques". *Handbook on NDT of Concrete*. V. M.

L. Weizheng and Y. Yiyoung, "Ultrasonic detection of cement concrete pavement thickness." *14th World Conference on Non-destructive Testing*, New Delhi, India, pp. 839-842, 1996.

M.A. West, M.N. Webster and R.S. Sayles, "A new method for rough surface contact analysis", Proceedings of the IMechE C161/87, 1987.

M.A. West and R.S. Sayles, "A 3-dimensional method of studying 3-body contact geometry and stress on real rough surfaces," The 14th Leeds Lyon Symposium, *Interface Dymanics*, 1987.

D.J. Whitehouse and J.F. Achard, “The properties of random surfaces of significance in their contact,” Proceedings of the Royal. Society, Vol. A316, pp.97-121, 1970.

A.B. Woolbridge,” The effects of compressive stress on the ultrasonic response of steel-steel interfaces and of fatigue cracks,” CEGB Report NW/SSD/RR/42/79, North Western Region, 1979.

T.T. Wu et al. “Determination of the depth of a surface-breaking crack using transient elastic waves.” *J.Acoust. Soc. Am.* 97(3), pp. 1678-1686, 1995.

T.T. Wu and J.S. Fang, “A new method of measuring *in situ* concrete elastic constants using horizontally polarised conical transducers,” *J. Acoust. Soc. Am.* 101 (1), pp. 330-334, 1997.

I. Yalda-Mooshabad, F.J. Margetan, T.A. Gray and R.B. Thompson, “Reflection of Ultrasonic Waves from Imperfect Interfaces: A combined Boundary Element Method and Independent Scattering Model Approach,” *Journal of Nondestructive Evaluation*, Vol. 11, Nos. 3/4, 1992.

R.K. Young, Wavelet Theory and its Applications, Kluwer Academic Press, 1992.